Control and characterization of microtubule kinesin active fluid behavior

By

Teagan Bate

A Dissertation

Submitted to the Faculty

Of the

WORCESTER POLYTECHNIC INSTITUTE

In Partial Fulfillment of the Requirements for the

Degree of Doctor of Philosophy

in

Physics

_____

April, 2023

APPROVED:

_____

Kun-Ta Wu, PhD, Major Advisor, Physics Department, WPI

_____

Qi Wen, PhD, Dissertation Committee, Physics Department, WPI,

_____

Thomas Powers, PhD, Dissertation Committee, Engineering Department, Brown University

_____

Michael Norton, PhD, Dissertation Committee, Physics Department, Rochester Institute of Technology

ABSTRACT

The field of active matter is striving to make real connections with cell biology and develop useful materials. Microtubule kinesin active fluid is an active matter platform that provides an opportunity to advance our capabilities in *in-vitro* purified cytoskeletal active materials and cell simulations. The techniques of control and characterization we establish in this system create a vocabulary and fluency that will enable the engineering of new active matter systems to simulate biological phenomena and craft new functional materials. In addition, microtubule kinesin active fluid may yet shed light on the self-organization of diffusive and advective transport behavior in the crowded, active, and many-constituent cytoplasm, while continuing to reveal new characterization and control techniques. The work described in this dissertation expands these techniques of control and characterization, and provides new insight connecting kinesin kinetics, diffusion, and advection in the context of active cytoskeletal fluid.

In our first investigation, we explore the relationship of kinesin kinetics at the nanoscale to active fluid flow at the mesoscale. We control the mean speed of both gliding assays and active fluid with temperature. By measuring the activation energy from the velocity temperature profiles, we connect mesoscale fluid activity to nanoscale kinesin kinetics to understand their role in both 2D gliding assays and 3D active fluids.

Next, we investigate how flow couples to diffusional and advective mixing in active fluid. Having established temperature as an effective technique to control mean speed temporally, we show how to control mean speed spatiotemporally by applying temperature gradients to active fluid and investigate if such mean speed gradients can enhance mixing.

Next, we use light-released ATP to induce mean speed gradients. We find that as spatially released ATP spreads through samples, activity spreads with it, creating a propagating active-passive interface. Considering this evolution from a non-uniform to uniform activity as mixing, we find that the interface progression undergoes a transition from regular to super diffusive-like spreading at a critical Peclét number.

These works highlight the advancement of control and characterization techniques for microtubule kinesin active fluid and their associated intellectual merit which will inform the development of autonomous, limited self-assembling, controllable active materials, as well as supporting future investigations of the underlying mechanics of constituents and systems in living cells.

ACKNOWLEDGEMENTS

First, I would like to start by thanking my advisor, Professor Kun-Ta Wu. Kun-Ta and I arrived at Worcester Polytechnic Institute at the same time in August of 2017. I had just completed my undergraduate degree at the University of New Hampshire and Kun-Ta had just finished his postdoc with Professor Zvonomir Dogic at Brandeis University. We were both fresh starts. At the time, I was not yet focused on a specific research niche of interest. I do not recall competing to be Kun-Ta's student nor being headhunted. Another words, our partnership was initiated more by chance than by either of our grand intentions. However, retrospectively, this meeting was both serendipitous and momentous. Now, I hold my scientific career at the core of my life, and consider my interest in active matter, soft matter, complex fluids and biophysics as an essential driving force for my future. In those first months, I did not understand the level of commitment, energy, and persistence required to be a great research assistant. Kun-Ta pushed me to dedicate myself to the work we were both relying on under practical pressures: publications, grants, etc. This was a hard time. However, I consistently decided to trust Kun-Ta. Thus, overtime, I began to develop an insight into his perspective and wisdom. Through the combination of Kun-Ta's consistent support and guidance, and my decision to trust his perspective, I have developed into the scientist I am today. I therefore wish to thank Kun-Ta for being the critical force that enabled me to develop the scientific perspective and skills I have thus far. Ending up loving the science itself in the process is the essential key that enabled this to work, and I think it is essential in any PhD. We are not in this for the money. I believe that this spark and passion for the experience of scientific discovery is innate, but in the context of working with others, it is best nurtured when it resonates with a similar innate passion in one's mentor, as mine has with Kun-Ta's. Though I am Kun-Ta's first PhD graduate, I expect that many great scientists will develop under the tutelage and support of Wu lab.

Next, I would like to thank all the Wu lab team members I had the opportunity to work alongside in the course of my six years here. As one of Kun-Ta's first graduate students with Edward Jarvis, I often had the privilege of playing a mentorship role with talented students; many during their first experience in scientific research. This allowed me to learn how to play the role of guide and support, and to have the luxury of enjoying the comradery and liveliness of burgeoning researchers. This was a great boon for me, and I expect it will be a critical foundation for any future mentorship I am lucky enough to enjoy. I would like to especially acknowledge my current undergraduate student Ezra Taylor, who has been working with me for nearly a year and contributed significantly to the data in the final chapter of this dissertation and my best work at Wu lab. He is a steadfast research assistant already. However, his distinguishing quality is an interest in experiments and passion for asking great questions. I believe these qualities will lead him on a journey of discovery. Good luck Ezra! I also want to thank both Edward Jarvis and Josh Dickie, who have been my colleagues here at Wu lab. Over the years, they supported and worked with me on experiments in both of my publications. They also proved steadfast friends outside of the lab, where we had great conversations due to our deep mutual understanding of our shared work and the enviroment of graduate school. I would like to appreciate the energy of group meetings in Wu lab. In our job applications, we may claim to have come up with a specific idea or solution to a problem. In reality, these leaps often occur in a group meeting, and seem to grow organically from everyone present, untraceable to any one individual, our minds in some cooperative network, producing solutions more powerful than the sum of the parts, so to speak. Kun-Ta, along with all the members of Wu lab, have created and sustained this wonderful enviroment of interest and creativity, which has been a great enviroment to do a PhD.

Next, I would like to acknowledge the great role that the Brandeis MRSEC community has played in my experience. Here at WPI, Wu lab is a lone island of microtubule kinesin active fluid. However, through Kun-Ta's ties with Brandeis, our lab members have been generously included in the Brandeis MRSEC community. The

Brandeis MRSEC Winter School has been a scientific highlight every year, and the friends and network I have gained through the MRSEC over the years has laid the foundation of my scientific network. I especially want to thank John Berezney and Mike Norton. Both have been invaluable friends, colleagues, and mentors to me through these years. Mike is now at RIT and is one of my committee members for this dissertation. Thanks Mike! Being a few steps ahead of me in the path has allowed them to shed light on the challenges I have been facing from a perspective not too far removed. They also have shared with me their own challenges and unsolved questions. They are some of the most interesting and talented scientists in the field. I am confident they will go on to do more fascinating science and guide more young scientists to pursue research perspicaciously. I will continue to lean on them for friendship and advice.

In addition to Mike and Kun-Ta, I would like to thank Professor Qi Wen and Professor Thomas Powers for serving on both my proposal and dissertation committee over the years. As one of the few fellow biophysicists at WPI, Qi has supported both Kun-Ta and myself through the development of Wu lab and my journey to my defense. I am grateful to have Tom as a member of my committee. Our lab has been lucky to have ongoing collaboration with his wonderful group at Brown University. To have theorists and experimentalists energetically interested in each other's work and striving to connect them to create a larger story has created a great enviroment bridging Brown and WPI. Tom's deep experience in marrying theory and experiment in soft matter, active matter, and complex fluids has provided a powerful perspective on this work.

I would also like to thank Qi's student Jiazhang Chen, who has become one of my good friends here at WPI. Jaz, Josh, and I have got in the habit of having dinner together on a semi-regular basis, and it has not been too hard, because it is always easy to say yes to spending time in this company. Conversations ranged from philosophy and culture to discussions of food, games, booze, and of course, physics. Regardless of the topic, we always seem to have a good time together, and go home well fed and smiling.

Next, I would like to thank my friends outside of the lab and physics at WPI. Sabine, Peter, and Ann-Marie were my rock climbing partners in these latter years. As early risers, we have spent three mornings a week together on the wall. In rock climbing, you literally trust your life to your belay partners. I think this encourages a strong *tie* between climbers. This has been an essential space for me to clear my head, which tends to be enforced when you are up in the air clinging to the wall. Equally important to exercise and mental hygiene is all the great conversation I got to have with them over these years. I will think of these times as I enter whatever climbing gym is next in my future. I'd also like to thank the members of my DnD group, Sabine, Patryck, Abhinav, Gabi, Peter and Nik. When the workload was high, they stole me away once a week to spend hours in companionship, gaming and fun. I will think of them when I think of WPI.

I would like to specially thank a few of my friends outside of WPI; Eric, Amanda, Chris, and Dom, who allowed me to step outside of the rigors of graduate life for precious moments of love, friendship, adventure, and appreciation of the present. They have been a wellspring of fulfillment and happiness in my life.

I would like to thank my parents, John and Shirley. Of course, without them, everything would have been impossible. One way or another, it has worked out that both are my close friends and confidants. Throughout my journey through graduate school, I have always shared the experience with them, and their love, support, and perspective has shaped my outlook and decisions. Words cannot describe the immensity of their contribution to this success. Finally, I would like to thank my brothers Colin, Dylan and Will. As with parents, one is particularly lucky when siblings turn out to be kindred spirits. Their friendship and steadfast support have added great richness and stability to my life in graduate school.

CONTENTS

CHAPTER 1: INTRODUCTION A new thrust has emerged in the past decade in the field of active matter Its aim is twofold: to understand the underlying mechanics of cells, and to develop self-assembling controllable active materials[1-5]. These goals are pursued by investigating and modeling biomimetic active systems, often composed of biological constituents, such as microtubules and kinesin motors, *in-vitro*. The two aims are synergistic. As the community engineers controllable biomimetic active systems, they discover subtle properties of the collective behavior of constituents, bringing insight to the complex collective behavior of cells. As we understand microbiology more *in-vivo*, we are inspired to leverage the natural strengths and capabilities of biological components in the design of biomimetic active materials.

My work herein focuses on controlling microtubule kinesin active fluid with temperature, nanoscale constituent design, and non-uniform activation patterning to contribute to these goals.

1.1 ACTIVE MATTER Microtubule kinesin active fluid is an active matter system. Active matter systems are made up of many autonomous constituent agents[3,5]. These agents individually consume chemical fuel at the microscale to become motile[3,5]. Due to the continuous internal microscale energy injection and autonomous motility of components, active matter is inherently non-equilibrium. Non-equilibrium systems may be intuitively characterized by their time-reversal asymmetry, which becomes obvious to an observer when watching dynamic processes played in reverse. Distinguishing a system as active matter can be subtle. For example, there are passive systems that while satisfying the non-equilibrium requirement, are driven by external energy injection, rather than internal, and thus are not classified as active matter, such as Rayleigh-Bénard convection (Fig. 1a)[6,7].

Hierarchical self-organization is a key emergent behavior of both soft matter and active matter systems. A hierarchy is a system of organization in which the elements are grouped in ranks, one above the other. Self-organization occurs hierarchically across scales in biology (all organisms are active matter[8]). In biology, hierarchical self-organization begins with DNA and protein folding, progressing to the development and organization of organelles, to single cells, which already represent an unfathomable complexity. Yet it continues to tissues, organs, organism communities, and finally entire ecosystems.

The ability of autonomous agents in active matter to self-assemble hierarchically through the nano- to the mesoscale allow nanoscale engineering to control vast collective mesoscale behaviors. Developing simple internal controls on constituents and external controls on entire systems to enable global controllability of collective behavior represents the key thrust of the biomimetic active fluid community to pave the way to limited self-assembling, autonomous, controllable active materials. This goal is analogously represented in microbiology by the behavior and capabilities of neutrophils in pursuing bacteriophages among red blood cells[9]. The neutrophil is autonomous and created by limited self-assembly. After self-

FIG. 1: RAYLEIGH-BÉNARD CONVECTION Logarithm of the magnitude of the buoyancy gradient in simulated Rayleigh-Bénard convection (adopted from Fodor *et al.*, Boundary Layer Meteorol., 2019, **172** (3), 371-396).

assembling from its DNA programing, it chases the bacteriophage on its own, powered by its internal fuel reservoir which can be replenished from the environment, all at the microscale.

The field of swarm robotics has been evolving for three decades and is garnering increasing attention from both industry and academics. One future system such swarm roboticists imagine are swarms of microscopic, bio-inclusive and or biomimetic soft robots which may use hierarchical self-assembly for certain tasks[10]. These systems will have applications in agricultural pest control and drug delivery[10]. If this future is to be realized, active matter physicists and swarm roboticists will need to collaborate. The progression of applied science will continue to blur the boundaries between niches and fields from previously disparate disciplines.

> "How many times when you are working on something frustratingly tiny have you said to yourself: If I could only train an ant to do this! ... . What I would like to suggest is ... training an ant to train a mite to do this. What are the possibilities of small but movable machines?" – Richard Feynman, 1959

1.2 COMPLEX FLUIDS AND SOFT MATTER Active matter distinguishes itself from the fields of complex fluids and soft matter by its internally driven, far-from-equilibrium nature. However, active matter has been built on the theory and tools of complex fluids and soft matter, and they often share emergent collective behaviors due to self-organization.

Complex fluids may be considered a sub-field of soft matter. Complex fluids are mixtures that have coexisting phases: suspensions, granular materials, foams, and emulsions. Their rheological properties often deviate - sometimes exotically - from those of fluids with a single phase. Soft matter or soft condensed matter is a subfield of condensed matter that deals with systems that are deformed at stresses comparable to thermal fluctuations, including gels, colloids, foams, liquid crystals, granular materials, polymers, and liquids, among others. Therefore, there is significant overlap between soft matter and complex fluids. Systems in soft matter tend to express their key behaviors at room temperatures and produce unusual behaviors due to their tendency to self-organize at mesoscopic scales thereby producing collective effects. Active matter systems are comprised of soft condensed materials in mixtures of multiple phases and so are strongly interlinked with the fields of soft matter and complex fluids. Active matter systems are distinguished by their internally driven, non-equilibrium nature.

1.3 EXTENT OF ACTIVE MATTER SCIENCE – ANIMALS AND THE MACROSCALE The broad classification of active matter results in a large and diverse inclusion of systems across the micro-, meso-, and macroscale, including nonliving systems; such as self-propelled colloidal particles, vibrated granular rods, and robot swarms, as well as living systems; such as the cytoskeleton of living cells,

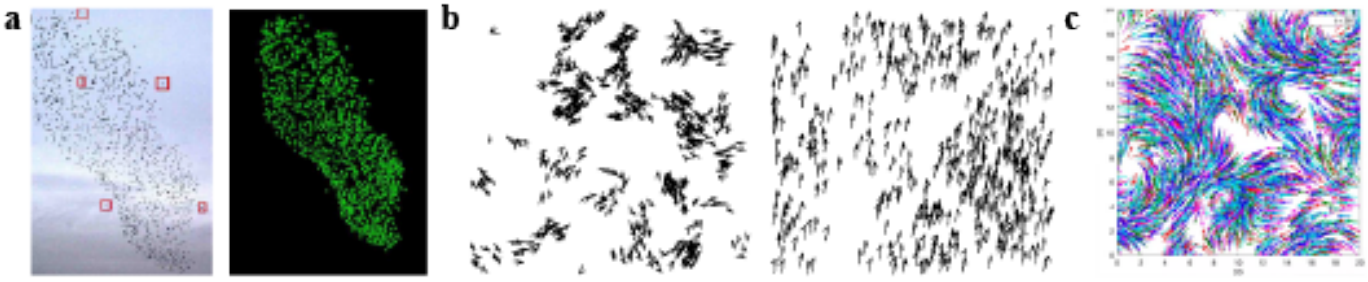

FIG. 2: BAT RECOVERY, STARLING MURMURATION, VICSEK MODEL a) Starling flock murmuration and analysis (adopted from Ballerini *et al.*, PNAS, 2008, **105** (4), 1232-1237) **b**) Vicsek model exhibiting flocking at low densities and ordered motion at high densities for small noise (adopted from Vicsek *et al*., PRL, 1995, **75** (6), 1226-1229). **c**) Vicsek model simulation in mid density, low noise flocking state by Wu lab undergraduate Meng Lian, December 2020. Contributed to PICIP: https://www.compadre.org/PICUP/exercises/Exercise.cfm?I=488

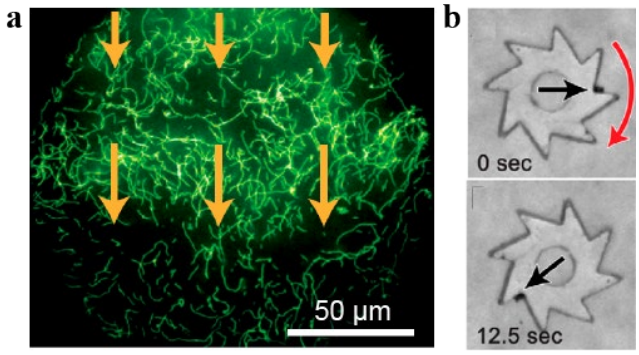

FIG. 3: PROPAGATING ACTIN DENSITY WAVES, BACTERIAL RACHET GEARS a) Traveling density wave in actin motility assay, scale bar 50 µm (adopted from Schaller *et al.*, Nature, 2010, 467 (7311) 73-77). **b**) 380 µm diameter 50 µm thick gears fabricated by photolithography immersed in a bacterial bath are propelled and spun by bacterial collisions with ratchets (adopted from Sokolov *et al.*, PNAS, 2010, 107 (3), 969-74).

flocks of animals, bacterial suspensions, and *in-vitro* mixtures of biofilaments and motor proteins purified from cells[3].

Works like Ballerini *et al.*, 2008 on the murmuration of starlings show the commonality of self-organization and collective motion characteristic of active matter in animals at large macroscopic scales (Fig. 2a)[11,12]. While these system's agents may have such complexity in the behavior of individual agents that their spontaneity is invalidated[13,14], their qualitative flocking dynamics may be recapitulated in large part by simplistic models.

The Vicsek model was a pioneering simulation in the active matter field that showed self-organized collective motion behaviors like flocking can be reproduced in model systems with extremely low complexity of individual agents, including only constant forward motion, noise, and attraction to neighbors (Fig. 2b)[15]. Vicsek *et al.*, 1995 found that flocking was dependent on several parameters, of which number density and interaction strength were critical factors. Work by undergraduate student Meng Lian in Wu Lab reproduced the exploration of this parameter space and found a rich diversity of dynamic flocking patterns (Fig. 2c), inspired by other works that had investigated the Vicsek model. One example is the work Chaté *et al.*, 2008 that explored variations on the Vicsek model and found steady states of progressing linear density waves under periodic boundary conditions[16].

1.4 EXTENT OF ACTIVE MATTER SCIENCE – BIOMIMETICS AND THE MICRO- TO MESOSCALE

The collective phenomenon of linear density waves observed in the Vicsek model was later reproduced experimentally by Schaller *et al.* 2011 in a dense actin myosin motility assay (Fig. 3a)[17,18]. The Vicsek model shows how active matter systems built from individuals following simple rules tend to produce emergent mesoscale processes of diversity and richness, highly sensitive to the parameter space, due to collective behavior.

At the other end of the scale of purely biological active matter are studies of bacterial suspensions. Two works, Leonardo *et al.*, 2010 and Sokolov *et al.*, 2010, show the potential to extract micromechanical work from systems powered by ATP, the chemical fuel of the biological world. They introduced free floating, quasi-two-dimensional rachet gears to bacterial suspensions, which subsequently rotate in a direction that can be determined by the design of the rachet gear (Fig. 3b)[19,20]. The ability to turn the rachet gears stems from the simple trajectory mechanics of individual bacteria, which rebound when striking a surface at an obtuse angle but follow the contour when striking at an acute angle. By leveraging the mechanics of individual agents in the design of parts interacting at the mesoscale, they extract mechanical work from the system. Theoretical work by Yeomans suggests

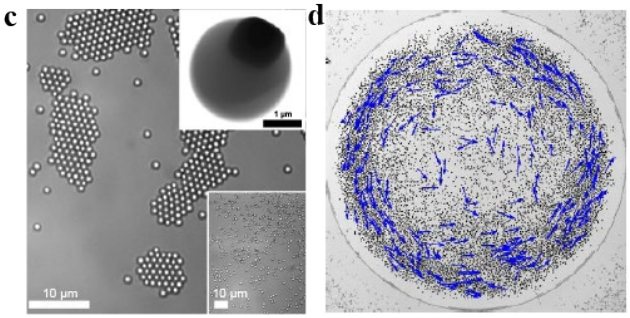

FIG. 4: ACTIVE COLLOIDAL PARTICLES c) Active TPM colloidal spheres with protruding hematite cubes are propelled in H_2O_2 by blue light and form crystal structures (adopted from Palacci *et al.*, Science, 2013, 339 (6122), 936-940). **d**) Quincke rollers form vortex swarm in circular confinement (adopted from Bricard *et al.*, Nat. Commun., 2015, 6 (1), 7470)

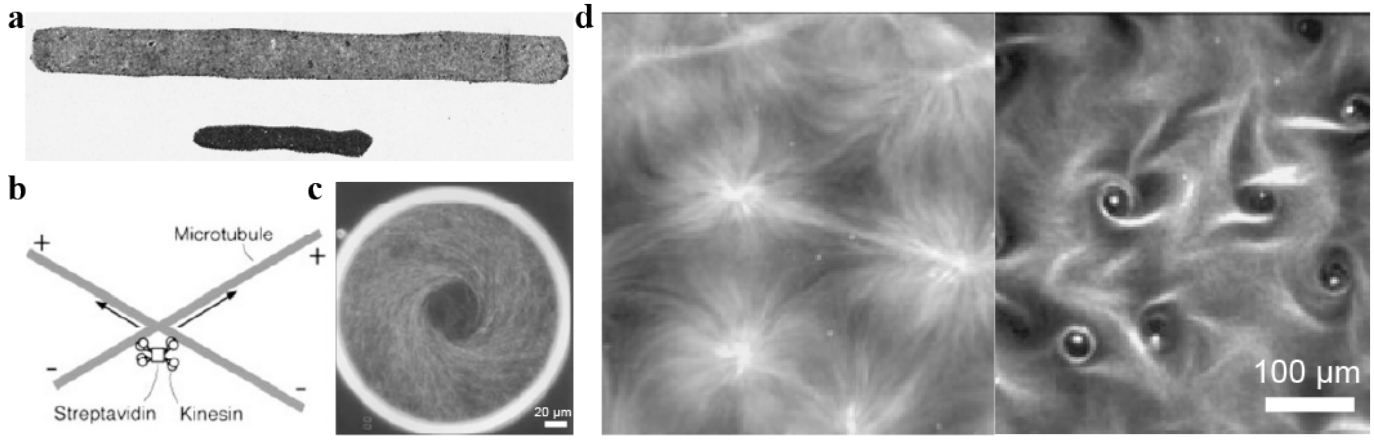

FIG. 5: IN-VITRO PURIFIED CYTOSKELETAL RECONSTITUTIONS a) *in-vitro* contractile cytoskeletal gel shows the shrinking of actin-myosin network after addition of "muscle juice", which contains concentrated ATP (adopted from Szent-Györgyi, J. Gen. Physiol., 2004, 123 (6), 631-641). **b**) Schematic of kinesin-streptavidin construct crosslinking and sliding adjacent microtubules. **c**) Self-organized vortex formation of microtubule and kinesin motor complex mixture in a disc confinement of diameter 90 µm and thickness 5 µm. **d**) Irregular lattices of asters (left) and vortices (right) formed by self-organization in mixture of microtubules and kinesin motor complexes. (b-d adopted from Nédélec *et al.*, Nature, 1997, 389 (6648), 305-308)

that this effect can be extended to nematic active matter systems[21].

Beyond purely biological active matter systems, there is a broad range of studied systems that incorporate synthetic elements with biological, as well as purely synthetic active systems. Two examples of purely synthetic systems are active colloids and Quincke rollers. Palacci *et al.*, 2013 demonstrated the ability of microscale colloidal surfers controlled by light to self-organize into living crystals (Fig. 4c)[22]. The colloids were formed from hematite cubes encapsulated in tripropylene glycol monomethyl ether (TPM). They are distributed to the surface of a bath of hydrogen peroxide. Blue-violet light catalyzes a reaction between the hematite and hydrogen peroxide, causing them to self-propel and traverse the surface. Brownian rotation turns their trajectories into random walks. They have an attraction to neighboring particles due to osmotic effects, as well as exclusion zones. These properties allow them to crystallize. In addition, their orientations are responsive to magnetic fields, allowing control of such organization.

Palacci *et al.*, 2013 found that critical surface densities of the surfers, among other parameters, were responsible for different phases both without crystallization and with different types of crystallization. Quincke rollers or colloidal rollers are another type of active colloid system that is purely synthetic active matter. When a sufficient electric field is applied to insulating spheres in a conducting fluid, surface charge fluctuations lead to a net electrostatic torque rotating spheres transversely to the applied electric field. This rotation mobilizes the spheres, and they roll around with random trajectories. Bricard *et al.*, 2013 exploited this effect on poly(methyl methacrylate (PMMA) microspheres immersed in hexadecane confined to glass microchannel to create a system of motile colloids[23]. In their initial exploration they found that by confining the rollers to a racetrack confinement the rollers could be preferentially directed to self-organize and circumnavigate it and by careful observation they discovered more subtle banded propagation in their collective motion[23]. In their follow up work, they showed that given parameter choices above a critical surface density, only a simple confinement of a disc was necessary for rollers to self-organize into a global vortical flow (Fig. 4d)[24].

Vicsek, Palacci and Bricard's work suggest that surface density is an essential critical parameter determining the emergence and quality of self-organization across many active matter systems. However, recent theoretical studies of self-propelled particle models indicate that such a coupling between local density and order can be suppressed from a topological perspective, that the interaction between

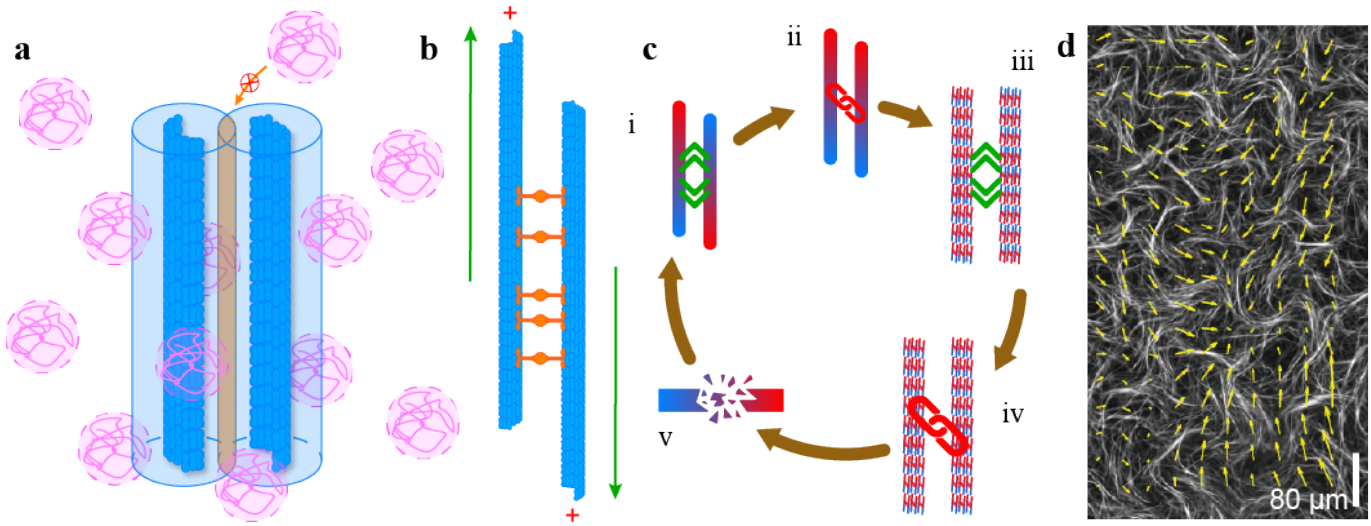

FIG. 6: MICROTUBULE KINESIN ACTIVE FLUID a) When microtubule (opaque blue) exclusion volumes (transparent blue) overlap (transparent orange) depletant molecules (pink) cannot enter. Therefore, Brownian collisions of depletant on microtubules occurs everywhere except between them, resulting in depletion force which binds microtubules in parallel. **b**) Microtubules bound in parallel by depletion forces allow the crosslinking of many kinesin complexes (orange). When the chiral polarity of microtubules (which determines kinesin walking direction) is anti-parallel, the microtubules slide in extensile motion. **c**) The repeating cycle of active fluid. i) Anti-parallel polarity microtubules slide apart. ii) In parallel polarity microtubules kinesin complexes crosslink, but walking in the same direction, do not lead to extensile sliding: the microtubule pair locks. iii) Polarity sorted microtubules accumulate in crosslinked and depleted bundles. When two such polarity sorted bundles meet, the bundles heal together and slide apart when anti-parallel in polarity. iv) Polarity sorted crosslinking and bundling occurs hierarchically up in scale across bundle sizes. v) When bundles reach critical buckling length under extension they buckle and the cycle begins again, where it may start at different stages depending on level of fragmentation. A dynamic equilibrium distribution of bundle sizes is established based on activity level, degree of crosslinking, viscoelasticity, and many other factors. **d**) Microtubule kinesin active fluid viewed on a large scale (d adopted from Sanchez *et al.*, Nature, 2012, 491 (7424), 431-4).

individuals in flocks is density invariant[25]. Nonetheless, from an experimental perspective, agent density is the single most critical factor in enabling emergent self-organization in active matter.

1.5 MICROTUBULE KINESIN ACTIVE FLUID Our experimental niche, microtubule kinesin active fluid, is a bio-synthetic system with nanoscale constituents that hierarchically self-assemble to produce emergent behavior at the mesoscale. Active fluid experiments have their roots in *in-vitro* cytoskeletal active gel experiments.

In 1864, Kühne extracted protein from muscle in concentrated salt solution naming it "myosin", recognizing that it was responsible for muscle rigor[26]. Later, by the 1930s, understanding of proteins and their purification and analysis had grown significantly. Szent-Györgyi made a landmark discovery in his 1942 work when he found that polymerized threads of myosin B contracted upon the addition of boiled muscle juice, the active component of which was identified as ATP (Fig. 5a)[26]. This was essentially the first *in-vitro* cytoskeletal active gel experiment.

Forty years later, Urrutia *et al.*, 1991 would develop the first *in-vitro* microtubule-kinesin active experiment that used purified kinesin and microtubules, as opposed to biological extracts with many more constituents[27]. This work among others represents a niche that was emerging in biophysics in the 1980s and 90s; a term that emerged at the turn of the 20th century[28]. The community rallied around the idea of isolating specific biological components to reveal their characteristic mechanics and co-dependence with other components in simple *in-vitro* systems[27,29-44]. The goal of these studies, which remains one of the central goals of biophysics today, was to leverage the understanding of purified cellular components in the understanding of *in-vivo* cellular systems[1].

Following the development of *in-vitro* purified kinesin experiments, the landmark work Nédélec *et al.*, 1997 developing and exploring *in-vitro* purified microtubule kinesin active cytoskeletal gel laid the groundwork for the niche of microtubule

kinesin active fluid[34,45]. They introduced kinesin motor complexes to a solution of microtubules. The complexes bind kinesin stalk-to-stalk, forming groups with multiple outwards facing heads. Each kinesin is able to bind to a microtubule, thus forming pairs of microtubules, passively crosslinked by kinesin motor complexes (Fig. 5b). Continued crosslinking of microtubule pairs leads to the self-assembly of a network. When ATP is introduced, the kinesin motors walk towards the plus end of the microtubules[27]. In the conglomerate system, each pair of microtubules will have their side of the crosslinking kinesin cluster begin to traverse their length, in either direction relative to their mate, dependent on their random initial alignment. This causes different species of movement, such as sliding and end-to-end anchoring.

As these movements propagate through the network the interactions become complex, involving contrasting forces. Once the system reaches a quasi-steady state, a diverse array of gorgeous morphological patterns of density and alignment expressed at the mesoscale are revealed (Fig. 5c&d). These patterns of hierarchical self-assembly; global vortices, arrays of local vortices, and arrays of asters, are sensitive to both the topology of confinement and relative constituent concentrations of the system. Both methods of control would become key in future experimental studies of active matter. The remarkable work Nédélec *et al.*, 1997, along with its follow up Surrey *et al.*, 2001, which further explored the constituent concentration phase space and varied motor type, paved the way for the experimental study of pattern formation in active matter[3].

The seminal work, Sanchez *et al.,* 2012, "Spontaneous motion in hierarchically assembled active matter"[46], added depletant to this system of microtubules and kinesin motor clusters*,* a decade after Nédélec *et al.*, 1997 pioneered their inspiring system of microtubules and kinesin motor clusters. The initiation of the niche of microtubule kinesin active fluid lies with this sole work.

By introducing depletant, microtubules are bound in parallel when their exclusion volumes overlap. Bound microtubules form pairs which aggregate into bundled networks (Fig. 6). The parallel nature of the co-binding of microtubules allows enormous numbers of kinesin clusters to bind and crosslink microtubules along their mutual lengths. When the system is supplied with ATP the kinesin begins walking towards the plus end of their microtubules. If a pair of microtubules, or pair of polarity sorted microtubule bundles, is aligned in parallel, then the clusters simply walk down their mutual length - the microtubules remaining relatively stationary. However, if the microtubules' directions are aligned antiparallel, the motors begin to walk in opposite directions on each side of the cluster and pull on the adjacent microtubules, causing them to slide apart. When the density of microtubules is increased sufficiently, microtubules form polarity sorted bundles up to hundreds of micrometers long. When bundles diffuse within proximity, depletion forces cause them to adhere or heal together. As antiparallel bundles extend, hydrodynamic drag and collision with other bundles lead to buckling of the extending pairs. After buckling, the fractured pieces encounter further bundles, healing, extending, and buckling again. This process then repeats across the many bundles in the system, forming a bundled active network (Fig. 6). The result is a self-mixing active fluid or gel, microtubule-kinesin active fluid (heretofore referred to as active fluid).

In contrast to earlier more dispersed networks such as Nédélec *et al.*, 1997's microtubule-kinesin network, the enforcement of parallel alignment and microtubule bundling by depletion in active fluid vastly increased simultaneous binding and walking of kinesin clusters on neighboring filaments, transforming the network into a continuously active state with internally generated flows.[34,45,46] "…Compared to [more] dispersed networks, the proximity and alignment of depletion-bundled microtubules greatly increases the probability of kinesin clusters simultaneously binding and walking along neighboring filaments, thus enhancing the overall activity."[46] "In contrast to classical polymer gels, which respond only passively to externally imposed stresses, [active fluid] exhibited internally

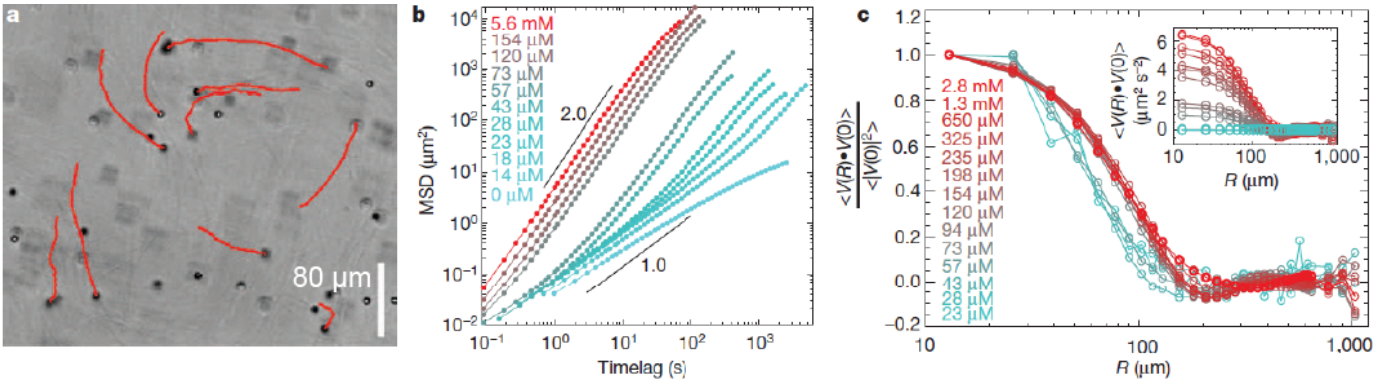

FIG. 7: MEASURING ACTIVE FLUID FLOW a) Polystyrene microsphere tracer particles 3 μm in diameter embedded in active fluid to track fluid flow. Trajectory histories shown in red. **b**) Mean squared displacement of tracer particles as a function of timelag for sweep of ATP concentration. As ATP concentration increases, activity increases, and ≲100 s tracer MSD becomes ballistic. **c**) Normalized same-time spatial velocity-velocity correlation functions for a sweep of ATP concentrations, higher ATP, and resultant higher activity shows longer correlation lengths. (adopted from Sanchez *et al.*, Nature, 2012, 491 (7424), 431-4).

generated fluid flows."[46] Active fluid is an active matter system, hierarchically self-assembling *in-vitro* from synthetic and purified biological components, powered by continuous energy injection at the microscale, and producing emergent collective behavior at multiple length scales.

Sanchez *et al.*, 2012 introduced brush coated tracers, fluorescent polystyrene microspheres, to the active fluid system. The coating on the tracers allows them to remain unbound from any constituents in the system; their trajectory is due only to their collision with components and the fluid flow created by activity. Particle image velocimetry allows the quantification of the particles trajectory and thus the flow in the system.

By measuring the mean squared displacement (MSD) of tracers in bulk flow, they show that the tracer trajectories transition from regular diffusion to super diffusion as activity increases (mean speed of all tracers), which they tune by varying ATP concentration (Fig. 7b). They also show that the characteristic length scale from the same time spatial velocity-velocity correlation functions increases with increasing activity (Fig. 7c)[*]. These results established what is the central method for measuring the spatiotemporal behavior of active fluid flow quantitatively: tracer particles. Image velocimetry of tracer particles is how much of the data in the field of active fluid is generated.

The other central method for observation of active fluid is fluorescent dying of MT bundles, though these observations tend to be qualitative. Other methods include Gagnon *et al.*, 2020's recent pioneering of a micro-rheology device that integrates with a microscope and uses a PolScope to measure local MT orientation by birefringence[47-49].

The results of super-diffusion at high flow speeds in Sanchez *et al.*, 2012 prospected that active fluid would show unusual non-equilibrium phenomenon under continued investigation, joining the growing list of studied active matter systems with rich and surprising collective behaviors. Next, Sanchez *et al.*, 2012 established the microtubule-kinesin active nematic (heretofore referred to as active nematic). Knowing that at a sufficient concentration rod-like molecules will form nematic liquid-crystalline phases at interfaces, Sanchez *et al.*, 2012 showed that when active fluid was confined to an oil-water interface it adhered and formed an active liquid crystal with dynamic +1/2 and -1/2 topological defects familiar to the field of traditional liquid crystals. However, this liquid crystal exhibited fast streaming flows and continuous defect nucleation and annihilation. Active matter physicists who were familiar with soft matter liquid crystals realized the

[*] Sanchez et al., 2012 states that after normalization the spatial velocity-velocity correlation functions and characteristic length scale is invariant across ATP concentrations, however this is qualitative and is refuted in their follow up work Henkin et al., 2014, which shows that correlation length is ATP dependent (Fig. 8).

potential richness of this new system, especially in regard to theoretical models, and a robust community of experimental investigators and theoretical simulationists has emerged in the subsequent decade[1-5].

> "EACH [CELL] IS IN EFFECT A VERITABLE MICRO-MINIATURIZED FACTORY CONTAINING THOUSANDS OF EXQUISITELY DESIGNED PIECES OF INTRICATE MOLECULAR MACHINERY ... FAR MORE COMPLICATED THAN ANY MACHINE BUILT BY MAN AND ABSOLUTELY WITHOUT PARALLEL IN THE NON-LIVING WORLD ..."[50] – MICHAEL DENTON, 1985

1.6 CONTROL OF ACTIVE FLUID My work has been primarily concerned with methods of controlling the behavior of active fluid. I will therefore outline the general categories of control that have been established for active fluid and notable representative works of these methods. In these cases, and my work, I am referring to control over experimental conditions, except for optimal control theory, which will also be discussed.

Established methods of active fluid control fall under eight loose categories: constituent concentration, confinement, boundary condition, electromagnetic, inclusion of additional biological or synthetic systems, DNA, temperature, light, and the theoretical optimal control. These categories will tend to overlap, such as boundary conditions and electromagnetic control, as well as electromagnetic control and inclusion of additional biological or synthetic systems. For the field of active fluid to address the objective of active matter to design controllable smart materials, many or all methods of control may be combined simultaneously in a system to achieve the control aims.

Norton *et al.*, 2020 seeks to develop an optimal control theory to enable real-time predictive software to mediate between the desired input and actuation of individual control elements in order to produce desired outputs[51]. In this theory, control is actuated by applying spatiotemporal perturbations, as opposed to controlling experimental conditions[52,53].

1.6.1 CONCENTRATION Constituent concentration manipulation has been the central control scheme for active fluid with many works using it as a common tool to explore the parameter space of active fluid behavior. The groundwork of this method of control was laid immediately following Sanchez *et al.*, 2012 by Henkin *et al.*, 2014 "Tunable dynamics of microtubule-based active isotropic gels", which extended the image velocimetry measurements of tracers first realized in Sanchez *et al*, 2012[54].

They repeated the measurements of mean squared displacement and equal-time spatial autocorrelation functions for a sweep of ATP concentrations and additionally measured the space and time averaged mean speed as well as the

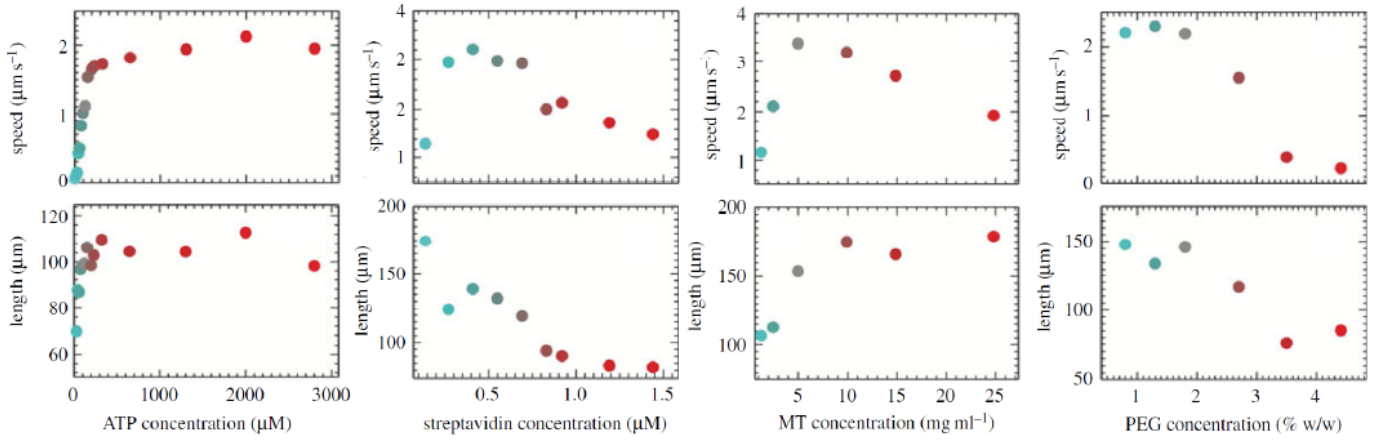

FIG. 8: MEAN SPEED AND CORRELATION CONTROL BY CONCENTRATION Mean speed of active fluid flow measured from tracer particles and correlation lengths measured from spatial velocity-velocity autocorrelation functions for varying ATP, streptavidin (kinesin complexes), microtubule (MT) and depletant (polyethylene glycol [PEG]) concentrations (adopted from Henkin *et al.*, Phil. Trans. R. Soc. A, 2014, 372 (2029)).

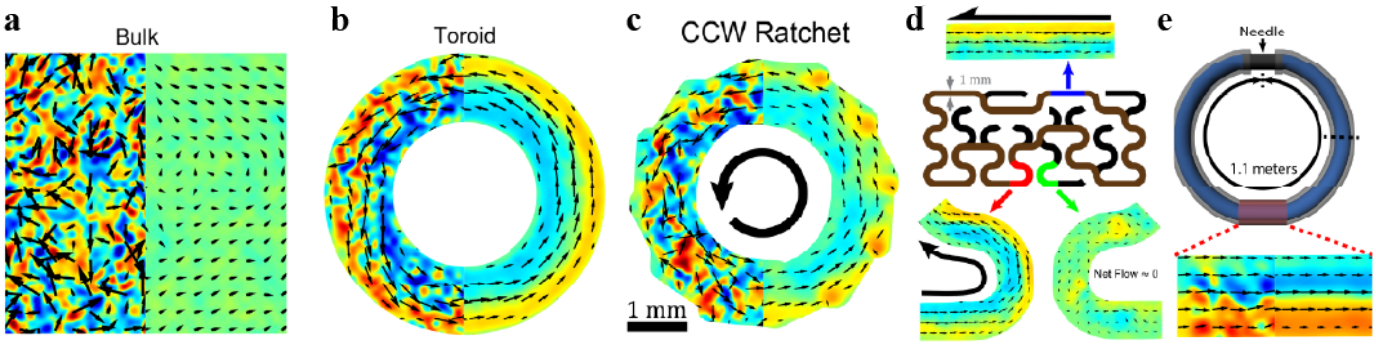

FIG. 9: COHERENCE CONTROLLED BY CONFINEMENT **a**) Bulk flow of active fluid is isotropic unless confined in specific curvatures, cross-sectional sizes, and aspect ratios. **b**) Confining active fluid to toroidal confinement with cross-sectional size comparable to characteristic length scale of bundles and with width-to-height aspect ratios $\left|\frac{h-w}{\max(h,w)}\right| \lesssim 0.5$ results in coherently organized self-pumping flow. **c**) Introducing rachets to the confinement shape allow circulation direction to be controlled. **d**) Active fluid will coherently organize in self-pumping flow in any shape with appropriate curvatures, aspect ratios, and cross-sectional sizes, demonstrated by observation of coherent flow in maze with dead ends. **e**) Coherent self-pumping flow arises regardless of total volume and path length, demonstrated by observing coherent flow in 1.1 m long tube. (adopted from Wu *et al*, Science, 2017, 355 (6331)).

correlation lengths measured from the autocorrelation functions. They then applied these same measurements to variations of kinesin motor cluster, microtubule, and depletant concentrations, as well as ratios of kinesin to streptavidin in kinesin motor clusters (Fig. 8). This simultaneously established the calibration of constituent concentrations to maximize mean speed as a standard practice in the field while outlining the response of these measurables over the available parameter space in preparation for the development of theoretical models and simulations yet to come. They mapped the response of correlation length and mean speed for each parameter, showing that mean speed can be controlled from zero to maximum with various mixture concentrations. ATP quickly saturated both in the hundreds of micromoles. The other parameters saturated speed and correlation length, but led to decay of both at supersaturation, likely due to overwhelming crosslinking, crowding, bundling, and excess free motors in the cases of, Kinesin clusters, microtubules, depletant, and kinesin respectively. Importantly, it began to illustrate the tunability of active fluid.

1.6.2 CONFINEMENT In 2014, Kun-Ta Wu joined Dogic for his postdoc, and his culminating work, Wu *et al.*, (2017) "Transition from turbulent to coherent flows in confined three-dimensional active fluids" established confinement design as a control method for active fluid which can induce self-organized coherent flow at the macroscale[55]. Following inspiration of circular self-organization seen across many active matter systems upon circular confinement, including Quincke rollers, bacterial suspensions, and sperm[23,24,56-58], they confined active fluid to toroids and cylinders. They found that active fluid self-organizes into self-pumping, coherent flows (Fig. 9). This coherence is sensitive to a parameter phase space of width/height aspect ratio and toroidal radius. They found that the flow speed

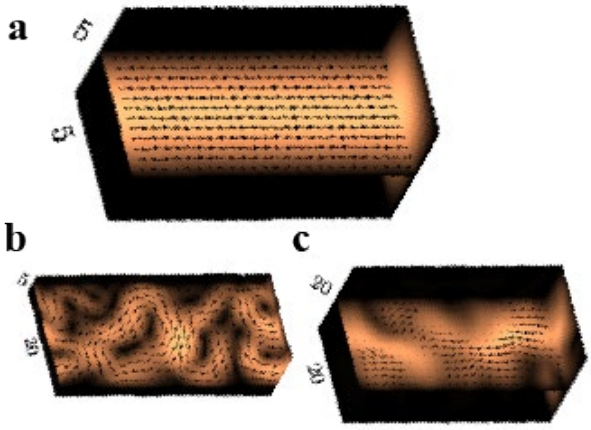

FIG. 10: COHERENCE AND CONFINMENT IN SIMULATION Different aspect ratios and cross-sectional sizes of confinement in nematohydrodynamic simulation show that **a**) smaller, 1:1 aspect ratio produces the most uniform coherence, whereas **b**) confinements that are too thin or **c**) too large exhibit isotropy or weak coherence (adopted from Varghese *et al*., PRL, 2020, 125 (26), 268003).

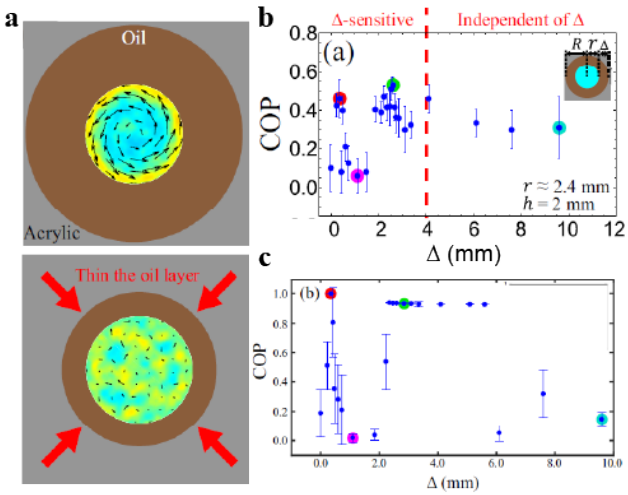

FIG. 11: CONTROL OF COHERENCE WITH LIQUID-LIQUID BOUNDARY a) Circulation of an active fluid droplet in oil is controlled by the surrounding oil layer thickness. **b**) This dependence is highly sensitive and non-monotonic for thin oil layer thicknesses. c) These results are reproduced by nematohydrodynamic simulation. (a-c adopted from Chen *et al.*, Sci. Rep., 2021, 11 (1), 13965).

profile across the width is non-uniform, flowing fastest on the outside of the turn with a sharp drop off to the outer edge. The clockwise or counterclockwise direction of coherent flow is random but can be controlled by the introduction of rachets to the outer profile of the toroid (Fig. 9c). Too many teeth induce turbulent-like flow disrupting laminar flow and limiting the obtainable circulation order parameter.

They found that the self-organization of active fluid is very robust under critical choices of channel aspect ratio, and that as long as the topological curvature of the toroid was maintained, coherence would occur independent of length scale. They were successful in obtaining self-pumping flow in a 1.1-meter circumference tube linked in a circle to form a toroid, as well as in winding mazes (Fig. 9d&e). Even when they introduced dead-ends to the mazes, the active fluid was able to ignore them and navigate the circular solution successfully.

They also demonstrated the use of SOAX[59] analysis on three-dimensional confocal z-scans of active fluid to reveal the three-dimensional structure of the bundled active network, the first three-dimensional microscopy introduced to microtubule-kinesin active fluid study. They found that the transition to coherence was correlated with the thickness of the nematic-wetting layer where active fluid met the boundary walls. A smooth transition of nematic order from the boundary is required to induce coherence.

Recently, work by Varghese *et al.* 2020 developed a theoretical model and nemato-hydrodynamic simulation that successfully recapitulated the emergence of coherent self-pumping flow when the aspect ratio of toroidal confinement is properly tuned (Fig. 10)[60]. They showed that the phenomenon was unique to three-dimensional active fluid as opposed to active nematics and explored the necessary parameter space to obtain coherence.

Since Wu *et al.*, 2017, no works have capitalized on the self-organization of active fluid in toroidal confinement experimentally, however, Bate *et al.,* 2019, Fan *et al.*, 2021 and Bate *et al.*, 2022, all use channel height variation in rectangular confinements in order to tune mean speed and correlation length of active fluid without altering ATP concentration[61-63]. Fan *et al.*, 2021 thoroughly explores the response of key measurables, such as correlation time, correlation length, mean speed, fluctuation, and MSD, for different confinement geometries and sizes utilizing three-dimensional

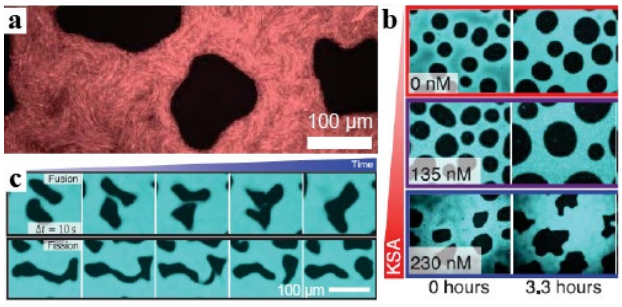

FIG. 12: PHASE SEPARATION IN ACTIVE FLUID a) Liquid-liquid phase separated mixture with polyethylene glycol-rich (dark) and dextran-rich (red) domains where active fluid is partitioned to the dextran phase. **b**) Increasing KSA concentration increases active fluid flow mean speed resulting in increased deformations of the liquid-liquid interface. **c**) At high mean speeds turbulent-like interface fluctuations results in dynamical state in which droplets incessantly fuse and fission. (adopted from Adkins *et al.*, Science, 2022, 377 (6607), 768-772).

particle tracking implemented with a focus plane method[62].

The highest mean speeds of active fluid, ~20 μm/s, have been obtained at large volumes (>0.5 mm on a side) and high temperatures (~40°C)[61]. The current speed record may be broken if toroidal confinement is used to obtain coherent flow (which flows faster than chaotic flow[55]) while using large volumes and high temperatures.

Later, work by Chen et al. has been the first to address the effects of soft boundary conditions on active fluid behavior[64,65]. Chen *et al.*, 2021 shows that coherent flow in active fluid confined to droplets within oil is controlled by the thickness of oil volume outside the droplet due to flow coupling between active fluid and oil across the boundary (Fig. 11)[66]. Furthermore, when the oil layer thickness is small, the coherence becomes highly sensitive to surrounding oil thickness, and this dependence is non-monotonic (Fig. 11). These results are reproduced by active nematohydrodynamic simulations (Fig. 11). Importantly, Chen et al. demonstrated that this method of control can be affected *in*-situ, by implementing confinement which can alter its interior size by mechanical switching.

Recent work by Adkins *et al.,* 2022 introduced active fluid to a liquid-liquid phase separated polyethylene glycol (PEG)-polysaccharide dextran mixture[65]. They found active fluid was partitioned to the dextran phase. Depending on the preparation and orientation of gravity, they obtain droplets of the PEG phase within a dextran background or a bulk phase separation of the two phases. Due to the ultralow interfacial tension of the PEG-dextran interface the active fluid induces large deformations (Fig. 12)[67]. By adjusting the concentration of Kinesin-streptavidin motor clusters (KSA), and thus the mean speed of activity, they controlled the degree of surface fluctuations and at high activities induced a new dynamical phase in the system exhibiting constant fission and fusion of PEG droplets (Fig. 12).

This work suggests the potential to use liquid-liquid phase separation materials as a confinement for active fluid which is self-limiting and dynamically controllable in the pursuit of replicating a synthetic neutrophil[1,9]. The use of soft boundary conditions to control active fluid is in its infancy, however multiple active nematic works have explored the subject[2,68-71]. One of particular note in regard to the work in Chen *et al.*, 2021 is Thijssen *et al.*, 2021. Here, Thijssen shows similarly that active nematic activity is controlled by the depth of the oil layer below the active nematic layer, and that defect density and alignment patterning can be controlled. Furthermore, Thijssen *et al.*, 2021 uses micropatterned structures to exert control of such patterning essentially orthogonally in space[72].

1.6.3 ELECTROMAGNETIC Electromagnetic control has not yet been applied to 3D active fluid. However, its spectacular examples in 2D active nematics suggest it as a potentially key future method of controlling 3D active fluid. Guillamat *et al.*, 2016 (PRE) initially explored the effects of the viscosity of the interface adjacent to an active nematic, finding that the viscosity controlled the activity[73]. Extending this work in Guillamat *et al*., 2016 (PNAS), they introduced a passive liquid crystal to the soft interface with the active nematic, octyl-cyanobiphenyl (8CB). 8CB enters a smectic A phase under a specific range of applied magnetic field strength, and the pattern of the smectic is controllable by the morphology of the magnetic field[74]. The smectic layers have a higher friction with the active nematic layer and thus the pattern of the passive liquid crystal controls the activity pattern of the active nematic. Guillamat *et al*., 2016 (PNAS) uses this cascade of effects to create a pattern of adjacent rows of running defects (Fig. 13).

Guillamat *et al.*, 2017 (Nat Commun) goes on to create active nematic swirls with 8CB, but without requiring control by a magnetic field (Fig. 13)[68,75-77]. However, it is unclear how such a boundary friction technique will be applied to three-dimensional active

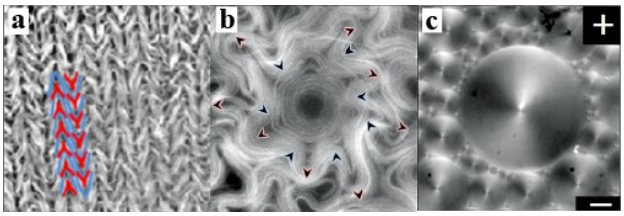

FIG. 13: MAGNETIC CONTROL OF ACTIVE NEMATICS VIA SU8 INCLUSION a) Ordering of active nematic defects in columns due to contact with synthetic nematic layer of octyl-cyanobiphenyl (8CB) under magnetic field. Defect orientations indicated in red and blue (adopted from Guillamat *et al.*, PNAS, 2016, 113 (20), 5498-502). **b**) Swirl of defects in active nematic induced by frictional contact with **c**) 8CB which self-organizes toroidal focal conic domains into the Apollonian gasket fractal tiling under controlled conditions, but without requiring a magnetic field (b & c adopted from Guillamat *et al.*, Nat Commun, 2017, 8 (1), 564).

fluid. Another work utilizing electromagnetic control is Kim *et al.*, 2007 which, following a number of works showing that microtubule orientation could be controlled by applying electric fields[78-81], used an electric field to control the alignment and direction of microtubule movement in a gliding assay, suggesting that microtubule alignment and extensile behavior could be controlled by an electric field in active fluid[82]. However, the microtubules adhesion to the kinesin layer in the gliding assay was necessary to prevent them being entirely pulled away by the electric field. As active fluid is a free suspension of microtubules, this represents a significant challenge. Perhaps the next step should be applying this technique to 2D active nematics, which are strongly confined to the oil-water interface.

1.6.4 INCLUSION OF ADDITIONAL BIOLOGICAL SYSTEMS The works by Guillamat previously mentioned utilized the introduction of a passive liquid crystal to realize control by magnetic field on an active nematic. This is an example of control of microtubule kinesin active systems by the introduction of additional systems. Specific to active fluid as opposed to active nematics, there are two notable examples of controlling the system by introduction of additional systems. The first is Duclos *et al.*, 2020, which saturated the active fluid system with a passive colloidal nematic of filamentous fd viruses which infect *E. Coli*[83]. These viral filaments are approximately 880 nm in length and 6.6 nm in diameter with a persistence length of 2200 nm and will enter a cholesteric followed by smectic phase as volume fraction reaches sufficient levels[84].

Duclos imaged the active fluid fd composite with three-dimensional confocal light-sheet microscopy. The birefringence of the suspended fd rods allowed the spatiotemporal evolution of local nematic order to be revealed in the three-dimensional liquid crystal at relatively high resolution, down to the micron scale. In two-dimensional liquid crystals, there are line and point topological defects; by analyzing the nematic orientation data, Duclos showed that topological defects express as loops in three-dimensional active liquid crystal, exhibiting spontaneous loop nucleations, annihilations, splits and merges similar to those found in two-dimensions (Fig. 14)[83]. This work showed that introducing additional soft matter systems to active fluid can be used as a tool to enable measurement which advances our capabilities of observing active fluid.

Berezney *et al.*, 2022 also introduced a system of passive filaments to active fluid. However, they used filamentous actin filaments which have an

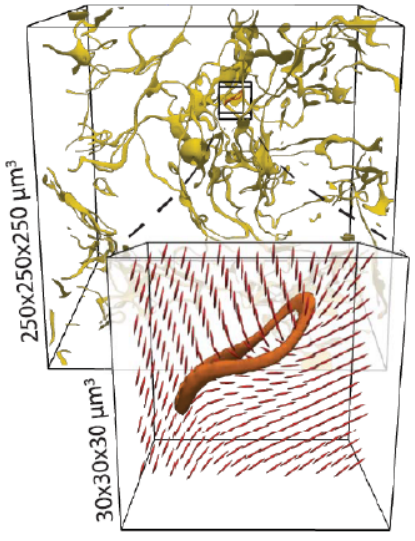

FIG. 14: 3D ACTIVE NEMATIC DISCLINATION LOOPS Entangled network of curvilinear singularities in elastic distortion map (yellow) of 3D active nematic composed of active fluid and fd virus reveal isolated loop disclinations (orange) corresponding to local nematic director field (red) extracted from fd virus birefringence (adopted from Duclos *et al.*, Science, 2020, 367 (6482), 1120-1124).

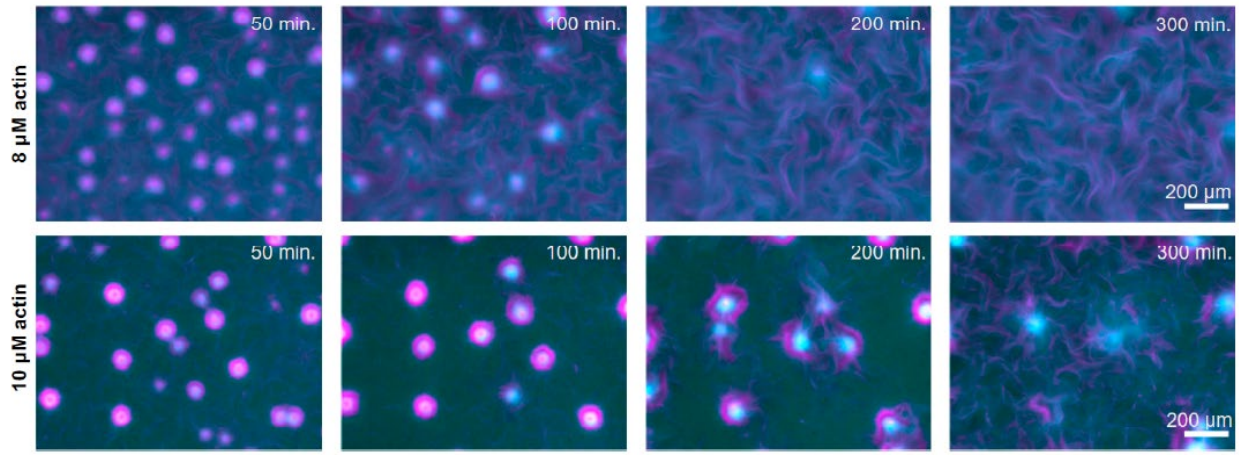

FIG. 15: ACTIN-MICORTUBULE KINESIN COMPOSITE Adding filamentous actin (magenta) to microtubule (cyan) kinesin active fluid induces array of contracted asters. The concentration of actin determines the stability and lifetime of asters (adopted from Berezney *et al.*, PNAS, 2022, 119 (5)).

available cross linker, which bound the integrated actin filaments into an entangled network. Furthermore, the degree of crosslinking, and the subsequent phenomenology of the actin network, was controllable by the crosslinker concentration. By varying the concentration of the embedded actin network, Berezney discovered an incredible new dynamic morphology: regular global patterns of layered asters whose temporal evolution depended on actin density, and whose individual structure oscillated in a controllable way (Fig. 16)[85]. The composite gel of microtubule kinesin active fluid and passive entangled actin network enters a phase of global bulk contraction at sufficiently high actin concentrations. By introducing an additional network whose properties are controllable by concentration, Berezney showed that new patterns of dynamic self-organization can be obtained which exhibit regular, controllable, self-limited structures, pointing the way to self-limited assembling active materials.

1.6.5 DNA HYBRIDIZATION Short DNA strands (10-30 base pairs) are used as mechanical linkers to enable self-assembling objects in the fields of DNA coated colloids and DNA origami, enabling the programmatical design of crystals and other structures at the microscale. These coded mechanical linkers have been incorporated to active fluid in Tayar *et al.*, 2021 by conjugating complementary strands to SNAP tagged kinesin motors and then hybridizing the DNA to form DNA-kinesin dimers[86]. Using a pair of complementary DNA strands to link kinesin provides additional tunable mechanical properties to kinesin dimers that subsequently effect the behavior of active fluid and active nematics. The hybridization overlap length of complementary strands controls the binding strength of kinesin dimers in crosslinking, and very long strands induce a stretching regime, where after two kinesin bind to adjacent microtubules, they must stretch their DNA crosslink before generating sliding. The DNA strands can be imbued with intercalating dye, enabling fluorescence anisotropy of bundle orientation via a polarizing filter (Fig. 16a)[86].

Another work incorporating mechanical DNA linking to a microtubule kinesin active system is Keya *et al.*, 2018, though it is not an active fluid. Microtubule kinesin gliding assays, first developed early on in 1985, lay microtubules onto a glass surface coated with kinesin motors[44]. When the aqueous reservoir above the 2D system is saturated with ATP, the kinesin walks under the microtubules, causing them to glide around like trains on the surface. This simpler system links microtubule and kinesin kinetics one-to-one; microtubules are limited to a gliding speed identical to the maximum kinesin walking rate. In Keya *et al.*, 2018, two species of

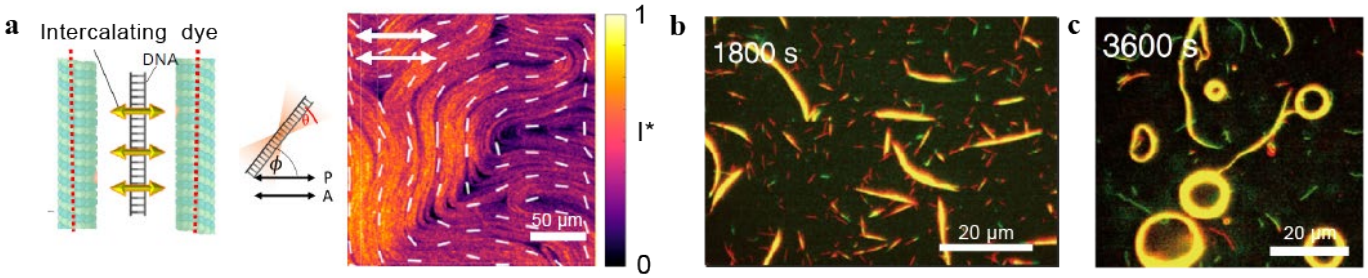

FIG. 16: DNA IN MICROTUBULE KINESIN ACTIVE SYSTEMS a) DNA motor clusters are labeled with an intercalating dye. When the dye is illuminated with polarized light the intercalated dyes are exited. Analyzing the emitted fluorescence with a colinear analyzer reveals the orientation of motor clusters and thus local microtubule orientation by the emitted fluorescence intensity (adopted from Tayar *et al.*, Nature Communications, 2018, 9 (1), 453). **b**) Microtubule gliding assay with two species of microtubules (red and green) which are each labeled with a non-complimentary DNA strand. Adding an associative linker links the non-complimentary strands, clustering the microtubules into traveling swarms. **c**) Polymerizing microtubules with GTP as opposed to traditional GMPCPP results in reduced flexural rigidity, causing their persistence length in the gliding assay to be less than half that of more rigid GMPCPP microtubules. This results in a drastic phase change in collective motion of associated microtubules, which form circular swarms (b & c adopted from Keya *et al*., Nature Communications, 2018, 9 (1), 453).

microtubules were produced by coating them in two non-complementary DNA strands and dyeing them red and green so they can be differentiated[87]. Although the two species of microtubules have non-complementary DNA, the addition of a linker or associative DNA strand, which is complementary to both, will link them in a complete chain. Thus, initially, the two species of microtubules glide independently, but when the linker is introduced by *in-situ* microfluidic flow-thru, the red and green microtubules link and form traveling clusters. They also programmed a dissociative strand, which when introduced to the system, is more favorable for the linker to bind to then to the two complementary strands, and so the dissociative strand removes the linker from the chains, breaking apart the clustered groups of gliding red and green microtubules (Fig. 16). By switching the microtubule polymerization hydrolysis mechanism from the conventional Guanosine-5'-[(α,β)-methyleno]triphosphate (GMPCPP), a slowly hydrolysable analog of Guanosine triphosphate (GTP), to Guanosine triphosphate they produce microtubules with short persistence lengths, which form incredible self-organized rotating circular clusters on addition of associative linker strands. By programming DNA sequences both the rigid linear swarms and flexible circular swarms may coexist independently.

Keya introduces azobenzene to the DNA strands, which allows their hybridization to be switched on and off by shining visible and UV light respectively. Combining optical and DNA control, they demonstrate that logic gates can be expressed by the various resulting outputs of swarming and self-organization. Orthogonal controls are controls which achieve a single change in output behavior from a single input and are non-interacting with other orthogonal controls. Thus multiple orthogonal controls may be implemented to achieve multiple independent output behaviors simultaneously[87]. The immense degree of orthogonal control of self-organization shown over the microtubule kinesin active system in this work suggests not only the great potential of applying DNA hybridization and optogenetics (light activation of confirmational protein change) to active fluid, but also resonates strongly with the overarching goal in the community to create autonomous, controllable active materials. DNA linking and optogenetics will likely play a significant role in future design of such systems. It also highlights the necessity for orthogonal control strategies. Controls such as temperature and concentration are non-orthogonal. Optogenetics and the specificity of DNA binding will provide one route to orthogonal control options.

1.6.6 CONSTITUENT VARIATION Ongoing and recent work has exchanged key elements of active fluid to control and manipulate its dynamical expression. Tayar *et al.*, 2021, previously described, which exchanges kinesin-streptavidin clusters for DNA

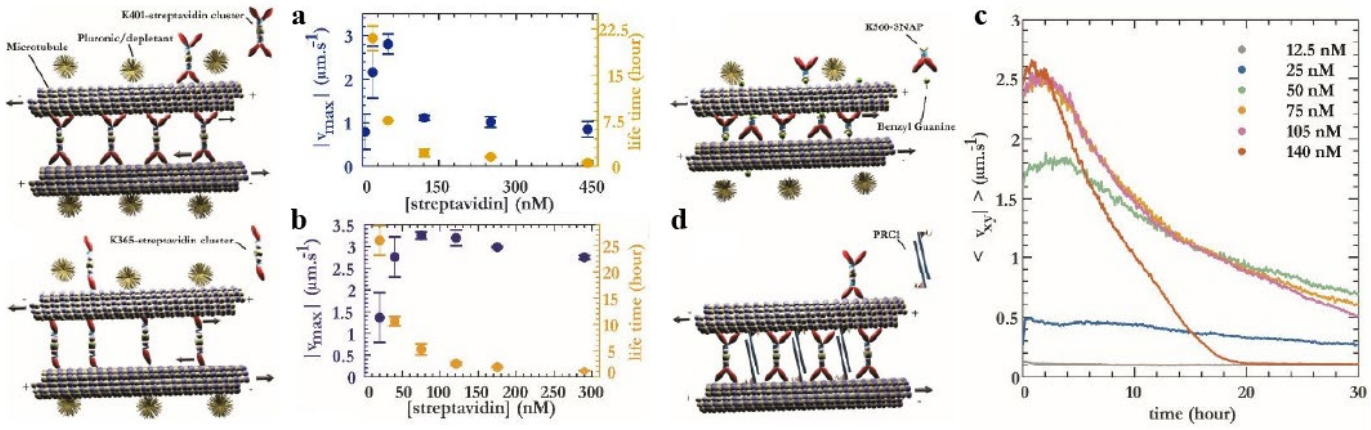

FIG. 17: MOTOR PROCESSIVITY IN ACTIVE FLUID a) Active fluid built with processive K401-streptavidin clusters degrades in maximum mean speed after increasing past saturation concentration. **b**) Active fluid built with non-processive K365-straptavidin clusters retains maximum mean speeds even after increasing past saturation concentrations. The lifetime of both processive K401 and non-processive K365 active fluids decrease exponentially as motor complex concentration increases. **c**) The direct to microtubule binding K560-SNAP motor results in an active fluid with very long lifetimes with a constant decay in mean speed. **d**) The passive microtubule cross linker allows active fluid to be built without depletant. (a-d adopted from Chandrakar *et al.*, Soft Matter, 2022, 18 (9), 1825-1835).

Kinesin dimers, is one such example. There are many subcategories of kinesin motors, with different structures and functions[88]. Using some types of motors in the microtubule-kinesin system with depletant will alter the resulting system such that it is no longer active fluid[89]. However, some kinesin variations can be introduced to active fluid while retaining its essential behavior. The different qualities of applicable kinesin cascade up from the nanoscale to alter the behavior of active fluid. In this way, engineering kinesin motor structures at the nanoscale control mesoscale self-organization of active fluid.

Chandrakar *et al.*, 2022 (preprint 2018) focuses on the control of active fluid by altering constituent makeup[90]. They explored the response of mean speed, the lifetime of sample activity, and correlation length evolution to variations in motor type. Kinesin-401 (K401) is the standard, two headed processive motor used in active fluid, which walks to the plus end of microtubules before detaching. They found that active fluid powered by K365, a non-processive, one-headed kinesin motor, obtained lower mean speeds but had less speed variation over the sample's activity lifetime relative to K401 (Fig. 17). In addition, K365 retained maximum mean speeds over mean speed saturation concentrations of kinesin clusters, whereas K401 loses mean speed over the mean speed saturation concentration of kinesin clusters (Fig. 17). They theorize based on previous studies of kinesin stepping that this difference is due to greater motor interference in the double-headed processive K401 than the single-headed non-processive K365[91]. Both had significantly reduced lifetimes of sample activity as kinesin cluster concentration was increased past the mean speed saturation concentration (Fig. 17). In addition to the mean speed retention, Bate *et al.*, 2019 showed that K365 has a lower activation energy than K401 (has a more stable mean speed variation under temperature variation), and that when mixed 50/50 with K401, results in even lower activation energy than in either motor type alone, exhibiting highly stable speeds across changing temperatures[61].

Chandrakar *et al.*, 2022 use SNAP tagged K560, a longer version of the double-headed processive motor, to bind the kinesin stalk directly to Benzyl Guanine (BG) labeled MT (BGMT). In this variation, as the kinesin is not clusterized but bound directly by the stalk to one microtubule in a pair, it walks only on one of the microtubules in a bound pair. This resulted in substantially extended lifetimes of sample activity (30 h+), but a more dramatically decaying mean speed over the course of the sample's

activity lifetime (Fig. 17). Finally, they replaced the depletant in the system with a passive microtubule crosslinker, protein regulator of cytokinesis-1 (PCR1), which resulted in substantially lower mean speeds, but established a version of active fluid independent of depletant, which was subsequently necessary to realize such systems as the combined F-actin microtubule kinesin active fluid previously discussed in Berezney *et al.*, 2021.. Engineering the components of active fluid will be essential to the development of active materials and compliments other control methods such as light and DNA control. Being creative and flexible in regards to the molecular composition and design of active fluid will allow it to realize its full potential in the development of active materials.

1.6.7 TEMPERATURE The only work currently exploring the response of active fluid to temperature change is Bate *et al.*, 2019, reproduced in Chapter 2. It shows that temperature controls the mean speed of active fluid by increasing kinesin stepping rates which follow the Arrhenius law[41,92-95], though changes in the fluid's temperature also effect its rheology[96]. Active fluid is only practically stable between ~16° and ~36° F, which can only affect a ~45% decrease in mean speed from maximum[61]. However, temperature control of mean speed is a valuable tool as it can tune mean speed *in-situ*. In Bate *et al.*, 2019 we show that not only can mean speed be controlled temporally *in-situ* but that it is also reversable. This contrasts with the control of mean speed by concentration, which has not been implementable *in-situ* with active fluid and is irreversible.

1.6.8 LIGHT Another method for *in-situ* control is optical control. Currently, there are two methods for controlling active stress by shining light on active fluid, opto-kinesin clusters, and caged ATP. Improved light induced dimers (iLID) replace the standard biotin-streptavidin bound kinesin clusters with a new binding system. In this system, there are two species of kinesin, one with the iLID domain, the other with its polypeptide binding partner[97]. Under exposure to ~488 nm light, the kinesin with iLID domains undergo a conformational change allowing them to bind to kinesin with polypeptides. Otherwise, the binding of the two species of kinesin is inhibited. The result is that significant kinesin clusterization only occurs under blue light, and thus activity only occurs while active fluid is exposed to blue light.

Ross *et al.*, 2019 introduced the iLID system to microtubule kinesin active fluid and exhibited the degree of spatiotemporal control of activity that it enables through the use of a digital micromirror device (DMD) projector[97]. The digital micromirror device chip is an array of actuatable micromirrors. When the desired wavelength and intensity light is reflected off it, it enables high resolution spatiotemporal light patterning on a surface, in this case active fluid samples. Using disc shaped activation areas, they create contractile asters whose contraction speed and characteristic size is controllable by the excitation diameter of the disc (Fig. 18). After an aster has been initiated it can be dragged by moving the excitation disc, and when two adjacent disc activation areas are connected by a line, it induces the asters to snap together (Fig. 18). The maximum aster speed is controlled by their initial separation. They show that bar shaped activations and different bar-based shapes, such as crosses, Ts, and Ls, result in persistent symmetric and nonsymmetric vortical flow patterns (Fig. 18). This work showcases light activation and the iLID kinesin system as a promising method of spatiotemporally controlling active stresses *in-situ*.

Recent work in collaboration with Ross in Lemma *et al.*, 2022 (preprint) has established the groundwork outlining the basic capabilities and limitations of the iLID system for spatiotemporal control[98]. They find that opto-K401 active fluid has higher mean speeds than that of opto-K365 (up-to three times faster). However, opto-K401's mean speed decays on repeated re-activations (on the scale of hours), while opto-K365 maintains a constant mean speed after repeated reactivations. In addition,

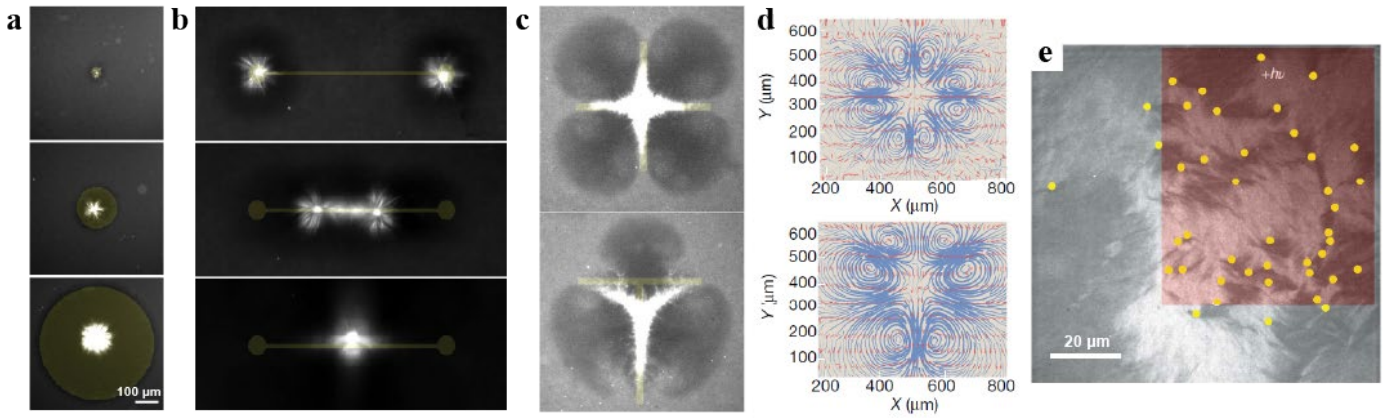

FIG. 18: OPTOGENETIC CONTROL OF ACTIVE FLUID a) iLID-click kinesin dimers are activated in microtubule kinesin active fluid by blue light whose shape is controlled by a digital micromirror device (DMD). Disc illumination pattern induces the formation of contractile asters whose size is controlled by the disc diameter. **b**) Connecting two discs with a line causes the asters to be connected and snap together. **c**) Bar shape activation patterns result in stable, continuous vortical flow patterns around growing asters. **d**) Particle image velocimetry reveals the eddy-like flow fields. Antisymmetric activation patterns result in antisymmetric flow patterns. (a-d adopted from Ross *et al.*, Nature, 2019, 572 (7768), 224-229) **e**) Spatially controlled light activation of actin-myosin nematic results in the sequestering of +1/2 defects to the activation region (adopted from Zhang *et al.*, Nat Mater, 2021, 20 (6), 875-882).

they analyze the "dark speed", or mean speed under no photoactivation. Due to the possibility of kinesin self-oligiolization some small fraction of kinesin may form dimers without a binding agent or in disregard to a disabled binding agent, resulting in low mean speeds, usually less than ~5% of maximum speed, under optimal binding and activation conditions[86]. Speeds lower than ~0.3 µm/s measured by tracer particles may be indistinguishable from noise, as the drift speed of the tracers due to Brownian motion is comparable. Nonetheless, Lemma *et al.*, 2022 measures the speed over repeated activations, and finds that while opto-K365 maintains a minimum dark speed, opto-K401's dark speed increases over repeated re-activations. Finally, they measure the characteristic time required to reach full activity after initiating light activation and the characteristic time required to reach null activity after stopping light activation. They find that opto-K365 has faster on-off times at ~8 and 13 s respectively, compared to opto-K401 on-off times of 14 and 33 s respectively. Thus, opto-K365 should be chosen when repeatable mean speeds and low dark speeds are required for repeated activations, and rapid temporal control is required. However, if maximum mean speed is desired over those characteristics, opto-K401 should be chosen. It should be noted that motors continue to bind to, step along, and detach from microtubules when not dimerized, resulting in continuous fuel consumption[99].

The other active fluid work that has used opto-Kinesin to date is Najma *et al.*, 2022, which used spatially confined activation of high light intensity to trigger higher activity which induces in-plane instability, and low intensity light to trigger lower activity which induces out-of-plane instability, demonstrating how optogenetics can control a specific self-organizational property of active fluid spatiotemporally.

The other type of light activation method used thus far in active fluid is the release of caged ATP by ultraviolet light (UV). Caged ATP is ATP which has been esterified by a blocking group, rendering it non-hydrolyzable by kinesin motors. Upon exposure to ~365 nm UV light the blocking group is ejected, and the resulting ATP molecule is once again hydrolysable by kinesin motors. By saturating a solution with caged ATP, when it is exposed to UV light, ATP is released only in the exposure area, from which it will begin to spread out from by diffusion. Berezney *et al*., 2021, previously described, utilized caged ATP to control the

initiation of flows in the full area of samples, allowing micrograph capture of the initial activity state[85].

In Bate *et al.*, 2022, described in Chapter 3, we used spatially controlled release of caged ATP to create checkerboard patterns of initial activity. By controlling the grid size of the checkerboard pattern, we were able to control the mixing time of simultaneously released suspended dye[63]. In comparison to optogenetics, the light release of caged ATP may be used to control the spatial control of activation, but its subsequent spatiotemporal progression is controlled by the diffusion and advection of ATP in the active fluid, whereas optogenetics enables arbitrary spatiotemporal control of activity, within the limitations of active fluid dynamics. However, spatially non-uniform release of caged ATP presents a rich phenomenology of active fluid self-mixing for study, as shown in Bate *et al.*, 2022.

Other notable works outside of the active fluid niche have utilized optogenetic control. Keya, *et al.,* 2018, previously described, utilized DNA binding between microtubules to affect light-controlled clusterization[87]. By incorporating Azobenzene to the DNA, which can force de-hybridization of associated DNA on exposure to UV light and allows hybridization under exposure to visible light, Keya controlled binding and thus clustering with light.

Our ongoing work seeks to combine the methods of DNA kinesin dimers used in Tayar, *et al.*, 2021, previously mentioned, and light controlled azobenzene DNA to create another optogenetic control system for active fluid. As shown in Keya, *et al.*, 2018, within the limitation of diminishing returns over re-activation, azobenzene DNA Kinesin dimers would maintain or sustain activity without constant light activation, as opposed to the currently established iLID optogenetic kinesin system which requires continuous blue light to remain active.

Regarding the optogenetic control of active nematics, Zhang *et al.*, 2021, in an actin-myosin system similar to microtubule-kinesin active nematics, showed that optogenetic control of activity allowed the confinement of defects to spatially confined activation regions[100]. Their simulations, which are theoretically equivalent to microtubule-kinesin active nematic simulations, indicate that both individual defects and defect patterns can be controlled spatiotemporally, similar to the spatiotemporal control of asters achieved in Ross *et al.*, 2019 (Fig. 18). They realized this to a degree by the guidance of a defect trajectory in a curved path. However, more experimental realization of these potentials was limited without the use of digital micromirror device light projection technology.

In all, the combination of optogenetic control of activity in active fluid and digital micromirror device light projection technology is the most promising method for arbitrary spatiotemporal patterning of activity in active fluid and nematics, and thus is perhaps the single most crucial control method to develop on the path to autonomous, controllable, self-limited assembly active materials. Combining such light activity control with a method of self-limiting confinement, such as liquid-liquid phase separation, could result in controllable mobile droplets, effectively reproducing the neutrophil synthetically, which would be an experimental proof of concept on the road to delivering such self-limiting, autonomous, controllable active materials to applications such as whole blood pharmaceuticals.

1.6.9 OPTIMAL CONTROL The final method of control discussed, optimal control, is distinct from the previous methods as it is a mathematical theory of control, rather than a direct method. It seeks to find an optimized control input to a system over a finite time interval such that an objective function is optimized. The control theory has been applied to space engineering to deliver a rocket with minimal fuel consumption[101]. It is currently theoretical in the field of active matter and has been explored for active nematics in Norton *et al.*, 2020[51]. Norton

computationally showed the potential of the system to actively transform and directly control the spatiotemporal vortical and defect patterning in the nematic, via control of the active stress field. It accomplishes a complete level of actuation over the patterning of the spatiotemporal nematic structure by constantly reacting to the current state of the nematic, in real time. Though the theory is in development, along with the techniques of optogenetic control and digital micromirror device light patterning technology it suggests a system that would allow the automated defect and vortical patterning of active nematics, and perhaps even active fluid someday. This would require a microscopy system that constantly monitors the nematic order and vorticity of a sample in real time, computes the optimized spatiotemporal active stress patterning to drive the system to or maintain a desired state for a given moment, and then applies that pattern via digital micromirror device light patterning. This is perhaps the ultimate dream of spatiotemporal active nematic and active fluid control: the ability to supply the observation system with an arbitrary spatiotemporal defect or vorticity pattern, and have it compute and apply the necessary spatiotemporal pattern of activity by responding in real time to the system state. The realization of this strategy will be a significant milestone in the development of smart active materials. It is on the horizon now that spatiotemporal control has been proven experimentally with optogenetics and digital micromirror device light patterning.

1.6.10 LIMITED SELF-ASSEMBLY Active fluid is self-assembling and self-organizing, but it is not self-limiting. Self-assembly is the process by which individual units assemble due to their intrinsic mutual attractions into complex materials and structures. Self-limiting assembly is a bio-inspired strategy to develop programmable units perform self-assembly that naturally terminates at a controllable finite size without the need for external control. This behavior, constantly performed by living systems, has the potential to revolutionize

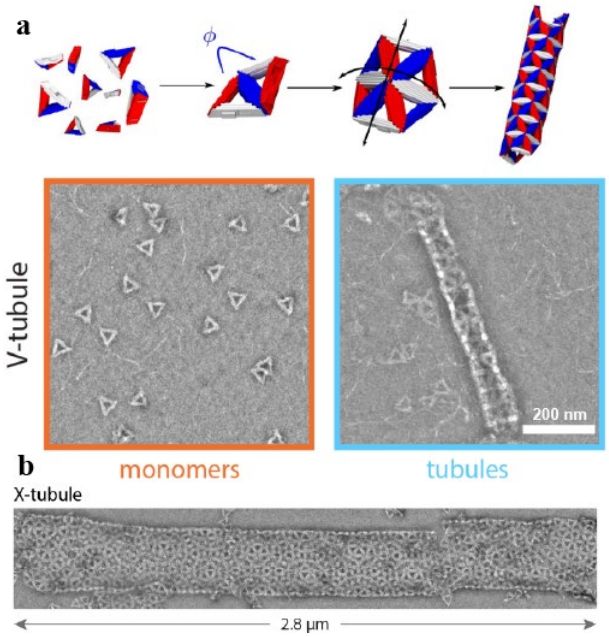

FIG. 19: DNA ORIGAMI AND SELF-LIMITING ASSEMBLY a) Triangular subunits of DNA origami which bind blue to blue, red to red, and white to white, form dihedral angles self-assembling into tubules which are limited by curving into a cylinder. **b)** Tubule size is controlled by changing the dihedral angle formed by subunits, tuned by adjusting the subunit structure. (adopted from Hayakawa *et al.*, arXiv, 2022, 2203.01421)

nanotechnology. To reach the goal of limited self-assembling active materials, limited self-assembly must be introduced to active fluid or a new system must be devised.

This path is being paved in the field of self-assembly, wherein DNA origami is one of the most promising paradigms[102]. Hayakawa *et al.*, 2022 (preprint) has established the experimental realization of limited self-assembling tubulins from DNA origami colloids, which utilize curvature as the limitation method in their self-assembly (Fig. 19)[103]. In this method, the accumulating self-assembly of an object is constrained by curvature, introduced by the shape of the building blocks, in this case leading the growing edge of the tube to wrap around and connect, limiting its shape. The other proposed strategy for self-limitation is frustration, which utilizes poorly fitting building blocks leading to an accumulation of angle frustration as a material sheet grows from a nucleation point, leading to self-limitation without closed geometry being necessary[104]. These two strategies represent the

thrust to establish the theoretical and experimental ability to synthesize limited self-assembling nano and microstructures which will be essential to engineer limited self-assembling materials.

Such nanoscale self-limited objects could be incorporated to active matter as constituents, for instance replacing microtubules in microtubule kinesin active fluid, or as self-assembling confinement structures. Since DNA attraction, folding, and morphology is programmable, it would allow active matter constituents, structures, and confinements to be engineered and hierarchically from the nanoscale to the mesoscale in order to gain new levels of detailed control over active matter morphology and mobility. Recent advancements in the prediction of protein structure from amino acid sequence using machine learning algorithms such as AlphaFold suggest a future where proteins may be programmatically engineered similar to DNA[105,106]. Given that there are 20 amino acids, as opposed to the four nucleotides of DNA, it is a more complex problem. However, if successful, the technology to synthetically engineer and replicate protein structures would transform the world, and inevitably change the field of active matter, allowing unprecedented creative freedom in the design of constituents and confinements.

1.7 CONCLUSION Concentration, confinement, electromagnetics, boundaries, inclusion of additional biological systems, DNA, temperature, motor design and crosslinking, and light are the methods of controlling active fluid and adjacent systems that have been established, while optimal control has yet to be realized experimentally. Each has its advantages and limitations, but in assorted combinations, they have the potential to enable active fluid and nematics to be a central prototype system in the creation of autonomous, self-assembling, active materials.

This dissertation outlines my contributions in the control of microtubule kinesin active fluid, which resulted in three peer-reviewed publications[61,63,107]. These works explore the control of active fluid mean speed by temperature and the related measurements such as activation energy, and the mixing and fluid dynamics of active fluid with nonuniform activity, controlled by spatial release of caged ATP, respectively. In addition, this dissertation will include the ongoing work exploring the effect of a temperature gradient and subsequent activity gradient on mixing and fluid dynamics in active fluid. These works highlight the details of these control methods and associated intellectual merit which will inform the development of autonomous, limited self-assembling, controllable active materials, as well as unveiling the underlying mechanics of constituents and systems in living cells[1].

1.8 REFERENCES

1 Needleman, D. & Dogic, Z. Active matter at the interface between materials science and cell biology. *Nature Reviews Materials* **2** (2017). https://doi.org:10.1038/natrevmats.2017.48

2 Zhang, R., Mozaffari, A. & de Pablo, J. J. Autonomous materials systems from active liquid crystals. *Nature Reviews Materials* **6**, 437-453 (2021). https://doi.org:10.1038/s41578-020-00272-x

3 Marchetti, M. C. *et al.* Hydrodynamics of soft active matter. *Reviews of Modern Physics* **85**, 1143-1189 (2013). https://doi.org:10.1103/RevModPhys.85.1143

4 Ramaswamy, S. Active matter. *Journal of Statistical Mechanics: Theory and Experiment* **2017**, 054002 (2017). https://doi.org:10.1088/1742-5468/aa6bc5

5 Gompper, G. *et al.* The 2020 motile active matter roadmap. *Journal of Physics: Condensed Matter* **32**, 193001 (2020). https://doi.org:10.1088/1361-648x/ab6348

6 Pandey, A., Scheel, J. D. & Schumacher, J. Turbulent superstructures in Rayleigh-Bénard convection. *Nature Communications* **9**, 2118 (2018). https://doi.org:10.1038/s41467-018-04478-0

7 Fodor, K., Mellado, J. P. & Wilczek, M. On the Role of Large-Scale Updrafts and Downdrafts in Deviations From Monin–Obukhov Similarity Theory in Free Convection. *Boundary-Layer Meteorology* **172**, 371-396 (2019). https://doi.org:10.1007/s10546-019-00454-3

8 Ramaswamy, S. The Mechanics and Statistics of Active Matter. *Annual Review of Condensed Matter Physics* **1**, 323-345 (2010). https://doi.org:10.1146/annurev-conmatphys-070909-104101
9 Rogers, D. (Vanderbilt University, 1959).
10 Dorigo, M., Theraulaz, G. & Trianni, V. Reflections on the future of swarm robotics. *Science Robotics* **5**, eabe4385 (2020). https://doi.org:10.1126/scirobotics.abe4385
11 Makris, N. C. *et al.* Fish Population and Behavior Revealed by Instantaneous Continental Shelf-Scale Imaging. *Science* **311**, 660-663 (2006). https://doi.org:10.1126/science.1121756
12 Ballerini, M. *et al.* Interaction ruling animal collective behavior depends on topological rather than metric distance: Evidence from a field study. *Proceedings of the National Academy of Sciences* **105**, 1232-1237 (2008). https://doi.org:10.1073/pnas.0711437105
13 Skoyles, J. Starlings' patterns are not spontaneous. *Nature* **530**, 419-419 (2016). https://doi.org:10.1038/530419a
14 Gautrais, J. *et al.* Deciphering Interactions in Moving Animal Groups. *PLOS Computational Biology* **8**, e1002678 (2012). https://doi.org:10.1371/journal.pcbi.1002678
15 Vicsek, T., Czirók, A., Ben-Jacob, E., Cohen, I. & Shochet, O. Novel Type of Phase Transition in a System of Self-Driven Particles. *Physical Review Letters* **75**, 1226-1229 (1995). https://doi.org:10.1103/PhysRevLett.75.1226
16 Chaté, H., Ginelli, F., Grégoire, G., Peruani, F. & Raynaud, F. Modeling collective motion: variations on the Vicsek model. *The European Physical Journal B* **64**, 451-456 (2008). https://doi.org:10.1140/epjb/e2008-00275-9
17 Schaller, V., Weber Christoph, A., Hammerich, B., Frey, E. & Bausch Andreas, R. Frozen steady states in active systems. *Proceedings of the National Academy of Sciences* **108**, 19183-19188 (2011). https://doi.org:10.1073/pnas.1107540108
18 Schaller, V., Weber, C., Semmrich, C., Frey, E. & Bausch, A. R. Polar patterns of driven filaments. *Nature* **467**, 73-77 (2010). https://doi.org:10.1038/nature09312
19 Di Leonardo, R. *et al.* Bacterial ratchet motors. *Proc Natl Acad Sci U S A* **107**, 9541-9545 (2010). https://doi.org:10.1073/pnas.0910426107
20 Sokolov, A., Apodaca, M. M., Grzybowski, B. A. & Aranson, I. S. Swimming bacteria power microscopic gears. *Proc Natl Acad Sci U S A* **107**, 969-974 (2010). https://doi.org:10.1073/pnas.0913015107
21 Thampi, S. P., Doostmohammadi, A., Shendruk, T. N., Golestanian, R. & Yeomans, J. M. Active micromachines: Microfluidics powered by mesoscale turbulence. *Science Advances* **2**, e1501854 (2016). https://doi.org:10.1126/sciadv.1501854
22 Palacci, J., Sacanna, S., Steinberg, A. P., Pine, D. J. & Chaikin, P. M. Living Crystals of Light-Activated Colloidal Surfers. *Science* **339**, 936-940 (2013). https://doi.org:10.1126/science.1230020
23 Bricard, A., Caussin, J.-B., Desreumaux, N., Dauchot, O. & Bartolo, D. Emergence of macroscopic directed motion in populations of motile colloids. *Nature* **503**, 95-98 (2013). https://doi.org:10.1038/nature12673
24 Bricard, A. *et al.* Emergent vortices in populations of colloidal rollers. *Nature Communications* **6**, 7470 (2015). https://doi.org:10.1038/ncomms8470
25 Cavagna, A. & Giardina, I. Bird Flocks as Condensed Matter. *Annual Review of Condensed Matter Physics* **5**, 183-207 (2014). https://doi.org:10.1146/annurev-conmatphys-031113-133834
26 Szent-Györgyi, A. G. The Early History of the Biochemistry of Muscle Contraction. *Journal of General Physiology* **123**, 631-641 (2004). https://doi.org:10.1085/jgp.200409091
27 Urrutia, R., McNiven, M. A., Albanesi, J. P., Murphy, D. B. & Kachar, B. Purified kinesin promotes vesicle motility and induces active sliding between microtubules in vitro. *Proceedings of the National Academy of Sciences* **88**, 6701-6705 (1991). https://doi.org:10.1073/pnas.88.15.6701
28 Rickey Welch, G. An analogical "field" construct in cellular biophysics: History and present status. *Progress in Biophysics and Molecular Biology* **57**, 71-128 (1992). https://doi.org:https://doi.org/10.1016/0079-6107(92)90005-Q
29 Visscher, K., Schnitzer, M. J. & Block, S. M. Single kinesin molecules studied with a molecular force clamp. *Nature* **400**, 184-189 (1999). https://doi.org:10.1038/22146
30 Coy, D. L., Wagenbach, M. & Howard, J. Kinesin Takes One 8-nm Step for Each ATP That It Hydrolyzes*. *Journal of Biological Chemistry* **274**, 3667-3671 (1999). https://doi.org:https://doi.org/10.1074/jbc.274.6.3667
31 Young, E. C., Mahtani, H. K. & Gelles, J. One-Headed Kinesin Derivatives Move by a Nonprocessive, Low-Duty Ratio Mechanism Unlike That of Two-Headed Kinesin. *Biochemistry* **37**, 3467-3479 (1998). https://doi.org:10.1021/bi972172n

32 Hancock, W. O. & Howard, J. Processivity of the Motor Protein Kinesin Requires Two Heads. *Journal of Cell Biology* **140**, 1395-1405 (1998). https://doi.org:10.1083/jcb.140.6.1395

33 Schnitzer, M. J. & Block, S. M. Kinesin hydrolyses one ATP per 8-nm step. *Nature* **388**, 386-390 (1997). https://doi.org:10.1038/41111

34 Ndlec, F. J., Surrey, T., Maggs, A. C. & Leibler, S. Self-organization of microtubules and motors. *Nature* **389**, 305-308 (1997). https://doi.org:10.1038/38532

35 Kojima, H., Muto, E., Higuchi, H. & Yanagida, T. Mechanics of single kinesin molecules measured by optical trapping nanometry. *Biophysical Journal* **73**, 2012-2022 (1997). https://doi.org:https://doi.org/10.1016/S0006-3495(97)78231-6

36 Coppin, C. M., Pierce, D. W., Hsu, L. & Vale, R. D. The load dependence of kinesin's mechanical cycle. *Proceedings of the National Academy of Sciences* **94**, 8539-8544 (1997). https://doi.org:10.1073/pnas.94.16.8539

37 Vale, R. D. *et al.* Direct observation of single kinesin molecules moving along microtubules. *Nature* **380**, 451-453 (1996). https://doi.org:10.1038/380451a0

38 Meyhöfer, E. & Howard, J. The force generated by a single kinesin molecule against an elastic load. *Proceedings of the National Academy of Sciences* **92**, 574-578 (1995). https://doi.org:10.1073/pnas.92.2.574

39 Svoboda, K. & Block, S. M. Force and velocity measured for single kinesin molecules. *Cell* **77**, 773-784 (1994). https://doi.org:https://doi.org/10.1016/0092-8674(94)90060-4

40 Svoboda, K., Schmidt, C. F., Schnapp, B. J. & Block, S. M. Direct observation of kinesin stepping by optical trapping interferometry. *Nature* **365**, 721-727 (1993). https://doi.org:10.1038/365721a0

41 Anson, M. Temperature dependence and arrhenius activation energy of F-actin velocity generated in vitro by skeletal myosin. *Journal of Molecular Biology* **224**, 1029-1038 (1992). https://doi.org:https://doi.org/10.1016/0022-2836(92)90467-X

42 Howard, J., Hudspeth, A. J. & Vale, R. D. Movement of microtubules by single kinesin molecules. *Nature* **342**, 154-158 (1989). https://doi.org:10.1038/342154a0

43 Collins, C. A. & Vallee, R. B. Temperature-dependent reversible assembly of taxol-treated microtubules. *Journal of Cell Biology* **105**, 2847-2854 (1987). https://doi.org:10.1083/jcb.105.6.2847

44 Vale, R. D., Reese, T. S. & Sheetz, M. P. Identification of a novel force-generating protein, kinesin, involved in microtubule-based motility. *Cell* **42**, 39-50 (1985). https://doi.org:https://doi.org/10.1016/S0092-8674(85)80099-4

45 Surrey, T., Nédélec, F., Leibler, S. & Karsenti, E. Physical Properties Determining Self-Organization of Motors and Microtubules. *Science* **292**, 1167-1171 (2001). https://doi.org:10.1126/science.1059758

46 Sanchez, T., Chen, D. T., DeCamp, S. J., Heymann, M. & Dogic, Z. Spontaneous motion in hierarchically assembled active matter. *Nature* **491**, 431-434 (2012). https://doi.org:10.1038/nature11591

47 Gagnon, D. A. *et al.* Shear-Induced Gelation of Self-Yielding Active Networks. *Phys Rev Lett* **125**, 178003 (2020). https://doi.org:10.1103/PhysRevLett.125.178003

48 DeCamp, S. J., Redner, G. S., Baskaran, A., Hagan, M. F. & Dogic, Z. Orientational order of motile defects in active nematics. *Nat Mater* **14**, 1110-1115 (2015). https://doi.org:10.1038/nmat4387

49 Zhou, S., Sokolov, A., Lavrentovich, O. D. & Aranson, I. S. Living liquid crystals. *Proc Natl Acad Sci U S A* **111**, 1265-1270 (2014). https://doi.org:10.1073/pnas.1321926111

50 Denton, M. *Evolution: A Theory in Crisis*. (Adler & Adler, 1996).

51 Norton, M. M., Grover, P., Hagan, M. F. & Fraden, S. Optimal Control of Active Nematics. *Physical Review Letters* **125**, 178005 (2020). https://doi.org:10.1103/PhysRevLett.125.178005

52 Shankar, S., Scharrer, L. V. D., Bowick, M. J. & Marchetti, M. C. Spatiotemporal control of active topological defects. arXiv:2212.00666 (2022). <https://ui.adsabs.harvard.edu/abs/2022arXiv221200666S>.

53 Shankar, S. & Marchetti, M. C. Hydrodynamics of Active Defects: From Order to Chaos to Defect Ordering. *Physical Review X* **9** (2019). https://doi.org:10.1103/PhysRevX.9.041047

54 Henkin, G., DeCamp, S. J., Chen, D. T., Sanchez, T. & Dogic, Z. Tunable dynamics of microtubule-based active isotropic gels. *Philos Trans A Math Phys Eng Sci* **372** (2014). https://doi.org:10.1098/rsta.2014.0142

55 Wu, K. T. *et al.* Transition from turbulent to coherent flows in confined three-dimensional active fluids. *Science* **355** (2017). https://doi.org:10.1126/science.aal1979

56 Wioland, H., Woodhouse, F. G., Dunkel, J., Kessler, J. O. & Goldstein, R. E. Confinement Stabilizes a Bacterial Suspension into a Spiral Vortex. *Physical Review Letters* **110**, 268102 (2013). https://doi.org:10.1103/PhysRevLett.110.268102

57 Woodhouse, F. G. & Goldstein, R. E. Spontaneous Circulation of Confined Active Suspensions. *Physical Review Letters* **109**, 168105 (2012). https://doi.org:10.1103/PhysRevLett.109.168105

58 Riedel, I. H., Kruse, K. & Howard, J. A Self-Organized Vortex Array of Hydrodynamically Entrained Sperm Cells. *Science* **309**, 300-303 (2005). https://doi.org:10.1126/science.1110329
59 Xu, T. *et al.* SOAX: A software for quantification of 3D biopolymer networks. *Scientific Reports* **5**, 9081 (2015). https://doi.org:10.1038/srep09081
60 Varghese, M., Baskaran, A., Hagan, M. F. & Baskaran, A. Confinement-Induced Self-Pumping in 3D Active Fluids. *Phys Rev Lett* **125**, 268003 (2020). https://doi.org:10.1103/PhysRevLett.125.268003
61 Bate, T. E., Jarvis, E. J., Varney, M. E. & Wu, K. T. Collective dynamics of microtubule-based 3D active fluids from single microtubules. *Soft Matter* **15**, 5006-5016 (2019). https://doi.org:10.1039/c9sm00123a
62 Fan, Y., Wu, K.-T., Aghvami, S. A., Fraden, S. & Breuer, K. S. Effects of confinement on the dynamics and correlation scales in kinesin-microtubule active fluids. *Physical Review E* **104**, 034601 (2021). https://doi.org:10.1103/PhysRevE.104.034601
63 Bate, T. E. *et al.* Self-mixing in microtubule-kinesin active fluid from nonuniform to uniform distribution of activity. *Nature Communications* **13**, 6573 (2022). https://doi.org:10.1038/s41467-022-34396-1
64 Tayar, A. M. *et al.* Controlling liquid-liquid phase behavior with an active fluid. *arXiv e-prints*, arXiv:2208.12769 (2022).
65 Adkins, R. *et al.* Dynamics of active liquid interfaces. *Science* **377**, 768-772 (2022). https://doi.org:10.1126/science.abo5423
66 Chen, Y. C., Jolicoeur, B., Chueh, C. C. & Wu, K. T. Flow coupling between active and passive fluids across water-oil interfaces. *Sci Rep* **11**, 13965 (2021). https://doi.org:10.1038/s41598-021-93310-9
67 Liu, Y., Lipowsky, R. & Dimova, R. Concentration Dependence of the Interfacial Tension for Aqueous Two-Phase Polymer Solutions of Dextran and Polyethylene Glycol. *Langmuir* **28**, 3831-3839 (2012). https://doi.org:10.1021/la204757z
68 Guillamat, P., Hardouin, J., Prat, B. M., Ignes-Mullol, J. & Sagues, F. Control of active turbulence through addressable soft interfaces. *J Phys Condens Matter* **29**, 504003 (2017). https://doi.org:10.1088/1361-648X/aa99c8
69 Hardoüin, J. *et al.* Active boundary layers in confined active nematics. *Nature Communications* **13**, 6675 (2022). https://doi.org:10.1038/s41467-022-34336-z
70 Keber, F. C. *et al.* Topology and dynamics of active nematic vesicles. *Science* **345**, 1135-1139 (2014). https://doi.org:10.1126/science.1254784
71 Gao, T. & Li, Z. Self-Driven Droplet Powered By Active Nematics. *Phys Rev Lett* **119**, 108002 (2017). https://doi.org:10.1103/PhysRevLett.119.108002
72 Thijssen, K. *et al.* Submersed micropatterned structures control active nematic flow, topology, and concentration. *Proc Natl Acad Sci U S A* **118** (2021). https://doi.org:10.1073/pnas.2106038118
73 Guillamat, P., Ignés-Mullol, J., Shankar, S., Marchetti, M. C. & Sagués, F. Probing the shear viscosity of an active nematic film. *Physical Review E* **94**, 060602 (2016). https://doi.org:10.1103/PhysRevE.94.060602
74 Oswald, P. & Pieranski, P. *Smectic and columnar liquid crystals: Concepts and physical properties illustrated by experiments*. (2006).
75 Guillamat, P., Ignés-Mullol, J. & Sagués, F. Control of active nematics with passive liquid crystals. *Molecular Crystals and Liquid Crystals* **646**, 226-234 (2017). https://doi.org:10.1080/15421406.2017.1288007
76 Guillamat, P., Ignes-Mullol, J. & Sagues, F. Taming active turbulence with patterned soft interfaces. *Nat Commun* **8**, 564 (2017). https://doi.org:10.1038/s41467-017-00617-1
77 Guillamat, P., Ignes-Mullol, J. & Sagues, F. Control of active liquid crystals with a magnetic field. *Proc Natl Acad Sci U S A* **113**, 5498-5502 (2016). https://doi.org:10.1073/pnas.1600339113
78 Vassilev, P. M., Dronzine, R. T., Vassileva, M. P. & Georgiev, G. A. Parallel arrays of microtubles formed in electric and magnetic fields. *Bioscience Reports* **2**, 1025-1029 (1982). https://doi.org:10.1007/bf01122171
79 Stracke, R., Böhm, K. J., Wollweber, L., Tuszynski, J. A. & Unger, E. Analysis of the migration behaviour of single microtubules in electric fields. *Biochemical and Biophysical Research Communications* **293**, 602-609 (2002). https://doi.org:https://doi.org/10.1016/S0006-291X(02)00251-6
80 Jia, L., Moorjani, S. G., Jackson, T. N. & Hancock, W. O. Microscale Transport and Sorting by Kinesin Molecular Motors. *Biomedical Microdevices* **6**, 67-74 (2004). https://doi.org:10.1023/B:BMMD.0000013368.89455.8d
81 van den Heuvel, M. G. L., de Graaff, M. P. & Dekker, C. Molecular Sorting by Electrical Steering of Microtubules in Kinesin-Coated Channels. *Science* **312**, 910-914 (2006). https://doi.org:10.1126/science.1124258
82 Kim, T., Kao, M.-T., Hasselbrink, E. F. & Meyhöfer, E. Active Alignment of Microtubules with Electric Fields. *Nano Letters* **7**, 211-217 (2007). https://doi.org:10.1021/nl061474k

83 Duclos, G. *et al.* Topological structure and dynamics of three-dimensional active nematics. *Science* **367**, 1120-1124 (2020). https://doi.org:10.1126/science.aaz4547

84 Purdy, K. R. *et al.* Measuring the nematic order of suspensions of colloidal fd virus by x-ray diffraction and optical birefringence. *Physical Review E* **67**, 031708 (2003). https://doi.org:10.1103/PhysRevE.67.031708

85 Berezney, J., Goode, B. L., Fraden, S. & Dogic, Z. Extensile to contractile transition in active microtubule-actin composites generates layered asters with programmable lifetimes. *Proc Natl Acad Sci U S A* **119** (2022). https://doi.org:10.1073/pnas.2115895119

86 Tayar, A. M., Hagan, M. F. & Dogic, Z. Active liquid crystals powered by force-sensing DNA-motor clusters. *Proc Natl Acad Sci U S A* **118** (2021). https://doi.org:10.1073/pnas.2102873118

87 Keya, J. J. *et al.* DNA-assisted swarm control in a biomolecular motor system. *Nature Communications* **9**, 453 (2018). https://doi.org:10.1038/s41467-017-02778-5

88 Marx, A., Hoenger, A. & Mandelkow, E. Structures of kinesin motor proteins. *Cell Motility* **66**, 958-966 (2009). https://doi.org:https://doi.org/10.1002/cm.20392

89 Lemma, B., Mitchell, N. P., Subramanian, R., Needleman, D. J. & Dogic, Z. Active Microphase Separation in Mixtures of Microtubules and Tip-Accumulating Molecular Motors. *Physical Review X* **12**, 031006 (2022). https://doi.org:10.1103/PhysRevX.12.031006

90 Chandrakar, P. *et al.* Engineering stability, longevity, and miscibility of microtubule-based active fluids. *Soft Matter* **18**, 1825-1835 (2022). https://doi.org:10.1039/d1sm01289d

91 Bieling, P., Telley, I. A., Piehler, J. & Surrey, T. Processive kinesins require loose mechanical coupling for efficient collective motility. *EMBO reports* **9**, 1121-1127 (2008). https://doi.org:https://doi.org/10.1038/embor.2008.169

92 Hong, W., Takshak, A., Osunbayo, O., Kunwar, A. & Vershinin, M. The Effect of Temperature on Microtubule-Based Transport by Cytoplasmic Dynein and Kinesin-1 Motors. *Biophysical Journal* **111**, 1287-1294 (2016). https://doi.org:https://doi.org/10.1016/j.bpj.2016.08.006

93 Kawaguchi, K. & Ishiwata, S. Thermal activation of single kinesin molecules with temperature pulse microscopy. *Cell Motil Cytoskeleton* **49**, 41-47 (2001). https://doi.org:10.1002/cm.1019

94 Kawaguchi, K. & Ishiwata, S. i. Temperature Dependence of Force, Velocity, and Processivity of Single Kinesin Molecules. *Biochemical and Biophysical Research Communications* **272**, 895-899 (2000). https://doi.org:https://doi.org/10.1006/bbrc.2000.2856

95 Böhm, K. J., Stracke, R., Baum, M., Zieren, M. & Unger, E. Effect of temperature on kinesin-driven microtubule gliding and kinesin ATPase activity. *FEBS Letters* **466**, 59-62 (2000). https://doi.org:https://doi.org/10.1016/S0014-5793(99)01757-3

96 Likhachev, E. R. Dependence of water viscosity on temperature and pressure. *Technical Physics* **48**, 514-515 (2003). https://doi.org:10.1134/1.1568496

97 Ross, T. D. *et al.* Controlling organization and forces in active matter through optically defined boundaries. *Nature* **572**, 224-229 (2019). https://doi.org:10.1038/s41586-019-1447-1

98 L.M. Lemma, M. V., T.D. Ross, M. Thompson, A. Baskaran, Z. Dogic. Spatiotemporal patterning of extensile active stresses in microtubule-based active fluids. *arXiv* (2022). https://doi.org:https://arxiv.org/abs/2209.06277

99 Najma, B. *et al.* Competing instabilities reveal how to rationally design and control active crosslinked gels. *Nature Communications* **13**, 6465 (2022). https://doi.org:10.1038/s41467-022-34089-9

100 Zhang, R. *et al.* Spatiotemporal control of liquid crystal structure and dynamics through activity patterning. *Nat Mater* **20**, 875-882 (2021). https://doi.org:10.1038/s41563-020-00901-4

101 Biswas, M. H. A., Huda, M., Ara, M. & Rahman, M. Optimal Control Theory and It's Applications in Aerospace Engineering. *International Journal of Academic Research, Vol. 3, No. 2, Part II, pp. 349-357, 2011.* (2011).

102 Hagan, M. F. & Grason, G. M. Equilibrium mechanisms of self-limiting assembly. *Reviews of Modern Physics* **93**, 025008 (2021). https://doi.org:10.1103/RevModPhys.93.025008

103 Hayakawa, D. *et al.* Geometrically programmed self-limited assembly of tubules using DNA origami colloids. *arXiv e-prints*, arXiv:2203.01421 (2022).

104 Serafin, F., Lu, J., Kotov, N., Sun, K. & Mao, X. Frustrated self-assembly of non-Euclidean crystals of nanoparticles. *Nature Communications* **12**, 4925 (2021). https://doi.org:10.1038/s41467-021-25139-9

105 Jumper, J. *et al.* Highly accurate protein structure prediction with AlphaFold. *Nature* **596**, 583-589 (2021). https://doi.org:10.1038/s41586-021-03819-2

106 Yang, J. *et al.* Improved protein structure prediction using predicted interresidue orientations. *Proceedings of the National Academy of Sciences* **117**, 1496-1503 (2020). https://doi.org:10.1073/pnas.1914677117

107 Bate, T. E., Jarvis, E. J., Varney, M. E. & Wu, K. T. Controlling Flow Speeds of Microtubule-Based 3D Active Fluids Using Temperature. *J Vis Exp* (2019). https://doi.org:10.3791/60484

CHAPTER 2: COLLECTIVE DYNAMICS OF MICROTUBULE-BASED 3D ACTIVE FLUIDS FROM SINGLE MICROTUBULES*

*This chapter is an adaptation of Bate *et al.*, Soft Matter, 2019, **15** (25), 5006-5016.

2.1 ABSTRACT Self-organization of kinesin-driven, microtubule-based 3D active fluids relies on the collective dynamics of single microtubules. However, the connection between macroscopic fluid flows and microscopic motion of microtubules remains unclear. In this work, the motion of single microtubules was characterized by means of 2D gliding assays and compared with the flows of 3D active fluids. While the scales of the two systems differ by ~1,000×, both were driven by processive, non-processive or an equal mixture of both molecular motor proteins. To search for the dynamic correlation between both systems, the motor activities were tuned by varying temperature and ATP concentration, and the changes in both systems were compared. Motor processivity played an important role in active fluid flows but only when the fluids were nearly motionless; otherwise, flows were dominated by hydrodynamic resistance controlled by sample size. Furthermore, while the motors' thermal reaction led active fluids to flow faster with increasing temperature, such temperature dependence could be reversed by introducing temperature-varying depletants, emphasizing the potential role of the depletant in designing an active fluid's temperature response. The temperature response of active fluids was nearly immediate ($\lesssim$10 sec). Such a characteristic enables active fluids to be controlled with a temperature switch. Overall, this work not only clarifies the role of temperature in active fluid activity, but also sheds light on the underlying principles of the relationship between the collective dynamics of active fluids and the dynamics of their constituent single microtubules.

2.2 INTRODUCTION Materials are comprised of building blocks held together by pairwise interactions that determine their material properties as well as their phases. In equilibrium, material states satisfy the rule of free energy minimization, whereas away from equilibrium, that rule is no longer applicable. A material stays out of equilibrium and is termed active matter when its constituents locally consume chemical energy to generate mechanical work. Active matter can consist of living organisms (such as bacteria and epithelial cells) or nonliving entities (such as colloids, grains and cytoskeletal filaments)[1-13]. Each constituent is motile and interacts with its neighbors[14]. These microscopic interactions accumulate to produce flocking, swarming or circulation at the macroscopic scale[15-22]. These unique characteristics of active matter have found application in optical devices, molecular shuttles and parallel computation, reflecting the feasibility and versatility of active matter applications[23-26]. However, development of these applications will be limited if knowledge of self-organization of active matter remains immature; therefore, there is a need to clarify the underlying principles of the dynamics of self-organization[27]. Therefore, this work correlated cumulative macroscopic dynamics with microscopic dynamics of constituents. The correlation revealed the role of microscopic dynamics in the macroscopic self-organization of active matter.

In this work, the active matter was kinesin-driven, microtubule-based 3D active fluids, due to their high tunability and their robust dynamics[28-31]. The system was comprised of three main components: microtubules, kinesin motor clusters and depletants (Fig. 20a). Depletants induced depletion forces that bundled microtubules[32]. The bundled antiparallel microtubules were bridged by motor clusters which consumed adenosine triphosphate (ATP) to slide apart microtubules, causing interfilament sliding. The sliding collectively led microtubule bundles to extend (extensile bundles, Fig. 20b) until buckling instability caused them to break[33]. The broken bundles recombined because of depletion forces, and the dynamics repeated. In the steady state, the microtubules developed into 3D active gels with dynamics consisting of repeating cycles of bundling,

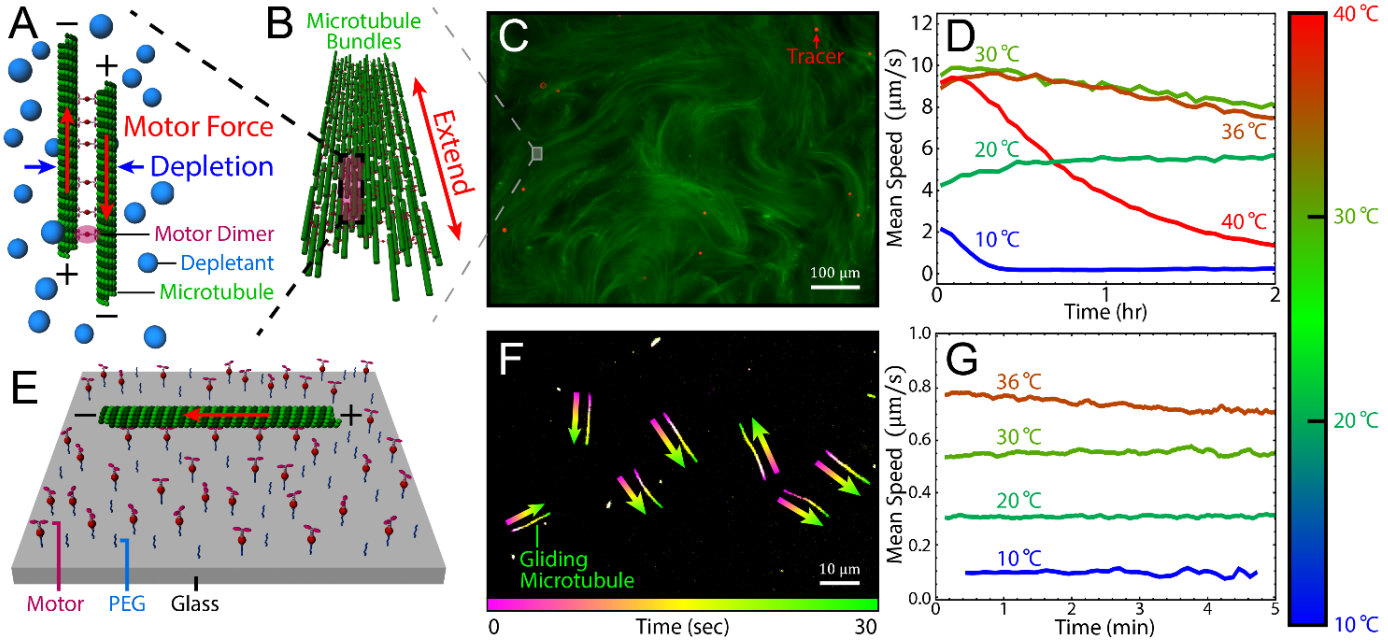

FIG. 20: COMPARISON OF TEMPERATURE-DEPENDENT DYNAMICS OF 3D MICROTUBULE-BASED ACTIVE FLUIDS WITH 2D MICROTUBULE GLIDING **a**) Pairs of microtubules were brought together by depletant-induced attraction (depletion). The bound microtubules were then bridged by motor clusters that slide apart antiparallel microtubules, causing interfilament sliding. **b**) The sliding resulted in the extension of microtubule bundles (extensile bundles). **c**) The collective dynamics of extensile bundles constituted active microtubule networks (green filaments), which constantly rearranged their structure while stirring surrounding aqueous fluids whose motion was revealed with tracers (red dots). **d**) Tracer trajectories were used to determine fluid mean speeds, which depended on temperature. **e**) Schematic of a microtubule gliding on a motor-coated surface (gliding assay). **f**) Stacking sequential images of gliding microtubules colored according to a time color bar revealed gliding trajectories, directions (magenta to green) and speeds (trajectory lengths). **g**) The mean speeds of microtubule gliding were nearly invariant for 5 min but the speeds increased with temperature.

extending and buckling (Fig. 20c)[11]. The gels stirred surrounding fluids, inducing flows (active fluids) whose motion could be visualized by doping the fluids with tracer particles. In this work, microtubule-based networks whose structures constantly rearranged are referred to as active gels, and the surrounding water driven by the motion of active gels as active fluids.

The flows of 3D active fluids originated from the motion of single microtubules whose dynamics could be characterized by monitoring a single 2D microtubule gliding on a kinesin-coated surface (gliding assay, Fig. 20e&f)[34]. To characterize the collective dynamics from a single microtubule, mean speeds of 3D flows and 2D gliding were compared as motor dynamics were varied by varying temperature and ATP concentration[35-38]. To examine the role of the motor stepping mechanism in active fluid behaviors, the flows and gliding were driven with processive motors, non-processive motors and an equal mixture of both. Processive motors exerted a force on microtubules continuously whereas non-processive ones detached after each force application[31,39-42]. Motor processivity dominated self-organization of active fluids only when the fluids were nearly still. At higher activity, active fluid dynamics were affected by hydrodynamic resistance[21,43]. Also, while the motor's rising reaction rates with elevated temperatures led active fluids to flow faster when heated, such temperature responses of active fluids could be reversed by introduction of temperature-dependent depletants, suggesting the potential for depletant-based control of an active fluid's temperature dependence[44]. Finally, the temperature response of active fluids was not only reversible but also nearly immediate. Such an instant response enabled the design of active fluids whose activities were switchable, reinforcing the feasibility of controlling active matter *in situ* using temperature instead of electromagnetic control[4,5,45-49].

2.3 MATERIALS AND METHODS

2.3.1 POLYMERIZING MICROTUBULES Active fluids

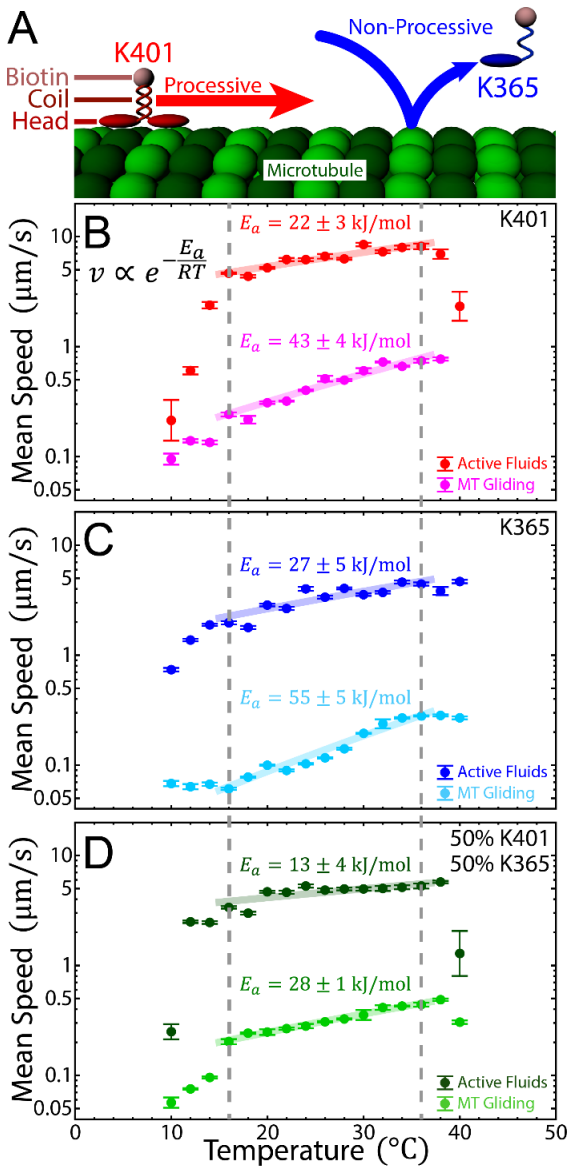

FIG. 21: TEMPERATURE RESPONSE OF ACTIVE FLUIDS AND MICROTUBULE GLIDING DRIVEN BY PROCESSIVE AND NON-PROCESSIVE MOTORS **a**) K401 motors walked along microtubules continuously without detaching (processive) whereas K365 motors detached after each step (non-processive). Both types of motors were biotinylated (pink spheres) to enable conjugation to streptavidin. Streptavidin conjugation enabled the formation of motor clusters in active fluids, as well as motor-coating of surfaces in a gliding assay (Fig. 20a&e). **b-d**) Mean speeds of active fluid flows and microtubule gliding as a function of temperature. Decreasing the temperature below 14°C destabilized microtubules; flows and gliding were suppressed. Heating above 38°C inhibited K401-associated activities, implying occurrences of malfunction in K401 motor clusters, whereas K365-driven systems remained active, demonstrating a stronger resistance to heat. Increasing the temperature from 16 to 36°C (between dashed gray lines) accelerated flows and gliding driven by K401 and K365 but not for an equal mixture of both (50% K401 and 50% K365). Active fluids driven by both types of motors had temperature-insensitive flows. Error bars represent the standard deviations of time-averaged mean speeds. Each mean speed *vs.* temperature (16–36°C) was fit to the Arrhenius law: mean speed, $\boldsymbol{v = A\, e^{-E_a/RT}}$, where $\boldsymbol{R}$ = 8.31 J/mol K was the gas constant, $\boldsymbol{A}$ was the pre-exponential factor, $\boldsymbol{T}$ was temperature, and $\boldsymbol{E_a}$ was the activation energy (solid curves in B-D).

were powered by kinesin-driven microtubules, comprised of α- and β-tubulin dimers. Tubulins were purified from bovine brains with three cycles of polymerization and depolymerization[50]. To polymerize microtubules, 8 mg/mL purified tubulins was mixed with 600 μM guanosine-5′[(α,β)-methyleno]triphosphate (GMPCPP, Jena Biosciences, NU-4056) and 1 mM dithiothreitol (DTT, Fisher Scientific, AC165680050) in microtubule buffer (M2B: 80 mM PIPES, 2 mM $MgCl_2$, 1 mM EGTA, pH 6.8)[51]. To image the polymerized microtubules, 3% of tubulin mixture was labeled with Alexa Fluor 647 (Invitrogen, A-20006). The mixture was incubated at 37°C for 30 min, then annealed at room temperature for 6 hr[11]. Polymerized microtubules were stored at –80°C until use.

2.3.2 SYNTHESIZING KINESIN CLUSTERS Our active matter's power source originated from kinesin motors. The motors were expressed in the *Escherichia coli* derivative Rosetta 2 (DE3) pLysS cells (Novagen, 71403) transformed with DNA plasmids derived from the *Drosophila melanogaster* kinesin (DMK) gene. In this paper, plasmids were used that included the DMK's first 401 N-terminal DNA codons, which was long enough to permit the folding of the processive motor protein (K401)[40]. To determine the role of processivity in active gel dynamics, we employed another plasmid with the first 365 codons, which directs the expression of non-processive motors (K365, Fig. 21b)[41]. To drive active gels, the motors needed to be tagged with biotin and then clustered. Therefore, the motors were biotinylated at their N terminals (BIO) and then tagged with a histidine tag (H6), enabling purification of the motors using immobilized metal ion affinity chromatography (IMAC) with gravity nickel columns (GE Healthcare, 11003399)[52]. Thus, processive motors consisted of K401-BIO-H6, and non-processive ones of K365-BIO-H6[40,41]. To cluster either biotinylated motor, streptavidin tetramers were used as the clustering agent; 1.8 μM streptavidin (Invitrogen, S-888) was mixed with

M2B containing 120 μM DTT and either 1.5 μM processive motors or 5.4 μM non-processive motors, followed by 30 min incubation at 4°C[30,31]. The clustered motors were aliquoted and stored at –80°C.

2.3.3 PREPARING KINESIN-DRIVEN, MICROTUBULE-BASED ACTIVE FLUIDS Active fluids were driven by ~0.1% active gels, which were comprised mainly of microtubules, kinesin motors and depletants (Fig. 20a). To synthesize active gels, 1.3 mg/mL microtubules was mixed with 120 nM motor clusters in high salt M2B (M2B + 3.9 mM $MgCl_2$). To bundle microtubules, either 0.8% polyethylene glycol (PEG 20k, Sigma, 81300) or 2% pluronic F127 (Sigma, P2443) was added as a depletant. The gel's activity was supported by motors stepping along microtubules from minus to plus ends[53]. Each step consumed adenosine triphosphate (ATP), which was converted to adenosine diphosphate (ADP); therefore, the stepping was fueled with 1.4 mM ATP (Sigma, A8937)[38]. However, the consumption of ATP decreased its concentration and slowed the stepping rate[37,38]. To prevent such deceleration, ATP concentration was maintained by reverting each stepping-induced ADP back to ATP with 2.8% v/v stock pyruvate kinase/lactate dehydrogenase (PK/LDH, Sigma, P-0294). To support the reversion, the enzymes were fed with 26 mM phosphenol pyruvate (PEP, BeanTown Chemical, 129745)[11,54]. In this work, samples were imaged with fluorescent microscopy whose quality decreased with time due to photobleaching effects. To reduce these effects, the active gel mixtures were doped with 2 mM Trolox (Sigma, 238813) and oxygen-scavenging enzymes, including 0.038 mg/mL catalase (Sigma, C40) and 0.22 mg/mL glucose oxidase (Sigma, G2133), fed with 3.3 mg/mL glucose (Sigma, G7528). The system was based on proteins, which needed to be stabilized with reducing agents; therefore, the mixtures were doped with 5.5 mM DTT. Finally, active fluids were transparent; to track their motion, ~0.0004% v/v Alexa 488-labeled 3 μm polystyrene microspheres (Polyscience, 18861) were added as tracers (Fig. 20c). Mixing the aforementioned ingredients completed the synthesis of the active fluids. However, different samples of active fluids prepared in the same way could behave differently due to pipetting-induced uncertainties. To reduce such uncertainties and enhance experimental reproducibility, a batch of the above mixture without microtubules (premixture) was prepared[30]. The premixture was aliquoted and stored at –80°C. Before each experiment, active fluids were prepared by mixing one aliquot of premixture with microtubules. After the mixing, the sample was activated: motors started to consume ATP while stepping along microtubules.

2.3.4 CHARACTERIZING ACTIVE FLUID ACTIVITY The activated sample created turbulent-like mixing flows[11,21]. To observe the flows microscopically, the samples were loaded into a polyacrylamide-coated glass flow cell (~20×5×0.1 mm^3 = 10 μL), and sealed with UV glue (Norland Products, NOA81)[31,55]. Once sealed in flow cells, active fluids were imaged with epifluorescent microscopy: Alexa 647-labeled microtubules were imaged with a Cy5 filter cube (Excitation: 618–650 nm, Emission: 670–698 nm, Semrock, 96376), and Alexa 488-labeled tracers were imaged with a green fluorescent protein (GFP) filter cube (Excitation: 440–466 nm, Emission: 525–550 nm, Semrock, 96372) (Fig. 20c). To characterize active fluids' activity, tracers were imaged sequentially, and their trajectories were tracked with the Lagrangian tracking algorithm[56]. The trajectories $r_i(t)$ revealed the history of their instant speeds $v_i(t) \equiv dr_i(t)/dt$, which determined the evolution of the fluid's mean flow speed $\bar{v}(t) \equiv \langle v_i(t) \rangle_i$. At 20°C, active fluids flowed at ~6 μm/s for hours, until ATP and PEP were depleted (Fig. 20d)[21]. At 30–36°C, the flows sped up to ~10 μm/s but slowed down gradually because the bundles coarsened over time which built up friction to hamper bundle extension. At 40°C, the flows quickly decayed due to malfunctioning kinesin motor clusters. At 10°C, the flows decelerated nearly to a stop (~0 μm/s) due to depolymerization of GMPCPP-stabilized microtubules. The variation of fluid mean speeds

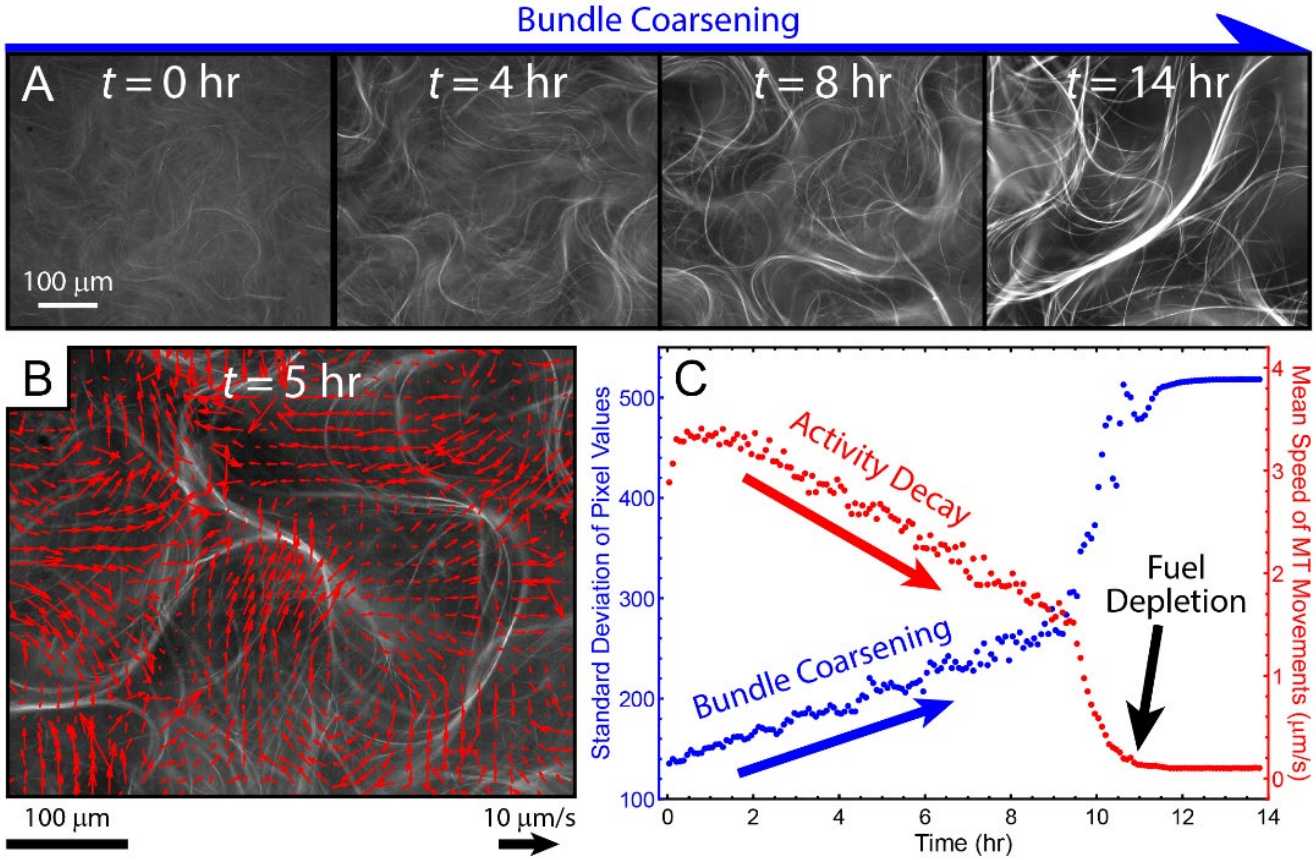

FIG. 22: COARSENING OF MICROTUBULE BUNDLES CAUSES DECAYS IN MICROTUBULE ACTIVITY a) Sequential images of microtubules at 20°C at t = 0–14 hr. The microtubules formed bundles which coarsened over time. **b)** Velocity fields of movements of microtubule bundles. The velocities were measured by tracking the motion of microtubule bundles with a particle-image-velocimetry algorithm (PIVlab version 2.02). **c)** Standard deviation of pixel values in microtubule images compared with mean speed of microtubule movements. Bundle coarsening enhanced image contrast which increased standard deviation of the image's pixel values. The increase in the standard deviation was accompanied by the deceleration of microtubule movements, suggesting that bundle coarsening slowed down activity. Activity lasted for ~11 hr before fuel depletion.

depended on bundle coarsening and stability of microtubules and kinesin motor clusters, all of which varied with temperature.

2.3.5 COARSENING OF MICROTUBULE BUNDLES Dynamics of active fluids slowed down gradually over time (Fig. 20d). This decay was hypothesized to be related to structural change of active gels. To verify this hypothesis, microtubules were imaged in active gels at 20°C for 14 hr. In the beginning, microtubules were distributed mostly homogeneously, but over time, microtubules formed bundles that grew thicker (Fig. 22). Thickness growth enhanced image contrast, which allowed characterization of bundle coarsening by measuring the standard deviation of pixel values. The standard deviation increased with time, reflecting the growth of bundle thickness (blue in Fig. 22c). To examine whether the bundle coarsening caused the activity decay, the velocity field of microtubule bundle movements and their mean speeds as a function of time were measured (Fig. 22b&c)[11,57]. The mean speeds decreased over time accompanied by bundle coarsening, which suggested that the coarsening of microtubule bundles slowed down their movements. The slower bundle movements led to slower active fluid flows. Fortunately, this activity decay was slow and did not impact measurement results if the observation window was short. For example, at 20°C, bundle movements slowed from ~3 to ~2 μm/s in 8 hr (Fig. 22c) but the decay effect was negligible during t = 1–2 hr, the chosen observation window.

2.3.6 CHARACTERIZATION OF MICROTUBULE DEPOLYMERIZATION To examine the temperature dependence of the stability of GMPCPP-stabilized

microtubules, microtubule lengths were monitored in microtubule gliding samples for 50 min at 10–20°C. However, gliding microtubules were motile and did not stay within a microscope field during the measurement window; therefore the sample was deprived of ATP to immobilize microtubules. The stationary microtubules were seen to shrink in lengths at 10°C whereas at 20°C the length was better preserved (Fig. 23a), similar to results of previous studies using taxol-treated microtubules[58]. To measure microtubule lengths, a filament tracking algorithm was used to trace microtubules in each image (pink curves), revealing microtubule length l decreased with time t. To characterize the length decay, the time-averaged rate of the length shrinking k was measured by fitting l *vs.* t to a line function, followed by extracting the line slope (inset in Fig. 23b). The time-averaged rates were measured for 10–13 microtubules to determine mean shrinking rate $\bar{k}$. The microtubules shrank below 16°C, implying microtubule depolymerization (Fig. 23b). Therefore, to ensure that microtubule depolymerization did not affect the investigation of active fluid dynamics, this analysis involved only temperature data at ≥16°C.

2.3.7 TEMPERATURE-INDUCED MALFUNCTION FOR KINESIN CLUSTERS In this work, sample temperatures were varied to explore collective dynamics of active fluids. Maintaining fluid activity required kinesin to bridge pairs of microtubules while stepping toward microtubule plus ends (Fig. 20a). The dynamics required functional kinesin and formation of kinesin clusters. To ensure that both requirements were met, performance of kinesin clusters was examined in the explored temperature range, by adapting Böhm *et al.*'s method[35]. K401 motor clusters were pre-incubated at 20–40°C for 1 hr. The pre-incubated motors were used to prepare active fluid samples, in which time-averaged mean speeds of developed flows were measured at 20°C, and the mean speed was plotted as a function of the pre-incubation temperature (red dots in Fig. 24a). Mean speeds remained almost invariant (~5 μm/s) for the pre-incubation temperatures between 20 and 36°C. Above ~36°C, mean speeds dropped to ~0 μm/s, accompanied by microtubules developing into short, stationary bundles (top image in Fig. 24b). This result was in contrast to the cases without pre-incubation, in which microtubules developed into the long, extending bundles (Fig. 20c). These two observations suggested that K401 clusters were incapable of bridging and sliding pairs of microtubules after incubation at > 36°C. In this work, non-processive motor K365 was also used. To examine temperature impact on K365 motor clusters,

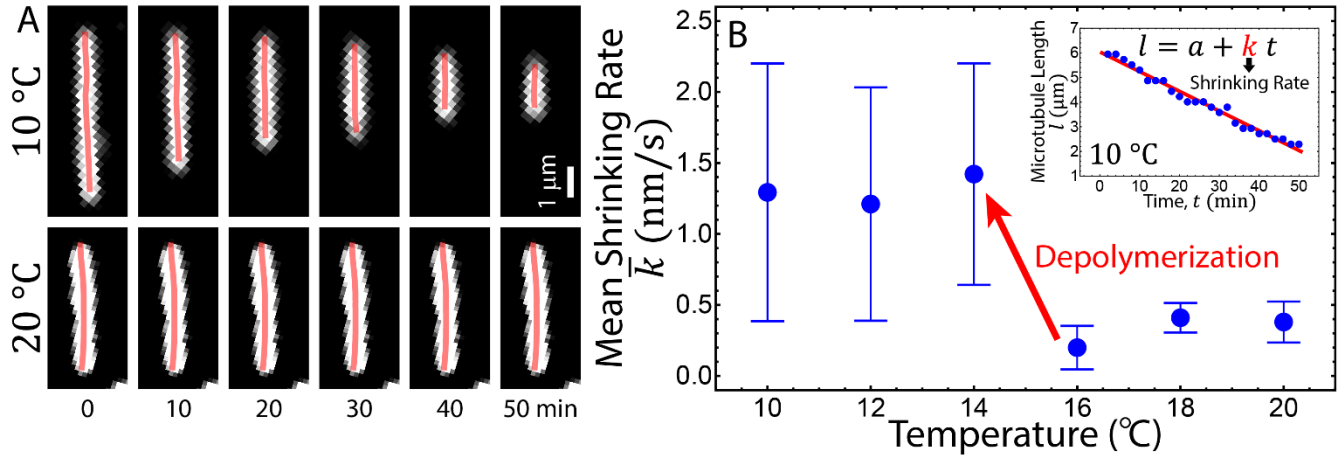

FIG. 23: GMPCPP-STABILIZED MICROTUBULES DEPOLYMERIZE BELOW 16°C **a**) Contrast enhanced images of GMPCPP-stabilized microtubules at 10 and 20°C (top and bottom rows) from $t = 0$ to 50 min (left to right). Each microtubule image was traced by a snake algorithm to measure the microtubule lengths (pink line). **b**) Mean shrinking rate $\bar{\boldsymbol{k}}$ of microtubule length as a function of temperature. Error bars represent the standard deviations of measurements on 10–13 microtubules. Cooling microtubules below 16°C speeded up shrinking, indicating microtubule depolymerization below 16°C (red arrow). Inset: Time-averaged shrinking rate $\boldsymbol{k}$ was measured by fitting the microtubule length $\boldsymbol{l}$ *vs.* time $\boldsymbol{t}$ (blue dots) to a line function $\boldsymbol{l = a + kt}$ with $\boldsymbol{a}$ and $\boldsymbol{k}$ as fitting parameters (red line).

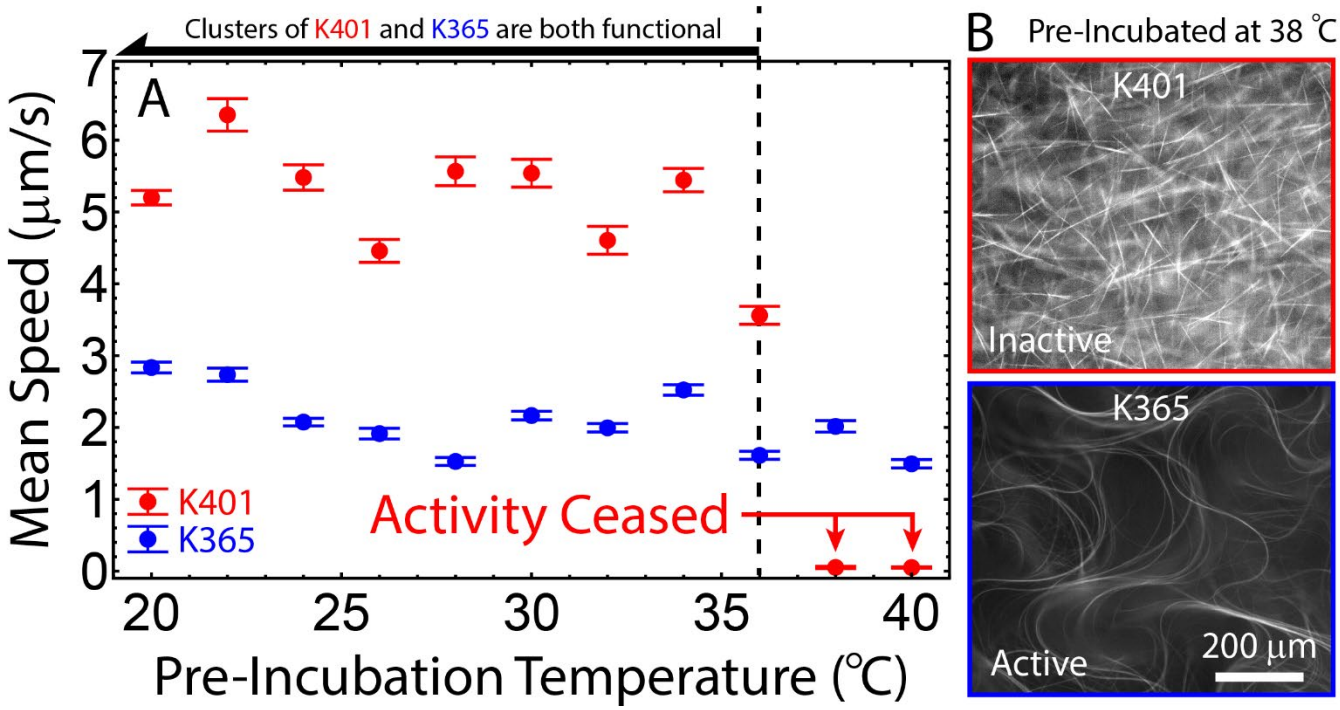

FIG. 24: TEMPERATURE-INDUCED MALFUNCTION FOR KINESIN CLUSTERS **a**) Mean speed of active fluid flows at 20°C driven by pre-incubated motors as a function of pre-incubation temperature. Error bars represent the standard deviations of time-averaged mean speeds. Pre-Incubating K401 clusters at $T \gtrsim 38$°C ceased flows of active fluids (~0 μm/s), in contrast to the case for K365 clusters. Both types of motor clusters were functional below ~36°C. **b**) Images of microtubule-based gels with clusters of K401 (top) and K365 (bottom) pre-incubated at 38°C. The pre-incubated K401 clusters failed to develop long, extensile bundles; the microtubules were stationary. In contrast, the pre-incubated K365 clusters remained capable of sustaining active gel activity.

the same experiments were repeated. The K365 clusters remained stable at 20–40°C (blue dots in Fig. 24a). The motor clusters were able to drive microtubules into active gels after pre-incubation at 38°C (bottom image in Fig. 24b), suggesting that K365 clusters were more heat resistant than K401 clusters. While the underlying mechanisms causing such a difference remained an open question, in this work with both types of motors, the data was fitted, analyzed and compared at $\lesssim 36$°C, to avoid the intervention of malfunctioning motor clusters in the analysis results.

2.3.8 SEPARATING ACTIVE KINESIN MOTOR PROTEINS To ensure the expressed motor proteins were capable of hydrolyzing ATP to produce mechanical work when in contact with microtubules, 0.7 mg/mL kinesin was incubated with 2 mg/mL microtubules, 3.57 mM DTT and 1.4 mM ATP at ~23°C for 30 min. Functioning motors hydrolyzed ATP, then detached from microtubules after $\gtrsim$100 steps[39,59], while malfunctioning motors bound to microtubules without detaching. After incubation, the functioning and malfunctioning motors were separated by 15-min, 100,000 *g* centrifugation at 37°C. The malfunctioning motors sedimented with microtubules while active motors remained suspended. The suspended active motors were then aliquoted and stored at –80°C.

2.3.9 GLIDING MICROTUBULES ON KINESIN-COATED SURFACES To evaluate the dynamics of 3D microtubule-based active fluids from dynamics at the scale of single microtubules, individual microtubules were placed on kinesin-coated surfaces (gliding assay, Fig. 20f). To prepare such surfaces, cleaned glass coverslips and slides were etched by 10 min of sonication in 100 mM potassium hydroxide (KOH). The etched glasses were incubated in 1 mg/mL PEG silane (Laysan Bio, MPEG-SIL-2000-1g) and 39 μg/mL biotinylated PEG silane (Laysan Bio, Biotin-PEG-SIL-3400-1g) in ethanol at 70°C for 5 min. The former coated the glass surface with PEG, preventing proteins from sticking to the bare glass surfaces; the

latter activated the surfaces with biotin, which was further conjugated to streptavidin through 30 min incubation in 1 mg/mL streptavidin in M2B at 4°C. After incubation, the unbound streptavidin was washed out with M2B. The coated streptavidin was subsequently conjugated to biotinylated kinesin motors by 20 min incubation in ~0.5 mg/mL clarified biotinylated kinesin motor proteins in M2B at 4°C. After incubation, the free kinesin motors were washed out with M2B, leaving the glass surfaces coated with kinesin motors.

The coated motors were then bound to microtubules through 2 min incubation of the coated slides in 50 µg/mL Alexa 647-labeled microtubules in M2B at ~23°C. After incubation, the unbound microtubules were washed out with M2B. To activate microtubule gliding, slides were loaded with ATP solution (5.6 mM DTT, 3.33 mg/mL glucose, 255 µg/mL glucose oxidase, 39 µg/mL catalase, 2 mM Trolox, 1.42 mM ATP in high salt M2B), enabling the kinesin motors to hydrolyze ATP while driving microtubule gliding (Fig. 20**e**). To promote surface adsorption of microtubules, 0.4% PEG was added to the solution. PEG also induced depletion among microtubules; however, no bundle formation was observed, suggesting that 0.4% PEG provided insufficient depletion to bundle microtubules in this gliding assay[9,10]. To monitor gliding, microtubules were sequentially imaged with fluorescence microscopy using Cy5 filter cubes and a 60× objective (Nikon, CFI Plan Fluor 60X NA 0.85, MRH00602) for 5 min (Fig. 20f). The sequential images allowed tracking of the gliding of each microtubule with the Lagrangian tracking algorithm[56]. The trajectories revealed gliding speeds *vs.* time, which were averaged over different microtubules to determine mean gliding speeds. At 20°C, microtubules glided on K401-coated surfaces at ~0.3 µm/s (Fig. 1g).

2.3.10 CONTROLLING SAMPLE TEMPERATURE To tune motor activity locally, sample temperature was varied. The sample was cooled or heated through contact with a peltier (TE Technology, CH-109-1.4-1.5, Fig. 6a). Peltier performance depended on the direction and amplitude of the applied direct current, which was regulated by a temperature controller (TE Technology, TC-720)[60]. The controller read the sample temperature through a thermal sensor (TE Technology, MP-3022), and the sample temperature was compared with the target temperature to determine the applied current through a proportional-integral-derivative (PID) algorithm[61]. The controller was connected to a computer for recording sample temperatures. The recorded temperatures showed a fluctuation of ≲0.3°C, demonstrating the stability of the temperature control (Fig. 25b). Such controllability enabled characterizing the sample's

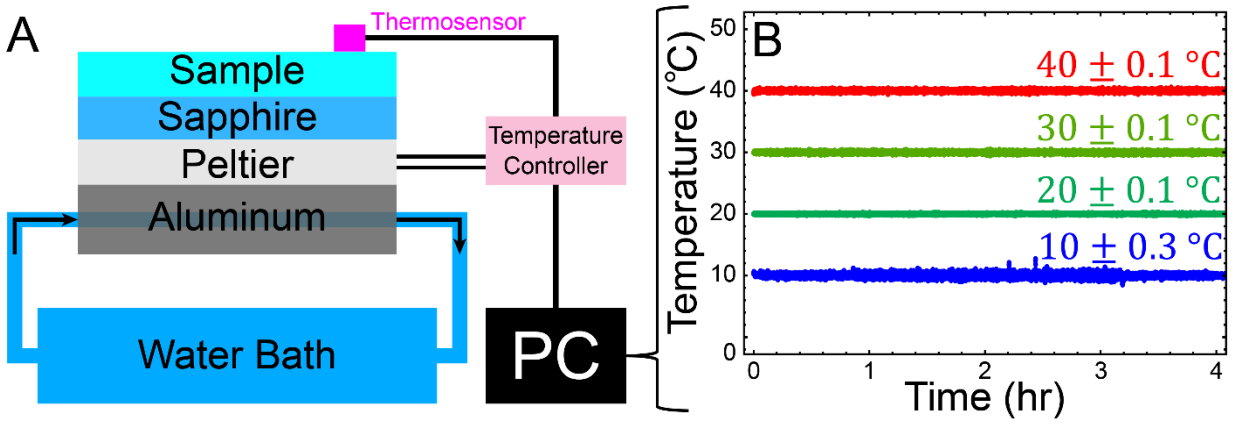

FIG. 25: PID-BASED TEMPERATURE CONTROL a) Schematic of temperature control setup. The setup sat on an aluminum stage whose temperature was regulated by internal circulating flows with a room temperature water bath. The stage supported a peltier, which cooled or heated the sample. To even the sample temperature, a sapphire was inserted between the sample and peltier. The peltier was controlled by a temperature controller that set the power of heating or cooling based on reading the sample temperature with a thermosensor. The read temperatures were recorded on an attached computer to track the temperature stability of each experiment. **b)** Recorded sample temperatures for experiments at 10–40°C. Sample temperatures were controlled and monitored throughout experiments. Over the course of 4 hours, temperatures fluctuated within ±0.1–0.3°C.

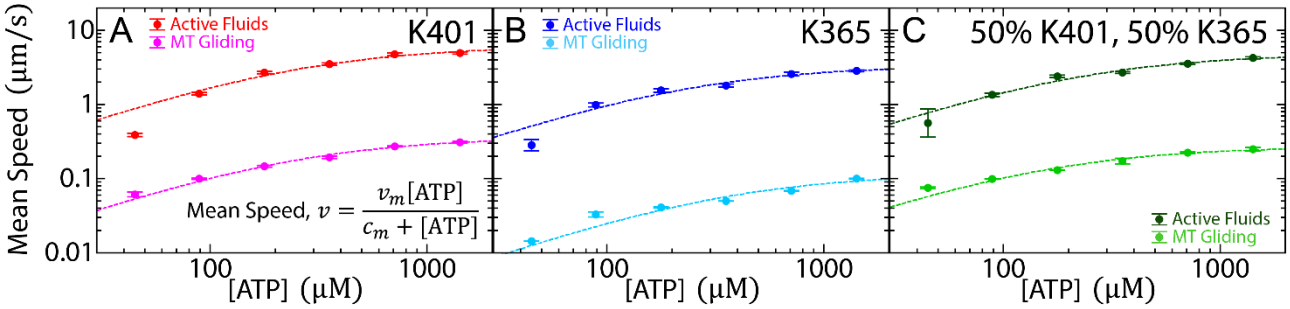

D	Active Fluids	MT Gliding	Active Fluids	MT Gliding	Active Fluids	MT Gliding
v_m (μm/s)	6.2 ± 0.5	0.36 ± 0.02	3.4 ± 0.3	0.12 ± 0.02	4.8 ± 0.3	0.27 ± 0.01
c_m (μM)	270 ± 60	260 ± 30	250 ± 60	380 ± 130	240 ± 50	170 ± 30

FIG. 26: INCREASING ATP CONCENTRATIONS ACCELERATED ACTIVE FLUID FLOWS AND MICROTUBULE GLIDING a-c) Mean speed of active fluids and microtubule gliding at 20°C as a function of ATP concentration. Error bars represent the standard deviations of time-averaged mean speeds. Each mean speed (v) *vs.* ATP concentration was fitted to Michaelis–Menten kinetics: $\boldsymbol{v = v_m[\mathrm{ATP}]/(c_m + [\mathrm{ATP}])}$, where $\boldsymbol{v_m}$ was the saturation speed and $\boldsymbol{c_m}$ was the ATP concentration at 50% saturation speed, $\boldsymbol{v_m/2}$ (dashed curves), with $\boldsymbol{v_m}$ and $\boldsymbol{c_m}$ as fitting parameters. **d**) Table of fitting parameters. The fitting errors were ~15% on average, demonstrating the extent of the theoretical validity in both active fluids and microtubule gliding.

response to temperature.

2.3.11 TUNING KINESIN-DRIVEN DYNAMICS WITH TEMPERATURE AND ATP CONCENTRATION In this work, kinesin dynamics were tuned with temperature and ATP concentration[35,38]. First, mean speeds of K401-driven active fluids and microtubule gliding were measured as a function of time between 10 and 40°C. In the active fluid system, the change in mean speed depended on temperature (Fig. 20d). At 20°C, the mean speed was nearly constant, whereas above or below 20°C, the mean speed decayed with time. To characterize system activity, mean speeds were averaged within a common window, between t = 1 and 2 hr. During the first hour of data acquisition, mean speeds could change drastically due to the malfunction of kinesin motor clusters at higher temperatures and microtubule depolymerization at lower temperatures. Because of this, the beginning of the averaging window was set to 1 hr. After the first hour the mean speed of the system still exhibited gradual change over time due to the coarsening of microtubule bundles. Coarsening was a common issue in this active fluid system[31]; therefore, averaging for a 1 hr period ensured analysis with sufficient statistics while reducing the influence of the coarsening effect. On the other hand, the mean speeds in the microtubule gliding assay were nearly time independent (Fig. 20g). The choice of averaging windows did not affect analysis results in the gliding assay. However, the image acquisition setup had an issue of slow focal plane drift. The drift was only a few microns, but it blurred images of microtubules gliding on the glass surface after 10–30 min of image acquisition, depending on ambient temperature. Analysis on blurry microtubule images was not reliable. Therefore, mean speeds of microtubule gliding were averaged during the first 5 min (t = 0–5 min), to ensure analysis with sufficient statistics while reducing the out-of-focus issue. Averaging mean speeds in active fluids and gliding systems revealed their temperature dependence (Fig. 2b).

To illustrate the role of motor processivity, measurements were repeated with K401 replaced by K365 (Fig. 2c). The former stepped along microtubules continuously; the latter detached after each step (Fig. 2a)[40,41]. To characterize how the different stepping mechanisms interacted to impact system dynamics, the measurements were repeated with both types of motors mixed in equal amounts. In active fluids, motor clusters were replaced with equal concentrations of K401 and K365 clusters (60 nM); in the gliding assay, the coated motors were

50% K401 and 50% K365 (Fig. 21d).

Lowering ATP concentrations slows down motor stepping, leading to slower dynamics in active fluid and gliding systems[11,38]. In this work, ATP concentration was also varied over the ranges between 45 and 1,400 μM while keeping the temperature at 20°C (Fig. 26). These experiments not only characterized how systems driven by different types of motors responded to temperature and ATP concentration, but also enabled the search for a dynamic connection between the two distinct but related systems by correlating mean speeds of 3D active fluid flows and 2D microtubule gliding (Fig. 27).

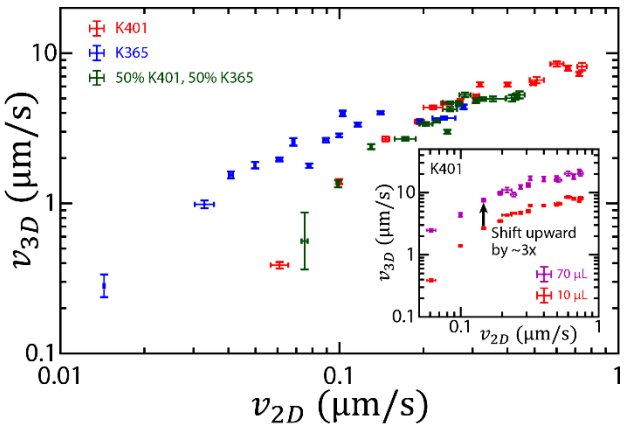

FIG. 27: CROSS-COMPARISON OF MEAN SPEEDS OF MICROTUBULE-BASED ACTIVE FLUID FLOWS IN 3D (v_{3D}) AND KINESIN-DRIVEN MICROTUBULE GLIDING IN 2D (v_{2D}). Microtubule gliding represented the activity of a single microtubule, whereas flows of active fluids represented the collective dynamics of multiple microtubules. Both motions were driven by either K401 (processive, red), K365 (non-processive, blue) or an equal mixture of both (dark green). Tuning up kinesin dynamics by increasing temperature or ATP concentration accelerated fluid flows and microtubule gliding. When gliding was ≳0.2 μm/s, the v_{3D}-v_{2D} correlation was nearly identical among the explored systems, whereas below ~0.2 μm/s, the systems with different motor processivities had different v_{3D}-v_{2D} correlations. Inset: K401-driven v_{3D}-v_{2D} for 10- (red) and 70- (purple) μL samples. Enlarging sample volume by a factor of 7 speeded up v_{3D} by ~3-fold, suggesting that volume played a role in scaling the fluid's collective dynamics. Error bars represent the standard deviations of time-averaged mean speeds.

2.3.12 MEASURING DEPLETANT SIZES WITH DYNAMIC LIGHT SCATTERING The dynamics of the active fluids relied not only on the interfilament sliding driven by kinesin motor clusters but also on the microtubule bundling induced by depletants (Fig. 20a). Characterizing the role of depletants in these active fluids required determination of depletant sizes. However, the depletants were <100 nm, which could not be imaged with optical microscopy. Instead, their sizes were measured with dynamic light scattering (Malvern Panalytical, Zetasizer NANO S90). To perform such a measurement, the depletants were suspended in high salt M2B loaded into a glass cuvette (Starna, 1-G-10). The cuvette center was exposed to a laser of wavelength λ = 633 nm. The laser beam was scattered by the suspended depletant. The scattered light was collected by a detector angled from the beam by θ = 7° (Fig. 28a). The collected light intensities $I(t)$ fluctuated because of depletant diffusion. Therefore their autocorrelation functions $g(\tau) \equiv \langle I(t)\rangle_t \langle I(t+\tau)\rangle_t / \langle I(t)\rangle_t^2$ decayed exponentially with a decay rate Γ proportional to the depletant's diffusion coefficient D:

$$\Gamma = \frac{32\pi^2 n^2 \sin^2\left(\frac{\theta}{2}\right)}{\lambda^2} D, \qquad 1$$

where n was the refractive index of the solution (Fig. 9b inset)[62,63]. Here, the solution refractive index was assumed to be similar to that of water, $n \approx n_w = 1.33$. The diffusion was tied to suspension sizes: $D = k_B T/3\pi\eta d$, where k_B was the Boltzmann constant, η was water viscosity and d was suspension diameter (Einstein relation)[64]. Therefore, through measuring the decay rate, the depletant sizes were determined: PEG, ~11 nm; pluronic F127, ~8 nm (Fig. 28b). To examine the impact of temperature on depletants, these sizes were measured from 10 to 40°C, revealing that the size of PEG was nearly invariant. In contrast, the size of pluronic increased rapidly from 20°C to 25°C and saturated at ~23 nm at 25°C (Fig. 28b). Such a change implied micelle formation, and the temperature dependence of pluronic-induced depletion[44,65]. To examine the impact of temperature-dependent depletion in active fluids, PEG was replaced with pluronic and the time-averaged mean speeds were measured from 10 to 40°C (Fig. 28c).

2.4 RESULTS AND DISCUSSION Self-organization of active fluids relied on cumulative dynamics of pairs of microtubules sliding apart (Fig. 20a-c)[11]. However, since these microtubules were ~1 μm long[11], monitoring individual interfilament sliding in 3D bulk was challenging. Instead, the sliding dynamics were assumed to be similar to those of single microtubule gliding on a 2D motor-coated surface (gliding assay, Fig. 20e&f)[10,34]. In this work, a gliding assay was used as a model system to characterize the motility of single microtubules driven by kinesin motors. Because activities of both systems originated from kinesin motor proteins that consume ATP to generate mechanical work whose energy transducing rates could be tuned with ATP concentration and temperature, microtubule gliding speeds were compared with flow speeds of active fluids to reveal the dynamic relationship between the two systems.

2.4.1 TEMPERATURE DEPENDENCE OF ACTIVE FLUIDS AND MICROTUBULE GLIDING ASSAY FOLLOWS THE ARRHENIUS LAW To characterize the dynamic connection between the two systems, their temperatures were varied between 10 and 40°C while their mean speeds were measured (Fig. 21b). Kinesin-driven systems have been known to be temperature dependent as kinesin is a mechanochemical enzyme whose reaction is diffusion-limited; additionally, kinesin stepping behaviors require diffusion and are therefore temperature-dependent[39,66,67]. This temperature dependence has been described using the Arrhenius Law: reaction rate $k \propto e^{-E_a/RT}$, where $R = 8.31$ J/mol K is the gas constant, T is temperature, and E_a is the activation energy[35,68,69]. The activation energy represents the reaction barrier; a larger activation energy implies a more temperature-sensitive reaction. The activation energy has been measured in the kinesin-driven gliding assay system to be 10–100 kJ/mol[35,36,45]. The variation in previously measured activation energies depended on the specific motor mechanism. To illustrate how the motor mechanism impacts the activation energy in both of our systems, active fluids and microtubule gliding were driven with three different motor systems: processive motors (K401), non-processive motors (K365), and an equal mixture of both (50% K401 and 50% K365,

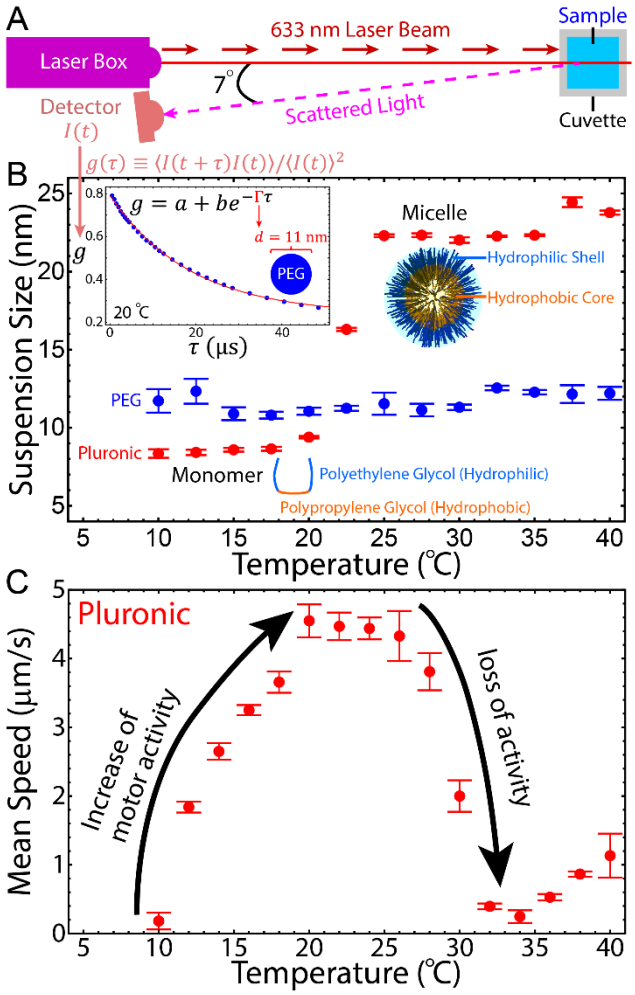

FIG. 28: MICELLE FORMATION OF THE PLURONIC SUPPRESSES FLOWS OF ACTIVE FLUIDS a) Schematics of measurement of suspension sizes with dynamic light scattering. The suspension sizes were measured by first exposing a sample to a laser beam. The laser beam was scattered by the suspension; the scattered light was then collected to measure autocorrelation functions $\boldsymbol{g(\tau)}$, which were analyzed to determine the suspension size. **b**) Suspension size as a function of temperature. Error bars represent the standard deviations of 3 measurements. PEG sizes remained nearly invariant (~11 nm) from 10 to 40°C (blue dots), whereas pluronic sizes remained at ~8 nm below 20°C, followed by an increase to ~23 nm between 20 and 25°C (red dots). The increased size suggested the formation of micelles. Inset: Intensity autocorrelation function of light scattered by 0.8% PEG in high salt M2B at 20°C. The autocorrelation function decayed exponentially; its decay rate $\boldsymbol{\Gamma}$ implied PEG sizes. **c**) Flow mean speeds of active fluids doped with 2% pluronic as a function of temperature. Increasing the temperature from 10 to 20°C accelerated the flows due to more active motors along with more stabilized microtubules, whereas above 20°C, pluronic started to form micelles while the fluids lost speed. Error bars represent the standard deviations of time-averaged mean speeds.

termed mixed-motor). K401 are double-headed processive motors that step along microtubule protofilaments hand-over-hand without detaching, whereas K365 are single-headed non-processive motors which detach after each step (Fig. 21a)[31,41,42]. A single processive kinesin can propel a microtubule in a gliding assay, whereas 5-6 motors are required if the kinesin is non-processive[42].

To measure activation energies of the three different motor systems, the mean speeds of microtubule gliding were measured between 10 and 40°C, followed by fitting the mean speed *vs.* temperature to the Arrhenius equation: $v = Ae^{-E_a/RT}$ with A and E_a as fitting parameters. Only the data between 16 and 36°C was used in these fittings, for the following reasons. First, the GMPCPP-stabilized microtubules depolymerized below 16°C. It seemed likely that data confounded by depolymerization (< 16 °C) would not exhibit the same dynamics as data derived from stable microtubules ($\geq$ 16°C). Second, motors used in these experiments that were pre-incubated at $T > 36$°C did not develop the same dynamics with respect to microtubules, indicating the malfunctioning of the motor clusters[35]. For the above reasons, these microtubule-kinesin systems were deemed to be unstable at $T < 16$°C and $T > 36$°C; therefore, the data in these ranges was not be mixed nor analyzed with data derived from systems in which microtubules and kinesin clusters were both stable (16–36°C). As such, in this temperature range, the activation energies were measured in processive, non-processive and mixed-motor systems to be 43, 55 and 28 kJ/mol, respectively (magenta, cyan and light green in Fig. 21b-d). Two observations resulted from these measurements. First, the activation energy of non-processive motor system was higher than that of the processive system, possibly because non-processive motors detached from microtubules after each step. After detaching, the motors were not able to propel the microtubules until they had diffused back to the microtubules. The diffusion process was temperature-dependent; therefore, K365-driven dynamics were more temperature-

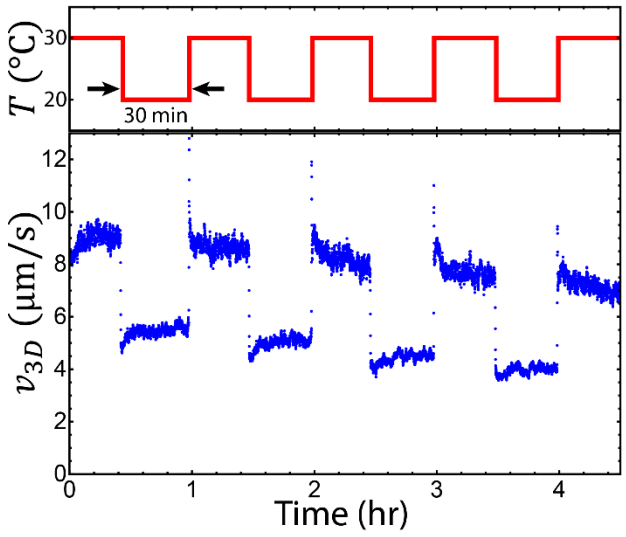

FIG. 29: CYCLING TEMPERATURE ALTERNATED FLOW SPEEDS OF ACTIVE FLUIDS. THE FLOWS WERE DRIVEN BY KINESIN DYNAMICS THAT WERE TUNED WITH TEMPERATURES IN A REVERSING CYCLE. Tuning up and down kinesin dynamics periodically led flows to accelerate and decelerate accordingly, demonstrating *in-situ* control of active fluid dynamics with temperature.

sensitive, which led to a higher activation energy. Second, the mixed-motor system had the lowest activation energy. The result is counterintuitive as one might expect that mixing motors should not alter the activation energy. However, the measurement results suggested that cooperation between processive and non-processive motors led to less temperature sensitive dynamics (lower E_a). Gaining insights into the impact of motor cooperation effects requires further studies which may involve computation and models considering each motor's association and dissociation rates along with their stepping rates and duty cycles[34].

Following characterization of the gliding assay, we shifted the focus to the active fluid system. In this system, mean speeds of active fluid flows were measured between 10 and 40°C, and activation energy was determined by fitting the mean speed *vs.* temperature (16–36°C) to the Arrhenius equation. The activation energies in processive, non-processive and mixed-motor systems were 22, 27, and 13 kJ/mol, respectively (red, blue and dark green in Fig. 21b-d). Three observations resulted from these measurements. First, mixed-motor system had

the lowest activation energy of the three, consistent with the results of the gliding assay and demonstrating the need for further studies about cooperation between the two types of motors. Second, the activation energies of processive and non-processive motor systems were nearly indistinguishable (within fitting errors, Fig. 21b-d). Such similarity indicates that the motor processivity does not play an important role in the active fluid system. This result is contrary to the results in the gliding assay, but consistent with previous studies by Chandrakar *et al.*, which showed that active fluids with different nanoscopic mechanisms develop similar macroscopic dynamics[31]. Finally, activation energies in active fluid systems were lower than in the corresponding gliding assay systems that used the same motors. The underlying mechanism that causes such a reduction is unclear, but it is possible that the mechanism involves the intervention of temperature-dependent hydrodynamic viscosity. Viscosity plays an important role in self-organization of fluids, and within the temperature range that we explored here (16–36°C), the viscosity changes by ~60%[70]. Therefore, to better interpret the dynamics of active fluids requires development of a more sophisticated computational model that considers not only microtubule-associated motor dynamics but also hydrodynamics involving fluid viscosity.

2.4.2 ATP DEPENDENCE OF ACTIVE FLUIDS AND MICROTUBULE GLIDING ASSAY ARE CAPTURED BY MICHAELIS–MENTEN KINETICS Motor activities are affected not only by temperature but also by ATP concentration[35,38]. Varying [ATP] changes motor hydrolysis rate linearly until it reaches the saturation maximum (Michaelis–Menten kinetics)[71]. Such a kinetic theory has been applied to gliding assays[37,38,72]:

$$\text{Mean speed, } v = v_m[\text{ATP}]/(c_m + [\text{ATP}]),$$

where v_m is the saturation maximum speed and c_m is the ATP concentration leading to half saturation, $v_m/2$. In numerous previous studies, the measured v_m ranged from 100 to 1,000 nm/s[35,41,73,74]. To measure v_m in the gliding assay, mean speed of microtubule gliding was measured as a function of [ATP] between 45 and 1,400 μM, followed by fitting the mean speed *vs.* [ATP] to Michaelis–Menten kinetics with c_m and v_m as fitting parameters (Fig. 26). In processive, non-processive and mixed-motor systems, the measured v_m was 360, 120 and 270 nm/s, respectively (Fig. 26d**)**. Two observations resulted from these measurements. First, the v_m for non-processive motors was lower than for processive motors, which was consistent with previous studies showing that the lower speed of the non-processive motors was due to their lower duty cycles[41]. Second, the v_m in mixed-motor system was nearly the average of that of the other two systems, suggesting that each type of motor proportionately contributed driving force to propel microtubules. This observation demonstrated the feasibility of tuning microtubule gliding speeds based on the proportion of surface coating of fast and slow motors.

To examine how v_m was impacted when motor dynamics were accumulated in millimeter-scale active fluid flows, mean speeds of active fluid flows for [ATP] = 45–1,400 μM were measured, followed by fitting the mean speed *vs.* [ATP] to Michaelis–Menten kinetics (Fig. 26a-c). In processive, non-processive and mixed-motor systems, v_m was measured as 6.2, 3.4 and 4.8 μm/s, respectively (Fig. 26d). Three observations resulted from these measurements. First, the non-processive motor system had a lower v_m than the processive one. Second, v_m of the mixed-motor system was the average of the other two. Both results were consistent with those from the gliding assay, demonstrating that dynamics in active fluids and the gliding assay were connected. Third, v_m in active fluids was ~10× faster than in the gliding assay. This difference suggests that the dynamics in active fluids result from the collected dynamics of millions of motors at nanoscale.

2.4.3 CROSS-COMPARING 3D ACTIVE FLUID FLOWS WITH 2D MICROTUBULE GLIDING To gain deeper

insight into the collective dynamics of active fluids, the mean speed of active fluids (v_{3D}) and microtubule gliding (v_{2D}) were cross-compared at the same temperature and ATP concentration (Fig. 27). Gliding exhibited the dynamics of single microtubules at the micron scale, whereas fluids exhibited the collective dynamics of multiple microtubules at the millimeter scale. The comparison revealed the dynamic correlation between the two systems. In the fast gliding regime ($v_{2D} \gtrsim 0.2$ μm/s), the v_{3D}-v_{2D} correlation was nearly indistinguishable among the explored systems (processive, non-processive and mixed-motor), consistent with the previous observation that motor processivity did not significantly impact active fluid dynamics. However, this similarity faded at gliding speeds $v_{2D} \lesssim 0.2$ μm/s. Decreasing v_{2D} by ~70% decelerated the corresponding v_{3D} by ~250% in processive motor-associated systems (red and green), whereas in non-processive motor systems (blue), a similar variation in v_{2D} (~70%) led to a smaller change in v_{3D} (~80%). Such an observation came mainly from the experiments with decreasing [ATP] (Fig. 26). Low [ATP] has been demonstrated to cause processive motors to pause between steps[75-80]. The pausing motors have been shown to firmly attach to microtubules[81], implying that the pausing motor clusters can crosslink microtubule networks, thus mechanically increasing the hindering load for each motor[34,82]. The load decreases motor stepping rate and consequently inhibits microtubule network activities, which leads to slower flows of active fluids[77,83]. In contrast, in the non-processive system, motors detach after each step and therefore have a lower probability of crosslinking microtubules[31,41], resulting in faster active fluid flows in the range $v_{2D} \lesssim 0.2$ μm/s. This cross-comparison broadened the previous finding regarding motor processivity in active fluids: motor processivity did not play an important role in dynamics of active fluids only when the corresponding gliding assay was in the fast regime ($v_{2D} \gtrsim 0.2$ μm/s). In the slow ($v_{2D} \lesssim 0.2$ μm/s) or low [ATP] regime, the dynamics were influenced by motor processivity.

Fluid dynamics are governed by the Navier-Stokes equation, and the role of hydrodynamics in active fluids remains to be elucidated[84]. To advance understanding of such a role, measurements of v_{3D}-v_{2D} were repeated with K401-driven active fluids but in a flow cell 7× thicker (~20×5×0.7 mm^3 = 70 μL). The thicker cell induced lower hydrodynamic resistance and therefore supported faster flows (Fig. 27 inset)[21,43].Moreover, the larger cell did not impact the v_{3D} - v_{2D} correlation except that it shifted v_{3D} upward by ~3-fold (arrow in the inset). The shift indicated that in active fluids, hydrodynamics played the role of scaling, consistent with previous studies showing that flow profiles of confinement-induced coherent flows scaled with confinement size[21].

2.4.4 REVERSING TEMPERATURE DEPENDENCE OF KINESIN-DRIVEN ACTIVE FLUIDS Kinesin motor-driven active fluids were influenced by temperature according to the Arrhenius Law (Fig. 21b-d)[35,68,69]. However, to what extent such dependence in active fluids could be controlled remained unexplored. To seek an alternative for tuning the temperature dependence of active fluids, the temperature-independent depletant PEG was replaced with temperature-dependent pluronic F127 (Fig. 28b). Measurements of mean speed *vs.* temperature showed that, as with PEG, F127-doped active fluids moved faster as temperature increased from 10°C; however, above 20°C, fluids decelerated rapidly (Fig. 28c). Such deceleration was caused by two factors. First, increasing temperatures above 20°C triggered the formation of micelles (Fig. 28b)[44]. Micellization consumed pluronic monomers, reducing depletion between pairs of microtubules. Lack of sufficient depletion suppressed microtubule bundling as well as interfilament sliding; thus fluid activity was inhibited. Second, formation of pluronic micelles created hydrophobic cores which potentially bound to kinesin, causing denaturing[65,85]. The denatured motors could not support fluid activity. Verifying these arguments requires additional studies, such as characterizing depletion

change during pluronic micellization and clarifying the impact of hydrophobic cores of pluronic micelles on kinesin motor proteins. Nevertheless, this work demonstrates a potential means to reverse the temperature dependence of kinesin-driven active fluids by harnessing the temperature-dependent characteristics of pluronics.

2.4.5 TUNING ACTIVE FLUIDS IN SITU Supporting active fluid flows require both motor and depletion forces (Fig. 20c). The depletion force can be regulated by changing concentrations of depletants suspended in fluids; therefore, changing depletants requires either preparing another sample or flowing fresh active fluids into microfluidic devices[86].Both methods erase the original materials and replace with new fluids which wipe out the original sample's history. Preserving the materials and sample history while tuning fluid activity locally can be achieved by varying motor dynamics with temperature. While motor-driven gliding has been demonstrated to respond to temperature reversibly and instantly, to what degree such reversibility along with the fast response can be derived to 1,000× larger active fluids remains unclear[45]. Here, the temperature of active fluids was alternated between 20 and 30°C every 30 min. The alternation accelerated and decelerated motor dynamics periodically, which led active fluids to flow faster and slower accordingly (Fig. 29). Moreover, active fluids responded to temperature changes nearly instantly ($\lesssim$ 10 sec). Such an instant response demonstrated the feasibility of designing active fluids with switchable flows, paving the way for the creation of valveless microfluidic devices.

2.5 CONCLUSIONS We have cross-compared 3D flows of active fluids with 2D microtubule gliding when both systems are driven by processive, non-processive and an equal mixture of both molecular motors. The comparison highlighted the roles of hydrodynamics and motor processivity. The hydrodynamic influence was long ranged (~1 millimeter), scaling the resulting dynamics, whereas motor processivity-induced influence was short ranged (~1 micron), controlling the dynamics in slow flow regimes. The results implied that the ranges of influences dominated their roles in the collective dynamics of molecular motor-driven, cytoskeleton-based active matter. However, to what extent this conclusion can be generalized to generic active matter remains an open question. Such a question can be explored by adapting this method of comparison, which connects microscopic with macroscopic dynamics, for advancing the knowledge of collective dynamics of active matter.

2.6 CONFLICTS OF INTERESTS

There are no conflicts to declare.

2.7 AUTHOR CONTRIBUTIONS

T.E.B. and E.J.J. performed the research; T.E.B., E.J.J. and K.T.W. designed the experiments; T.E.B. characterized temperature dependence of 3D active fluids; E.J.J. acquired data in the gliding assay; M.E.V. performed dynamic light scattering; T.E.B., E.J.J., M.E.V. and K.T.W. analyzed the data; T.E.B., E.J.J., and K.T.W. wrote the manuscript. All authors have reviewed the manuscript.

2.8 ACKNOWLEDGEMENTS

Plasmids of K401-BCCP-H6 and K365-BCCP-H6 were gifts from Zvonimir Dogic. We thank Arne Gericke for the use of his Zetasizer NANO S90 in our light-scattering measurements. This research was performed using computational resources supported by the Academic & Research Computing group at Worcester Polytechnic Institute. We acknowledge Brandeis MRSEC (NSF-MRSEC-1420382) for use of the Biological Materials Facility (BMF).

2.9 REFERENCES

1 Dell'Arciprete, D. *et al.* A growing bacterial colony in two dimensions as an active nematic. *Nature Communications* **9**, 4190 (2018). https://doi.org:10.1038/s41467-018-06370-3

2 Yu, S.-M. *et al.* Substrate curvature affects the shape, orientation, and polarization of renal epithelial cells. *Acta Biomaterialia* **77**, 311-321 (2018). https://doi.org:https://doi.org/10.1016/j.actbio.2018.07.019

3 Wioland, H., Lushi, E. & Goldstein, R. E. Directed collective motion of bacteria under channel confinement. *New Journal of Physics* **18**, 075002 (2016). https://doi.org:10.1088/1367-2630/18/7/075002
4 Aubret, A., Youssef, M., Sacanna, S. & Palacci, J. Targeted assembly and synchronization of self-spinning microgears. *Nature Physics* **14**, 1114-1118 (2018). https://doi.org:10.1038/s41567-018-0227-4
5 Driscoll, M. *et al.* Unstable fronts and motile structures formed by microrollers. *Nature Physics* **13**, 375-379 (2017). https://doi.org:10.1038/nphys3970
6 Morin, A., Desreumaux, N., Caussin, J.-B. & Bartolo, D. Distortion and destruction of colloidal flocks in disordered environments. *Nature Physics* **13**, 63-67 (2017). https://doi.org:10.1038/nphys3903
7 Narayan, V., Ramaswamy, S. & Menon, N. Long-Lived Giant Number Fluctuations in a Swarming Granular Nematic. *Science* **317**, 105-108 (2007). https://doi.org:10.1126/science.1140414
8 Blair, D. L. & Kudrolli, A. Collision statistics of driven granular materials. *Physical Review E* **67**, 041301 (2003). https://doi.org:10.1103/PhysRevE.67.041301
9 Huber, L., Suzuki, R., Krüger, T., Frey, E. & Bausch, A. R. Emergence of coexisting ordered states in active matter systems. *Science* **361**, 255-258 (2018). https://doi.org:10.1126/science.aao5434
10 Farhadi, L., Fermino Do Rosario, C., Debold, E. P., Baskaran, A. & Ross, J. L. Active Self-Organization of Actin-Microtubule Composite Self-Propelled Rods. *Frontiers in Physics* **6** (2018).
11 Sanchez, T., Chen, D. T., DeCamp, S. J., Heymann, M. & Dogic, Z. Spontaneous motion in hierarchically assembled active matter. *Nature* **491**, 431-434 (2012). https://doi.org:10.1038/nature11591
12 Guillamat, P., Ignes-Mullol, J. & Sagues, F. Taming active turbulence with patterned soft interfaces. *Nat Commun* **8**, 564 (2017). https://doi.org:10.1038/s41467-017-00617-1
13 Foster, P. J., Fürthauer, S., Shelley, M. J. & Needleman, D. J. From cytoskeletal assemblies to living materials. *Current Opinion in Cell Biology* **56**, 109-114 (2019). https://doi.org:https://doi.org/10.1016/j.ceb.2018.10.010
14 Vicsek, T., Czirók, A., Ben-Jacob, E., Cohen, I. & Shochet, O. Novel Type of Phase Transition in a System of Self-Driven Particles. *Physical Review Letters* **75**, 1226-1229 (1995). https://doi.org:10.1103/PhysRevLett.75.1226
15 Kumar, N., Soni, H., Ramaswamy, S. & Sood, A. K. Flocking at a distance in active granular matter. *Nature Communications* **5**, 4688 (2014). https://doi.org:10.1038/ncomms5688
16 Toner, J., Tu, Y. & Ramaswamy, S. Hydrodynamics and phases of flocks. *Annals of Physics* **318**, 170-244 (2005). https://doi.org:https://doi.org/10.1016/j.aop.2005.04.011
17 Buhl, J. *et al.* From Disorder to Order in Marching Locusts. *Science* **312**, 1402-1406 (2006). https://doi.org:10.1126/science.1125142
18 Keya, J. J. *et al.* DNA-assisted swarm control in a biomolecular motor system. *Nature Communications* **9**, 453 (2018). https://doi.org:10.1038/s41467-017-02778-5
19 Yu, J., Wang, B., Du, X., Wang, Q. & Zhang, L. Ultra-extensible ribbon-like magnetic microswarm. *Nature Communications* **9**, 3260 (2018). https://doi.org:10.1038/s41467-018-05749-6
20 Schaller, V., Weber, C., Semmrich, C., Frey, E. & Bausch, A. R. Polar patterns of driven filaments. *Nature* **467**, 73-77 (2010). https://doi.org:10.1038/nature09312
21 Wu, K. T. *et al.* Transition from turbulent to coherent flows in confined three-dimensional active fluids. *Science* **355** (2017). https://doi.org:10.1126/science.aal1979
22 Woodhouse, F. G. & Goldstein, R. E. Spontaneous Circulation of Confined Active Suspensions. *Physical Review Letters* **109**, 168105 (2012). https://doi.org:10.1103/PhysRevLett.109.168105
23 Aoyama, S., Shimoike, M. & Hiratsuka, Y. Self-organized optical device driven by motor proteins. *Proceedings of the National Academy of Sciences* **110**, 16408-16413 (2013). https://doi.org:10.1073/pnas.1306281110
24 Hess, H. *et al.* Molecular Shuttles Operating Undercover: A New Photolithographic Approach for the Fabrication of Structured Surfaces Supporting Directed Motility. *Nano Letters* **3**, 1651-1655 (2003). https://doi.org:10.1021/nl0347435
25 Nicolau, D. V. *et al.* Parallel computation with molecular-motor-propelled agents in nanofabricated networks. *Proceedings of the National Academy of Sciences* **113**, 2591-2596 (2016). https://doi.org:10.1073/pnas.1510825113
26 Suzuki, K., Miyazaki, M., Takagi, J., Itabashi, T. & Ishiwata, S. i. Spatial confinement of active microtubule networks induces large-scale rotational cytoplasmic flow. *Proceedings of the National Academy of Sciences* **114**, 2922-2927 (2017). https://doi.org:10.1073/pnas.1616001114
27 Needleman, D. & Dogic, Z. Active matter at the interface between materials science and cell biology. *Nature Reviews Materials* **2** (2017). https://doi.org:10.1038/natrevmats.2017.48
28 Ndlec, F. J., Surrey, T., Maggs, A. C. & Leibler, S. Self-organization of microtubules and motors. *Nature* **389**, 305-308 (1997). https://doi.org:10.1038/38532

29 Surrey, T., Nédélec, F., Leibler, S. & Karsenti, E. Physical Properties Determining Self-Organization of Motors and Microtubules. *Science* **292**, 1167-1171 (2001). https://doi.org:10.1126/science.1059758
30 Henkin, G., DeCamp, S. J., Chen, D. T., Sanchez, T. & Dogic, Z. Tunable dynamics of microtubule-based active isotropic gels. *Philos Trans A Math Phys Eng Sci* **372** (2014). https://doi.org:10.1098/rsta.2014.0142
31 Chandrakar, P. *et al.* Engineering stability, longevity, and miscibility of microtubule-based active fluids. *Soft Matter* **18**, 1825-1835 (2022). https://doi.org:10.1039/d1sm01289d
32 Hilitski, F. *et al.* Measuring Cohesion between Macromolecular Filaments One Pair at a Time: Depletion-Induced Microtubule Bundling. *Physical Review Letters* **114**, 138102 (2015). https://doi.org:10.1103/PhysRevLett.114.138102
33 Lakkaraju, S. K. & Hwang, W. Critical Buckling Length versus Persistence Length: What Governs Biofilament Conformation? *Physical Review Letters* **102**, 118102 (2009). https://doi.org:10.1103/PhysRevLett.102.118102
34 Arpağ, G. *et al.* Motor Dynamics Underlying Cargo Transport by Pairs of Kinesin-1 and Kinesin-3 Motors. *Biophysical Journal* **116**, 1115-1126 (2019). https://doi.org:https://doi.org/10.1016/j.bpj.2019.01.036
35 Böhm, K. J., Stracke, R., Baum, M., Zieren, M. & Unger, E. Effect of temperature on kinesin-driven microtubule gliding and kinesin ATPase activity. *FEBS Letters* **466**, 59-62 (2000). https://doi.org:https://doi.org/10.1016/S0014-5793(99)01757-3
36 Kawaguchi, K. & Ishiwata, S. i. Temperature Dependence of Force, Velocity, and Processivity of Single Kinesin Molecules. *Biochemical and Biophysical Research Communications* **272**, 895-899 (2000). https://doi.org:https://doi.org/10.1006/bbrc.2000.2856
37 Coy, D. L., Wagenbach, M. & Howard, J. Kinesin Takes One 8-nm Step for Each ATP That It Hydrolyzes*. *Journal of Biological Chemistry* **274**, 3667-3671 (1999). https://doi.org:https://doi.org/10.1074/jbc.274.6.3667
38 Schnitzer, M. J. & Block, S. M. Kinesin hydrolyses one ATP per 8-nm step. *Nature* **388**, 386-390 (1997). https://doi.org:10.1038/41111
39 Thorn, K. S., Ubersax, J. A. & Vale, R. D. Engineering the Processive Run Length of the Kinesin Motor. *Journal of Cell Biology* **151**, 1093-1100 (2000). https://doi.org:10.1083/jcb.151.5.1093
40 Martin Douglas, S., Fathi, R., Mitchison Timothy, J. & Gelles, J. FRET measurements of kinesin neck orientation reveal a structural basis for processivity and asymmetry. *Proceedings of the National Academy of Sciences* **107**, 5453-5458 (2010). https://doi.org:10.1073/pnas.0914924107
41 Young, E. C., Mahtani, H. K. & Gelles, J. One-Headed Kinesin Derivatives Move by a Nonprocessive, Low-Duty Ratio Mechanism Unlike That of Two-Headed Kinesin. *Biochemistry* **37**, 3467-3479 (1998). https://doi.org:10.1021/bi972172n
42 Hancock, W. O. & Howard, J. Processivity of the Motor Protein Kinesin Requires Two Heads. *Journal of Cell Biology* **140**, 1395-1405 (1998). https://doi.org:10.1083/jcb.140.6.1395
43 Acheson, D. J. *Elementary Fluid Dynamics*. (Clarendon Press, 1990).
44 Bohorquez, M., Koch, C., Trygstad, T. & Pandit, N. A Study of the Temperature-Dependent Micellization of Pluronic F127. *Journal of Colloid and Interface Science* **216**, 34-40 (1999). https://doi.org:https://doi.org/10.1006/jcis.1999.6273
45 Kawaguchi, K. & Ishiwata, S. Thermal activation of single kinesin molecules with temperature pulse microscopy. *Cell Motil Cytoskeleton* **49**, 41-47 (2001). https://doi.org:10.1002/cm.1019
46 Palacci, J., Sacanna, S., Steinberg, A. P., Pine, D. J. & Chaikin, P. M. Living Crystals of Light-Activated Colloidal Surfers. *Science* **339**, 936-940 (2013). https://doi.org:10.1126/science.1230020
47 Bricard, A. *et al.* Emergent vortices in populations of colloidal rollers. *Nature Communications* **6**, 7470 (2015). https://doi.org:10.1038/ncomms8470
48 Ross, T. D. *et al.* Controlling organization and forces in active matter through optically defined boundaries. *Nature* **572**, 224-229 (2019). https://doi.org:10.1038/s41586-019-1447-1
49 Soni, V. *et al.* The odd free surface flows of a colloidal chiral fluid. *Nature Physics* **15**, 1188-1194 (2019). https://doi.org:10.1038/s41567-019-0603-8
50 Castoldi, M. & Popov, A. V. Purification of brain tubulin through two cycles of polymerization–depolymerization in a high-molarity buffer. *Protein Expression and Purification* **32**, 83-88 (2003). https://doi.org:https://doi.org/10.1016/S1046-5928(03)00218-3
51 Hyman, A. A., Salser, S., Drechsel, D. N., Unwin, N. & Mitchison, T. J. Role of GTP hydrolysis in microtubule dynamics: information from a slowly hydrolyzable analogue, GMPCPP. *Molecular Biology of the Cell* **3**, 1155-1167 (1992). https://doi.org:10.1091/mbc.3.10.1155
52 Spriestersbach, A., Kubicek, J., Schäfer, F., Block, H. & Maertens, B. in *Methods in Enzymology* Vol. 559 (ed Jon

R. Lorsch) 1-15 (Academic Press, 2015).
53 Vale Ronald, D. & Milligan Ronald, A. The Way Things Move: Looking Under the Hood of Molecular Motor Proteins. *Science* **288**, 88-95 (2000). https://doi.org:10.1126/science.288.5463.88
54 Chen, D. T. N., Heymann, M., Fraden, S., Nicastro, D. & Dogic, Z. ATP Consumption of Eukaryotic Flagella Measured at a Single-Cell Level. *Biophys J* **109**, 2562-2573 (2015). https://doi.org:10.1016/j.bpj.2015.11.003
55 Lau, A. W. C., Prasad, A. & Dogic, Z. Condensation of isolated semi-flexible filaments driven by depletion interactions. *Europhysics Letters* **87**, 48006 (2009). https://doi.org:10.1209/0295-5075/87/48006
56 Ouellette, N. T., Xu, H. & Bodenschatz, E. A quantitative study of three-dimensional Lagrangian particle tracking algorithms. *Experiments in Fluids* **40**, 301-313 (2006). https://doi.org:10.1007/s00348-005-0068-7
57 Thielicke, W. & Stamhuis, E. J. PIVlab – Towards User-friendly, Affordable and Accurate Digital Particle Image Velocimetry in MATLAB. *Journal of Open Research Software* **2** (2014). https://doi.org:10.5334/jors.bl
58 Collins, C. A. & Vallee, R. B. Temperature-dependent reversible assembly of taxol-treated microtubules. *Journal of Cell Biology* **105**, 2847-2854 (1987). https://doi.org:10.1083/jcb.105.6.2847
59 Chen, G.-Y., Arginteanu, D. F. J. & Hancock, W. O. Processivity of the Kinesin-2 KIF3A Results from Rear Head Gating and Not Front Head Gating*. *Journal of Biological Chemistry* **290**, 10274-10294 (2015). https://doi.org:https://doi.org/10.1074/jbc.M114.628032
60 Taylor, R. A. & Solbrekken, G. L. Comprehensive system-level optimization of thermoelectric devices for electronic cooling applications. *IEEE Transactions on Components and Packaging Technologies* **31**, 23-31 (2008). https://doi.org:10.1109/TCAPT.2007.906333
61 Åström, K. J. & Murray, R. *Feedback Systems: An Introduction for Scientists and Engineers*. (2008).
62 Frisken, B. J. Revisiting the method of cumulants for the analysis of dynamic light-scattering data. *Appl. Opt.* **40**, 4087-4091 (2001). https://doi.org:10.1364/AO.40.004087
63 Clark, N. A., Lunacek, J. H. & Benedek, G. B. A Study of Brownian Motion Using Light Scattering. *American Journal of Physics* **38**, 575-585 (1970). https://doi.org:10.1119/1.1976408
64 Chaikin, P. M. & Lubensky, T. C. *Principles of Condensed Matter Physics*. (Cambridge University Press, 2000).
65 Alexandridis, P. & Alan Hatton, T. Poly(ethylene oxide)□poly(propylene oxide)□poly(ethylene oxide) block copolymer surfactants in aqueous solutions and at interfaces: thermodynamics, structure, dynamics, and modeling. *Colloids and Surfaces A: Physicochemical and Engineering Aspects* **96**, 1-46 (1995). https://doi.org:https://doi.org/10.1016/0927-7757(94)03028-X
66 Gilbert, S. P., Webb, M. R., Brune, M. & Johnson, K. A. Pathway of processive ATP hydrolysis by kinesin. *Nature* **373**, 671-676 (1995). https://doi.org:10.1038/373671a0
67 Vale, R. D. *et al.* Direct observation of single kinesin molecules moving along microtubules. *Nature* **380**, 451-453 (1996). https://doi.org:10.1038/380451a0
68 Anson, M. Temperature dependence and arrhenius activation energy of F-actin velocity generated in vitro by skeletal myosin. *Journal of Molecular Biology* **224**, 1029-1038 (1992). https://doi.org:https://doi.org/10.1016/0022-2836(92)90467-X
69 Hong, W., Takshak, A., Osunbayo, O., Kunwar, A. & Vershinin, M. The Effect of Temperature on Microtubule-Based Transport by Cytoplasmic Dynein and Kinesin-1 Motors. *Biophysical Journal* **111**, 1287-1294 (2016). https://doi.org:https://doi.org/10.1016/j.bpj.2016.08.006
70 Likhachev, E. R. Dependence of water viscosity on temperature and pressure. *Technical Physics* **48**, 514-515 (2003). https://doi.org:10.1134/1.1568496
71 Fersht, A. *Enzyme Structure and Mechanism*. (W.H. Freeman, 1985).
72 Howard, J., Hudspeth, A. J. & Vale, R. D. Movement of microtubules by single kinesin molecules. *Nature* **342**, 154-158 (1989). https://doi.org:10.1038/342154a0
73 Huang, Y.-M., Uppalapati, M., Hancock, W. O. & Jackson, T. N. Microtubule transport, concentration and alignment in enclosed microfluidic channels. *Biomedical Microdevices* **9**, 175-184 (2007). https://doi.org:10.1007/s10544-006-9019-1
74 Hua, W., Young, E. C., Fleming, M. L. & Gelles, J. Coupling of kinesin steps to ATP hydrolysis. *Nature* **388**, 390-393 (1997). https://doi.org:10.1038/41118
75 Schnitzer, M. J., Visscher, K. & Block, S. M. Force production by single kinesin motors. *Nature Cell Biology* **2**, 718-723 (2000). https://doi.org:10.1038/35036345
76 Visscher, K., Schnitzer, M. J. & Block, S. M. Single kinesin molecules studied with a molecular force clamp. *Nature* **400**, 184-189 (1999). https://doi.org:10.1038/22146
77 Svoboda, K. & Block, S. M. Force and velocity measured for single kinesin molecules. *Cell* **77**, 773-784 (1994).

https://doi.org:https://doi.org/10.1016/0092-8674(94)90060-4
78 Meyhöfer, E. & Howard, J. The force generated by a single kinesin molecule against an elastic load. *Proceedings of the National Academy of Sciences* **92**, 574-578 (1995). https://doi.org:10.1073/pnas.92.2.574
79 Coppin, C. M., Pierce, D. W., Hsu, L. & Vale, R. D. The load dependence of kinesin's mechanical cycle. *Proceedings of the National Academy of Sciences* **94**, 8539-8544 (1997). https://doi.org:10.1073/pnas.94.16.8539
80 Kojima, H., Muto, E., Higuchi, H. & Yanagida, T. Mechanics of single kinesin molecules measured by optical trapping nanometry. *Biophysical Journal* **73**, 2012-2022 (1997). https://doi.org:https://doi.org/10.1016/S0006-3495(97)78231-6
81 Mori, T., Vale, R. D. & Tomishige, M. How kinesin waits between steps. *Nature* **450**, 750-754 (2007). https://doi.org:10.1038/nature06346
82 Bieling, P., Telley, I. A., Piehler, J. & Surrey, T. Processive kinesins require loose mechanical coupling for efficient collective motility. *EMBO reports* **9**, 1121-1127 (2008). https://doi.org:https://doi.org/10.1038/embor.2008.169
83 Carter, N. J. & Cross, R. A. Mechanics of the kinesin step. *Nature* **435**, 308-312 (2005). https://doi.org:10.1038/nature03528
84 Soni, H., Pelcovits, R. A. & Powers, T. R. Enhancement of Microorganism Swimming Speed in Active Matter. *Physical Review Letters* **121**, 178002 (2018). https://doi.org:10.1103/PhysRevLett.121.178002
85 Dee, K. C., Puleo, D. A. & Bizios, R. *An Introduction to Tissue-Biomaterial Interactions*. (Wiley, 2003).
86 Zhang, S. *et al.* Tuning Nanoparticle Structure and Surface Strain for Catalysis Optimization. *Journal of the American Chemical Society* **136**, 7734-7739 (2014). https://doi.org:10.1021/ja5030172

CHAPTER 3: EFFECT OF ACTIVITY GRADIENT CONTROLLED BY TEMPERATURE ON MICROTUBULE KINESIN ACTIVE FLUID SELF-MIXING

3.1 INTRODUCTION Turbulence is known to be critical to mixing speed and efficiency, fractalizing vortices into smaller sizes, greatly increasing the relative contact and stretching of elements, and thus intensifying velocity gradients on a small scale as groups of fluid elements with opposing trajectories slide past each other[1-5]. However, in microfluids, since the characteristic length scale is small, the Reynolds numbers are small, preventing formation of turbulence[6-10]. Existing methods of microfluid mixing seek to induce chaotic turbulent-like advection by passing laminar flow over disruptive confinement surface geometries or by injecting energy externally with stirring rods, low frequency vibration, and ultraviolet light exposure among other methods[7,8,11-14]. Microtubule active fluid is an interesting candidate for enhancing microfluidic mixing as it produces chaotic advection with internal energy injection, so that it does not require special confinement geometries or external energy injection to enhance mixing[15-18].

An existing theory of passive advective fluid mixing supposes the following: the stretching of the initial separation of two fluid elements dX to a later separation dx is $\lambda = \frac{dx}{dX}$[5]. Normalizing the stretching rate by the stretching and averaging over space and time we obtain the specific stretching rate

$$f \equiv \frac{\mathrm{D}\lambda}{\mathrm{D}t}\Big/\lambda = \boldsymbol{D}:\boldsymbol{mm}, \qquad 1$$

where $\frac{\mathrm{D}}{\mathrm{D}t}$ is the total derivative, $\boldsymbol{D} \equiv \frac{1}{2}[\nabla \boldsymbol{u} + (\nabla \boldsymbol{u})^{\mathrm{T}}]$ is the stretching tensor, and $\boldsymbol{m} = \frac{\boldsymbol{dx}}{|\boldsymbol{dx}|}$ is the instantaneous orientation of the later fluid element separation[5]. The mixing efficiency, or the fraction of locally dissipated energy that is used to stretch fluid elements, is then

$$e_\lambda \equiv \frac{\boldsymbol{D}:\boldsymbol{mm}}{\sqrt{\boldsymbol{D}:\boldsymbol{D}}} \leq 1. \qquad 2$$

According to this theory, mixing efficiency depends on orientation of fluid elements and velocity gradients.

In a typical nematohydrodynamic model of active fluid with a non-dimensionalized Stokes flow forced by rods with elongating flow

$$\nabla^2 \boldsymbol{u} - \nabla p - \nabla \cdot (\alpha \mathbf{Q}) = 0 \qquad 3$$

where α is the active stress parameter, which is generally proportional to mean speed, and $\mathbf{Q}$ is the nematic order of rods, we may consider linearly separating the active stress paramter in the Stokes limit $Re \to 0$ into a spatially uniform and spatially nonuniform part, $\alpha = \alpha_0 + \alpha_1(r)$, with $\boldsymbol{u} = \boldsymbol{u}_0 + \boldsymbol{u}_1$, so that we can write

$$\begin{cases} \nabla^2 \boldsymbol{u}_0 - \nabla p - (\alpha_0 + \alpha_1)\nabla \cdot \mathbf{Q} = 0 \\ \nabla^2 \boldsymbol{u}_1 - \nabla p - \nabla \alpha_1 \cdot \mathbf{Q} = 0 \end{cases}. \qquad 4$$

Now, we can consider two contributions to stretching, one that depends on local activity magnitude, $\alpha = \alpha_0 + \alpha_1(r)$, and one that depends on the gradient of local activity, $\nabla\alpha_1$, so that $\boldsymbol{D} = \boldsymbol{D}_0 + \boldsymbol{D}_1(\nabla\alpha_1)$. Here, we ask whether introducing a monotonic spatial gradient in mean speed could enhance specific stretching rate, compared to a case of identical total mean speed with spatially uniform mean speed. If this is true, we might expect more spatially intense activity gradients to increase this effect, where a step function in mean speed would be ideal.

In our previous work, we measured the activation energy of kinesin motors in 2D microtubule kinesin gvliding assays and 3D microtubule kinesin active fluid by controlling activity with temperature[19]. We showed that temperature allows reversible *in-situ* temporal control of bulk activity in active fluid[19]. Here, we develop the method of applying temperature gradients enabling the *in-situ* spatiotemporal control of active fluid activity, with the objective of

enhancing micromixing in active fluid with mean speed gradients. We also ask if activity gradients across the entire sample length could induce large scale convective flow patterns such as in Rayleigh-Bénard convection and Moffat Eddies, as theoretical works on microtubule active nematics have predicted large scale vorticity pattern induced by activity gradients[22-29]. Such large-scale flow patterns would greatly increase the characteristic length scale of the flow, and hence the Peclét number $\mathrm{Pe} = \frac{l_c v}{\mathrm{D}}$, which describes the ratio of advective to diffusional transport in a system. We therefore hypothesize that increasing the Peclét number with large scale flows could enhance the transport of tracer particles in the total system.

The discussed theory of mixing in fluids focuses on mixing by stretching and folding but does not take diffusional mixing into account. When Peclét numbers are low, diffusion dominates the transport of suspended components[14]. To have a complete view of mixing across advective and diffusional transport regimes, both the specific stretching $\langle|f|\rangle_{x,y,t}$ (Eq. 1) and mean squared displacement $\langle\Delta x^2\rangle$ will be considered, where the effective diffusion coefficient $\mathrm{D_{eff}}$ and exponent α describe the magnitude and anomalous diffusivity respectively, from the diffusion equation

$$\langle\Delta x^2\rangle = 2d\mathrm{D_{eff}}\Delta t^{\alpha}. \qquad 5$$

The chaotic advection produced by active fluid self-mixing is known to induce mean squared displacement of embedded tracer particles that are magnitudes greater than diffusion in passive fluids, with ballistic effective diffusion exponents in short time scales, which is similar to behavior seen in enmeshed active Brownian particles and tracer particles in the cytoplasm[30,31]. From the perspective of mean squared displacement, we can consider the transport of tracer particles in active fluid as effective diffusional mixing.

We find that while mean speed controls both the specific stretching rate and effective diffusion coefficient, they are independent of mean speed gradient within the limited range explored. However, we find that insight into the relationship between effective diffusional and advective transport in the context of active flow may contribute to a better understanding of mixing in the intermediate Peclét range.

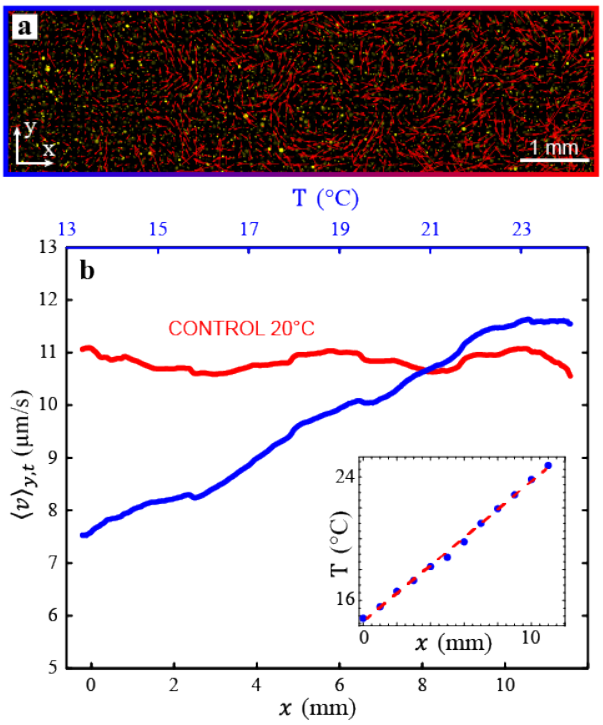

FIG. 30: ACTIVE FLUID UNDER TEMPERATURE GRADIENT a) Micrograph of active fluid sample, total channel dimensions 22 x 4 x 0.5 mm. The FOV is 12.378 x 3.773 mm, centered in the middle of the channel. The microtubule fluorescence channel is not shown, only tracer particles are shown (yellow). A temperature gradient across the sample's horizontal length (blue indicating cold on left red indicating hot on right) induces an activity gradient, indicated by instantaneous normalized velocity field overlay $\boldsymbol{v}^*$ (red arrows). **b)** Mean speed profile $\langle \boldsymbol{v} \rangle_{y,t}$ as a function of horizontal position $\boldsymbol{x}$ and temperature $\boldsymbol{T}$ for a temperature gradient sample (blue), compared to a uniform temperature sample at 20°C (red). Other samples were approximately 0.1 mm thick. This samples thickness was increased to 0.5 mm to exacerbate the mean speed gradient, as mean speed scales with confinement height. Inset: Temperature measurements $\boldsymbol{T}$ as a function of position $\boldsymbol{x}$ across brass bar from separate experiment show that the temperature changes linearly from cold side to hot side of sample area.

3.2 RESULTS

We explore the response of mixing by observing the effective diffusion coefficient $\mathrm{D_{eff}}$, diffusion exponent α, and specific stretching rate $\langle|f|\rangle_{x,y,t}$ in microtubule-kinesin active fluid experiments with

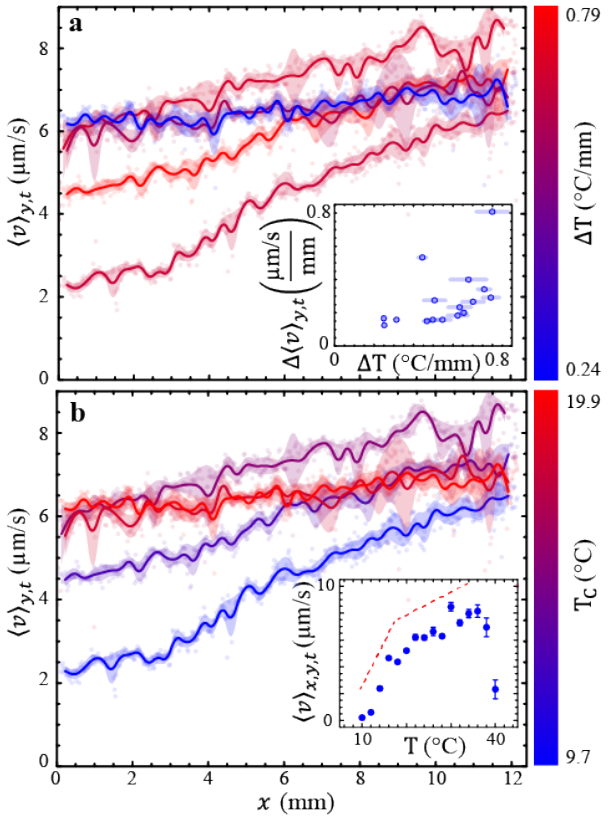

FIG. 31: CONTROLLING MEAN SPEED WITH TEMPERATURE GRADIENT Mean speed profile $\langle v \rangle_{y,t}$ as a function of position x for selected active fluid temperature gradient experiments. Curves are averages of non-overlapping bins of size 10, with an interpolation order of 2. The transparent curves are the standard deviation of each bin, also with an interpolation order of 2. The data is shown in transparent points. **a**) The mean speed profile $\langle v \rangle_{y,t}$ has a partial dependence on temperature gradient ΔT (color bar) achieved across the sample. Inset: Mean speed gradient $\Delta \langle v \rangle_{y,t}$ as a function of temperature gradient ΔT. Error bars are standard deviation of temperature data from measured time range (20 m) **b**) The mean speed profile $\langle v \rangle_{y,t}$ also has a partial dependence on the cold temperature T_C (color bar) of the temperature gradient (blue side of Fig. 1a) due to the higher sensitivity of active fluid mean speed in the 10 – 16°C range (b inset). In order to maximize the activity gradient $\Delta \langle v \rangle_{y,t}$, the temperature gradient ΔT must be maximized and the cold temperature T_C must be minimized to 10°C, below which microtubules depolymerization rate increases. **Inset**: Mean speed $\langle v \rangle_{x,y,t}$ as a function of temperature T for uniform temperature active fluid shows a more rapid change in mean speed $\langle v \rangle_{x,y,t}$ from 10 – 16°C, along with die-offs below 10 and above 36°C. Error bars are standard deviation of mean speed data for measured time range (1 h). Dashed red line is an illustration and not a regression line.

varying mean speed $\langle v \rangle_{x,y,t}$ and mean speed gradients $\Delta \langle v \rangle_{y,t}$.

3.2.1 TEMPERATURE GRADIENT INDUCES MEAN SPEED GRADIENT In our previous work we showed that mean speed $\langle v \rangle_{x,y,t}$ of microtubule kinesin active fluid may be controlled *in-situ* by temperature T (Fig. 31b inset)[19]. Now, we implement a linear temperature gradient ΔT across active fluid samples (Fig. 31b inset). We find that colder areas of active fluid exhibit slower chaotic flows while hotter areas exhibit faster flows, as measured by embedded tracer particles (Fig. 31a). By averaging the instantaneous mean speed maps over time t for the imaging duration (30 m to 1 h depending on sample conditions), then averaging them over the samples y axis direction (perpendicular to the applied temperature gradient), we reveal the samples steady state mean speed profile $\langle v \rangle_{y,t}$ as a function of distance x (Fig. 31b, blue). Mean speed $\langle v \rangle_{y,t}$ increases linearly over the samples horizontal distance x as the temperature T increases, creating a mean speed gradient $\Delta \langle v \rangle_{y,t}$. Meanwhile, a control experiment performed at a uniform temperature of 20°C maintains a constant mean speed across the samples horizontal distance x (Fig. 31b, red). Although the response of mean speed to temperature was previously measured to be nonlinear over 10 to 40°C, the response shown in the thicker sample is nearly linear, whereas the response of thin samples was slightly exponential (Fig. 31b, 31a&b). We hypothesize that long-range hydrodynamic interactions act to smooth mean speed gradients by averaging the velocities of adjacent fluid elements[19,32,33].

3.2.2 TEMPERATURE CONTROLS MEAN SPEED GRADIENTS The temperature gradient ΔT across the samples x distance is determined by the temperatures on the cold T_C and hot T_H sides of the sample, which governs the mean speed profile $\langle v \rangle_{y,t}$ across the sample. We find that although a significant change in temperature ΔT across the sample is required for a strong mean speed gradient $\Delta \langle v \rangle_{y,t}$, the temperature gradient ΔT is not the only factor that determines the mean speed gradient $\Delta \langle v \rangle_{y,t}$ (Fig. 31a inset). This is due to the nonlinear response of mean speed $\langle v \rangle_{x,y,t}$ to temperature (Fig. 31b inset). Because the response of mean speed to

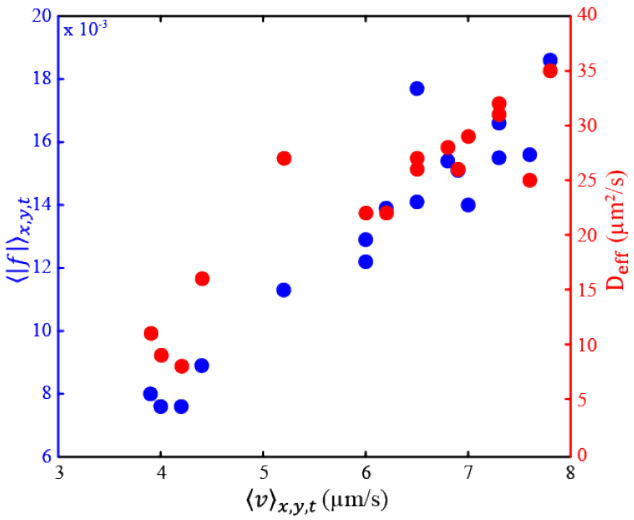

FIG. 33: STRETCHING AND DIFFUSION SCALE WITH MEAN SPEED Specific stretching rate $\langle|\boldsymbol{f}|\rangle_{x,y,t}$ (blue dots) and effective diffusion coefficients $\mathbf{D_{eff}}$ (red dots) as a function of mean speed $\langle\boldsymbol{v}\rangle_{x,y,t}$ for all temperature gradient experiments. Both specific stretching rate $\langle|\boldsymbol{f}|\rangle_{x,y,t}$ and effective diffusion coefficients $\mathbf{D_{eff}}$ scale with mean speed $\langle\boldsymbol{v}\rangle_{x,y,t}$.

temperature is stronger from 10 to ~ 20°C than from ~20 to ~36°C, the temperature of the cold side T_C plays a significant role in determining the achieved mean speed profile and mean speed gradient (Fig. 31b).

3.2.3 MODIFIED DIFFUSIVE TRANSPORT Here, we consider the transport of tracers as effective diffusional mixing[14,34,35]. We measure the mean squared displacement $\langle\Delta x^2\rangle$ as a function of time lag Δt for experiments with varying mean speed $\langle v\rangle_{x,y,t}$ and mean speed gradients $\Delta\langle v\rangle_{y,t}$, extracting the effective diffusion coefficient D_{eff} and exponent α (Fig. 32, Eq. 5). We found that the effective diffusion coefficient scales with the mean speed (Fig. 33). As mean speed of flow increases, the fluid element displacement is enhanced along with tracer displacement, corresponding to the measurements of previous works[34,35]. We use the term "effective" diffusion because in active fluid, except in cases of extremely low activity, it exhibits high Peclét numbers and subsequent super diffusion ($\alpha > 1$) in the low time lag Δt regime, whereas conventional diffusion refers to Brownian motion $\mathrm{Pe} = 0$ & $\alpha = 1$. To isolate the effects of activity gradient on mixing enhancement, we compared the effective diffusion coefficients D_{eff} of experiments with varying mean speed gradients $\Delta\langle v\rangle_{y,t}$ but similar mean speeds $\langle v\rangle_{x,y,t}$ (Fig. 34). We found that the effective diffusion coefficient D_{eff} was independent of mean speed gradient $\Delta\langle v\rangle_{y,t}$. While increasing mean speed $\langle v\rangle_{x,y,t}$ enhanced diffusional mixing D_{eff}, scaling linearly, increasing mean speed gradients $\Delta\langle v\rangle_{y,t}$ did not provide further enhancement. Because of the effect of hydrodynamics on smoothing the flow of adjacent fluid elements, and the limitations of the experimental method to apply temperature gradients ΔT over small distances x, we were limited to explore a low range of mean speed gradients $\Delta\langle v\rangle_{y,t}$. Future work could increase these gradients. Light activated kinesin dimers may provide an experimental pathway to higher mean speed gradients[36-39].

3.2.4 ANOMALOUS DIFFUSION We found that active fluid exhibited initially super diffusive tracer transport at shorter time lag Δt, which decays into a regular diffusive transport regime at longer time lag

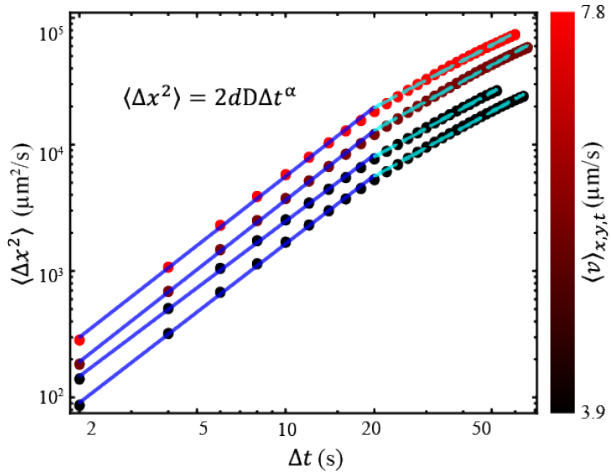

FIG. 32: MEAN SQUARED DISPLACEMENT Mean squared displacement $\langle\Delta x^2\rangle$ as a function of time lag Δt for selected temperature gradient experiments with varying mean speed $\langle v\rangle_{x,y,t}$ (color bar). Each are fit to $\langle\Delta x^2\rangle = 2d\mathrm{D}\Delta t^{\alpha}$ to extract the effective diffusion coefficients D and exponents α for the super-diffusive (blue lines) and regular-diffusive (cyan dashed lines) regimes. Across all temperature gradient experiments, the average effective diffusion exponents are $\langle\alpha_{super}\rangle = 1.75 \pm 0.07$, $\langle\alpha_{regular}\rangle = 1.26 \pm 0.05$. Averaging both the super and regular regimes $\langle\alpha_{total}\rangle = 1.52 \pm 0.26$.

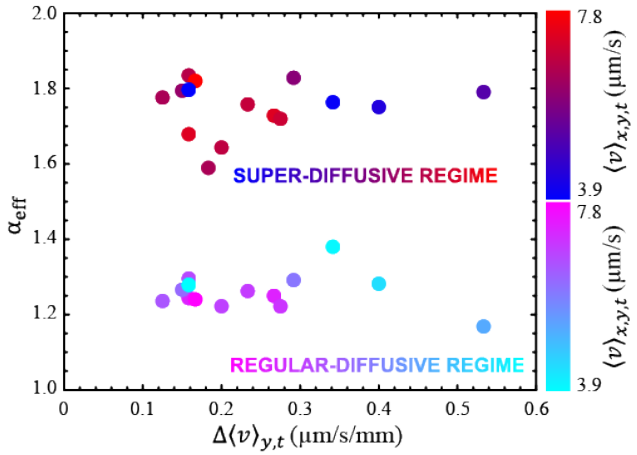

FIG. 35: ANOMALOUS DIFFUSION IS INDEPENDENT Effective diffusion exponent α_{eff} as a function of activity gradient $\Delta\langle v\rangle_{y,t}$ and mean speed $\langle v\rangle_{x,y,t}$. Effective diffusion exponents α_{eff} are measured separately for super-diffusive (mean speed $\langle v\rangle_{x,y,t}$ color bar blue to red), and regular-diffusive regimes (mean speed $\langle v\rangle_{x,y,t}$ color bar cyan to magenta) (Fig. 32). Effective diffusion exponents α_{eff} are independent of both activity gradient $\Delta\langle v\rangle_{y,t}$ and mean speed $\langle v\rangle_{x,y,t}$ with averages $\langle\alpha_{super}\rangle = 1.75 \pm 0.07$, and $\langle\alpha_{regular}\rangle = 1.26 \pm 0.05$ for all temperature gradient experiments.

Δt, similar to active Brownian particle systems[30,34]. We see the same behavior across our varying mean speed and activity gradient experiments (Fig. 32). Therefore, we consider the super-diffusive and regular-diffusive regimes separately. The transition from super to regular diffusive regimes was estimated to occur at $\Delta t = 20$ s for all experiments. To see if mean speed gradients control anomalous diffusion, we compared the diffusion exponent α across experiments with varying mean speeds $\langle v\rangle_{x,y,t}$ and mean speed gradients $\Delta\langle v\rangle_{y,t}$ (Fig. 35). Unlike the effective diffusion coefficient, we do not expect anomalous diffusion to be controlled by mean speed, so we did not compare experiments with similar mean speeds separately, but rather all experiments of all mean speeds simultaneously[34,35]. We found that both in the super-diffusive and regular diffusive regimes the diffusion exponent α was independent of mean speed gradient $\Delta\langle v\rangle_{y,t}$, with $\langle\alpha_{super}\rangle = 1.75 \pm 0.07$ and $\langle\alpha_{regular}\rangle = 1.26 \pm 0.05$. Averaging both the super and regular regimes $\langle\alpha_{total}\rangle = 1.52 \pm 0.26$. As with the effect of mean speed gradient of effective diffusion coefficient, the limited range of explored mean speed gradients may not have been enough for modified anomalous diffusion to emerge.

3.2.5 SPECIFIC STRETCHING RATE We find that specific stretching rate $\langle|f|\rangle_{x,y,t}$ scales linearly with mean speed $\langle v\rangle_{x,y,t}$, similar to the effective diffusion coefficient; as activity increases, both effective diffusional mixing and stretching and folding increase (Fig. 32, Eq. 1). Next, in order to isolate the effects of mean speed gradients $\Delta\langle v\rangle_{y,t}$ from mean speed $\langle v\rangle_{x,y,t}$ on the specific stretching rate, we compare the specific stretching rate of experiments with varying mean speed gradients but similar mean speeds (Fig. 36). We find that as with the effective diffusion coefficient the specific stretching rate is independent of mean speed gradient. As discussed with the effective diffusion coefficient, stronger mean speed gradients may be required to have a significant effect. Future work could increase the temperature gradient or turn to light activated kinesin dimers as a method for achieving a larger activity gradients[36-39].

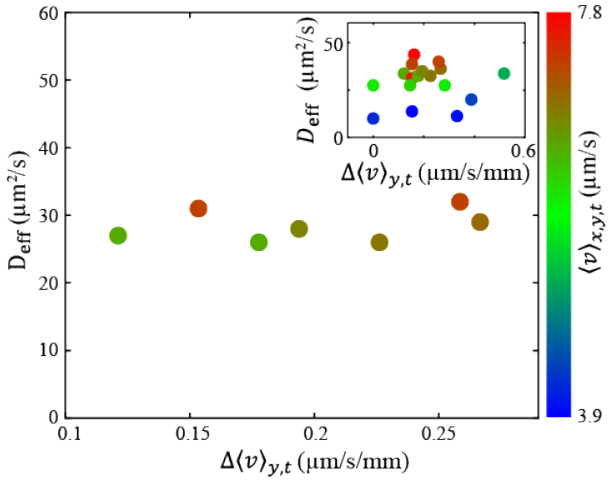

FIG. 34: EFFECT OF MEAN SPEED GRADIENT ON DIFFUSION Selected effective diffusion coefficient D_{eff} of samples with similar mean speeds as a function of activity gradient $\Delta\langle v\rangle_{y,t}$ and mean speed $\langle v\rangle_{x,y,t}$ (color bar). Similar mean speeds are selected in order to isolate the effect of activity gradient $\Delta\langle v\rangle_{y,t}$, as effective diffusion coefficient D_{eff} has a strong dependence on mean speed $\langle v\rangle_{x,y,t}$ (Fig. 4). **Inset** effective diffusion coefficient D_{eff} as a function of activity gradient $\Delta\langle v\rangle_{y,t}$ for all mean speeds $\langle v\rangle_{x,y,t}$ (color bar).

3.3 METHODS For synthesis of microtubules and kinesin motors, preparation of microtubule kinesin active fluid, and sample imaging technique, refer to the previous section, Collective Dynamics of Microtubule-Based 3D Active Fluids from Single Microtubules.

3.3.1 TEMPERATURE GRADIENT Slide samples were attached to a 3/16 in (≈ 4.8 mm) x 1 in (25.4 mm) x 6 in (203.2 mm) brass bar (McMaster 8954K174) by a small 1/2 in (12.7 mm) binder clip (McMaster 12755T71) which did not touch directly on the sample chamber, but on the coverslip surface adjacent to the channel. Two thermocouples (McMaster 9251T71) were attached at each end of the sample channel on the coverslips by copper tape (Fig. 37, see Collective Dynamics of Microtubule-based 3D Active Fluids from Single Microtubules for sample channel assembly). Two 40 mm x 40 mm Peltiers (McMaster 9383N14) were applied to the brass bar mediated by thermal paste (Digi-Key 345-1007-ND) to heat and cool the sides of the brass bar, controlled by a PID controller (TE Technology, TC-720). A custom CNC milled aluminum reservoir was attached to the other side of the Peltiers, also mediated by thermal paste. The assembly was held in place by a 3D printed manifold which fit to the microscope stage (Fig. 37). During experiments, the reservoir was filled with ethanol. Dry ice was then gradually introduced while the Peltiers PID controller was set to 20°C on both sides. Too much dry ice overwhelmed the Peltiers by making the reservoir temperature too cold, depending on the highest and lowest set temperature. Once dry ice was added, the Peltiers were gradually adjusted to their high and low targets. The maximum gradients were

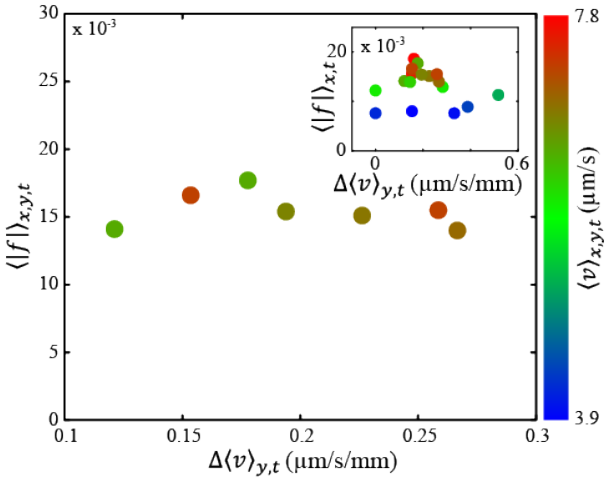

FIG. 36: EFFECT OF MEAN SPEED GRADIENT ON STRETCHING Selected specific stretching rate $\langle|f|\rangle_{x,y,t}$ of samples with similar mean speeds as a function of activity gradient $\Delta\langle v\rangle_{y,t}$ and mean speed $\langle v\rangle_{x,y,t}$ (color bar). Similar mean speeds are selected in order to isolate the effect of activity gradient $\Delta\langle v\rangle_{y,t}$, as specific stretching rate $\langle|f|\rangle_{x,y,t}$ has a strong dependence on mean speed $\langle v\rangle_{x,y,t}$ (Fig. 4). **Inset** Specific stretching rate $\langle|f|\rangle_{x,y,t}$ as a function of activity gradient $\Delta\langle v\rangle_{y,t}$ for all mean speeds $\langle v\rangle_{x,y,t}$ (color bar).

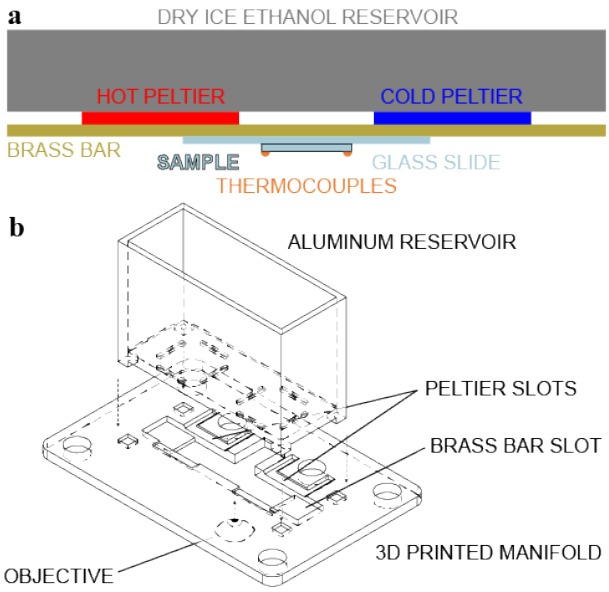

FIG. 37: TEMPERATURE GRADIENT MICROSCOPY a) Diagram of temperature gradient microscopy device. Two Peltiers, one cooling (cold Peltier, blue), and one heating (hot Peltier, red) induce a linear temperature gradient (Fig. 1b inset**)** across a brass bar (dark yellow). The sample, in a microfluid channel formed by sandwiching two parafilm spacers between a glass slide and coverslip (light blue), is placed on the brass bar and clamped by a binder clip, applying the temperature gradient to the sample. Thermocouples (orange) are applied with copper tape to each side of the coverslip to monitor sample temperature gradient. The extreme heating and cooling of the Peltiers requires a strong heat sync. An aluminum reservoir (grey) is placed on the Peltiers and filled with a dry ice and ethanol mixture. Using this method, the maximum and minimum temperatures of the Peltiers achieved was ~55°C and ~-8°C. As the edge of the Peltiers are not at the edge of the sample, the maximum and minimum temperatures experienced by the sample are lower and higher respectively. **b**) Schematic of CNC milled aluminum dry ice and ethanol reservoir and 3D printed microscope stage manifold. The reservoir has feet which press fit into the 3D printed manifold, between which the brass bar and Peltiers are compressed, mediated by silicon based thermal paste. The 3D printed manifold then fits into the microscope stage, and the sample is observed by the objective from below.

achieved by setting them to 55 and -8°C. The Peltiers were not efficient or powerful enough to continue past these values given the experimental configuration. While the experiments were being imaged, the dry ice level in the ethanol bath was monitored, and more was added to keep it at a steady level. Future temperature gradient microscopy prototypes could explore using smaller Peltiers, stacked Peltiers decreasing in area, and CPU fan cooling, as well as adjustable distances between Peltiers.

3.4 CONCLUSION We have hypothesized that mean speed gradients can enhance both effective diffusional and advective mixing in active fluid. We found that while mean speed scaled both the effective diffusion coefficient and specific stretching rate, the limited exploration of mean speed gradients did not reveal any mixing enhancement. However, the comparison of effective diffusion coefficient and specific stretching rate in this investigation supplies a broader insight to active cytoskeletal systems. When we use mean squared displacement analysis in a system where the Peclét number is high, we find that effective diffusive transport is governed by flows[34,35]. In active fluid, active Brownian particles in crosslinked networks, and cells, there is a critical time scale indicating the relaxation of the system from super diffusion to regular diffusion of tracers[30,31,34,35]. This behavior seems to be activity independent. Recent work has explored different spatiotemporally dependent regimes of anomalous diffusive transport in microtubule actin-myosin composites, revealing sub-diffusion regimes[40]. Future work could explore the connection of effective diffusion to active flow by examining the relationship of velocity-velocity autocorrelation times and lengths to the critical time scale of anomalous diffusion regime transitions, especially as active flow approaches zero $\mathrm{Pe} \to 0$. By comparison to simulation, the effect of microtubule network gelation at low activity levels on effective diffusion could be elucidated[41]. This connection can bridge the gap between diffusion dominated and advective dominated regimes in active cytoskeletal systems by uniting the diffusive and advective theory.

3.5 REFERENCES

1 Liepmann, H. W. & Laufer, J. Investigations of free turbulent mixing. (1947).

2 Fernando, H. J. S. Turbulent Mixing in Stratified Fluids. *Annual Review of Fluid Mechanics* **23**, 455-493 (1991). https://doi.org:10.1146/annurev.fl.23.010191.002323

3 Ivey, G. N., Winters, K. B. & Koseff, J. R. Density Stratification, Turbulence, but How Much Mixing? *Annual Review of Fluid Mechanics* **40**, 169-184 (2008). https://doi.org:10.1146/annurev.fluid.39.050905.110314

4 Dimotakis, P. E. TURBULENT MIXING. *Annual Review of Fluid Mechanics* **37**, 329-356 (2005). https://doi.org:10.1146/annurev.fluid.36.050802.122015

5 Ottino, J. M. Mixing, Chaotic Advection, and Turbulence. *Annual Review of Fluid Mechanics* **22**, 207-254 (1990). https://doi.org:10.1146/annurev.fl.22.010190.001231

6 Ottino, J. M., Wiggins, S. R., Ottino, J. M. & Wiggins, S. Introduction: mixing in microfluidics. *Philosophical Transactions of the Royal Society of London. Series A: Mathematical, Physical and Engineering Sciences* **362**, 923-935 (2004). https://doi.org:10.1098/rsta.2003.1355

7 Lee, C. Y., Chang, C. L., Wang, Y. N. & Fu, L. M. Microfluidic mixing: a review. *Int J Mol Sci* **12**, 3263-3287 (2011). https://doi.org:10.3390/ijms12053263

8 Wang, S., Huang, X. & Yang, C. Mixing enhancement for high viscous fluids in a microfluidic chamber. *Lab Chip* **11**, 2081-2087 (2011). https://doi.org:10.1039/c0lc00695e

9 Lee, C.-Y., Wang, W.-T., Liu, C.-C. & Fu, L.-M. Passive mixers in microfluidic systems: A review. *Chemical Engineering Journal* **288**, 146-160 (2016). https://doi.org:https://doi.org/10.1016/j.cej.2015.10.122

10 Balasuriya, S. Dynamical systems techniques for enhancing microfluidic mixing. *Journal of Micromechanics and Microengineering* **25**, 094005 (2015). https://doi.org:10.1088/0960-1317/25/9/094005

11 Eggl, M. F. & Schmid, P. J. Mixing enhancement in binary fluids using optimised stirring strategies. *Journal of Fluid Mechanics* **899** (2020). https://doi.org:10.1017/jfm.2020.448

12 Kazemi, S., Nourian, V., Nobari, M. R. H. & Movahed, S. Two dimensional numerical study on mixing enhancement in micro-channel due to induced charge electrophoresis. *Chemical Engineering and Processing - Process Intensification* **120**, 241-250 (2017). https://doi.org:10.1016/j.cep.2017.07.007
13 Ward, K. & Fan, Z. H. Mixing in microfluidic devices and enhancement methods. *J Micromech Microeng* **25** (2015). https://doi.org:10.1088/0960-1317/25/9/094001
14 Ober, T. J., Foresti, D. & Lewis, J. A. Active mixing of complex fluids at the microscale. *Proc Natl Acad Sci U S A* **112**, 12293-12298 (2015). https://doi.org:10.1073/pnas.1509224112
15 Thampi, S. P., Golestanian, R. & Yeomans, J. M. Vorticity, defects and correlations in active turbulence. *Philosophical Transactions of the Royal Society A: Mathematical, Physical and Engineering Sciences* **372**, 20130366 (2014). https://doi.org:doi:10.1098/rsta.2013.0366
16 Alert, R., Joanny, J.-F. & Casademunt, J. Universal scaling of active nematic turbulence. *Nature Physics* **16**, 682-688 (2020). https://doi.org:10.1038/s41567-020-0854-4
17 Thampi, S. P. & Yeomans, J. M. Active turbulence in active nematics. *The European Physical Journal Special Topics* **225**, 651-662 (2016). https://doi.org:10.1140/epjst/e2015-50324-3
18 Tan, A. J. *et al.* Topological chaos in active nematics. *Nature Physics* **15**, 1033-1039 (2019). https://doi.org:10.1038/s41567-019-0600-y
19 Bate, T. E., Jarvis, E. J., Varney, M. E. & Wu, K. T. Collective dynamics of microtubule-based 3D active fluids from single microtubules. *Soft Matter* **15**, 5006-5016 (2019). https://doi.org:10.1039/c9sm00123a
20 Lemma, L. M., DeCamp, S. J., You, Z., Giomi, L. & Dogic, Z. Statistical properties of autonomous flows in 2D active nematics. *Soft Matter* **15**, 3264-3272 (2019). https://doi.org:10.1039/C8SM01877D
21 Schnitzer, M. J. & Block, S. M. Kinesin hydrolyses one ATP per 8-nm step. *Nature* **388**, 386-390 (1997). https://doi.org:10.1038/41111
22 Shankar, P. N. Moffatt eddies in the cone. *Journal of Fluid Mechanics* **539**, 113-135 (2005). https://doi.org:10.1017/S0022112005005458
23 Moffatt, H. K. Viscous and resistive eddies near a sharp corner. *Journal of Fluid Mechanics* **18**, 1-18 (1964). https://doi.org:10.1017/S0022112064000015
24 Dean, W. R. & Montagnon, P. E. On the steady motion of viscous liquid in a corner. *Mathematical Proceedings of the Cambridge Philosophical Society* **45**, 389-394 (1949). https://doi.org:10.1017/S0305004100025019
25 Rayleigh, L. XXIII. Hydrodynamical notes. *The London, Edinburgh, and Dublin Philosophical Magazine and Journal of Science* **21**, 177-195 (1911). https://doi.org:10.1080/14786440208637021
26 Pandey, A., Scheel, J. D. & Schumacher, J. Turbulent superstructures in Rayleigh-Bénard convection. *Nature Communications* **9**, 2118 (2018). https://doi.org:10.1038/s41467-018-04478-0
27 Fodor, K., Mellado, J. P. & Wilczek, M. On the Role of Large-Scale Updrafts and Downdrafts in Deviations From Monin–Obukhov Similarity Theory in Free Convection. *Boundary-Layer Meteorology* **172**, 371-396 (2019). https://doi.org:10.1007/s10546-019-00454-3
28 Doering, C. R. Turning up the heat in turbulent thermal convection. *Proceedings of the National Academy of Sciences* **117**, 9671-9673 (2020). https://doi.org:10.1073/pnas.2004239117
29 Ruske, L. J. & Yeomans, J. M. Activity gradients in two- and three-dimensional active nematics. *Soft Matter* **18**, 5654-5661 (2022). https://doi.org:10.1039/D2SM00228K
30 Joo, S., Durang, X., Lee, O. c. & Jeon, J.-H. Anomalous diffusion of active Brownian particles cross-linked to a networked polymer: Langevin dynamics simulation and theory. *Soft Matter* **16**, 9188-9201 (2020). https://doi.org:10.1039/D0SM01200A
31 Caspi, A., Granek, R. & Elbaum, M. Diffusion and directed motion in cellular transport. *Physical Review E* **66**, 011916 (2002). https://doi.org:10.1103/PhysRevE.66.011916
32 Fan, Y., Wu, K.-T., Aghvami, S. A., Fraden, S. & Breuer, K. S. Effects of confinement on the dynamics and correlation scales in kinesin-microtubule active fluids. *Physical Review E* **104**, 034601 (2021). https://doi.org:10.1103/PhysRevE.104.034601
33 Bate, T. E. *et al.* Self-mixing in microtubule-kinesin active fluid from nonuniform to uniform distribution of activity. *Nature Communications* **13**, 6573 (2022). https://doi.org:10.1038/s41467-022-34396-1
34 Sanchez, T., Chen, D. T., DeCamp, S. J., Heymann, M. & Dogic, Z. Spontaneous motion in hierarchically assembled active matter. *Nature* **491**, 431-434 (2012). https://doi.org:10.1038/nature11591
35 Henkin, G., DeCamp, S. J., Chen, D. T., Sanchez, T. & Dogic, Z. Tunable dynamics of microtubule-based active isotropic gels. *Philos Trans A Math Phys Eng Sci* **372** (2014). https://doi.org:10.1098/rsta.2014.0142

36 Ross, T. D. *et al.* Controlling organization and forces in active matter through optically defined boundaries. *Nature* **572**, 224-229 (2019). https://doi.org:10.1038/s41586-019-1447-1
37 Qu, Z. *et al.* Persistent fluid flows defined by active matter boundaries. *Communications Physics* **4**, 198 (2021). https://doi.org:10.1038/s42005-021-00703-3
38 Lemma, L. M. *et al.* Spatiotemporal patterning of extensile active stresses in microtubule-based active fluids. arXiv:2209.06277 (2022). <https://ui.adsabs.harvard.edu/abs/2022arXiv220906277L>.
39 Najma, B. *et al.* Competing instabilities reveal how to rationally design and control active crosslinked gels. *Nature Communications* **13**, 6465 (2022). https://doi.org:10.1038/s41467-022-34089-9
40 Sheung, J. Y. *et al.* Motor-driven advection competes with crowding to drive spatiotemporally heterogeneous transport in cytoskeleton composites. *Frontiers in Physics* **10** (2022). https://doi.org:10.3389/fphy.2022.1055441
41 Gagnon, D. A. *et al.* Shear-Induced Gelation of Self-Yielding Active Networks. *Phys Rev Lett* **125**, 178003 (2020). https://doi.org:10.1103/PhysRevLett.125.178003

CHAPTER 4: SELF-MIXING IN MICROTUBULE-KINESIN ACTIVE FLUID FROM NONUNIFORM TO UNIFORM DISTRIBUTION OF ACTIVITY*

*This chapter is an adaptation of Bate *et al*., Nature Communications, 2022, **13** (1), 6573.

4.1 ABSTRACT Active fluids have applications in micromixing, but little is known about the mixing kinematics of systems with spatiotemporally-varying activity. To investigate, UV-activated caged ATP is used to activate controlled regions of microtubule-kinesin active fluid and the mixing process is observed with fluorescent tracers and molecular dyes. At low Péclet numbers (diffusive transport), the active-inactive interface progresses toward the inactive area in a diffusion-like manner that is described by a simple model combining diffusion with Michaelis-Menten kinetics. At high Péclet numbers (convective transport), the active-inactive interface progresses in a superdiffusion-like manner that is qualitatively captured by an active-fluid hydrodynamic model coupled to ATP transport. Results show that active fluid mixing involves complex coupling between distribution of active stress and active transport of ATP and reduces mixing time for suspended components with decreased impact of initial component distribution. This work will inform application of active fluids to promote micromixing in microfluidic devices.

4.2 INTRODUCTION Miniaturization enhances production efficiency in chemical engineering, biological engineering, and pharmaceutical manufacturing[7,8]. For example, microreactors—millimeter-scale devices with channels to mix chemicals and induce chemical reactions—are used to synthesize materials[4,9], test enzymes[11], and analyze protein conformations[6,12]. These devices require mixing to homogenize reactants, which is challenging because fluid dynamics at the micron scale are dominated by laminar flow. Mixing at a macroscopic scale is achieved by turbulence-induced advection repeatedly stretching and folding components until a uniform state is reached[13], but at a microscopic scale, turbulence is inhibited (Reynolds number $\ll 1$) and mixing is dominated by molecular diffusion, which is slow and difficult to control. Approaches such as serpentine design[15] and vibrating bubbles[16] have been developed to enhance micromixing, but these are driven by external energy sources and thus require external components that limit miniaturization[7,17].

Active fluids—fluids with microscopic constituents that consume local fuel to generate movement[5,18-26]—have the potential to enhance mixing at the micron scale. Active fluids self-organize into chaotic turbulence-like flows[27-31] that promote micromixing by repeatedly stretching and folding fluid, even at low Reynolds numbers[32]. Prior work on active mixing has focused on active systems with uniform activity distribution[32-34]. However, mixing processes often start from a state of nonuniformity. Nonuniform distributions of activity in active fluid systems can cause complex dynamics[35-42]. Spatiotemporal patterns of activity that are prescribed from an external source[39,40] or emerge as an additional dynamical variable that coevolves with the system[35-37] have been studied. However, the effect of nonuniform distributions of activity on mixing has not been elucidated.

Here, we study the mixing dynamics of a microtubule-kinesin suspension whose activity is governed by the transport of ATP, the system's energy source. We control the initial distribution of ATP by using caged ATP that can only fuel the fluid after exposure to ultraviolet (UV) light. This allows us to repeatedly observe the transient dynamics that carry the system from heterogeneous activity to homogeneous activity. We explore mixing dynamics ranging from diffusion-dominated to convection-dominated by varying the ATP concentration, composition of kinesin motors, flow cell geometry, and initial distribution of ATP. We contextualize the results with models at two levels of complexity. A simple model captures the mixing dynamics in a diffusion-limited regime, whereas a more complex model that includes active-fluid hydrodynamics

reproduces aspects of observed enhanced transport and activity-dependent progression of the active-inactive interface.

4.3 RESULTS

4.3.1 SELF-MIXING OF ACTIVE AND INACTIVE FLUIDS For the experiments presented herein, we select a 3D microtubule-kinesin active fluid because it enhances micromixing[5,32], has tunable activity[10,14,43-46], and has established models describing its flow behaviors[47-50]. In microtubule-kinesin active fluid, microtubules self-assemble by depletion into bundles that extend spontaneously, driving chaotic vortical flows. The extension is driven by kinesin motor dimers that hydrolyze ATP to walk along pairs of antiparallel microtubules and force them in opposite directions (Fig. 38a)[5]. We augment the microtubule-kinesin system with UV light-activated chemistry that allows us to create distinct patterns of activity. In this light-activated system, the ATP is caged—its terminal phosphate is esterified with a blocking group (Fig. 38b)—such that it cannot be hydrolyzed by kinesin motors until the blocking group is removed by exposure to UV light[1]. In this system, the activation of the fluid is irreversible. After the fluid is activated, the action of the kinesin motors causes the microtubule network to become a 3D self-rearranging isotropic active gel consisting of extensile microtubule bundles that buckle and anneal repeatedly until the ATP is exhausted[5]. To quantify the evolution of the activity distribution, we suspend fluorescent tracers in the solvent and monitored the tracer motion to extract the speed distribution of active fluid flows (Fig. 38d). To observe the structure of the active suspension, we label microtubules with Alexa 647 (Fig. 38c).

When the fluid is in its inactive state, before it has been activated by UV light, the kinesin motor dimers are bound to microtubules, creating a quiescent crosslinked microtubule network that behaves like an elastic gel (Fig. 38c, top panel). The inactive gel is essentially isotropic, but after the fluid is loaded into a rectangular flow cell ($20 \times 4 \times 0.1$ mm^3) we observe some alignment of the bundles near the boundary (Fig. 39)[2]. To create an active-inactive interface, we use a mask to apply UV light to one side of the sample, which releases the ATP and activates the fluid on that side only (Fig. 38c, second panel). The spatial pattern of activity evolves from a sharp interface to become increasingly diffuse as the initially active region invades the inactive region (Fig. 38d, second and third panels). We quantify this evolution of activity distribution with the normalized speed profile (Fig. 38e), which shows how the interface between regions widens and shifts as the active and inactive parts of the microtubule system blend over a period of hours.

4.3.2 CHARACTERIZATION OF THE MIXING DYNAMICS Active fluids enhance the motion of suspended tracers from diffusive (having a mean squared displacement [MSD] proportional to time lapse: MSD ~ $\Delta t^{a}$with a =1) to superdiffusive ($a >$ 1)[5,34,43]. The progression of the active-inactive interface can also be described as diffusion-like or superdiffusion-like as follows: Suppose the displacement of the active-inactive interface is Δx and the squared interface displacement increases with time as $\Delta x^2 \sim 2P_{\mathrm{I}}\, t^{\gamma}$ with the interface progression coefficient P_{I} and the interface progression exponent γ. If $\gamma = 1$, the progression of the active-inactive interface is defined as diffusion-like; if $\gamma > 1$, the progression of the active-inactive interface is defined as superdiffusion-like.

Because active fluids enhance microscale transport, we hypothesize that the active-inactive interface would progress in a superdiffusion-like manner ($\gamma > 1$). To test this hypothesis, we quantify the displacement of the active-inactive fluid interface as a function of time (Fig. 40a inset) and find that motion of the interface decelerates as the active fluid mixes with the inactive fluid such that the squared interface displacement progresses as $\Delta x^2 \sim t^{\gamma}$ with an interface progression exponent $\gamma \approx 1$ (Fig. 40a). We repeat the γ measurement for caged ATP concentrations from 0.5 to 8 mM (0.5 mM is enough to maximize the flow speed of active fluid[4]) and consistently find that $\gamma \approx 1$ across this range (Fig.

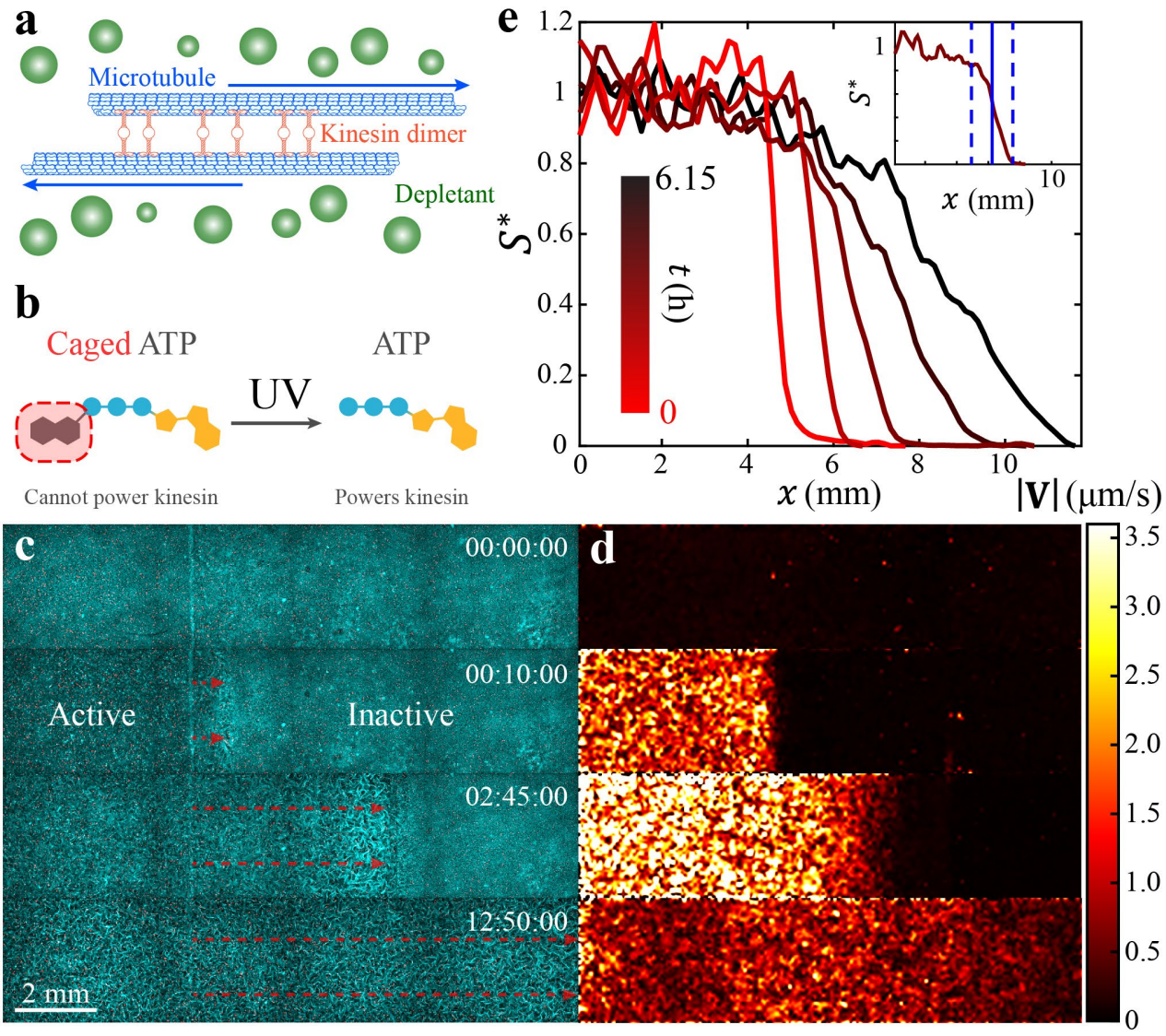

FIG. 38: MIXING OF ACTIVATED AND INACTIVE MICROTUBULE-KINESIN FLUID (a) Microscopic dynamics in microtubule-kinesin active fluid. Depletants force microtubules into bundles where the microtubules can be bridged by kinesin motor dimers. The kinesin motors walk along the microtubules, forcing them to slide apart. The collective sliding dynamics cause the microtubules to form an extensile microtubule network that stirs the surrounding solvents and causes millimeter-scale chaotic flows[5]. (b) To develop an experimental system where we can create a distinct boundary between active and inactive fluid, we synthesize microtubule-kinesin active fluid with caged ATP. The caged ATP is not hydrolysable by kinesin motors, and thus cannot power the active fluid, until it is released by exposure to ultraviolet light[1]. This process is not reversible. (c) We expose only one side of the sample to ultraviolet light, which releases the ATP and activates the microtubule-kinesin mixture on that side of the channel. The released ATP disperses toward the unexposed region, which activates the inactive fluid and expands the active region until the system reaches an activity-homogeneous state. Because of the limited speed of multi-position imaging, only one-quarter of the active region is imaged. (d) Tracking tracer particles reveals the speed distribution of fluid flows, showing the activation of the left-hand side by UV light and the expansion of the active region into the inactive region. (e) Binning the same-time speeds vertically across the interface of active and inactive fluids reveals the speed profile S which is normalized as $\boldsymbol{S}^*(\boldsymbol{x}) \equiv [\boldsymbol{S}(\boldsymbol{x}) - \boldsymbol{s}_{\mathbf{in}}]/[\boldsymbol{s}_{\mathbf{a}} - \boldsymbol{s}_{\mathbf{in}}]$, where $\boldsymbol{s}_{\mathbf{a}}$ is the average of speed profiles in the active zone and $\boldsymbol{s}_{\mathbf{in}}$ is the average of speed profiles in the inactive zone. Inset: The interface of the active and inactive fluids is determined as the region where the normalized speed profile is between 0.2 and 0.8 (dashed blue lines). The position of the interface is determined as where the normalized speed profile is 0.5 (solid blue line).

40b). These results invalidate our hypothesis and suggest that the progression of active-inactive interface is diffusion-like. Notably, while the diffusive time-scaling γ remains consistent, the prefactor P_1 exhibits a monotonic but nonlinear dependence on caged ATP concentration (Fig. 40c).

4.3.3 MODELING WITH FICK ' S LAW AND MICHAELIS-MENTEN KINETICS In the experiments, the interface progression coefficient $\gamma \approx 1$, which suggests that diffusion dominates the dynamics of the active-inactive interface. To contextualize our observations, we construct a minimal model that

combines diffusion of ATP with a previously measured relation between ATP concentration and local fluid velocity[4]. Herein, we model ATP's dispersion using Fick's law of diffusion:

$$\frac{\partial C(\boldsymbol{r},t)}{\partial t} = D\nabla^2 C(\boldsymbol{r},t), \qquad 1$$

where $C(\boldsymbol{r},t)$ represents the spatial distribution of ATP concentrations at time t and D is the diffusion coefficient of ATP in active fluid. We choose $D = 140$ μm^2/s, which is one-fifth the diffusion coefficient of ATP in water[51], because the crosslinked microtubule network makes the fluid more viscous than water[52] and our measurement on diffusion coefficient of suspended fluorescein is one-fifth of its reported value in aqueous solution. To simplify the modeling, we consider a 1D active fluid system confined in a segment, $x = 0 - L$, where L = 20 mm is the segment length, and apply no-flux boundary conditions

$$\frac{\partial}{\partial x}C(x=0,t) = \frac{\partial}{\partial x}C(x=L,t) = 0. \qquad 2$$

To mimic the UV-activation process (Fig. 38c), we initiate the ATP concentration with a step function

$$C(x,t=0) = \frac{C_0}{2}\,\mathrm{erfc}\left(\frac{x-x_0}{2\sqrt{\epsilon D}}\right), \qquad 3$$

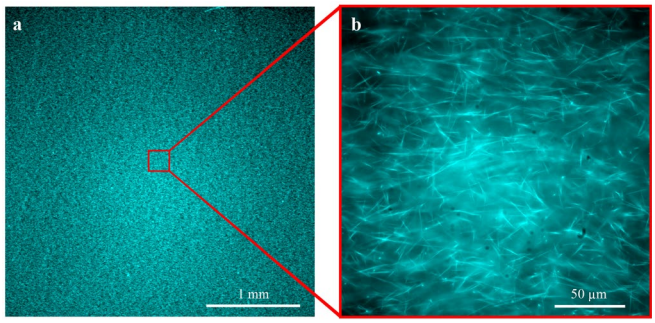

FIG. 39: MICROTUBULES IN INACTIVE FLUID LOADED INTO THE FLOW CELL BEFORE UV ACTIVATION (a) Micrograph of microtubules at millimeter scale. (b) Micrograph of microtubules at micrometer scale, showing an initial dominant alignment of microtubules parallel to the long edge of the flow cell (horizontal direction) caused by the shear flow induced by pipetting the sample into the cell[2].

where C_0 = 0.5–8 mM, the initial ATP concentrations in the activated region; erfc is the complementary error function; and x_0 = 10 mm is the initial position of the active-inactive interface. We choose $\epsilon = 0.001$ to generate a sharp concentration transition at the interface. We numerically solve Eqs. 1-3 to determine the spatial and temporal distribution of ATP concentrations (Fig. 41a). To relate the evolving ATP distribution to local flow speed, we leverage previous experimental results[4] that find the average velocity in bulk samples follows Michaelis-Menten kinetics

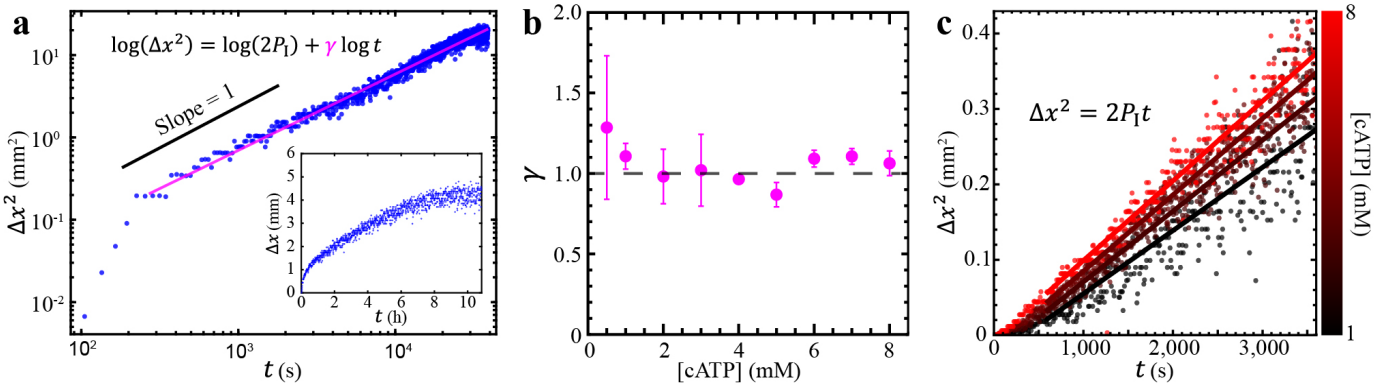

FIG. 40: THE PROGRESSION OF THE ACTIVE-INACTIVE INTERFACE IS GOVERNED BY A DIFFUSION-LIKE PROCESS OF ATP AT THE INTERFACE (a) Squared interface displacement ($\boldsymbol{\Delta x^2}$) as a function of time ($\boldsymbol{t}$) reveals a long-term ($\boldsymbol{t} \gtrsim 200$ s) linear relation: $\boldsymbol{\Delta x^2 \sim t^{\gamma}}$ with the interface progression exponent $\boldsymbol{\gamma \approx 1}$. Inset: The interface displacement versus time shows that the interface moves rapidly initially and then gradually slows down. (b) The interface progression exponent is $\boldsymbol{\gamma \approx 1}$ on average and is independent of the caged ATP concentration. Each error bar represents the standard deviation of ≥3 trials. (c) Selected examples of squared interface displacement versus time for four caged ATP concentrations from 1 mM (black) to 8 mM (red). The progression rate of the interface is characterized with an interface progression coefficient $\boldsymbol{P_I}$ determined by fitting the $\boldsymbol{\Delta x^2}$ vs. $\boldsymbol{t}$ data to $\boldsymbol{\Delta x^2 = 2P_I t}$ with $\boldsymbol{P_I}$ as the fitting parameter (colored lines). Increasing caged ATP concentrations increases the interface progression coefficient (steeper fit lines from black to red), which indicates that the interface progresses more quickly at higher caged ATP concentrations.

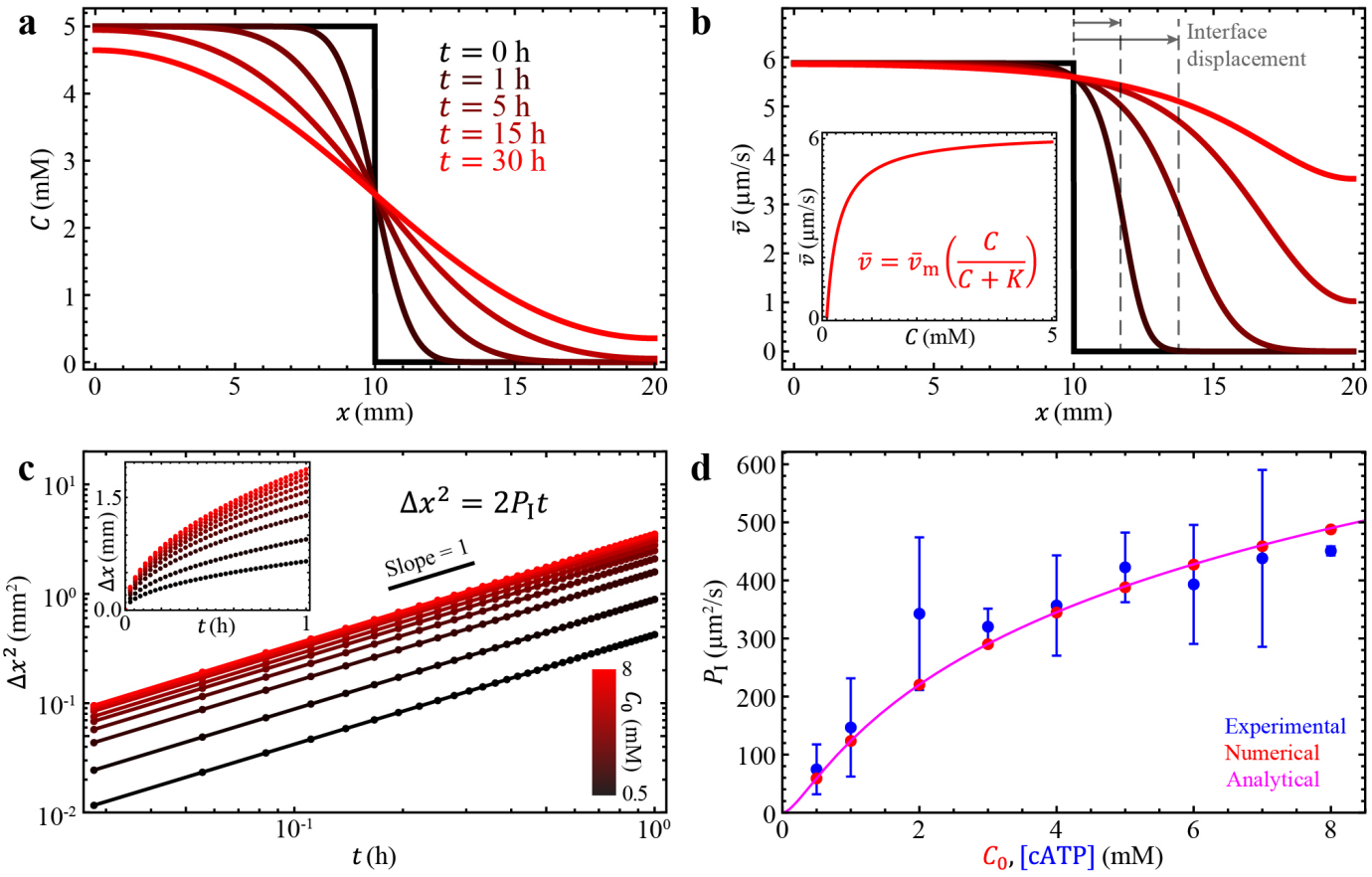

FIG. 41: FICK'S LAW OF DIFFUSION AND MICHAELIS-MENTEN KINETICS CAPTURES THE DIFFUSION-LIKE MIXING OF ACTIVE AND INACTIVE FLUIDS (a) The simulated distribution of ATP concentrations starts as a step function (black, $\boldsymbol{t} = 0$ h) and then develops into a smoothed hill function (red, $\boldsymbol{t} = 30$ h) as ATP evolves from a one-sided distribution to a homogeneous state. (b) The model converts the ATP distribution into the speed distribution of active fluid via Michaelis-Menten kinetics: $\bar{\boldsymbol{v}} = \bar{\boldsymbol{v}}_{\mathbf{m}}[C/(C + \boldsymbol{K})]$, where $\bar{\boldsymbol{v}}_{\mathbf{m}} =$ 6.2 μm/s and $\boldsymbol{K} = 270$ μM (based on our previous studies48). The corresponding mean speed distribution of active fluid evolves from a step function distribution (black, $\boldsymbol{t} =$ 0 h) to a near-constant function (red, $\boldsymbol{t} =$ 30 h). Inset: The plot of the Michaelis-Menten equation (Eq. 4). (c) In the simulation, the diffusion-driven mixing process leads the squared interface displacement to be proportional to time, regardless of initial ATP concentration $\boldsymbol{C_0}$ (see Supplementary Note 3 for derivation of $\boldsymbol{\Delta x^2 \propto t}$). Inset: Interface displacement increases rapidly with time initially, followed by a gradual deceleration similar to the experimental observation (Fig. 40 inset). (d) In the simulation, the interface progression coefficient $\boldsymbol{P_I}$ is determined by fitting the $\boldsymbol{\Delta x^2}$ vs. $\boldsymbol{t}$ data (Panel c) to $\boldsymbol{\Delta x^2 = 2P_I t}$ with $\boldsymbol{P_I}$ as fitting parameter. The model $\boldsymbol{P_I}$ increases with the initial concentration of ATP, $\boldsymbol{C_0}$ (red dots), similarly to how the experimentally analyzed $\boldsymbol{P_I}$ varies with caged ATP concentration (blue dots; each error bar represents the standard deviation of ≥3 trials). The model $\boldsymbol{P_I}$ and experimental $\boldsymbol{P_I}$ differ by only ~10%. The magenta curve shows the analytical solution, $\boldsymbol{P_I(C_0)}$ (Eq. 11), which reproduces the numerical results (red dots).

$$\bar{v}(x,t) = \bar{v}_{\mathrm{m}} \left[\frac{C(x,t)}{C(x,t) + K}\right], \qquad 4$$

where $\bar{v}$ is the mean speed of active fluid, $\bar{v}_{\mathrm{m}} = 6.2$ μm/s is the saturated mean speed, and $K = 270$ μM is the ATP concentration that leads to half of the saturated mean speed, $\bar{v}_{\mathrm{m}}/2$. The mean speed distributions (Fig. 41b) show that initially one side of the sample is activated (black) and then the sample evolves toward a more uniformly activated state (red). The squared interface displacement of the active-inactive interface increases linearly with time, $\Delta x^2 \sim t$ (Fig. 41c), which matches our experimental observation of $\gamma \approx 1$ (Fig. 40a&b). Further, we compare the dependency of the interface progression coefficient P_{I} (determined by fitting Δx^2 vs. t data to $\Delta x^2 = 2P_{\mathrm{I}}\, t$ with P_{I} as the fitting parameter; Fig. 40c&41c) on initial ATP concentrations between experiment and model and also find excellent agreement (differed by ~10%; Fig. 41d). Taken together, the agreement between simulation and experiment on the scaling of the dynamics (Fig. 40b&41c) and dependency on initial ATP concentration (Fig. 41d) indicate that the dispersion of ATP is dominated by diffusion and that Michaelis-

Menten kinetics are appropriate for a coarse-grained model to connect ATP concentration with local flow speed of active fluid[4], without the need to introduce a more complex hydrodynamic model[48,53].

4.3.4 ESTIMATION OF ATP MOLECULAR DIFFUSION COEFFICIENT IN CROSSLINKED MICROTUBULE NETWORKS ATP molecular diffusion plays an important role in our characterization of active-inactive fluid mixing. For example, we characterize the dominant mechanism in active transport (i.e., diffusion or convection) by introducing the Péclet number, Pe (Fig. 45&47)[54,55], which depends on the molecular diffusion coefficient of ATP. We also adopt Fick's law (Eq. 1) to model the dispersion of ATP in low Pe regimes (Fig. 41), which also requires the ATP diffusion coefficient. As such, it is important to determine the molecular diffusion coefficient of ATP. It is challenging to directly observe the diffusion of ATP, but fluorescein can be directly visualized, and thus we analyze the molecular diffusion coefficient of fluorescein in the inactive microtubule network as the basis for estimating the molecular diffusion coefficient of ATP in our active fluid system.

We observe and characterize the dispersion of fluorescein near the interface of caged and UV-uncaged fluorescein suspended in inactive microtubule-kinesin fluid (Fig. 47a&43a) and compare the observation with the solution of Fick's law (Eq. 1) to extract the corresponding molecular diffusion coefficient. For each micrograph, we average the gray values vertically to determine the gray value profile (Fig. 42a). We assume that the fluorescein concentration is proportional to the gray values, and thus the profiles of gray values should satisfy the Fick's law equation (Eq. 1), whose solution in a boundless 1D system takes the form of a complementary error function:

$$C(x,t) = \frac{C_0}{2}\,\mathrm{erfc}\left(\frac{x - x_0}{2\sqrt{D(t - t_0)}}\right), \qquad 5$$

where C_0 is the initial concentration of the suspended molecules, erfc is the complementary error function, and D is the molecular diffusion coefficient of the suspended molecules. Thus, the profiles of gray values (G.V.) should take the form of

$$\text{G.V.}(x,t) = g_0\,\mathrm{erfc}\left(\frac{x - x_0}{2\sqrt{\Gamma(t)}}\right) + g_0', \qquad 6$$

where g_0 is the prefactor and $\Gamma \equiv D(t - t_0)$. We add the constant g_0' to represent the gray value contributed from the background light in the microscope room. Then we fit this form to the profiles of gray values with g_0, g_0', x_0, and Γ as fitting parameters (Fig. 42b inset). The fit Γ is expected to be linear to time t, so we plot Γ as a function of time t and fit Γ vs. t to $\Gamma = D(t - t_0)$ with D and t_0 as fitting parameters (Fig. 42b&c), which reveals that the molecular diffusion coefficient of fluorescein in our inactive microtubule-kinesin system is $D = 97.4 \pm 0.2$ μm^2/s. This analyzed diffusion coefficient is one-fifth the value reported in aqueous solution (400-600 μm^2/s)[56-59]. We attribute this discrepancy to the rheologically complex environment of the inactive fluid that results from crosslinked microtubules[52]. We assume that the molecular diffusion of ATP molecules is similarly diminished in our experiments. The reported diffusion coefficient of ATP in water is 710 μm^2/s[51], and we therefore estimate the diffusivity of ATP to be 140 μm^2/s in our models and calculations (Fig. 41,45&47).

4.3.5 EFFECT OF FLOW SPEED-ATP RELATION ON ACTIVE-INACTIVE INTERFACE PROGRESSION IN THE FICK'S LAW-BASED MODEL We develop the Fick's law-based model (Fig. 41) to describe the experimentally observed mixing of active and inactive fluids (Fig. 40). Our model uses Michaelis-Menten kinetics to convert distribution of ATP to flow speed (Eq. 4) because flow speed is driven by microtubule motion, which in turn depends on the stepping rate of kinesin motors which follows Michaelis-Menten kinetics[60-62]. Our previous work

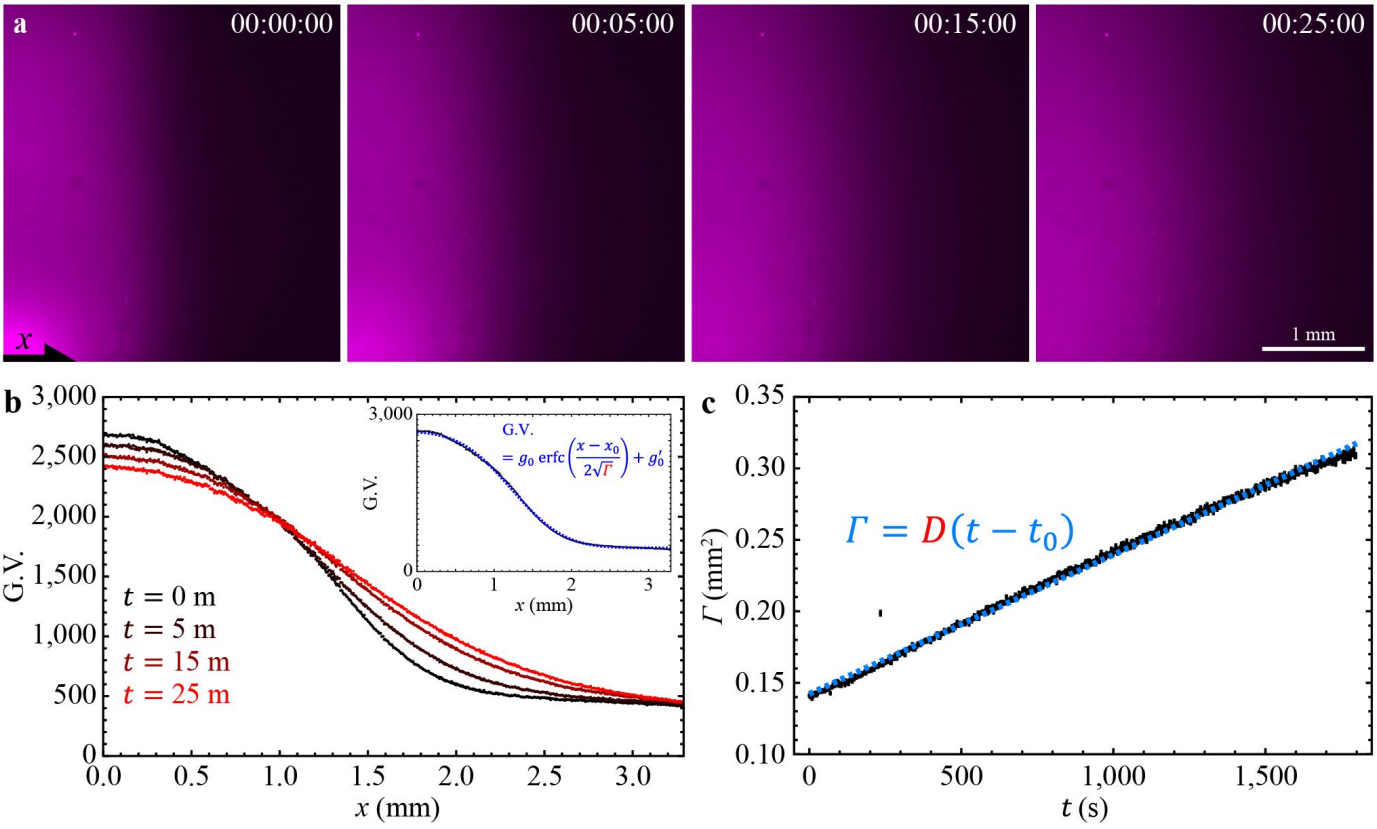

FIG. 42: ANALYSIS OF MOLECULAR DIFFUSION COEFFICIENT OF FLUORESCEIN SUSPENDED IN INACTIVE MICROTUBULE-KINESIN FLUID. The fluorescein is caged such that it only fluoresces after exposure to ultraviolet light (Fig. 10). (a) Micrographs of fluorescein near the edge of the ultraviolet light-exposed area. The time stamps indicate hour:minute:second. (b) Profiles of gray values in the micrographs shown in Panel a. Inset: The gray value profile of the micrograph at time 00:00:00 (black dots) is fit to a complementary error function (Eq. 6; blue dashed curve) to extract the parameter Γ which is expected to linearly increase with time t. (c) The fit parameter Γ as a function of time t (black dots) is fit to a line function (blue dashed line). The fit slope, $\boldsymbol{D}$ = 97.4±0.2 μm2/s, represents the molecular diffusion coefficient of fluorescein suspended in crosslinked microtubule networks.

shows that Michaelis-Menten kinetics reasonably connect flow speed of active fluid with ATP concentrations when the ATP concentration is above 100 μM[4]. Below this concentration, inactive kinesin motor dimers start to act as a crosslinkers in the microtubule network, causing the network to behave more like an elastic gel, and Michaelis-Menten kinetics fail to describe the flow speed because Michaelis-Menten kinetics is an enzyme-based model that does not consider network rheology.

As such, our adoption of Michaelis-Menten kinetics to convert ATP concentration to flow speed is an approximation for active fluid with high ATP concentrations (≳100 μM), and it is unclear how the results of our Fick's law-based model will change if we choose a different relation between ATP concentration and flow speed. Here we consider that the flow speed is connected to ATP concentration via a positive power-law exponent, $n > 0$, of the Michaelis-Menten relation:

$$\bar{v} = \bar{v}_{\mathrm{m}} \left(\frac{C}{C+K}\right)^{n}, \qquad 7$$

where $\bar{v}_{\mathrm{m}} = 6.2$ μm/s is the saturated mean speed of active fluid and $K = 270$ μM is the ATP concentration that leads to half of the saturated mean speed, $\bar{v}_{\mathrm{m}}/2$ (Fig. 43a)[4]. Then we explore how n will affect the predicted active-inactive interface progression in terms of progression exponent γ and coefficient P_{I}.

To find γ vs. n and P_{I} vs. n, we first consider the case of initial ATP concentration $C_0 = 8$ mM and solve the 1D Fick's law equation with the same boundary and initial conditions (Eqs. 1-3) for $C(x,t)$. Then we convert ATP concentration $C(x,t)$

to flow speed $\bar{v}(x,t)$ using our power-lawed Michaelis-Menten equation (Eq. 7), which shows that increasing power law exponents n leads to a slower progression of the active-inactive interface (Fig. 43b). However, such an n-induced variation in interface progression appears not to interfere with the relation of interface displacement with time; we find that the squared interface displacement increases linearly with time across our explored power-law exponents (n = 0.5-10; Fig. 43c), which suggests that interface progression exponent γ will equal 1 regardless of the value of the power-law exponent n in our explored range of exponents (Fig. 43d inset). Contrarily, we find that the interface progression coefficient decreases with increasing power-law exponents (Fig. 43d). Overall, our exploration reveals that the active-inactive interface progression exponent being 1 is a consequence of the diffusion-like process of ATP dispersion. This result is insensitive to the choice of flow speed-ATP model (Eq. 7), but the interface progression coefficient varies rapidly with the model choice. Increasing the power-law exponent from 0.5 to 10 decreases the interface progression coefficient from 740 to 34 μm^2/s. Given that our experimentally measured

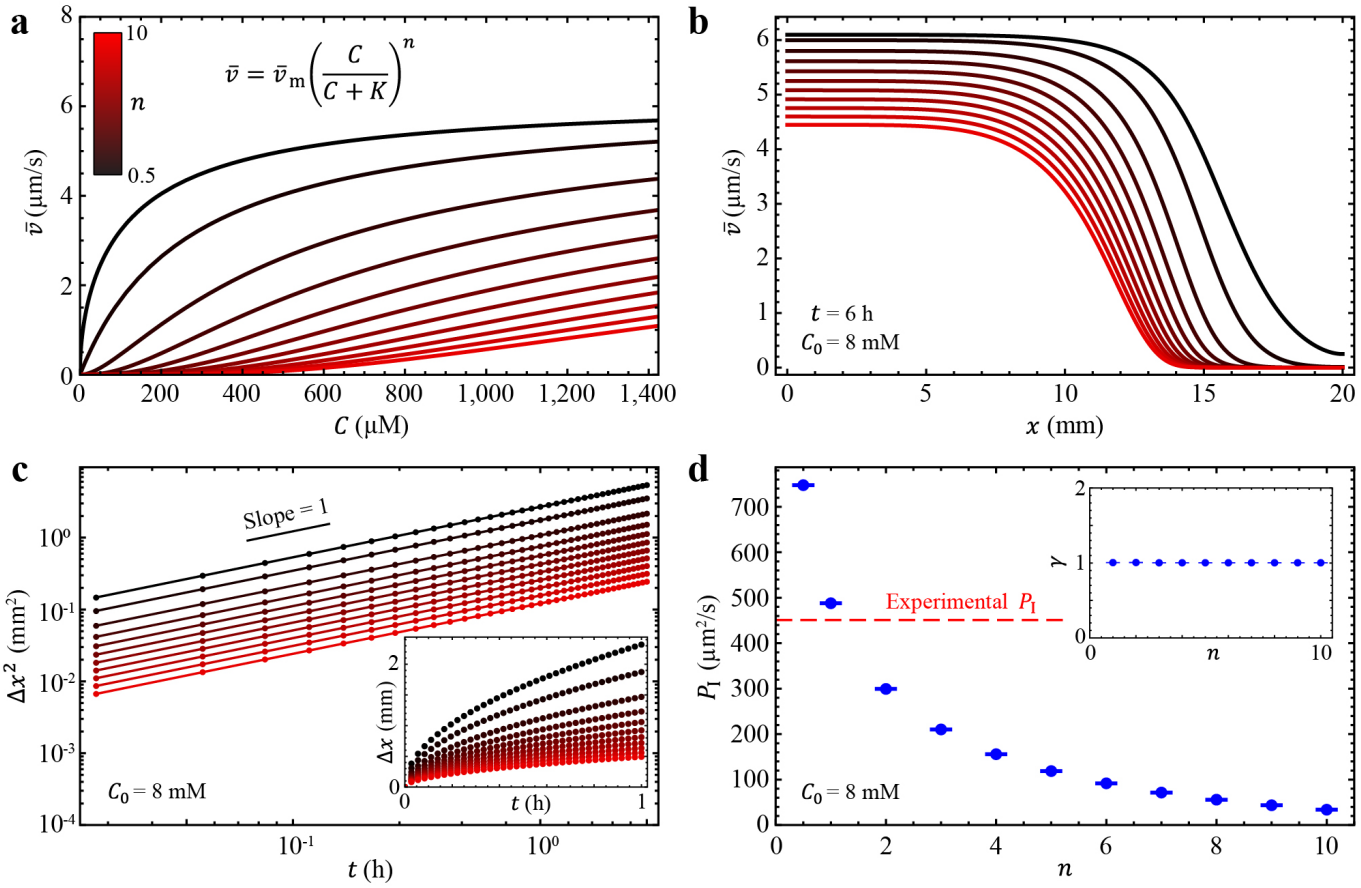

FIG. 43: EXPLORATION OF THE FICK'S LAW-BASED MODEL WITH VARIOUS FLOW SPEED-ATP RELATIONS The Fick's law-based model shows that the power-law exponent, n, in flow speed-ATP relation $\bar{\boldsymbol{v}} = \bar{\boldsymbol{v}}_{\mathbf{m}}\{[\mathrm{ATP}]/([\mathrm{ATP}] + \boldsymbol{K})\}^{\boldsymbol{n}}$, influences the interface progression coefficients but not the interface progression exponents. (a) Plot of flow speed of active fluid as a function of ATP concentration, $\bar{\boldsymbol{v}} = \bar{\boldsymbol{v}}_{\mathbf{m}}\{[\mathrm{ATP}]/([\mathrm{ATP}] + \boldsymbol{K})\}^{\boldsymbol{n}}$, with different power-law exponents $\bar{\boldsymbol{v}}_{\mathbf{m}}$ = 6.2 μm/s and $\boldsymbol{K}$ = 270 μM^4. (b) The distribution of flow speed at time $\boldsymbol{t}$ = 6 hours in the active fluid system for different power-law exponents. Each system has an initial ATP concentration of $\boldsymbol{C_0}$ = 8 mM. The curves are colored based on the n color bar in Panel a. (c) The corresponding squared interface displacement, $\boldsymbol{\Delta x^2}$, increases linearly with time, $\boldsymbol{t}$, for each explored power-law exponent $\boldsymbol{n}$. The curves are the fitting of $\boldsymbol{\log(\Delta x^2) = \log(2P_I) + \gamma \log t}$ with the interface progression coefficient, $\boldsymbol{P_I}$, and interface progression exponent, $\boldsymbol{\gamma}$, as fitting parameters. Inset: The corresponding interface displacement as a function of time for different power-law exponents. The dots and curves are colored based on the $\boldsymbol{n}$ color bar in Panel a. (d) The corresponding interface progression coefficient, $\boldsymbol{P_I}$, decreases with power-law exponent $\boldsymbol{n}$. The red dashed line represents the experimentally measured $\boldsymbol{P_I}$ = 451 ± 8 μm^2/s for 8 mM caged ATP concentration (Fig. 41d). The error bars represent the fitting error in Panel c. Inset: The interface progression exponents remain 1 across explored power-law exponents $\boldsymbol{n}$ = 0.5–10. The error bars represent the fitting error in Panel c.

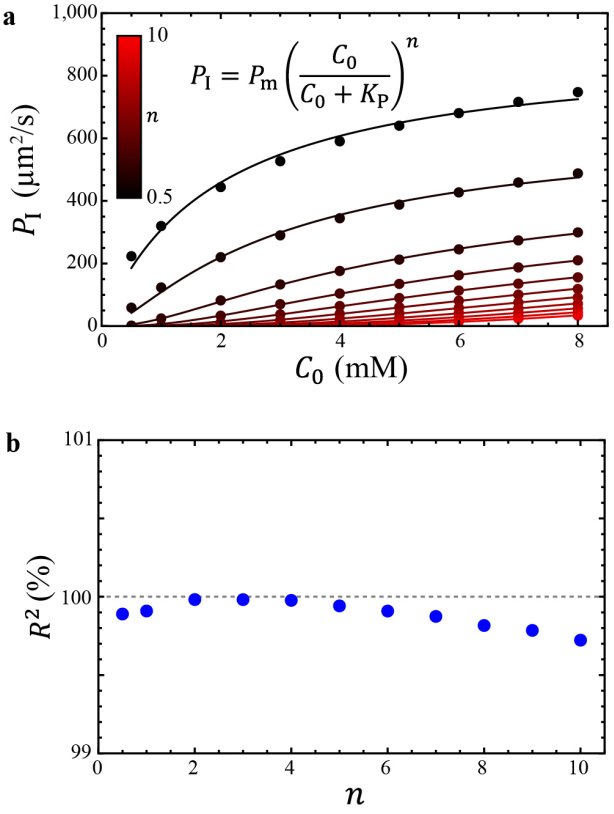

FIG. 44: THE ATP DEPENDENCE OF INTERFACE PROGRESSION COEFFICIENT $P_I(C_0)$IS INHERENT FROM THE ATP DEPENDENCE OF THE CORRESPONDING FLOW SPEED OF ACTIVE FLUID $\bar{v}(C)$ (a) Interface progression coefficient, $\boldsymbol{P_I}$, as a function of initial ATP concentration, $\boldsymbol{C_0}$, for different power-law exponents $\boldsymbol{n}$. The curves are the fitting to $\boldsymbol{P_I = P_m}\{[\mathrm{ATP}]/([\mathrm{ATP}] + \boldsymbol{K_P})\}^{\boldsymbol{n}}$ with $\boldsymbol{P_m}$ and $\boldsymbol{K_P}$ as fitting parameters. (b) The goodness of fit, $\boldsymbol{R^2}$, for power-law exponent data in Panel a.

interface progression coefficient P_I = 451 ± 8 μm²/s for 8 mM caged ATP concentration (Fig. 41d), this also suggests that selecting n = 1 (or slightly larger than 1) will best match our model with the experimental results (Fig. 43d) and that Michaelis-Menten kinetics (Eq. 4) is a good approximation to connect ATP concentrations with the local flow speed of active fluid.

The calculations in our Fick's law-based model reveals that the interface progression coefficient for a given C_0 depends on the selected flow speed-ATP relation (Fig. 43a), which implies that the ATP dependence of the interface progression coefficient P_I (C_0) should change with the selected flow speed-ATP relation as well. To investigate, we repeat the above calculation and determine the interface progression coefficients, P_I, as a function of initial ATP concentration, C_0, for power-law exponents n ranging from 0.5 to 10 (dots in Fig. 44a). Our analysis reveals that increasing the power-law exponents decreases P_I as a function of C_0 (Fig. 44a a) in a similar way that it does for flow speed (Fig. 43a). Inspired by this observation, we fit each P_I vs. C_0 to their corresponding power-lawed Michaelis-Menten equation with the same power-law exponent n:

$$P_I = P_m \left(\frac{C_0}{C_0 + K_P}\right)^n, \qquad 8$$

with P_m and K_P as fitting parameters (curves in Fig. 44a a). The resulting data fit well to the equations, with overall goodness of fit $R^2 \geq 0.99$ (Fig. 44a b). This suggests that the ATP dependence in the flow speed can pass to the resulting interface progression coefficient P_I. This analysis also shows that the consistency between the model $P_I(C_0)$ and experimentally measured P_I vs. C_0 (Fig. 41d) is under the condition of $n \approx 1$, which reenforces our assertion that adopting the Michaelis-Menten equation to convert ATP concentration to active fluid flow speed is an appropriate approach for building a coarse-grained model that matches the experimental results.

4.3.6 ANALYTICAL EXPRESSIONS FOR ACTIVE-INACTIVE INTERFACE PROGRESSION Our simple Fick's law-based model shows that the diffusion-like progression of the active-inactive interface is the consequence of diffusive dispersion of ATP (Fig. 41c). This result is based on numerical solutions of the Fick's law equation (Eq. 1); to gain deeper insight into the algebra underlying this modeling result, we consider the dynamics far from the boundary (i.e., discarding Eq. 2). The analytical solution to Fick's law (Eq. 1) subject to an initial step distribution is

$$C(x,t) = \frac{C_0}{2}\,\mathrm{erfc}\left(\frac{x - x_0}{2\sqrt{D\,t}}\right), \qquad 9$$

where x_0 is the initial location of the step. We find the rate of progression of the interface by substituting

Eq. 9 into Eq. 4 and solving for the active-inactive interface displacement Δx. Then the squared interface displacement can be written as:

$$\Delta x^2 = 4\,D\,t\,\left[\mathrm{erfc}^{-1}\left(\frac{2K}{C_0+2K}\right)\right]^2 = 2P_\mathrm{I}\,t, \qquad 10$$

where erfc^{-1} is the inverse of the complementary error function and the interface progression coefficient, P_I, is defined as

$$P_\mathrm{I} \equiv 2D\,\left[\mathrm{erfc}^{-1}\left(\frac{2K}{C_0+2K}\right)\right]^2. \qquad 11$$

Here, we find that, despite the nonlinearity of the flow speed-ATP conversion (Eq. 4), the interface progression coefficient depends linearly on the diffusion coefficient ($P_\mathrm{I} \propto D$; Eq. 11) and the progression of the interface remains diffusion-like ($\Delta x^2 \propto t$; Eq. 10), which is consistent with our numerical results ($\gamma = 1$; Fig. 41c). Moreover, the derived interface progression coefficient $P_\mathrm{I}(C_0)$ is almost identical to the numerical results (magenta curve and red dots in Fig. 41d). We thus reproduce the modeling results (γ and P_I) algebraically.

SUPERDIFFUSION-LIKE PROGRESSION OF ACTIVE-INACTIVE INTERFACE The success of the diffusion-limited model suggests that the active transport in the active fluid systems studied above is dominated by diffusion. This inspires us to question whether the progression of active-inactive interface will become superdiffusion-like when the active transport becomes convection-like[35,36]. To answer this question, we varied experimental parameters to explore a wider range of fluid flow speeds. To achieve lower flow speeds, we alter the composition of motor proteins by replacing a fraction of the processive motors (K401), which exert force on microtubules continuously, with nonprocessive motors (K365) that detach after each force application. The reduced number of processive motors has the net effect of driving the extensile motion of microtubules more slowly (Fig. 45a inset left)[4,10]. To achieve higher flow speeds, we increase

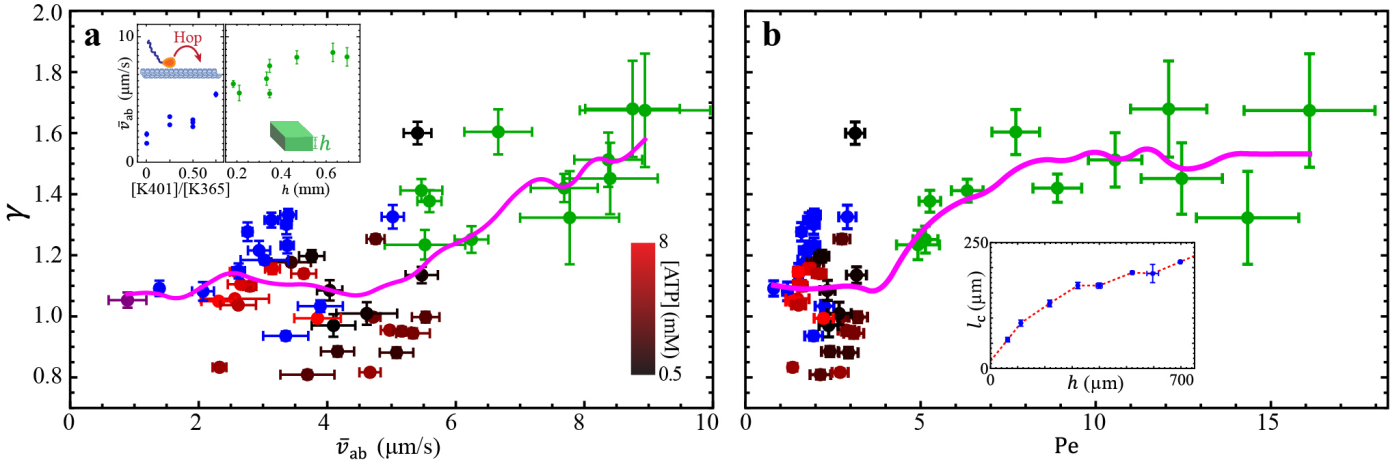

FIG. 45: TRANSITION OF ACTIVE-INACTIVE INTERFACE PROGRESSION Progression of the active-inactive interface transitions from diffusion-like ($\boldsymbol{\gamma} \approx 1$) to superdiffusion-like ($\boldsymbol{\gamma} > 1$) as the active transport changes from diffusion-dominated ($\mathbf{Pe} \lesssim 3$) to convection-dominated ($\mathbf{Pe} \gtrsim 3$). (a) The active-inactive interface progression exponent ($\boldsymbol{\gamma}$) increases with the flow-speed level of the active fluid ($\bar{\boldsymbol{v}}_\mathbf{ab}$). Shown are data from experiments with low ATP concentration (0.5 mM, black dots), high ATP concentration (8 mM, red dots), decreased flow speeds (from nonprocessive motors partially replacing processive motors; blue dots), increased flow speeds (from increased sample height; green dots)[4], and both nonprocessive motors and increased sample height (purple dot). The magenta curve represents the moving average of $\boldsymbol{\gamma}$. Although the analyzed $\boldsymbol{\gamma}$ from each experiment is noisy, the moving averaged $\boldsymbol{\gamma}$ exhibits an overall monotonic increase with the flow-speed level of active fluid $\bar{\boldsymbol{v}}_\mathbf{ab}$. Each dot represents one experimental measurement. Each error bar in $\boldsymbol{\gamma}$ represents the slope fitting error in $\mathbf{ln}\,\boldsymbol{\Delta x^2} = \mathbf{ln}(\boldsymbol{2P_\mathrm{I}}) + \boldsymbol{\gamma}\,\mathbf{ln}\,\boldsymbol{t}$ (Fig. 2a), and each error bar in $\bar{\boldsymbol{v}}_\mathbf{ab}$ represents the standard deviation of flow speeds in the active region. Inset: The flow-speed level of the active fluid is tuned by replacing processive motors (K401) with nonprocessive motors (K365) with the same overall motor concentrations (120 nM) (left)[10] or by altering the sample height (right)[4]. (b) The same data as in Panel a, plotted as a function of Péclet number, $\mathbf{Pe} \equiv \bar{\boldsymbol{v}}_\mathbf{ab}\boldsymbol{l_c}/\boldsymbol{D}$, where $\boldsymbol{l_c}$ is the correlation length of flow velocity in active fluid deduced from sample container height $\boldsymbol{h}$ (inset) and $\boldsymbol{D}$ is the diffusion coefficient of ATP. Each error bar in $\boldsymbol{\gamma}$ is the same as in Panel a, and each error bar in $\mathbf{Pe}$ represents propagated uncertainties from $\bar{\boldsymbol{v}}_\mathbf{ab}$ in Panel a and $\boldsymbol{l_c}$ in inset. Inset: Correlation length of flow velocity in active fluid $\boldsymbol{l_c}$ increases monotonically with sample container height $\boldsymbol{h}$[14]. The red dashed line represents the line interpolation of blue dots. The error bars represent the standard deviations of two trials.

the height of the sample container to decrease hydrodynamic drag (Fig. 45a inset right)[4,6]. Throughout these experiments, we keep the caged ATP concentration constant (5 mM).

As in the previous experiments, we analyze the spatiotemporal progression of activity to find the interface progression exponent γ as a function of the average flow speed in the bulk of the initially activated area, $\bar{v}_{\mathrm{ab}}$ (Fig. 45a). Because changing channel geometry alters the characteristic size of vortices in active fluids[14], we unify our datasets by plotting γ as a function of the Péclet number, Pe (Fig. 45b), defined as $\mathrm{Pe} \equiv \bar{v}_{\mathrm{ab}} l_{\mathrm{c}}/D$ where l_{c} is the correlation length of flow velocity and $D = 140$ $\mu m^2/s$ is our estimate of ATP diffusion in the system [54,55]. The Péclet number is a dimensionless quantity representing the ratio of convective transport rate to diffusive transport rate. A larger Péclet number (typically of order 10 or above) indicates convection-dominated active transport, and a smaller Péclet number (typically of order 1 or below) indicates diffusion-dominated active transport. Our data show that for $\mathrm{Pe} \lesssim 3$, the interface progression exponent remains $\gamma \approx 1$ (Fig. 45b), which corresponds to the regime captured by our model (Fig. 41). Then as Pe increases to greater than 3, γ grows monotonically (Fig. 45b). For the largest Pe explored in our experiments ($\mathrm{Pe} \approx 16$), γ reaches ~1.7, which indicates that convective processes are beginning to emerge and dominate the active transport. Overall, our data suggest that as the active transport transitions from diffusion-dominated ($\mathrm{Pe} \lesssim 3$) to convection-dominated ($\mathrm{Pe} \gtrsim 3$) regimes, the progression of active-inactive interfaces transitions from diffusion-like ($\gamma \approx 1$) to superdiffusion-like ($\gamma > 1$).

4.3.7 EFFECT OF SAMPLE CONTAINER HEIGHT ON THE CORRELATION LENGTHS AND TIMES OF FLOW VELOCITIES To characterize whether the mixing of our active fluid systems is driven by diffusion-dominated or convection-dominated active transport, we adopt a dimensionless quantity, the Péclet number: $\mathrm{Pe} \equiv \bar{v} l_{\mathrm{c}}/D$, where D is the diffusion coefficient of ATP, $\bar{v}$ is the flow mean speed of active fluid, and l_{c} is the correlation length of flow velocity of active fluid[54,55]. Determining Pe requires l_{c}, and our previous work shows that increasing the sample container height can increase l_{c}[14]. Thus, we characterize how the correlation lengths and correlation times of active fluid flows depend on the sample container height.

To extract the correlation lengths in our sample, we prepare an active fluid sample with uniform activity, dope the sample with fluorescent tracer particles, and monitor and track these tracers to reveal the flow velocity fields of active fluid in the sample $\mathbf{V}(\mathbf{r}, t)$ as a function of time t (Fig. 46a). Then we calculate the velocity autocorrelation function,

$$\Psi(\Delta\mathbf{r}, \Delta t) \equiv \int d\mathbf{r}\, dt\, \mathbf{V}(\mathbf{r} + \Delta\mathbf{r}, t + \Delta t) \cdot \mathbf{V}(\mathbf{r} + \Delta\mathbf{r}, t + \Delta t), \quad 12$$

by deploying the convolution theorem

$$\Psi = \mathcal{F}^{-1}\{\mathcal{F}\{\mathbf{V}\} \cdot \mathcal{F}\{\mathbf{V}\}^*\}, \quad 13$$

where $\mathcal{F}\{\ \}$ represents the Fourier transform, $\mathcal{F}^{-1}\{\ \}$ represents the inverse Fourier transform, and Θ^* represents the complex conjugate of any variable Θ. Then we normalize the correlation function as

$$\bar{\Psi}(\Delta\mathbf{r}, \Delta t) = \frac{\Psi(\Delta\mathbf{r}, \Delta t)}{\Psi(\mathbf{0}, 0)}, \quad 14$$

which allows us to determine the normalized same-time velocity autocorrelation function as $\bar{\Psi}(\Delta\mathbf{r}, 0)$ (Fig. 46b). To analyze the correlation lengths, we average the correlation function over orientations

$$\bar{\Psi}(\Delta r, 0) = \langle \bar{\Psi}(\Delta\mathbf{r}, 0) \rangle_{|\Delta\mathbf{r}| = \Delta r}, \quad 15$$

where $\langle\ \rangle_{|\Delta\mathbf{r}| = \Delta r}$ indicates averaging over the same magnitude of spatial displacement $\Delta\mathbf{r}$ (Fig. 46c). Then we define the correlation lengths l_{c} as the separation distance where the normalized correlation function decays to 0.5: $\bar{\Psi}(l_{\mathrm{c}}, 0) \equiv 0.5$. Repeating the analysis of l_{c} over the samples with heights varying from 60 to 700 μm reveals that the correlation

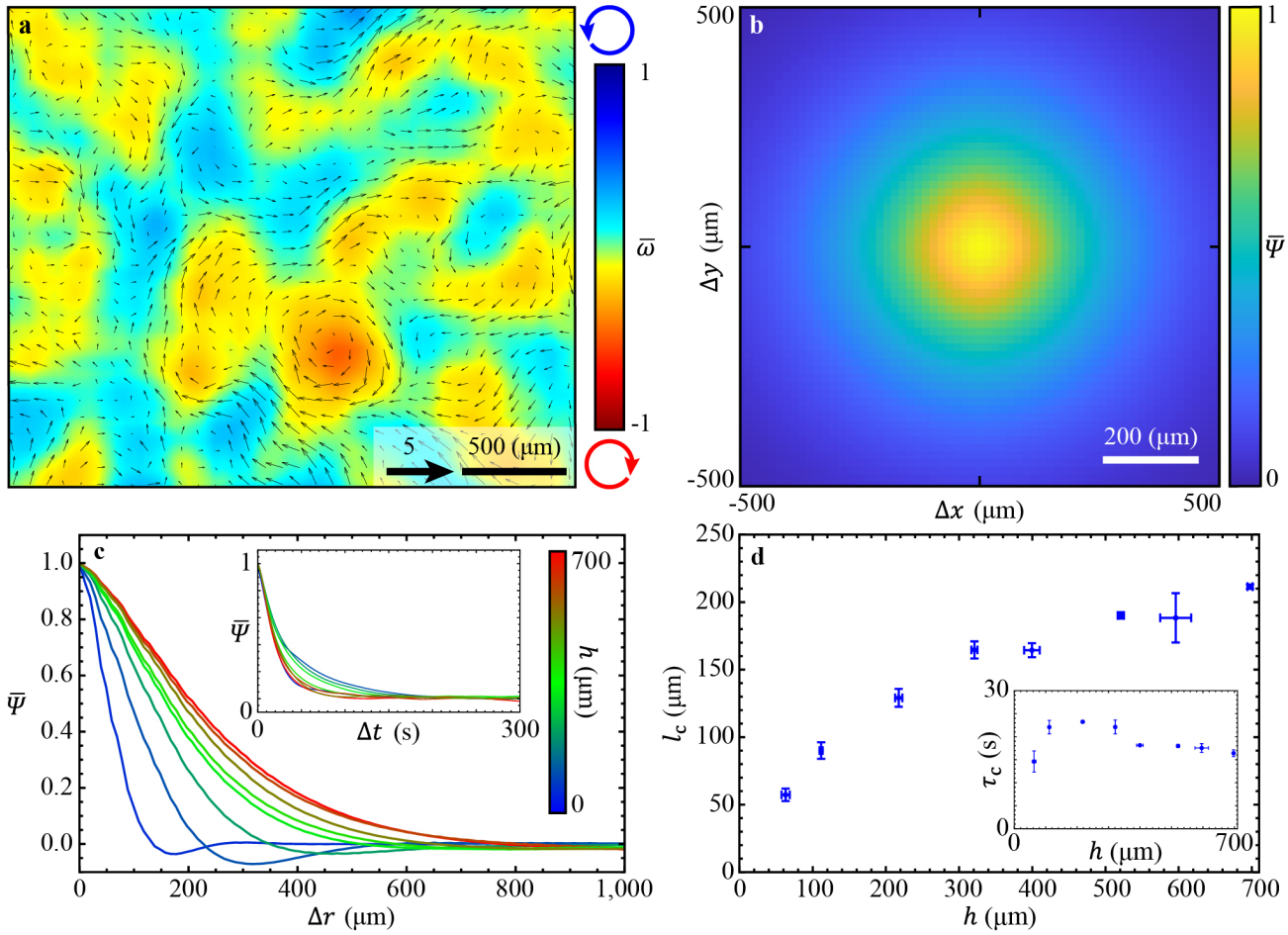

FIG. 46: INCREASING SAMPLE CONTAINER HEIGHT INCREASES THE CORRELATION LENGTHS OF FLOW VELOCITIES BUT DOES NOT SIGNIFICANTLY INFLUENCE THE CORRELATION TIMES (a) Normalized velocity field and vorticity color map of active fluid flows in a 700-μm-thick flow cell. The velocity field $\mathbf{V}$ is normalized by the mean speed of active fluid flow; the vorticity $\boldsymbol{\omega} \equiv [\nabla \times \mathbf{V}]_z$ is normalized by the triple of standard deviation of vorticity, $\bar{\boldsymbol{\omega}} \equiv \boldsymbol{\omega}/[3\ \mathrm{std}(\boldsymbol{\omega})]$[6]. (b) Map of normalized same-time spatial autocorrelation of flow velocity in the same sample as Panel a. (c) Normalized same-time spatial autocorrelation functions of flow velocity as a function of separation distance (Eq. 15) for various sample heights. Inset: Normalized same-position temporal autocorrelation functions of flow velocity for various sample heights. (d) The correlation lengths of flow velocity increase with sample height. The error bars represent the standard deviations of two trials. Inset: The correlation times of flow velocity remain nearly invariant (~20 s) for sample heights from 60 to 700 μm.

lengths increase from 60 to 210 μm (Fig. 46d). Given that the correlation lengths also represent the size of vortices in active fluid flow[53], our analysis suggests that across our explored sample heights the vortices expand by a factor of 3.5.

In addition to correlation lengths, our analysis also allows us to extract the correlation time, τ_c, which reveals how rapidly the flow patterns change (i.e., the lifetime of vortices). To determine the correlation time, τ_c, we follow a similar analysis except we analyze the normalized same-position temporal autocorrelation function $\bar{\Psi}(\mathbf{0}, \Delta t)$ (Fig. 46c inset) and define the correlation time τ_c as the time lapse when the normalized same-position temporal correlation function decays to 0.5: $\bar{\Psi}(\mathbf{0}, \tau_c) \equiv 0.5$. Our analysis reveals that the correlation time remains ~20 seconds across our explored sample heights (Fig. 46 inset), which suggests that the sample geometry does not play a significant role in the lifetime of the vortices. Overall, this work shows that increasing the sample container height enlarges the vortices but does not significantly affect their formation and deformation rates, which aligns with our previous studies about length scales of confined active fluid[14].

4.3.8 DISPERSION OF UV-ACTIVATED FLUORESCENT DYES To this point, we have characterized the mixing of active and inactive fluids by the progression of the interface between them;

however, like milk blending into coffee, the mixing process often involves dispersion of suspended components. To characterize how suspended components disperse during the progression of the active-inactive interface, we design another series of experiments with suspended components that are initially nonuniform. We dope inactive fluid with suspended UV-activated fluorescent dyes and expose one side of the sample container to UV light, which simultaneously activate the fluid and the fluorescent dye. We find that in an inactive sample ($\bar{v}_{\mathrm{ab}} = 0$), where dyes disperse only by molecular diffusion, the dye barely disperse, whereas in a sample where one side is activated ($\bar{v}_{\mathrm{ab}} = 8.2$ μm/s), the dyes are transported by active fluid flows and almost completely disperse through the sample in 4 hours (Fig. 47a). To quantify the dispersion rate, we adopt Saintillan and Shelley's method[33] to analyze the normalized multiscale norm of dye brightness as a function of time: $\hat{s}(t) \equiv |s(t)|/|s(0)|$, where

$$|s| \equiv \left[\sum_{\boldsymbol{k}} \frac{|s_{\boldsymbol{k}}|^2}{\sqrt{1 + l^2\, k^2}}\right]^{\frac{1}{2}}, \qquad 16$$

$s_{\boldsymbol{k}}$ is the Fourier coefficient at wave vector $\boldsymbol{k}$ in a Fourier expansion of the dye brightness and $l = 4.84$ μm is the pixel size of the micrographs. We find that the normalized multiscale norm decays faster as $\bar{v}_{\mathrm{ab}}$ increases from 0 to 8.2 μm/s (Fig. 47b). In light of reports that the norm decays exponentially[33], we quantify the decay rate by fitting the first hour $\hat{s}(t)$ data to $\ln \hat{s} = -t/t_0$ with t_0 (mixing time) as the fitting parameter (Fig. 10b inset) and find that the mixing time decreases with flow speed of active fluid (Fig. 47c inset). When the fluid is inactive ($\bar{v}_{\mathrm{ab}} = 0$), dye dispersion is dominated by molecular diffusion and the mixing time is 24 hours; slightly activating the fluid ($\bar{v}_{\mathrm{ab}} = 2$ μm/s) reduces the mixing time to 8 hours, which demonstrates that active fluid flows enhance the mixing process of suspended components[34].

To reveal how the mechanism of active transport (i.e., diffusion-dominated or convection-dominated) alters the mixing time, we analyze the mixing time as a function of the Péclet number and find that the mixing time monotonically decreases as the active transport becomes more convection-like (Fig. 47c). Notably, there is no discernible transition in mixing time as the active transport transitions from diffusion-dominated to convection-dominated, although there is a transition in the progression of active-inactive interfaces (Fig. 47b). This dependence of mixing time on the Péclet number in active-inactive fluid systems is similar to that in an activity-uniform active fluid system (Fig. 48b), which shows that Péclet number is the controlling parameter for mixing time of suspended components in active fluid systems, regardless of the distribution of activity.

4.3.9 MIXING KINEMATICS OF ACTIVITY-UNIFORM ACTIVE FLUID This work focuses on mixing in active fluid systems with nonuniform distribution of activity. We show that as the Péclet number of a system increases, the progression of the active-inactive interface changes from diffusion-like to superdiffusion-like (Fig. 45b) and the mixing times of suspended fluorescent dyes decrease (Fig. 47c). We decide that it would be elucidating to compare these results with those from active fluid systems with uniform activity distribution. A uniform active fluid system does not have an active-inactive interface, and thus we can not measure γ, but we measure mixing time of suspended fluorescein. We repeat the fluorescein-mixing experiments where the flow speed of active fluid are increased by increasing sample height (Fig. 47), but we perform the experiments in a system with uncaged ATP and thus flow speeds are uniformly distributed throughout the sample (Fig. 48b inset) and then we analyze the mixing time as a function of mean flow speed and Péclet number (Fig. 48). Our analysis reveals that the mixing time decreases with increasing Péclet number without a discernible transition, which we expect because a more convective active transport can mix

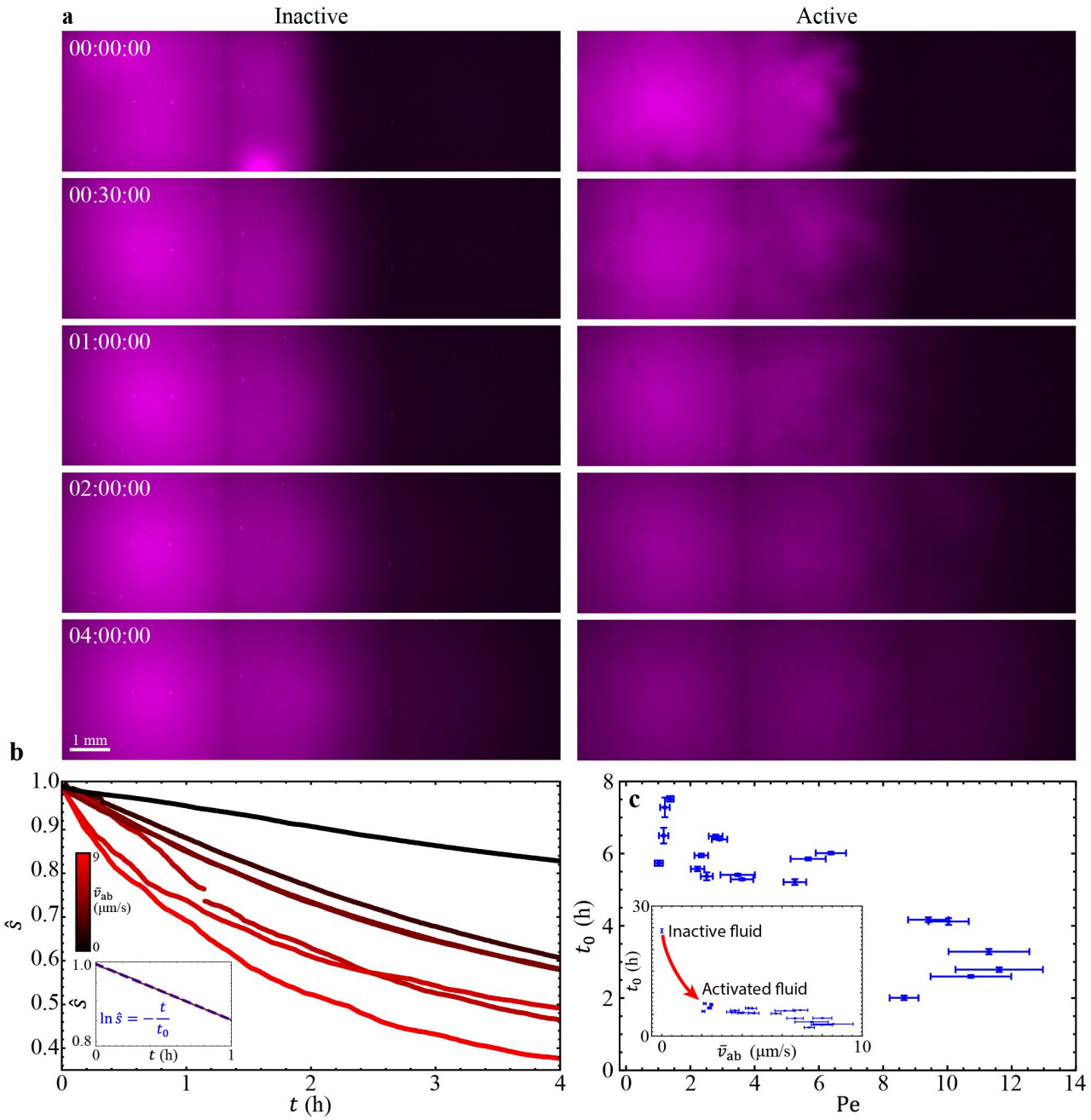

FIG. 47: ACTIVE FLUID FLOWS PROMOTE MIXING OF UV-ACTIVATED FLUORESCENT DYES, WHICH ARE INITIALLY ACTIVATED IN THE LEFT-HAND SIDE OF THE CONTAINER ONLY (a) Dispersion of UV-activated fluorescent dyes (magenta) in inactive ($\bar{v}_{ab} = 0$; left column) and active ($\bar{v}_{ab} = 8.2$ μm/s; right column) microtubule-kinesin fluid. Active fluid flows actively transport fluorescent dyes and enhance their dispersion. Time stamps are hour:minute:second. (b) Selected examples of normalized multiscale norm vs. time for different active bulk flow speeds, $\bar{v}_{ab}$. Normalized multiscale norm $\hat{s}(t)$ decreases faster in a faster-flowing active fluid system. Inset: The normalized multiscale norm, $\hat{s}(t)$, in log-linear axes behaves as a straight line, which suggests that the norm decays exponentially with time. The decay time scale t_0 (or mixing time) is determined by fitting the normalized multiscale norm versus time data to $\ln \hat{s} = -t/t_0$ with t_0 as the fitting parameter (dashed blue line). (c) The mixing time decreases monotonically with Péclet number, which demonstrates that a stronger convection mechanism leads to faster mixing of suspended components. Each dot represents one experimental measurement. Each error bar in t_0 represents the slope fitting error in $\ln \hat{s} = -t/t_0$ (Panel b inset), and each error bar in Pe (defined as $Pe \equiv \bar{v}_{ab} l_c / D$) represents propagated uncertainties from $\bar{v}_{ab}$ (see inset) and l_c. Inset: Mixing time, t_0, as a function of active bulk mean speed, $\bar{v}_{ab}$. Each error bar in t_0 is the same as in Panel c, and each error bar in $\bar{v}_{ab}$ represents the standard deviation of flow speeds in the active region. Notably, the mixing time of the inactive fluid system ($\bar{v}_{ab} = 0$) is 24 hours (top-left dot); minimally activating the fluid ($\bar{v}_{ab} = 2$ μm/s) reduces the mixing time to 8 hours.

the dye faster. Also, this result is similar to the one in active-inactive fluid systems (Fig. 47c), which suggests that the Péclet number is the controlling parameter for mixing time of suspended components

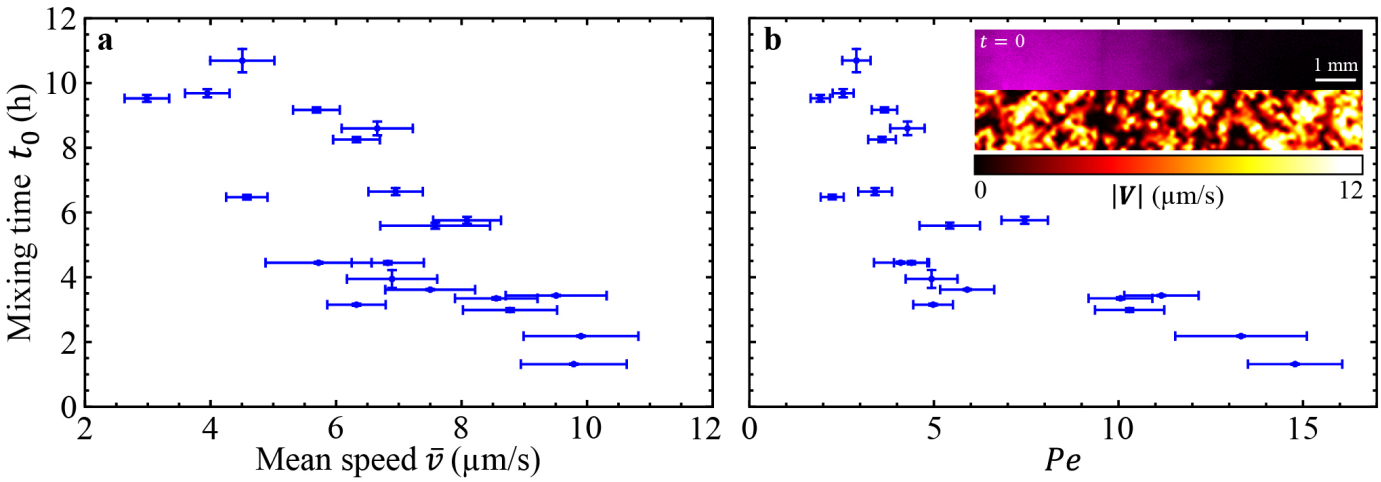

FIG. 48: MIXING TIME OF UV-ACTIVATED FLUORESCENT DYES DECREASES WITH INCREASING PÉCLET NUMBER FOR ACTIVITY-UNIFORM ACTIVE FLUID SYSTEMS (a) Mixing time as a function of mean speed of active fluid with uniform activity distribution. Accelerating active fluid flows accelerates the mixing process of suspended fluorescein, resulting in shorter mixing time $\boldsymbol{t_0}$. Each dot represents one experimental measurement. Error bars in $\boldsymbol{t_0}$ represent the slope fitting error as in Fig. 5b inset, and error bars in $\bar{\boldsymbol{v}}$ represent the standard deviation of time-averaged flow speeds. (b) Mixing time in activity-uniform active fluid systems decreases with increasing Péclet number. Inset: Micrograph of fluorescein uncaged by ultraviolet light exposure (magenta in upper half) and speed map of active fluid (lower half) in the beginning ($\boldsymbol{t} = 0$) of the dye-mixing sample that had mean speed $\bar{\boldsymbol{v}} \approx 9.8 \pm 0.8$ μm/s and mixing time $\boldsymbol{t_0} = 1.31 \pm 0.02$ h. Note that active fluid has uniform activity (flow speed distribution) in the beginning whereas the uncaged fluorescein is only distributed on one side (left) of the sample.

in active fluid systems, regardless of the distribution of activity.

4.3.10 CONTINUOUS ACTIVE FLUID MODEL Our experimental data show that as the active transport becomes more convection-like, the active-inactive interface progression transitions from diffusion-like to superdiffusion-like (Fig. 45b) and the mixing time of suspended components decreases monotonically (Fig. 47c). To determine whether this complex mixing process can be modeled with an existing active fluid model, we adopted Varghese et al.'s model[53] because it successfully describes the transition from coherent to chaotic flow in 3D microtubule-kinesin active fluid systems[6]. The model describes microtubules as self-elongating rods whose nematic order, $\mathbf{Q}$, is subject to spontaneous decay due to the rods' rotational molecular diffusion and reorientation by solvent flow. Thus, the dimensionless kinetic equation for Q can be written as:

$$\partial_{t^*}\mathbf{Q} + \mathbf{u}\cdot\boldsymbol{\nabla}_*\mathbf{Q} + \mathbf{Q}\cdot\boldsymbol{\Omega}^* - \boldsymbol{\Omega}^*\cdot\mathbf{Q} = -\mathbf{Q} + \nabla_*^2\mathbf{Q} + \lambda\left[\frac{2}{d}\mathbf{E}^* + \mathbf{Q}\cdot\mathbf{E}^* + \mathbf{E}^*\cdot\mathbf{Q} - \frac{2}{d}\mathrm{Tr}(\mathbf{Q}\cdot\mathbf{E}^*)\,\mathbf{I}\right], \quad 17$$

where t^* is the dimensionless time, $\boldsymbol{\nabla}_*$ is the dimensionless spatial gradient operator, ∇_*^2 is the dimensionless Laplacian operator, $\boldsymbol{\Omega}^* \equiv [(\boldsymbol{\nabla}_*\mathbf{u})^{\mathrm{T}} - \boldsymbol{\nabla}_*\mathbf{u}]/2$ is the dimensionless vorticity tensor, $\mathbf{E}^* \equiv [(\boldsymbol{\nabla}_*\mathbf{u})^{\mathrm{T}} + \boldsymbol{\nabla}_*\mathbf{u}]/2$ is the dimensionless strain rate tensor, $\lambda = 1$ is the flow alignment coefficient, and d is the system dimensionality. The dimensionless flow field u is governed by the Stokes equation

$$\nabla_*^2\mathbf{u} - \boldsymbol{\nabla}_* p^* - \boldsymbol{\nabla}_*\cdot\boldsymbol{\sigma}_{\mathrm{a}} = 0 \quad 18$$

and incompressibility constraint ($\boldsymbol{\nabla}_*\cdot\mathbf{u} = 0$), where p^* is the dimensionless pressure and $\boldsymbol{\sigma}_{\mathrm{a}} \equiv \alpha^*\mathbf{Q}$ is the dimensionless active stress exerted by self-elongating rods with a dimensionless activity coefficient α^* [63]. Because the activity coefficient increases with ATP concentration[64], we select an α ATP relation[65]

$$\alpha^* = \alpha_0^*\,\frac{C}{C+K}\ , \quad 19$$

where α_0^* is the dimensionless activity level, C is the ATP concentration, and $K = 270$ μM[4]. We select this relation because it captures the dynamics of microtubule bundle extension and kinesin kinetics (Michaelis-Menten), which play critical roles in the

activity of microtubule-kinesin active fluid systems[60,61]. Finally, given that ATP diffuses as a result of thermal fluctuation as well as flows with the active fluid, we model ATP dispersion with a convection-diffusion equation:

$$\partial_{t^*} C = D^* \nabla_*^2 C - \mathbf{u} \cdot \boldsymbol{\nabla}_* C, \qquad 20$$

where D^* is the dimensionless ATP molecular diffusion coefficient. To simplify modeling, we consider a 2D active fluid system ($d = 2$)[53] confined in a 112 × 22 rectangular boundary with no-slip boundary condition for flows ($\mathbf{u} = \mathbf{0}$) and no-flux boundary condition for rods ($\mathbf{n} \cdot \boldsymbol{\nabla}_* \mathbf{Q} = \mathbf{0}$, where n represents a unit vector normal to boundaries). To solve the equations for $\mathbf{Q}$, $\mathbf{u}$, and C (Eqs. 17,18&20), we determine the initial conditions as quiescent solvent ($\mathbf{u} = \mathbf{0}$) under uniform pressure ($p^* = 0$) with the rods in an isotropic state [$Q_{xx} = -Q_{yy} = 2.5 \times 10^{-4}\,\mathrm{rn}(\mathbf{r})$ and $Q_{xy} = Q_{yx} = 5 \times 10^{-4}\mathrm{rn}(\mathbf{r})$, where $\mathrm{rn}(\mathbf{r})$ is a spatially uniform random number between −1 and +1] and 5 mM of ATP distributed on only one side of the system. Then we evolve the fluid flows and ATP distributions for 200 units of dimensionless time ($t^* = 0$–200) with the finite element method[66].

Our modeling results show that in an inactive system ($\alpha_0^* = 0$; $D^* = 16$; Fig. 49a, left column), ATP disperses only by molecular diffusion, but when one side of the sample is activated ($\alpha_0^* = 25$; $D^* = 16$; middle column), the system develops chaotic turbulence-like mixing flows that actively transport the ATP toward the inactive region. In a third simulation where the ATP molecular diffusion rate is increased ($\alpha_0^* = 25$; $D^* = 64$; right column), the mixing process speeds up. These simulation results show that the process of ATP dispersion is controlled by both molecular diffusion of ATP and active fluid-induced convection.

To quantify the efficacy of ATP mixing by active fluid, we analyze the normalized multiscale norm of ATP concentrations as a function of time[33] for $\alpha_0^* =$ 0–25 and $D^* = 1$–128 (Eq. 16 with $l = 1$). We find that the norms decay exponentially with time: $\hat{s} \sim \exp(-t^*/t_0^*)$, where t_0^* is the dimensionless mixing time (Fig. 49b), which is consistent with results reported by Saintillan and Shelley[33]. We analyze mixing time as a function of dimensionless activity level, α_0^*, for each dimensionless molecular diffusion coefficient D^* (Fig. 49c) and find that when ATP diffuses slowly ($D^* \lesssim 16$; blue to light green curves), mixing time decreases with increasing activity level or faster active transport (Fig. 49b inset), which is consistent with our experimental observation (Fig. 47c). Our simulation also shows that as ATP diffuses sufficiently fast ($D^* \gtrsim 32$; olive and red curves), the mixing time is nearly independent of activity level. Overall, increasing both the molecular diffusion coefficient and the activity level decreases mixing time. Thus, our simulation shows that both molecular diffusion (represented as D^*) and active fluid-induced convection (related to α_0^*) play important roles to disperse and homogenize the suspended components; which mechanism dominates the dispersion depends upon the competition between these two mechanisms.

To demonstrate how the competition of these two mechanisms affects the progression of active-inactive interfaces, we analyze the interface progression exponent γ as a function of α_0^* for various diffusion coefficients D^* (Fig. 49c inset) and find that when the diffusion mechanism is relatively weak ($D^* = 2$; dark blue curve), the convection mechanism dominates the interface progression, leading it to progress in a superdiffusion-like, or more precisely, ballistic-like manner ($\gamma \approx 2$). Contrarily, as the diffusion mechanism becomes relatively strong ($D^* = 8$; light green curve), diffusion mechanisms dominate the interface progression, leading it to progress in a diffusion-like manner ($\gamma \approx 1$). Interestingly, we find that in an intermediate strength of diffusion mechanism ($D^* = 4$; dark green curve), increasing activity level α_0^* transitions the interface progression from diffusion-like to superdiffusion-like, which is consistent with

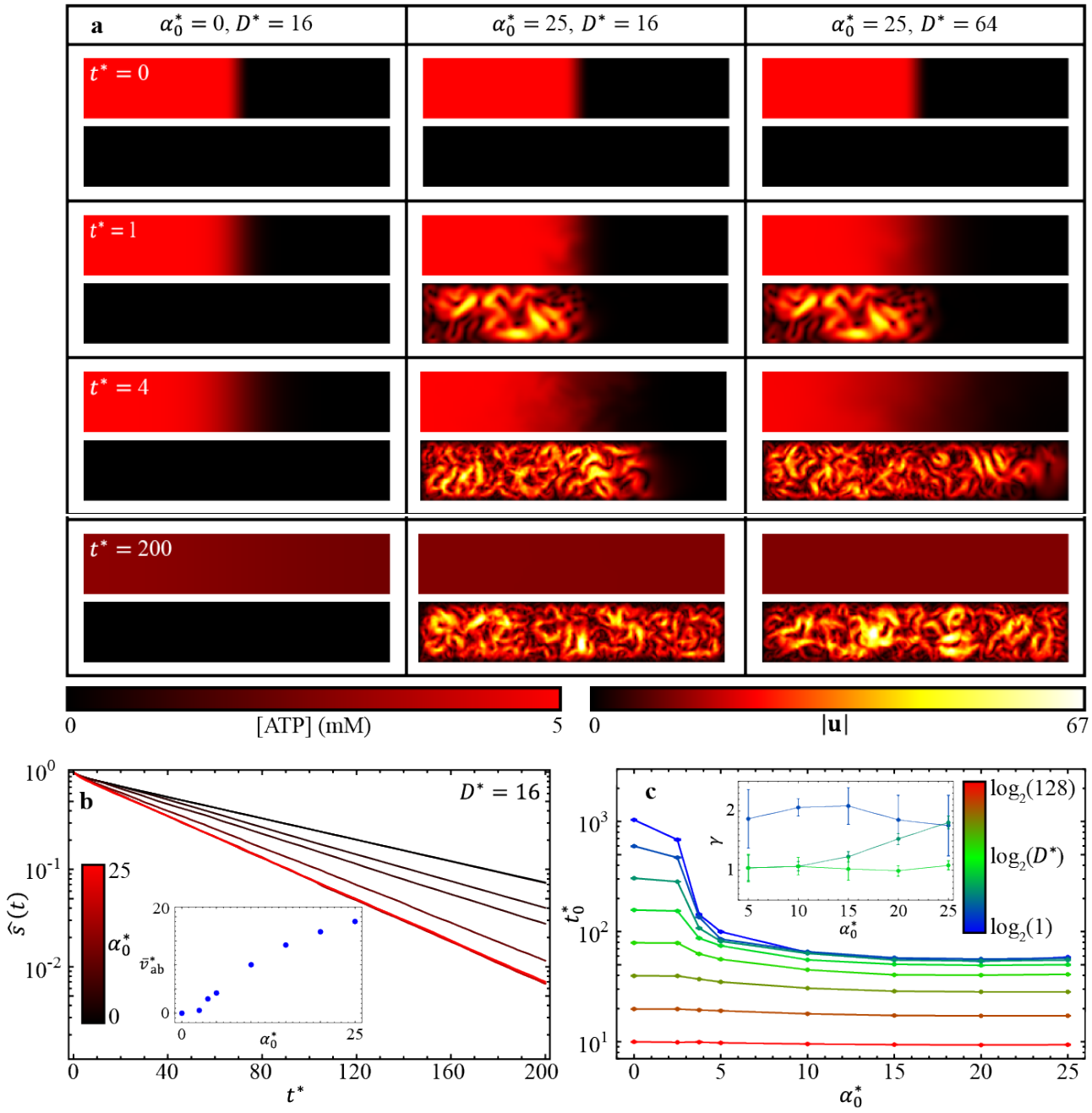

FIG. 49: A CONTINUOUS ACTIVE FLUID SIMULATION REVEALS THAT THE MIXING TIME OF ATP DEPENDS ON THE DIMENSIONLESS MOLECULAR DIFFUSION COEFFICIENT OF ATP AND THE DIMENSIONLESS ACTIVITY LEVEL OF ACTIVE FLUID (a) Table of ATP concentration (top panels) and active fluid flow speed (bottom panels) maps for various dimensionless activity levels $\boldsymbol{\alpha_0^*}$ and molecular diffusion coefficients $\boldsymbol{D^*}$. When the fluid has no activity ($\boldsymbol{\alpha_0^* = 0}$; left column), ATP disperses to the right side of the system only by molecular diffusion; the dispersion is enhanced when the active fluid starts to flow and actively transport ATP ($\boldsymbol{\alpha_0^* = 25}$; middle column). The dispersion is further enhanced when ATP diffuses significantly faster ($\boldsymbol{D^* = 64}$; right column) (b) Evolution of normalized multiscale norm for $\boldsymbol{\alpha_0^*}$ = 0–25 while keeping $\boldsymbol{D^* = 16}$. The normalized multiscale norms decay exponentially with time: $\boldsymbol{\hat{s} = \exp(-t^*/t_0^*)}$, where $\boldsymbol{t_0^*}$ is the dimensionless mixing time. Inset: Dimensionless mean speed of active fluid in active region $\boldsymbol{\bar{v}^*_{ab}}$ monotonically increases with dimensionless activity level $\boldsymbol{\alpha_0^*}$. (c) Dimensionless ATP mixing times, $\boldsymbol{t_0^*}$, as a function of dimensionless activity level, $\boldsymbol{\alpha_0^*}$, for various dimensionless molecular diffusion coefficients, $\boldsymbol{D^*}$. Increasing both $\boldsymbol{\alpha_0^*}$ and $\boldsymbol{D^*}$ decreases mixing time monotonically. Each error bar in $\boldsymbol{t_0^*}$ represents the fitting error of $\hat{\boldsymbol{s}}$ vs. $\boldsymbol{t^*}$ to $\boldsymbol{\ln \hat{s} = -t^*/t_0^*}$ (Panel b). Inset: Active-inactive interface progression exponent $\boldsymbol{\gamma}$ as a function of dimensionless activity level $\boldsymbol{\alpha_0^*}$ for dimensionless molecular diffusion coefficients $\boldsymbol{D^*}$ = 2 (dark blue), 4 (dark green), and 8 (light green). Each error bar in $\boldsymbol{\gamma}$ represents the slope fitting error as in Fig. 3a. Increasing $\boldsymbol{D^*}$ decreases $\boldsymbol{\gamma}$ (from dark blue to light green curve), whereas increasing $\boldsymbol{\alpha_0^*}$ increases $\boldsymbol{\gamma}$ (dark green curve).

our experimental observation (Fig. 45). Overall, our active-fluid hydrodynamic model qualitatively captures the mixing dynamics of active and inactive fluid systems in terms of active-inactive interface

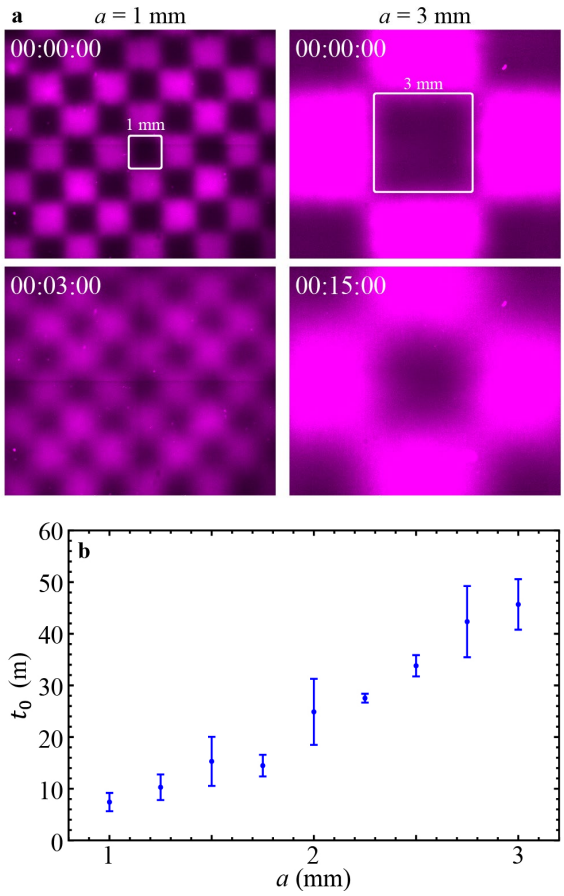

FIG. 51: FLUID ACTIVATED IN A CHECKERBOARD PATTERN MIXES FASTER WHEN THE CHECKERBOARD GRID IS SMALLER (a) Checkerboard-patterned UV lights are used to activate active fluid and caged fluorescent dyes. (b) The mixing time of the checkerboard-activated fluid increases with grid size, which demonstrates that the mixing efficacy of active fluid depends on distribution of activity: more nonuniform active fluid mixes the system more slowly. Each error bar in t_0 represents the standard deviation of two trials.

progression and dispersion of suspended components.

4.3.11 CHECKERED DISTRIBUTION OF DYES AND ACTIVITY Up until this point we have only explored one configuration of nonuniform active fluid systems: an activated bulk on one side of a channel adjacent to an inactive bulk on the other side. To explore how other spatial configurations of activity affect mixing, we use a checkerboard pattern of UV light to split the activated region into cells. As in previous experiments, 50% of the total fluid is activated. Fluid activated in a checkerboard pattern evolves to a homogeneous state more quickly than fluid that is activated on one side only (1 hour vs. 10 hours; Fig. 51a). UV-activated fluorescent dyes show that the mixing time decreases as the grid size decreases from 3 mm to 1 mm (Fig. 51b).

To elucidate how checkerboard mixing driven by active fluid differs from that driven by molecular diffusion alone, we apply our established active-fluid hydrodynamic model for both active ($\alpha^* = 25$) and inactive ($\alpha^* = 0$) fluid systems (Fig. 50a). As expected, we find that the mixing time increases monotonically with grid size for both active and inactive fluid systems (Fig. 50b), with the active fluid system (red curve) having a shorter mixing time than

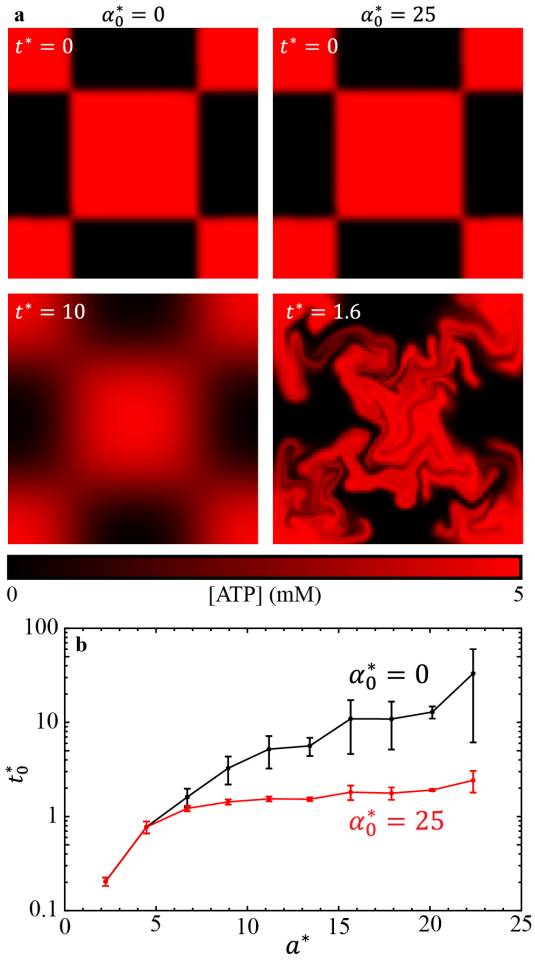

FIG. 50: SIMULATIONS WITH ATP INITIALLY DISTRIBUTED IN A CHECKERBOARD PATTERN IN A 45 × 45 SIMULATION BOX (a) Distributions of ATP (red) disperse from the checkerboard pattern (Eq. 23 with $\alpha^* = 22$) to a homogeneous state by molecular diffusion only (left; $D^* = 1$, $\alpha_0^* = 0$) and by the combination of molecular diffusion and active fluid-induced convection (right; $D^* = 1$, $\alpha_0^* = 25$). (b) The dimensionless mixing time of ATP increases monotonically with the dimensionless checkerboard grid size α^* in both active (red) and inactive (black) fluid systems. Error bars represent the standard deviation of two trials performed with different types of checkerboard pattern (Eqs. 23&24).

the inactive fluid system (black curve). Interestingly, we find that when the grid size is sufficiently small ($a \lesssim 5$), the active and inactive fluids have the same simulated mixing time. We also find that as the grid size increases from 5 to 22, the mixing time of the inactive fluid increases more than the mixing time of the active fluid (40× vs. 3×).

4.3.12 NETWORK MELTING MECHANISM MAY SLOW PROGRESSION OF ACTIVE-INACTIVE INTERFACE

Our active-inactive fluid experiments show that for the active-inactive interface to progress, not only does ATP need to be transported to the inactive fluid region, but also the inactive microtubule network needs to be activated from its inactive state. However, inactive microtubule networks behave like an elastic gel because the unfueled kinesin motor dimers are immobile and act as crosslinkers in the microtubule network[52], and after ATP is transported to the active-inactive interface, it takes time for the fueled motors to fluidize or melt the inactive microtubule network1 so the interface can progress. Thus, the active-inactive interface is expected to progress more slowly than it would if the network could melt instantly.

To examine this expectation, we analyze the normalized speed profile expected on the basis of ATP distribution and compare them with the measured normalized speed profile. We assume that the ATP is transported by the active fluid in the same way as fluorescein. Also, because ATP and fluorescein are both activated by UV light exposure, we assume that the distribution of dyes is similar to that of activated ATP, which implies that the fluorescein and activated ATP has similar concentration profiles: $C_{\mathrm{ATP}}(x,t)/C_{\mathrm{ATP0}} \approx C_{\mathrm{fluorescein}}(x,t)/C_{\mathrm{fluorescein0}}$ where $C_{\mathrm{X}}(x,t)$ represents the concentration of X and C_{X0} represents the initial concentration of X. We also assume that the gray values in the fluorescein micrographs are proportional to uncaged fluorescein concentration, which implies that the normalized concentration profile of uncaged fluorescein is similar to the normalized profile of gray values (G.V.) in the fluorescein micrographs: $C_{\mathrm{fluorescein}}(x,t)/C_{\mathrm{fluorescein0}} \approx \overline{\mathrm{G.V.}}(x,t)$. Thus, we can deduce the profile of ATP from normalized profile of gray values in fluorescein micrographs: $C_{\mathrm{ATP}}(x,t) \approx C_{\mathrm{ATP0}}\,\overline{\mathrm{G.V.}}(x,t)$. To extract the normalized profile of gray values in fluorescein micrographs, we consider the micrographs of fluorescein near the active-inactive interface (Fig. 52 a). Then we average the gray values of a micrograph vertically to get a profile of gray values, $\mathrm{G.V.}(x,t)$ (Fig. 52 c). To normalize the gray value profile, we adopt the baseline model, which introduces two baselines as the upper and lower references of the gray values: $L_{\mathrm{U}}(x,t)$ and $L_{\mathrm{L}}(x,t)$, where L_{U} is determined by fitting the gray value profile in the active bulk to a line (Fig. 11c, magenta curve on top left) and L_{L} is determined by fitting the gray value profile in the inactive bulk to a line (Fig. 52 c, magenta curve on bottom right). Then, the gray value profile can be normalized as

$$\overline{\mathrm{G.V.}}(x,t) \equiv \frac{\mathrm{G.V.}(x,t) - L_{\mathrm{U}}(x,t)}{L_{\mathrm{U}}(x,t) - L_{\mathrm{L}}(x,t)}. \qquad 21$$

This normalization model has been commonly used in the analysis of thermal melting curves of DNA[3]. Here, we adopt this normalization model to reduce the influences of background light and nonuniform illumination in our profile analysis. Once the normalized gray value profile is determined, we can deduce the profile of ATP concentrations (Fig. 52d). Then we convert the ATP concentration profile to flow speed profile of active fluid with the Michaelis-Menten equation (Eq. 4) followed by normalizing the flow speed profile (blue curve in Fig. 52e). This is the profile deduced from distribution of uncaged fluorescein. To compare the deduced speed profile with the directly measured speed profile, we analyze the tracer motion at the same time to extract the speed distribution of active fluid flow (Fig. 52b), average the speed distribution vertically to extract the speed profile, and normalize the profile (red curve in Fig. 52e). Our analysis shows that the normalized speed profile extracted from tracer motion (red curve in Fig. 52e) falls behind the profile deduced from

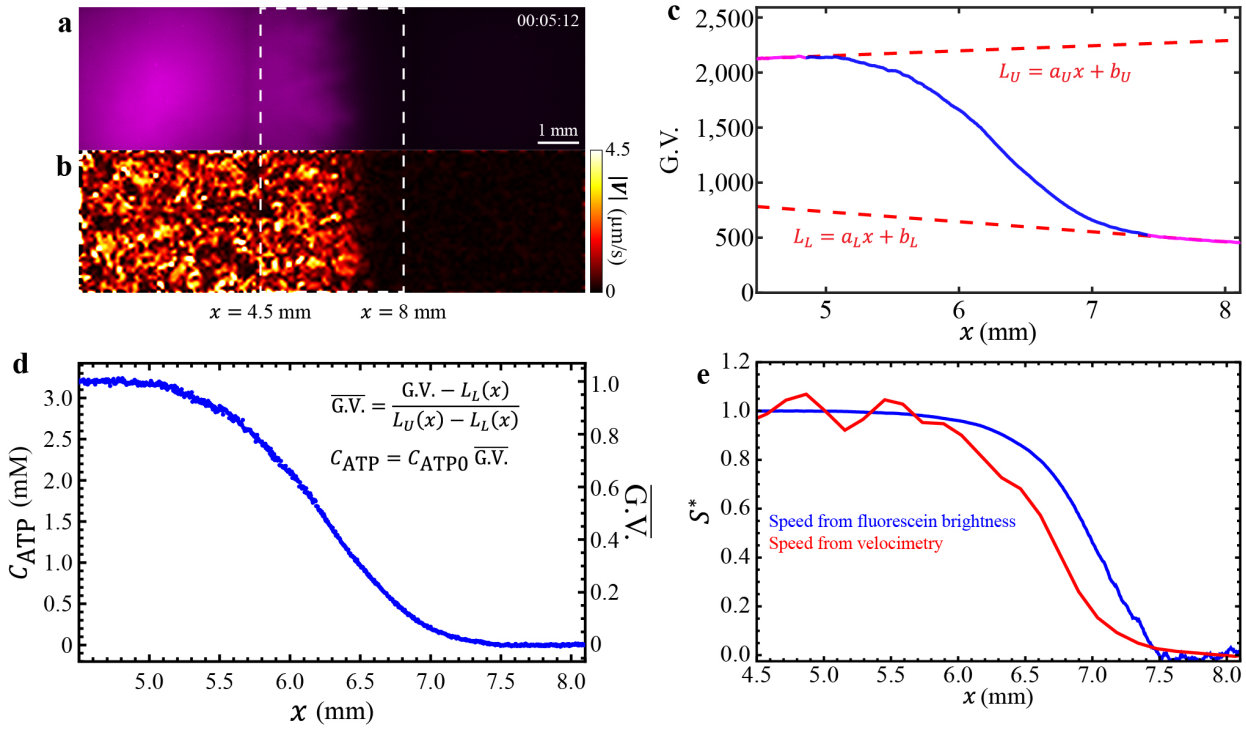

FIG. 52: THE ACTIVE-INACTIVE INTERFACE PROGRESSES MORE SLOWLY THAN EXPECTED FROM DISTRIBUTION OF ATP (a) Micrograph of fluorescein (magenta) in the active-inactive sample with an initial ATP concentration of $\boldsymbol{C}_{\mathrm{ATP0}} = 3.2$ mM. The fluorescein is initially caged and thus does not fluoresce; exposure of the left side of the sample to ultraviolet light both activate the microtubule-kinesin fluid and uncaged the fluorescein, allowing it to fluoresce. The white dashed rectangle is the region of interest in the analysis in Panels c-e. The time stamp represents hour:minute:second. (b) The corresponding map of flow speed of active fluid deduced from tracking the motion of tracers. (c) Profile of gray values of the fluorescein micrograph in Panel a. The profile is normalized with a baseline model[3] that includes an upper baseline determined by a line fitting to the gray value profile in the active bulk (the top-left magenta portion of the profile), $\boldsymbol{L_U} = \boldsymbol{a_U} + \boldsymbol{b_U}$ where $\boldsymbol{a_U} = 46$ mm^{-1} and $\boldsymbol{b_U} = 1{,}920$, and a lower baseline determined by a line fitting to the gray value profile in the inactive bulk (the bottom-right magenta portion of the profile), $\boldsymbol{L_L} = \boldsymbol{a_L} + \boldsymbol{b_L}$ where $\boldsymbol{a_L} = -91$ mm^{-1} and $\boldsymbol{b_L} = 1{,}190$. These two baselines serve as the upper and lower references for profile normalization. (d) The gray values are normalized by the baseline model (right axis). The profile of ATP concentrations is deduced by scaling the normalized profile of gray values by the initial concentrations of ATP, $\boldsymbol{C}_{\mathrm{ATP0}}$ (left axis). (e) The profile of ATP concentrations is converted to the profile of flow speed by the Michaelis-Menten equation (Eq. 4). The speed profile is normalized (blue curve) as in Fig. 1e and the normalized profile is then compared with the profile measured from the velocimetry of tracers (red curve). The profile analyzed from the velocimetry falls behind the profile deduced from fluorescein brightness, which suggests that the melting mechanism of the crosslinked microtubule network slows the progression of the active-inactive interface.

uncaged fluorescein distribution (blue curve), which demonstrates that the active-inactive interface progresses more slowly than expected from ATP distribution, and that the network melting plays a role in the progression of the active-inactive interface and can slow down the progression.

The network melting mechanism is absent in our active-fluid hydrodynamic model; the model assumes that the network can melt almost instantly upon arrival of ATP (with negligible warm-up time from the initial development of activity-driven instability in the extensile **Q** field[2,33]), so we expect that the profile discrepancies observed in the experiment (Fig. 52e) will not exist in our model. To examine the validity of our expectation, we analyze the profiles both directly from flow speed distribution and as calculated on the basis of ATP distribution. In the simulation, we can directly access the ATP distribution (Fig. 53a), which allows us to determine the corresponding ATP concentration profile (Fig. 53c inset). Then we convert the concentration profile to speed profile by the Michaelis-Menten equation (Eq. 4) followed by normalization to extract the normalized speed profile (blue curve in Fig. 53c). To compare this ATP-based profile with the profile from flow speed distribution, we consider the speed map at the same time (Fig. 53b), average the speed distribution vertically to get the speed profile, and normalize the profile to get the

normalized speed profile (red curve in Fig. 53c). The modeling results show that the ATP-based speed profile and the flow speed-based speed profile nearly overlap across the active-inactive interface, which means that, in the simulation, ATP and activity progress at the same pace. This is not consistent with experimental observations that the progression of activity falls behind ATP (Fig. 53e). This mismatch between experiments and model results support the existence of a network melting mechanism—in which the network needs to undergo a melting process before it can become fluidized—which is absent in the model.

4.4 DISCUSSION

The self-mixing process of microtubule-kinesin active fluid with nonuniform activity is driven by active transport at the active-inactive interface. We estimate the contributions of diffusive and convective transport using the Péclet number, Pe. We find that when the active transport is dominated by the diffusion mechanism ($\mathrm{Pe} \lesssim 3$), the active-inactive interface progresses in a diffusion-like manner ($\gamma \approx 1$; Fig. 40). These dynamics are quantitatively captured by a Fick's law-based model that quasi-statically related local activity to the local concentration of ATP by using a previously measured ATP-velocity relation (Fig. 41)[4].

As we raise the Péclet number ($\mathrm{Pe} \gtrsim 3$) by increasing both the local fluid velocity and mixing length scale, we find that the active-inactive interface concomitantly progresses in a more superdiffusion-like manner ($\gamma > 1$; Fig. 45). We observe experimentally that increasing the Péclet number decreases the mixing time of suspended fluorescent dyes (Fig. 47c), which demonstrates that more convective flow mixes the suspended components faster. These results, along with the progression of the active-inactive interfaces, are qualitatively captured by an active-fluid hydrodynamic model (Fig. 49c) that couples active stress-induced fluid flow and transport of ATP molecules (Eqs. 17-20).

Interestingly, while our hydrodynamic model predicts interface progression exponent $\gamma = 2$ for high activity levels (Fig. 49c inset), in our experiments γ appears to plateau at $\gamma \approx 1.7$ (Fig. 45b). Our model may have overestimated γ because the microtubule network in the inactive portion of the sample is crosslinked by immobile kinesin motor dimers that cause it to behave like an elastic gel. When the ATP molecules arrive at the active-inactive interface, they fuel the motor dimers, which fluidizes the network. Crucially, this fluidizing/melting process takes time to develop[2,52]. Thus, for the interface to progress, not only does ATP need to be transported to the inactive fluid region, but the ATP-fueled motors also needs time to melt the gel-like microtubule network into a fluid. Such melting dynamics can delay the progression of

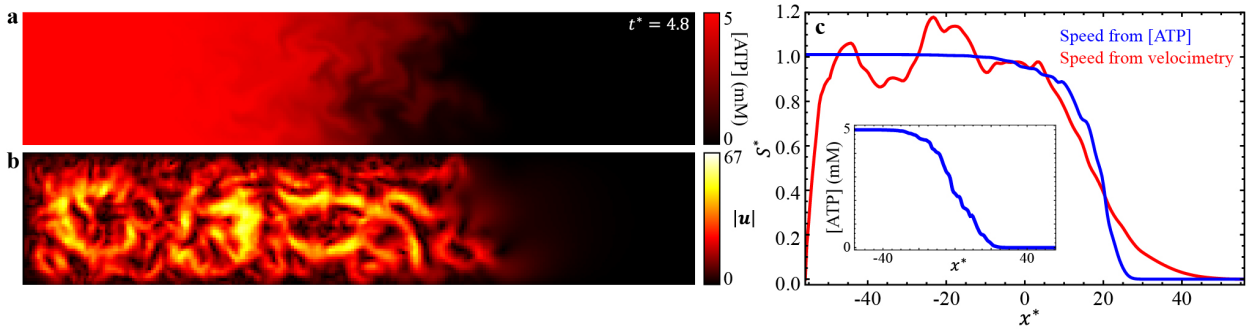

FIG. 53: IN SIMULATIONS OF ACTIVE-INACTIVE FLUID SYSTEMS, PROFILES OF ACTIVE FLUID FLOW AND PROFILES DEDUCED FROM ATP CONCENTRATION OVERLAP (a) Distribution of ATP concentrations in the active fluid simulation (Fig. 12) with with $\boldsymbol{\alpha_0^*} = 25$ and $\boldsymbol{D^*} = 2$ at $\boldsymbol{t^*} = 4.8$. (b) The corresponding distribution of flow speed. Note that the flow speed quickly drops to zero (black) as it approaches the boundaries because of the no-slip boundary condition. (c) The corresponding normalized speed profile analyzed from the distribution of flow speed (red curve) and the normalized speed profile deduced from the distribution of ATP (blue curve) nearly overlap at the active-inactive interface. This suggests that, in the simulation, the active fluid is activated almost immediately after the ATP is transported to its location. Inset: The profile of ATP concentrations in Panel a, averaged vertically.

the active-inactive interface and lower γ. In the simulation, the melting dynamics are absent; the network melts almost instantly as soon as ATP arrives at the inactive fluid, and γ only depends on active transport of ATP. Our studies of a potential network melting mechanism show that the progression of the active-inactive interface falls behind the progression of ATP molecules (Fig. 52e), whereas in the simulation the fronts of both coincide (Fig. 52c). Future research to elucidate the network melting dynamics can involve monitoring dyes, tracers, and microtubules simultaneously to reveal the correlations among ATP dispersion, active fluid flows, and microtubule network structure (melting). The process can be modeled with the active-fluid hydrodynamic model used herein, modified to include ATP-dependent rheological constants and additional relevant dynamic processes to represent the melting process of the gel-like network at the interface.

We also find that the distribution of activity has a significant effect on mixing time. Systems consisting of more, smaller active areas (checkerboard pattern; high uniformity [Fig. 51]) evolve to a homogeneous state faster than systems with the same total active area distributed as one piece (one side active; low uniformity [Fig. 38c]). This is likely because the smaller grid size increases the active-inactive interface area, which allows the active fluid to interact with inactive fluid more efficiently. Interestingly, our active-fluid hydrodynamic model shows that when the grid size is sufficiently small, the mixing times of active and inactive fluids are indistinguishable (Fig. 45b). This may be because the active fluid needs time to warm up from an initial quiescent state before reaching its steady activity state[2]. In experiments, the system has a warm-up time that may have been caused by network melting. Although a network melting mechanism is not included in the model, the simulated active fluid flow takes dimensionless time to rise because the onset of the flows is triggered by the initial activity-driven instability in extensile $\mathbf{Q}$ field, which takes finite dimensionless time to develop (~1 dimensionless time in this case)[2,33]. Thus, in cases where the grid size is sufficiently small, the model shows molecular diffusion completing the mixing before emergence of active fluid flows. We also find that mixing time in an active fluid system is less sensitive to initial distribution of activity than that in an inactive system (Fig. 45b), which suggests that introducing active fluid to a microfluidic system can drastically reduce the impact of the initial condition on mixing efficacy.

This study has limitations. Observations on the mixing of active microtubule-kinesin fluid and inactive microtubule-kinesin fluid may not be generalizable to cases in which active fluid mixes with other types of fluid. Also, we do not characterize the degree of chaos in the system, such as by measuring Lyapunov exponents and topological entropies[32]. Future research can track tracers in 3D and measure how these quantities change in the 3D isotropic active microtubule network at different strengths of active transport (i.e., Lyapunov exponent vs. Péclet number and topological entropy vs. Péclet number).

Another limitation of this study is that our results for interface progression transitioning from diffusion-like to superdiffusion-like (Fig. 45) are based on large length-scale data that we analyze considering the interface as one piece with a specific position coordinate (Fig. 40a). However, the interface is the region where ATP concentration decays from saturation ($> K$; see Eq. 4) to 0, and according to previous studies[5,43] tracer motion in this region should transition from superdiffusion-like to diffusion-like behaviors. Directly measuring the mean squared displacement of tracers across the active-inactive interface can elucidate the transition of the interface progression behaviors on the microscopic scale. Such measurements are not practical in our system because the active-inactive interface changes position and width with time (Fig. 38e); tracers initially in the diffusive zone can later be in the superdiffusive zone as the interface passes

by, and it will be difficult to distinguish between the diffusive and superdiffusive data. Future research to elucidate tracer behaviors at active-inactive interfaces can utilize fluid that is only active when it is exposed to light[39,40] to provide a stable activity gradient and thus obtain a reliable mean squared displacement of tracers at different parts of the interface.

Overall, this work demonstrates that mixing in nonuniform active fluid systems is fundamentally different from mixing in uniform active fluids. Mixing in nonuniform active fluid systems involves complex interplays among spatial distribution of ATP, active transport of ATP (which can be either diffusion-like or convection-like, depending on Péclet number), and a fluid-gel transition of the microtubule network at the interface[2]. This work paves the path to the design of microfluidic devices that use active fluid to promote or optimize the micromixing process8 to enhance production efficiency in chemical and biological engineering and pharmaceutical development[7]. The results may also provide insight into intracellular mixing processes, because the cytoplasmic streaming that supports organelles within cells is powered by cytoskeletal filaments and motor proteins that function similarly to microtubule-kinesin active fluid[67].

4.5 METHODS

4.5.1 POLYMERIZE MICROTUBULES Microtubules constitute the underlying network of microtubule-kinesin active fluid. Microtubules are polymerized from bovine brain α- and β-tubulin dimers purified by three cycles of polymerization and depolymerization[68,69]. The microtubules (8 mg/mL) are then stabilized with 600 μM guanosine-5′[(α,β)-methyleno]triphosphate (GMPCPP, Jena Biosciences, NU-4056) and 1 mM dithiothreitol (DTT, Fisher Scientific, AC165680050) in microtubule buffer (80 mM PIPES, 2 mM MgCl2, 1 mM ethylene glycol-bis(β-aminoethyl ether)-N,N,N’,N’-tetraacetic acid, pH 6.8) and polymerized by a 30-minute incubation at 37 °C and a subsequent 6-hour annealing at room temperature before being snap frozen with liquid nitrogen and stored at -80 °C. The microtubules are then labeled with Alexa Fluor 647 (excitation: 650 nm; emission: 671 nm; Invitrogen, A-20006) and mixed with unlabeled microtubules at 3% labeling fraction during polymerization to image microtubules for non-fluorescein experiments (Fig. 38,40&45). For fluorescein experiments, the microtubules are unlabeled (Fig. 47&51).

4.5.2 DIMERIZE KINESIN MOTOR PROTEINS Kinesin motor proteins power the extensile motion of sliding microtubule bundle pairs in active fluid by forming a dimer and walking on adjacent antiparallel microtubules to force them in opposite directions (Fig. 38a)[5,70]. We express kinesin in the *Escherichia coli* derivative Rosetta 2 (DE3) pLysS cells (Novagen, 71403), which we transform with DNA plasmids from *Drosophila melanogaster* kinesin (DMK) genes[71]. For most experiments in this paper, we use processive motors that include DMK’s first 401 N-terminal DNA codons (K401)[72]. To explore the effect of low mean speed of active fluid bulk on the interface progression exponent γ, we mix in fractions of nonprocessive motors whose plasmid includes DMK’s first 365 codons (K365, Fig. 45 inset left)[4,10,73]. The kinesin motors are tagged with 6 histidines enabling purification via immobilized metal ion affinity chromatography with gravity nickel columns (GE Healthcare, 11003399). To slide adjacent microtubule bundle pairs, kinesin motors need to be dimerized, so the kinesin motors are tagged with a biotin carboxyl carrier protein at their N terminals, which allow the kinesins to be bound with biotin molecules (Alfa Aesar, A14207)[5,68]. To dimerize the kinesin, we mix either 1.5 μM K401 processive motors or 5.4 μM K365 nonprocessive motors with 1.8 μM streptavidin (Invitrogen, S-888) and 120 μM DTT in microtubule buffer, incubate them for 30 minutes at 4 °C, and then snap freeze them with liquid nitrogen and store them at -80 °C.

4.5.3 PREPARE MICROTUBULE-KINESIN ACTIVE FLUID To prepare the active fluid, we mix 1.3 mg/mL

microtubules with 120 nM kinesin motor dimers and 0.8% polyethylene glycol (Sigma 81300), which acts as a depleting agent to bundle microtubules (Fig. 38a)[5]. Kinesin steps from the minus to the plus end of microtubules by hydrolyzing ATP and producing adenosine diphosphate[60]. To control the initial spatial distribution of ATP and thus the activity distribution of active fluid, we use 0.5 to 8 mM caged ATP (adenosine 5'-triphosphate, P3-(1-(4,5-dimethoxy-2-nitrophenyl)ethyl) ester, disodium salt and DMNPE-caged ATP, Fisher Scientific, A1049), which is ATP whose terminal phosphate is esterified with a blocking group rendering it nonhydrolyzable by kinesin motors unless exposed to 360-nm UV light. Exposure to UV light removes the blocking group (Fig. 38b) and allows the kinesin motors to hydrolyze the ATP into ADP and activate the active fluid[1,8]. The ATP hydrolyzation decreases ATP concentrations, which slow down the kinesin stepping rate and thus decrease active fluid flow speed[4,5,43,60,61]. To maintain ATP concentrations so as to stabilize the activity level of the active fluid bulk over the course of our experiments, we include 2.8% v/v pyruvate kinase/lactate dehydrogenase (Sigma, P-0294), which converts ADP back to ATP[5,74]. To feed the pyruvate kinase enzyme, we add 26 mM phosphenol pyruvate (BeanTown Chemical, 129745). We image the active fluid samples with fluorescent microscopy for 1 to 16 hours, which can bleach the fluorescent dyes and thus decrease the

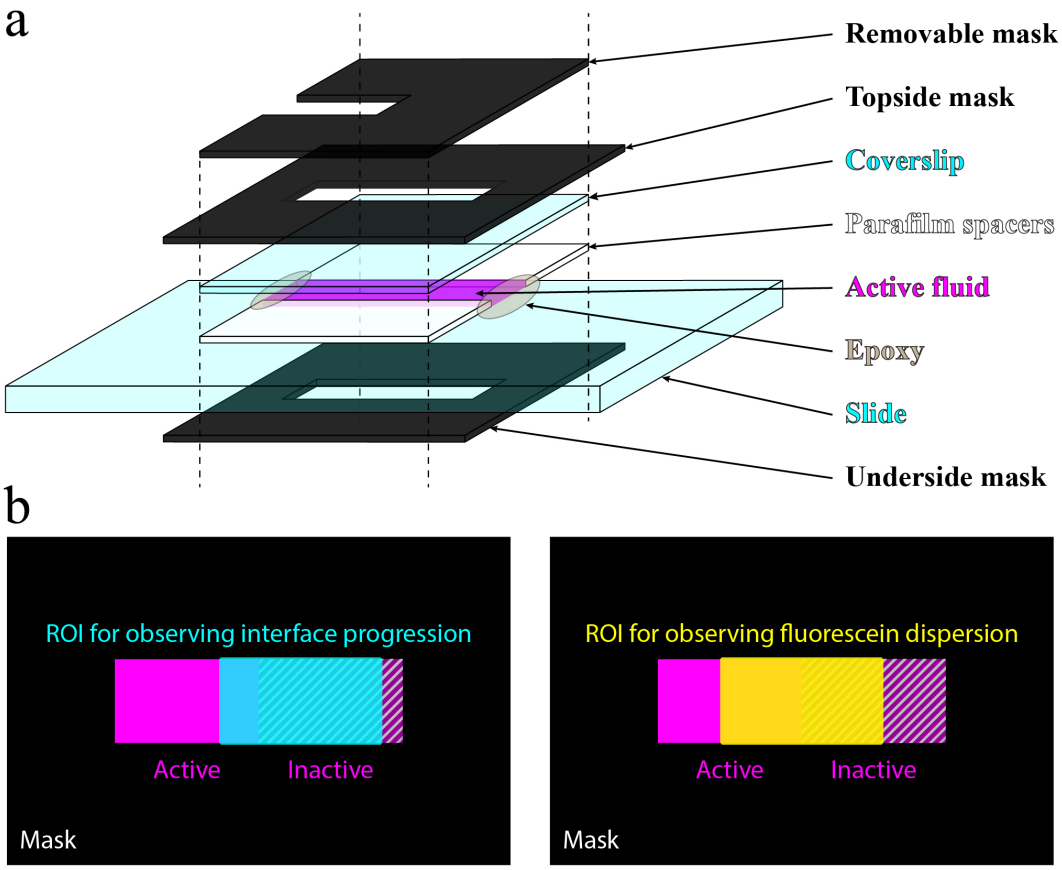

FIG. 54: REMOVABLE MASK ACTIVATES ONE SIDE OF THE SAMPLE (a) Active fluid is loaded into a glass flow cell consisting of a polyacrylamide-coated glass slide and coverslip with Parafilm as a spacer and sealed with epoxy. To prepare the active-inactive fluid system, we block one side of the sample (right half) with a removable mask. To prevent UV light from being scattered to the masked region by the epoxy and Parafilm, which can cause unwanted fluid activation in the masked region, we further block the rest of the sample, including epoxy and Parafilm, with 2 masks (one topside and one underside). After the UV exposure, we remove the masks to image the sample with fluorescent microscopy. (b) The sample is 20 mm long, which is wider than the field of view in our microscope even using a 4× objective, so we image 3 to 4 adjacent frames along the flow cell and stitch these frames into one large image. For the experiments monitoring active-inactive fluid interface progression (left), we select the region of interest (ROI) as one quarter of active area and most of the inactive area (cyan rectangle) to observe the progression of the interface (Fig. 38,40&45). For the experiments monitoring the dispersion of fluorescein (right), we select the ROI as half of the active and half of the inactive regions (yellow rectangle) to observe how one-sided dyes disperse to the rest of the sample.

image quality over the course of experiments. To reduce the photobleaching effect, we include 2 mM trolox (Sigma, 238813) and oxygen-scavenging enzymes consisting of 0.038 mg/mL catalase (Sigma, C40) and 0.22 mg/mL glucose oxidase (Sigma, G2133) and feed the enzymes with 3.3 mg/mL glucose (Sigma, G7528)[5]. To stabilize proteins in our active fluid system, we add 5.5 mM DTT. To track the fluid flows, we dope the active fluid with 0.0016% v/v fluorescent tracer particles (Alexa 488-labeled [excitation: 499 nm; emission: 520 nm] 3-µm polystyrene microspheres, Polyscience, 18861). To test how active fluid can mix suspended components, we introduce 0.5 to 6 µM caged, UV-activated fluorescent dyes (fluorescein bis-(5-carboxymethoxy-2-nitrobenzyl) ether, dipotassium salt; CMNB-caged fluorescein, ThermoFisher Scientific, F7103), which are colorless and nonfluorescent until exposed to 360-nm UV light[1]. The dye concentration is chosen to maintain a sufficient signal-to-noise ratio while avoiding brightness saturation in micrographs. Upon UV exposure, the fluorescein is uncaged and thus becomes fluorescent and can be observed with fluorescent microscopy. Because the fluorescent spectrum of the fluorescein overlaps with our Alexa 488 tracers, for our experiments with caged fluorescein (Fig. 47) we replace the tracers with Flash Red-labeled 2-µm polystyrene microspheres (Bangs Laboratories, FSFR005) and use unlabeled microtubules (0% labeling fraction) to prevent fluorescent interference from microtubules while imaging tracers.

4.5.4 PREPARE ACTIVE-INACTIVE FLUID SYSTEMS

To prepare the active-inactive fluid system, we load the inactive microtubule-kinesin fluid with caged ATP to a polyacrylamide-coated glass flow cell (20 × 4 × 0.1 mm^3) with Parafilm (Cole-Parmer, EW-06720-40) as a spacer sandwiched between a cover slip (VWR, 48366-227) and slide (VWR, 75799-268)36 and seal the channel with epoxy (Bob Smith Industries, BSI-201). Then we mask one side of the sample with a removable mask of opaque black tape (McMaster-Carr, 76455A21) attached to a transparent plastic sheet (Fig. 54) and shine UV light on the sample for 5 minutes before removing the

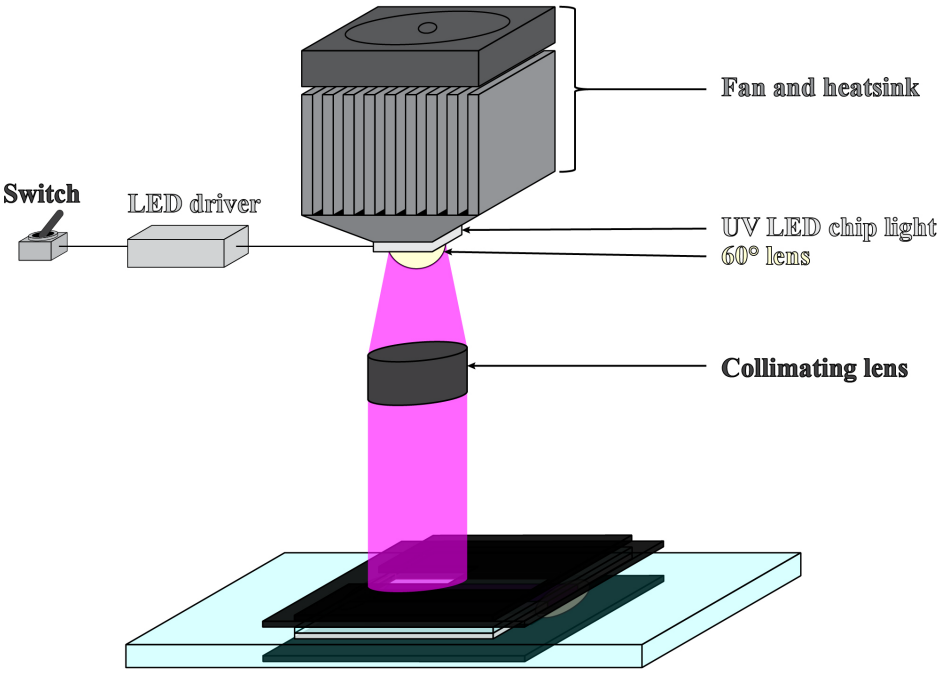

FIG. 55: SETUP TO APPLY UV LIGHT TO THE MASKED SAMPLE (FIG. 17)[1]. UV light is emitted with a UV LED chip (Amazon, B01DBZK2LM) powered by an LED driver (McMaster, 4305N124) and cooled with a fan-powered heatsink (Amazon, B01D1LD68C). To ensure that the light exposure was consistent across the sample, we parallelize the emitted UV light beams with a 60° lens (part of the heatsink) and a collimating lens (part of the microscope, Nikon, MEA54000).

mask (Fig. 55). In the unmasked region, the UV light releases the ATP from the blocking group and activates the fluid by allowing the ATP to fuel the local kinesin motors; in the masked region, the fluid remains quiescent (Fig. 38c)[1]. To explore how the progression exponent changes with active fluid bulk mean speed, we accelerate fluid flows by making the flow cell taller by stacking layers of Parafilm to decrease hydrodynamic resistance (Fig. 45 inset right)[4,6]. To explore how the spatial nonuniformity of activity influences the mixing efficacy of the active-inactive fluid system, we mask the sample with checkerboard-patterned masks (FineLine Imaging, Fig. 51a).

4.5.5 IMAGE SAMPLES WITH DUAL FLUORESCENT CHANNELS We image the active fluids with epifluorescent microscopy (Ti2-E Inverted Microscope, Nikon, MEA54000) with the commercial image acquisition software Nikon NIS Elements version 5.11.03. To capture a wide area of the sample (20 × 4 mm2), we use a 4× objective lens (CFI Plan Apo Lambda 4× Obj, Nikon, MRD00045, NA 0.2) to image 3 to 4 adjacent frames rapidly (≲3 s) and stitch the micrographs into one large image for flow and dye dispersion analyses.

Performing these analyses requires monitoring at least two components in two fluorescent channels in each sample; for example, the dye dispersion experiments (Fig. 47) requires analyzing fluorescent dyes (excitation: 490 nm; emission: 525nm) and Flash Red-labeled tracers (excitation: 660 nm; emission: 690 nm) simultaneously. This could have been accomplished by programming a microscope to rapidly switch back and forth between filter cubes, but this would have quickly worn down the turret motor and the time required to switch filter cubes (≳4 s) and move the stage to capture adjacent images and stitch them (~3 s) would have made the minimum time interval between frames ≳10 s, which would have prevented us from tracking high-density tracers (1000 mm^{-3} with a mean separation of 5 μm in a 0.1-mm-thick sample) whose speeds are 1 to 10 μm/s, even with a predictive Lagrangian tracking

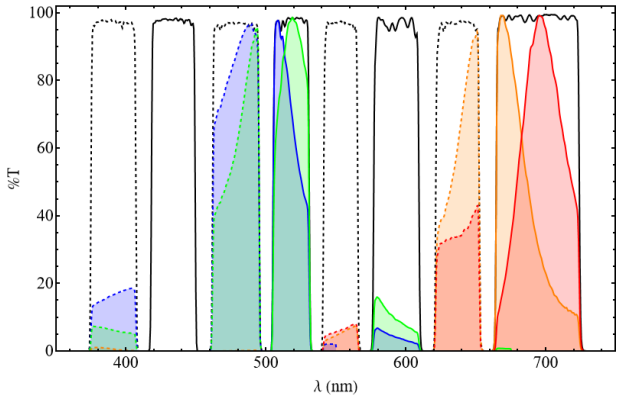

FIG. 56: MULTIBANDPASS FILTER CUBE SPECTRUM Excitation (black dashed) and emission (black) spectra of our multiband pass filter cube with transmittance %$\boldsymbol{T}$ and wavelength $\boldsymbol{\lambda}$ (Multi LED set, Chroma, 89402–ET). The filter cube is compatible with the fluorescent spectra of fluorescein (excitation: 490 nm [green dashed]; emission: 525 nm [green]), Alexa 488 (excitation: 499 nm [blue dashed]; emission: 520 nm [blue]), Alexa 647 (excitation: 650 nm [orange dashed]; emission: 671 nm [orange]), and Flash Red (excitation: 660 nm [red dashed]; emission: 690 nm [red]). Data source: www.chroma.com.

algorithm[75]. To overcome this technical challenge in imaging our samples, we establish a dual-channel imaging system that consisted of a multiband pass filter cube (Multi LED set, Chroma, 89402–ET) and voltage trigger (Nikon) placed between the light source (pE-300ultra, CoolLED, BU0080) and camera (Andor Zyla, Nikon, ZYLA5.5-USB3). Instead of changing filter cubes, the multiband pass filter cube allows us to switch between multiple emission and excitation bands by switching between channels with the same filter cube. We alternatively activate the blue (401–500 nm) and red (500–700 nm) LEDs to excite and observe the fluorescent dyes and tracers almost simultaneously. The LED light source communicates directly with the camera via voltage triggering to coordinate LED activation time and bypass computer control to further boost the light switching rate. This technique shortens our channel switching time to 3 to 5 μs; thus the time interval between image acquisitions of different fluorescent channels is only limited by exposure times of each channel. This setup allows us to image two fluorescent channels almost simultaneously (within milliseconds) and thus enables us to monitor two fluorescent components side-by-side, such as microtubules and tracers (Fig. 38c), caged

fluorescent dyes and tracers (Fig. 47c), and caged fluorescent dyes and microtubules.

4.5.6 ANALYZE POSITIONS OF ACTIVE-INACTIVE FLUID INTERFACES We characterize the mixing kinematics of active and inactive fluids by analyzing the interface progression exponents γ and coefficients P_{I} (FIG. 40,41&45.). These analyses require identification of the interface positions. We determine the interface positions by first tracking tracers in sequential images with the Lagrangian tracking algorithm[75], which reveals the tracers' trajectories $r_i(t)$ and corresponding instantaneous velocities $v_i \equiv d\mathbf{r}_i/dt$. Then we analyze the speed profile of tracers by binning the tracer speed $|v_i|$ across the width of the channel $S(x_j) \equiv \langle |v_i| \rangle_{i \in \mathrm{bin}\ j}$ where x_j is the horizontal x coordinate of the jth bin and the $\langle |v_i| \rangle_{i \in \mathrm{bin}\ j}$ represents the average speed of tracers in the j th bin. Then we normalize the speed profile by rescaling the speed profile to be 1 in the active zone and 0 in the inactive zone: $S^*(x) \equiv [S(x) - s_{\mathrm{in}}]/[s_{\mathrm{a}} - s_{\mathrm{in}}]$, where s_{a} is the average of speed profiles in the active zone and s_{in} is the average of speed profiles in the inactive zone (Fig. 1e). Then we define the width of the active-inactive fluid interface as where the normalized speed profile is between 0.2 and 0.8 (dashed lines in Fig. 1e inset) and the position of the interface x_{I} as where the normalized speed profile is 0.5 (solid line). The interface position is then analyzed for each frame, which allows us to determine the interface displacement $\Delta x \equiv x_{\mathrm{I}}(\Delta t) - x_{\mathrm{I}}(0)$ vs. time t (Fig. 3a inset) and the squared interface displacement Δx^2 vs. time t (Fig. 3a). To determine the interface progression exponent, γ, we fit $\log(\Delta x^2)$ vs. $\log(t)$ data to $\log(\Delta x^2) = \log(2P_{\mathrm{I}}) + \gamma \log(t)$, with P_{I} and γ as fitting parameters (Fig. 40b&45). To determine the interface progression coefficient, P_{I}, we assume $\gamma = 1$ and fit Δx^2 vs. t data to $\Delta x^2 = 2P_{\mathrm{I}}t$ with P_{I} as the fitting parameter (Fig. 40c,41c&d).

4.5.7 GENERATE FLOW SPEED MAP OF ACTIVE-INACTIVE FLUID SYSTEM To visualize the activity distribution in our active-inactive fluid system, we analyze the distribution of flow speed to generate flow speed maps (Fig. 38d). To complete this analysis, we analyze the flow velocities of fluids by analyzing the tracer motions in sequential images with a particle image velocimetry algorithm[76], which reveals the flow velocity field $\mathbf{V}(\mathbf{r}, t)$ and associated distribution of flow speed $|\mathbf{V}(\mathbf{r}, t)|$ in each frame. A heat color bar (Fig. 38d) is used to plot the speed distributions into color maps to reveal the evolution of speed distribution from the pre-activated state (black) to the homogeneously activated state (red/yellow).

4.5.8 NUMERICALLY SOLVE THE FICK'S LAW EQUATIONS We model diffusion-dominated active-inactive fluid mixing with the Fick's law equation, which requires us to solve for the concentration of ATP (Eq. 1). To simplify the modeling, we consider a one-dimensional active fluid system confined in a segment $x = 0 - L$ where $L = 20$ mm, the length of our experimental sample. Given that ATP is confined in the segment, we apply no-flux boundary conditions to the ATP concentrations (Eq. 2). In the experiment, we expose the left side of the sample to UV light to release ATP, so in our model the ATP concentration has a step function as its initial condition (Eq. 3). With the initial condition and boundary conditions, we solve the Fick's law equation to determine the spatial and temporal distribution of ATP. We used Mathematica 13.0 to numerically solve this differential equation with the NDSolveValue function by feeding Eqs. 1–3 into the function followed by specifying the spatial and temporal domains, which outputs the numerical solution of ATP concentration $C(x, t)$ and allows us to determine the evolution of ATP distribution (Fig. 41a). Then we convert the ATP distribution to mean speed distribution of active fluid by the Michaelis-Menten kinetics (Eq. 4; Fig. 41b inset), which shows a uniform mean speed in the left side of the sample followed by gradual activation of the right side of the system until a uniform state is reached (Fig. 41b). Then we define the position of the active-inactive fluid interface Δx as where the mean speed decays to

a half (Fig. 41c inset), which allows us to plot the squared interface displacement as a function of time (Fig. 41c). The plot in log-log axes exhibits a line with a unit slope, which suggests that the squared interface displacement is linearly proportional to time. By assuming this linear relation, we determine the interface progression coefficient P_{I} by fitting $\Delta x^2 = 2P_{\mathrm{I}}\, t$ with P_{I} as the fitting parameter. Finally, we repeat the calculation with different initial ATP concentrations in the left side of the system, C_0, and plot the interface progression coefficient, P_{I}, as a function of C_0. This plot allows us to compare the simulation results with the experimental measurements to examine the validity of our Fick's law-based model (Fig. 41d).

Numerically solve the active nematohydrodynamic equations. To model the mixing of active and inactive fluids, we adopt Varghese et al.'s active fluid model to include the dynamics of the ATP concentration field[30]. Our model has four main components: (1) the kinetic equation describing the kinematics of self-elongating rods that flow and orient with the solvent as well as diffuse translationally and rotationally (Eq. 17), (2) the Stokes equation describing how the solvent is driven by the active stress exerted by the self-elongating rods (Eq. 18), (3) the relation between α and ATP that describes how the active stress depends on the nonuniform ATP distribution (Eq. 19), and (4) the continuity equation of ATP transport that describes how ATP diffuses as well as flows with the solvent (Eq. 20). We numerically solve these coupled equations with appropriate boundary and initial conditions using the finite element method by first converting them to their weak forms and then implementing them symbolically in COMSOL Multiphysics™[66]. We show below the weak form of the convection-diffusion equation governing the evolution of ATP concentration field:

$$\int_{\Gamma} dx^*\, dy^*\, \tilde{T}\frac{\partial C}{\partial t^*} = -\int_{\Gamma} dx^*\, dy^*\, D^*\left(\frac{\partial \tilde{T}}{\partial x^*}\frac{\partial C}{\partial x^*} + \frac{\partial \tilde{T}}{\partial y^*}\frac{\partial C}{\partial y^*}\right) - \int_{\Gamma} dx^*\, dy^*\, \tilde{T}\left(u_x^*\frac{\partial C}{\partial x^*} + u_y^*\frac{\partial C}{\partial y^*}\right), \quad 22$$

where $\tilde{T}(x^*, y^*)$ is the test function and Γ represents the system spatial domain. After solving these equations, we determine the spatial and temporal distributions of ATP concentrations and active fluid flow speeds (Fig. 49a), which allows us to explore how the activity level of active fluid and molecular diffusion of ATP influences the mixing process of ATP in nonuniform active fluid systems (Fig. 49b&c).

4.5.9 SIMULATE DISPERSION OF CHECKERBOARD-PATTERNED ATP We apply our established hydrodynamic model to simulate how the initially checkerboard-patterned ATP disperses in active fluid and inactive fluid (Fig. 50). In this exploration, we use the same equations for $\mathbf{Q}$, $\mathbf{u}$ and C (Eqs. 17-20), along with their initial and boundary conditions, except that C is initialized in a checkerboard pattern in a 45 × 45 simulation box. We use two different checkerboard patterns for different trials. One has the xy-axis origin in the center of a grid square:

$$C(x, y, t = 0) = C_0 \bmod \begin{Bmatrix} \mathrm{mod}\left[\mathrm{ceil}\left(\frac{x^*}{a^*} - 0.5\right), 2\right] \\ + \mathrm{mod}\left[\mathrm{ceil}\left(\frac{y^*}{a^*} - 0.5\right), 2\right] + 1{,}2 \end{Bmatrix}, \quad 23$$

where $C_0 = 5$ mM is the initial ATP concentration, a^* represents the dimensionless grid size of the checkerboard pattern, $\mathrm{mod}(i, j)$ represents the remainder of i divided by j, and $\mathrm{ceil}(x)$ represents the rounding of x toward positive infinity (e.g., Fig. 50a with $a^* = 22$). The other checkerboard pattern has the xy-axis origin at a vertex of the grid:

$$C(x, y, t = 0) = C_0 \bmod \left\{ \begin{matrix} \bmod\left[\mathrm{ceil}\left(\frac{x^*}{a^*}\right), 2\right] \\ + \bmod\left[\mathrm{ceil}\left(\frac{y^*}{a^*}\right), 2\right] + 1{,}2 \end{matrix} \right\}. \quad 24$$

The simulation is performed for the dimensionless grid size a^* ranging from 2 to 22 for both active ($a^* = 25$) and inactive ($a^* = 0$) systems (Fig. 50a). We analyze the corresponding mixing time (averaged over 2 trials) as a function of a^* (Fig. 50b) to reveal how the a^*-dependence of mixing times differs in active and inactive fluid systems.

4.6 ACKNOWLEDGEMENTS T.E.B. and K.-T.W. would like to thank Drs. Seth Fraden and Aparna Baskaran of Brandeis University for insightful discussions on experiments and modeling in this manuscript. T.E.B. and K.-T.W. would also like to thank Dr. John Berezney of Brandeis University for assisting us in developing the UV light setup (Fig. 18). We thank Ellie Lin from Lin Life Science for her assistance on editing the manuscript to enhance its flow and readability. T.E.B., E.H.T., and K.-T.W. acknowledge support from the National Science Foundation (NSF-CBET-2045621). This research is performed with computational resources supported by the Academic & Research Computing Group at Worcester Polytechnic Institute. We acknowledge the Brandeis Materials Research Science and Engineering Center (NSF-MRSEC-DMR-2011846) for use of the Biological Materials Facility. Parts of the work by C.-C. C. are funded and supported through the National Science and Technology Council (NSTC), Taiwan, under grant No. 111-2221-E-006-102-MY3, and through the 2022 Early Career Award from the College of Engineering and the Headquarters of University Advancement at National Cheng Kung University, which is sponsored by the Ministry of Education, Taiwan. M.M.N. is supported by the U.S. Department of Energy, Office of Science, Office of Basic Energy Sciences under Award No. DE-SC0022280.

4.7 AUTHOR CONTRIBUTIONS STATEMENT T.E.B., M.E.V., and K.-T.W. performed the research and designed the experiments; M.E.V. initiated the experiments; T.E.B., M.E.V., E.H.T. and J.H.D. collected experimental data; T.E.B., M.E.V., and K.-T.W. organized and analyzed the data; T.E.B., E.H.T., C.-C.C., M.M.N. and K.-T.W. established the continuum simulation platform on modeling nonuniform active fluid systems; T.E.B. and K.-T.W. wrote the manuscript; and K.-T.W. supervised the research. All authors reviewed the manuscript.

4.8 REFERENCES

1 Berezney, J., Goode, B. L., Fraden, S. & Dogic, Z. Extensile to contractile transition in active microtubule-actin composites generates layered asters with programmable lifetimes. *Proc Natl Acad Sci U S A* **119** (2022). https://doi.org:10.1073/pnas.2115895119

2 Najma, B. *et al.* Competing instabilities reveal how to rationally design and control active crosslinked gels. *Nature Communications* **13**, 6465 (2022). https://doi.org:10.1038/s41467-022-34089-9

3 Analysis of Thermal Melting Curves. *Oligonucleotides* **13**, 515-537 (2003). https://doi.org:10.1089/154545703322860825

4 Bate, T. E., Jarvis, E. J., Varney, M. E. & Wu, K. T. Collective dynamics of microtubule-based 3D active fluids from single microtubules. *Soft Matter* **15**, 5006-5016 (2019). https://doi.org:10.1039/c9sm00123a

5 Sanchez, T., Chen, D. T., DeCamp, S. J., Heymann, M. & Dogic, Z. Spontaneous motion in hierarchically assembled active matter. *Nature* **491**, 431-434 (2012). https://doi.org:10.1038/nature11591

6 Wu, K. T. *et al.* Transition from turbulent to coherent flows in confined three-dimensional active fluids. *Science* **355** (2017). https://doi.org:10.1126/science.aal1979

7 Jeong, G. S., Chung, S., Kim, C.-B. & Lee, S.-H. Applications of micromixing technology. *Analyst* **135**, 460-473 (2010). https://doi.org:10.1039/B921430E

8 McCray, J. A., Herbette, L., Kihara, T. & Trentham, D. R. A new approach to time-resolved studies of ATP-requiring biological systems; laser flash photolysis of caged ATP. *Proceedings of the National Academy of Sciences* **77**, 7237-7241 (1980). https://doi.org:10.1073/pnas.77.12.7237
9 Haswell, S. J. *et al.* The application of micro reactors to synthetic chemistry. *Chemical Communications*, 391-398 (2001). https://doi.org:10.1039/B008496O
10 Chandrakar, P. *et al.* Engineering stability, longevity, and miscibility of microtubule-based active fluids. *Soft Matter* **18**, 1825-1835 (2022). https://doi.org:10.1039/d1sm01289d
11 Hadd, A. G., Raymond, D. E., Halliwell, J. W., Jacobson, S. C. & Ramsey, J. M. Microchip Device for Performing Enzyme Assays. *Analytical Chemistry* **69**, 3407-3412 (1997). https://doi.org:10.1021/ac970192p
12 Kakuta, M., Jayawickrama, D. A., Wolters, A. M., Manz, A. & Sweedler, J. V. Micromixer-Based Time-Resolved NMR: Applications to Ubiquitin Protein Conformation. *Analytical Chemistry* **75**, 956-960 (2003). https://doi.org:10.1021/ac026076q
13 Ottino, J. M. Mixing, Chaotic Advection, and Turbulence. *Annual Review of Fluid Mechanics* **22**, 207-254 (1990). https://doi.org:10.1146/annurev.fl.22.010190.001231
14 Fan, Y., Wu, K.-T., Aghvami, S. A., Fraden, S. & Breuer, K. S. Effects of confinement on the dynamics and correlation scales in kinesin-microtubule active fluids. *Physical Review E* **104**, 034601 (2021). https://doi.org:10.1103/PhysRevE.104.034601
15 Suzuki, H., Chih-Ming, H. & Kasagi, N. A chaotic mixer for magnetic bead-based micro cell sorter. *Journal of Microelectromechanical Systems* **13**, 779-790 (2004). https://doi.org:10.1109/JMEMS.2004.835775
16 Liu, R. H., Yang, J., Pindera, M. Z., Athavale, M. & Grodzinski, P. Bubble-induced acoustic micromixing. *Lab on a Chip* **2**, 151-157 (2002). https://doi.org:10.1039/B201952C
17 Ober, T. J., Foresti, D. & Lewis, J. A. Active mixing of complex fluids at the microscale. *Proc Natl Acad Sci U S A* **112**, 12293-12298 (2015). https://doi.org:10.1073/pnas.1509224112
18 Ramaswamy, S. Active fluids. *Nature Reviews Physics* **1**, 640-642 (2019). https://doi.org:10.1038/s42254-019-0120-9
19 Marchetti, M. C. *et al.* Hydrodynamics of soft active matter. *Reviews of Modern Physics* **85**, 1143-1189 (2013). https://doi.org:10.1103/RevModPhys.85.1143
20 Needleman, D. & Dogic, Z. Active matter at the interface between materials science and cell biology. *Nature Reviews Materials* **2** (2017). https://doi.org:10.1038/natrevmats.2017.48
21 Sokolov, A., Apodaca, M. M., Grzybowski, B. A. & Aranson, I. S. Swimming bacteria power microscopic gears. *Proc Natl Acad Sci U S A* **107**, 969-974 (2010). https://doi.org:10.1073/pnas.0913015107
22 Lushi, E., Wioland, H. & Goldstein, R. E. Fluid flows created by swimming bacteria drive self-organization in confined suspensions. *Proceedings of the National Academy of Sciences* **111**, 9733-9738 (2014). https://doi.org:doi:10.1073/pnas.1405698111
23 Palacci, J., Sacanna, S., Steinberg, A. P., Pine, D. J. & Chaikin, P. M. Living Crystals of Light-Activated Colloidal Surfers. *Science* **339**, 936-940 (2013). https://doi.org:10.1126/science.1230020
24 Gompper, G. *et al.* The 2020 motile active matter roadmap. *Journal of Physics: Condensed Matter* **32**, 193001 (2020). https://doi.org:10.1088/1361-648x/ab6348
25 Reinken, H. *et al.* Organizing bacterial vortex lattices by periodic obstacle arrays. *Communications Physics* **3**, 76 (2020). https://doi.org:10.1038/s42005-020-0337-z
26 Chen, Y. C., Jolicoeur, B., Chueh, C. C. & Wu, K. T. Flow coupling between active and passive fluids across water-oil interfaces. *Sci Rep* **11**, 13965 (2021). https://doi.org:10.1038/s41598-021-93310-9
27 Thampi, S. P. & Yeomans, J. M. Active turbulence in active nematics. *The European Physical Journal Special Topics* **225**, 651-662 (2016). https://doi.org:10.1140/epjst/e2015-50324-3
28 Wensink, H. H. *et al.* Meso-scale turbulence in living fluids. *Proceedings of the National Academy of Sciences* **109**, 14308-14313 (2012). https://doi.org:10.1073/pnas.1202032109
29 Doostmohammadi, A., Shendruk, T. N., Thijssen, K. & Yeomans, J. M. Onset of meso-scale turbulence in active nematics. *Nature Communications* **8**, 15326 (2017). https://doi.org:10.1038/ncomms15326
30 Alert, R., Joanny, J.-F. & Casademunt, J. Universal scaling of active nematic turbulence. *Nature Physics* **16**, 682-688 (2020). https://doi.org:10.1038/s41567-020-0854-4
31 Qi, K., Westphal, E., Gompper, G. & Winkler, R. G. Emergence of active turbulence in microswimmer suspensions due to active hydrodynamic stress and volume exclusion. *Communications Physics* **5**, 49 (2022). https://doi.org:10.1038/s42005-022-00820-7

32 Tan, A. J. *et al.* Topological chaos in active nematics. *Nature Physics* **15**, 1033-1039 (2019). https://doi.org:10.1038/s41567-019-0600-y
33 Saintillan, D. & Shelley, M. J. Instabilities and pattern formation in active particle suspensions: kinetic theory and continuum simulations. *Phys Rev Lett* **100**, 178103 (2008). https://doi.org:10.1103/PhysRevLett.100.178103
34 Kim, M. J. & Breuer, K. S. Enhanced diffusion due to motile bacteria. *Physics of Fluids* **16**, L78-L81 (2004). https://doi.org:10.1063/1.1787527
35 Del Junco, C., Estevez-Torres, A. & Maitra, A. Front speed and pattern selection of a propagating chemical front in an active fluid. *Phys Rev E* **105**, 014602 (2022). https://doi.org:10.1103/PhysRevE.105.014602
36 Vyborna, Y., Galas, J. C. & Estevez-Torres, A. DNA-Controlled Spatiotemporal Patterning of a Cytoskeletal Active Gel. *J Am Chem Soc* **143**, 20022-20026 (2021). https://doi.org:10.1021/jacs.1c06730
37 Wysocki, A., Winkler, R. G. & Gompper, G. Propagating interfaces in mixtures of active and passive Brownian particles. *New Journal of Physics* **18** (2016). https://doi.org:10.1088/1367-2630/aa529d
38 Blow, M. L., Thampi, S. P. & Yeomans, J. M. Biphasic, lyotropic, active nematics. *Phys Rev Lett* **113**, 248303 (2014). https://doi.org:10.1103/PhysRevLett.113.248303
39 Ross, T. D. *et al.* Controlling organization and forces in active matter through optically defined boundaries. *Nature* **572**, 224-229 (2019). https://doi.org:10.1038/s41586-019-1447-1
40 Zhang, R. *et al.* Spatiotemporal control of liquid crystal structure and dynamics through activity patterning. *Nat Mater* **20**, 875-882 (2021). https://doi.org:10.1038/s41563-020-00901-4
41 Shankar, S. & Marchetti, M. C. Hydrodynamics of Active Defects: From Order to Chaos to Defect Ordering. *Physical Review X* **9** (2019). https://doi.org:10.1103/PhysRevX.9.041047
42 Norton, M. M., Grover, P., Hagan, M. F. & Fraden, S. Optimal Control of Active Nematics. *Physical Review Letters* **125**, 178005 (2020). https://doi.org:10.1103/PhysRevLett.125.178005
43 Henkin, G., DeCamp, S. J., Chen, D. T., Sanchez, T. & Dogic, Z. Tunable dynamics of microtubule-based active isotropic gels. *Philos Trans A Math Phys Eng Sci* **372** (2014). https://doi.org:10.1098/rsta.2014.0142
44 Tayar, A. M., Hagan, M. F. & Dogic, Z. Active liquid crystals powered by force-sensing DNA-motor clusters. *Proc Natl Acad Sci U S A* **118** (2021). https://doi.org:10.1073/pnas.2102873118
45 Duclos, G. *et al.* Topological structure and dynamics of three-dimensional active nematics. *Science* **367**, 1120-1124 (2020). https://doi.org:10.1126/science.aaz4547
46 Lemma, L. M. *et al.* Multiscale Microtubule Dynamics in Active Nematics. *Phys Rev Lett* **127**, 148001 (2021). https://doi.org:10.1103/PhysRevLett.127.148001
47 Gao, T., Blackwell, R., Glaser, M. A., Betterton, M. D. & Shelley, M. J. Multiscale Polar Theory of Microtubule and Motor-Protein Assemblies. *Physical Review Letters* **114**, 048101 (2015). https://doi.org:10.1103/PhysRevLett.114.048101
48 Thampi, S. P., Golestanian, R. & Yeomans, J. M. Vorticity, defects and correlations in active turbulence. *Philosophical Transactions of the Royal Society A: Mathematical, Physical and Engineering Sciences* **372**, 20130366 (2014). https://doi.org:doi:10.1098/rsta.2013.0366
49 Doostmohammadi, A., Ignés-Mullol, J., Yeomans, J. M. & Sagués, F. Active nematics. *Nature Communications* **9**, 3246 (2018). https://doi.org:10.1038/s41467-018-05666-8
50 Vliegenthart, G. A., Ravichandran, A., Ripoll, M., Auth, T. & Gompper, G. Filamentous active matter: Band formation, bending, buckling, and defects. *Science Advances* **6**, eaaw9975 (2020). https://doi.org:doi:10.1126/sciadv.aaw9975
51 Bowen, W. J. & Martin, H. L. The diffusion of adenosine triphosphate through aqueous solutions. *Archives of Biochemistry and Biophysics* **107**, 30-36 (1964). https://doi.org:https://doi.org/10.1016/0003-9861(64)90265-6
52 Gagnon, D. A. *et al.* Shear-Induced Gelation of Self-Yielding Active Networks. *Phys Rev Lett* **125**, 178003 (2020). https://doi.org:10.1103/PhysRevLett.125.178003
53 Varghese, M., Baskaran, A., Hagan, M. F. & Baskaran, A. Confinement-Induced Self-Pumping in 3D Active Fluids. *Phys Rev Lett* **125**, 268003 (2020). https://doi.org:10.1103/PhysRevLett.125.268003
54 Tuval, I. *et al.* Bacterial swimming and oxygen transport near contact lines. *Proceedings of the National Academy of Sciences* **102**, 2277-2282 (2005). https://doi.org:doi:10.1073/pnas.0406724102
55 Senoussi, A., Galas, J.-C. & Estevez-Torres, A. Programmed mechano-chemical coupling in reaction-diffusion active matter. *Science Advances* **7**, eabi9865 (2021). https://doi.org:doi:10.1126/sciadv.abi9865
56 Radomsky, M. L., Whaley, K. J., Cone, R. A. & Saltzman, W. M. Macromolecules released from polymers: diffusion into unstirred fluids. *Biomaterials* **11**, 619-624 (1990). https://doi.org:https://doi.org/10.1016/0142-9612(90)90018-L

57 Saltzman, W. M., Radomsky, M. L., Whaley, K. J. & Cone, R. A. Antibody diffusion in human cervical mucus. *Biophysical Journal* **66**, 508-515 (1994). https://doi.org:https://doi.org/10.1016/S0006-3495(94)80802-1
58 Soeller, C. *et al.* Application of two-photon flash photolysis to reveal intercellular communication and intracellular Ca²⁺ movements. *Journal of Biomedical Optics* **8** (2003).
59 Casalini, T., Salvalaglio, M., Perale, G., Masi, M. & Cavallotti, C. Diffusion and Aggregation of Sodium Fluorescein in Aqueous Solutions. *The Journal of Physical Chemistry B* **115**, 12896-12904 (2011). https://doi.org:10.1021/jp207459k
60 Schnitzer, M. J. & Block, S. M. Kinesin hydrolyses one ATP per 8-nm step. *Nature* **388**, 386-390 (1997). https://doi.org:10.1038/41111
61 Coy, D. L., Wagenbach, M. & Howard, J. Kinesin Takes One 8-nm Step for Each ATP That It Hydrolyzes*. *Journal of Biological Chemistry* **274**, 3667-3671 (1999). https://doi.org:https://doi.org/10.1074/jbc.274.6.3667
62 Howard, J., Hudspeth, A. J. & Vale, R. D. Movement of microtubules by single kinesin molecules. *Nature* **342**, 154-158 (1989). https://doi.org:10.1038/342154a0
63 Aditi Simha, R. & Ramaswamy, S. Hydrodynamic Fluctuations and Instabilities in Ordered Suspensions of Self-Propelled Particles. *Physical Review Letters* **89**, 058101 (2002). https://doi.org:10.1103/PhysRevLett.89.058101
64 Guillamat, P., Hardouin, J., Prat, B. M., Ignes-Mullol, J. & Sagues, F. Control of active turbulence through addressable soft interfaces. *J Phys Condens Matter* **29**, 504003 (2017). https://doi.org:10.1088/1361-648X/aa99c8
65 Lemma, L. M., DeCamp, S. J., You, Z., Giomi, L. & Dogic, Z. Statistical properties of autonomous flows in 2D active nematics. *Soft Matter* **15**, 3264-3272 (2019). https://doi.org:10.1039/C8SM01877D
66 Kim, B. S., Lee, D. S., Ha, M. Y. & Yoon, H. S. A numerical study of natural convection in a square enclosure with a circular cylinder at different vertical locations. *International Journal of Heat and Mass Transfer* **51**, 1888-1906 (2008). https://doi.org:https://doi.org/10.1016/j.ijheatmasstransfer.2007.06.033
67 Woodhouse, F. G. & Goldstein, R. E. Cytoplasmic streaming in plant cells emerges naturally by microfilament self-organization. *Proceedings of the National Academy of Sciences* **110**, 14132-14137 (2013). https://doi.org:10.1073/pnas.1302736110
68 Bate, T. E., Jarvis, E. J., Varney, M. E. & Wu, K. T. Controlling Flow Speeds of Microtubule-Based 3D Active Fluids Using Temperature. *J Vis Exp* (2019). https://doi.org:10.3791/60484
69 Castoldi, M. & Popov, A. V. Purification of brain tubulin through two cycles of polymerization–depolymerization in a high-molarity buffer. *Protein Expression and Purification* **32**, 83-88 (2003). https://doi.org:https://doi.org/10.1016/S1046-5928(03)00218-3
70 Ndlec, F. J., Surrey, T., Maggs, A. C. & Leibler, S. Self-organization of microtubules and motors. *Nature* **389**, 305-308 (1997). https://doi.org:10.1038/38532
71 Baneyx, F. Recombinant protein expression in Escherichia coli. *Current Opinion in Biotechnology* **10**, 411-421 (1999). https://doi.org:https://doi.org/10.1016/S0958-1669(99)00003-8
72 Martin Douglas, S., Fathi, R., Mitchison Timothy, J. & Gelles, J. FRET measurements of kinesin neck orientation reveal a structural basis for processivity and asymmetry. *Proceedings of the National Academy of Sciences* **107**, 5453-5458 (2010). https://doi.org:10.1073/pnas.0914924107
73 Young, E. C., Mahtani, H. K. & Gelles, J. One-Headed Kinesin Derivatives Move by a Nonprocessive, Low-Duty Ratio Mechanism Unlike That of Two-Headed Kinesin. *Biochemistry* **37**, 3467-3479 (1998). https://doi.org:10.1021/bi972172n
74 Chen, D. T. N., Heymann, M., Fraden, S., Nicastro, D. & Dogic, Z. ATP Consumption of Eukaryotic Flagella Measured at a Single-Cell Level. *Biophys J* **109**, 2562-2573 (2015). https://doi.org:10.1016/j.bpj.2015.11.003
75 Ouellette, N. T., Xu, H. & Bodenschatz, E. A quantitative study of three-dimensional Lagrangian particle tracking algorithms. *Experiments in Fluids* **40**, 301-313 (2006). https://doi.org:10.1007/s00348-005-0068-7
76 Thielicke, W. & Stamhuis, E. J. PIVlab – Towards User-friendly, Affordable and Accurate Digital Particle Image Velocimetry in MATLAB. *Journal of Open Research Software* **2** (2014). https://doi.org:10.5334/jors.bl

CHAPTER 5: CONCLUSION In our first investigation, we explored the relationship of kinesin kinetics at the nanoscale to active fluid flow at the mesoscale. We controlled the mean speed of both gliding assays and active fluid with temperature. There is a reason temperature control techniques in *in-vivo* or *in-vitro* studies of active matter have limited representation. It changes many thermodynamic variables simultaneously: density, depletion energy, enzyme reaction rates, diffusion, viscosity, to name a few. This makes connecting measurements to underlying theory challenging. However, we overcame this challenge with the Arrhenius law, connecting mesoscale flow speed directly to activation energy[1-4]. By measuring mean speed temperature profiles, we extracted the activation energy of processive and non-processive kinesin motor systems, as well as in systems mixing both motor types. We applied this measurement to motility assays; where microtubule motion is more rigidly tied to kinesin stepping, and active fluid; where hydrodynamics play a significant role.

We found that activation energies were lower in active fluid than motility assays, showing that hydrodynamics and microtubule bundled networks serve to decrease the sensitivity of active fluid to temperature, mediating the relationship of kinesin kinetics and mesoscale flow. We found in both systems that the activation energy of non-processive motors was higher than non-processive. Kinesin kinetics are scaled by temperature, described by the Arrhenius law, because diffusion is controlled by temperature, described by the Stokes-Einstein equation[1-4]. Decreasing the diffusion time by increasing temperature means that ATP molecules will find their kinesin heads more rapidly, allowing the kinesin to step more rapidly. However, in the processive motor, one of the two kinesin heads is always anchored to the microtubule surface, decreasing the impact of diffusion by limiting the displacement of the un-anchored head to the individual motor length[5-7]. In the case of the non-processive motor, during stepping, the single head is detached; there is no local anchoring, therefore it is free to diffuse on a length scale of the motor complex, rather than just one motor length[6]. As the non-processive gliding assay and motility assay had higher activation energies; are more sensitive to temperature, this suggests that the freely diffusing non-processive motor heads are influenced more by diffusion, and that influence increases their stepping rate more rapidly as a function of temperature then for processive motors. Like Einstein in 1905, we measured a mesoscopic behavior and connected it to the behavior of constituent molecules[8].

Notably, we found that mixed processive and non-processive motors had approximately half the activation energy of the average of processive and non-processive motors in both gliding assays and active fluids. This indicates that the competition of the two motor cluster types in extensile bundle pairs is not as simple as averaging their velocities. It seems that faster processive motors dominate in the low temperature regime, whereas the slower non-processive motors dominate in the high temperature regime. This correlates with our previous conclusion, that at low temperatures, when diffusion plays less of a roll, the less diffusion and temperature sensitive processive motors dominate. When temperature is high, the diffusion sensitive non-processive motors dominate. However, kinetic mechanisms of this competition when mixed motor clusters crosslink a microtubule bundle pair remain an open question, for which future work could develop simulations based on both motor mechanics and diffusion.

We also compared the correlation of 2D gliding assay and 3D active fluid mean speeds. We found that at faster mean speeds, the non-processive, processive, and mixed motors coincided, but that at low mean speeds, when the effect of hydrodynamics decreases in 3D active fluid and the effect of diffusion increases, the processive systems diverged to be characteristically slower in the 3D active fluid. When processive motors are inactive, they are known to pause on the microtubule, causing kinesin clusters to act as passive crosslinkers when inactive[7,9-11].

Whether the mechanism of slowing the active fluid is decreasing temperature or ATP concentration, the result is that ATP molecules diffuse to kinesin less frequently. The much higher mean speeds of 3D active fluid than 2D gliding assays is due to three-dimensional network bundling and multiplication of extensile activity in active fluid[12-14]. Therefore, crosslinking has a greater relative effect on mean speed in active fluid than in gliding assays. We see that non-processive active fluid slows less at low mean speeds because non-processive motors, which can have a completely detached motor during pause, does not act as a passive crosslinker as often[6]. Lower crosslinking through the three-dimensional network means less resistance to the extensile activity of low fractions of stepping motors. Once again, we have connected mesoscale fluid activity to nanoscale kinesin kinetics to understand their role in both 2D gliding assays and 3D active fluids.

After learning the importance of diffusional transport of ATP in the coupling of nanoscale kinesin dynamics to mesoscale activity, we became curious about how flow couples to diffusional and advective mixing in active fluid. Having established temperature as an effective technique to control mean speed temporally over a bulk sample, we wanted to know if it was possible to control mean speed spatiotemporally by applying temperature gradients to active fluid, and if such mean speed gradients could enhance mixing. Passive theories of advective mixing suggest that mean speed gradients could enhance specific stretching rate and mixing efficiency over bulk flows[15,16]. In active fluid, effective diffusion of tracers is known to be coupled to the mean speed of flow[13,14]. We therefore also wanted to investigate whether mean speed gradients would enhance effective diffusion and control anomalous diffusion in active fluid.

We successfully established mean speed gradients across active fluid samples using a temperature gradient, however, we found that neither specific stretching rate, effective diffusion, nor anomalous diffusion were affected by the limited mean speed gradients we were able to obtain.

Next, we turned to light-released ATP in order to induce mean speed gradients. We found that as spatially released ATP spread through the sample, activity spread with it, creating a propagating active-passive interface. Considering this evolution from a non-uniform to uniform activity as mixing, we found that the interface progression underwent a transition from regular to super diffusive-like spreading at a critical Peclét number.

In addition, the mixing of dye spatially released alongside ATP went from slowly progressing mixing time to rapidly progressing mixing time as a function of active bulk mean speed at a similar critical Peclét number. This shows that mixing in active fluid is governed by the competition of diffusion and advection, and in non-uniform activity systems, there is a critical point at which advective transport rate overwhelms diffusive transport rate, leading to transition in mixing behavior. At moderate activity levels, we find that Fick's law, an entirely diffusive model, can recapitulate the active-inactive interface progression by mapping concentration to flow speed through Michaelis-Menton kinetics, even though any level of active flow drastically enhances effective diffusion, the progression of the active-inactive interface by transport of suspended material remains diffusive-like. Only when activity reaches sufficiently high levels does progression become advective-like, requiring accounting of hydrodynamic mixing models.

It is now well known that in active matter systems the effective diffusion coefficient is strongly controlled by activity[13,14]. In some of these systems, there is a critical time scales at which the effective diffusion transitions between different anomalous diffusive behaviors[17-19]. In order to connect advection and diffusion in active cytoskeletal networks, future studies could compare characteristic time and length scales of flow from tracer measurements and the critical time scales of diffusion measured from mean squared displacement in systems of varying activity and non-uniform activity. Furthermore, our active-passive interface work suggested that the gel-like quiescent inactive-

active fluid may require an effective melting before fluidizing, tied to the critical Péclet number observed in the non-uniform activity system for dye mixing times and active-inactive interface progression. Future work could seek to introduce a rheological field which ties viscosity to activity and ATP concentration to recover the time lag associated with effective melting.

The field of active matter is now striving to shed light on cell biology and develop useful materials, while discovering and characterizing beautiful physics[13,20-27]. Active fluid is a platform for developing our capabilities in *in-vitro* purified cytoskeletal active materials and cell simulations. At present, thorough, and direct comparisons to cell phenomenon and immediate applications are limited. However, the techniques of control and characterization lay a foundation for an active matter community that is constantly engineering new active matter systems of varying complexity and composition to simulate biological phenomena and develop materials with an ever-evolving fluency. In addition, active fluid itself may yet shed light on the self-organization of diffusive and advective transport behavior in the crowded, active, and many-constituent cytoplasm, while continuing to develop new characterization and control techniques such as the ones described earlier. The work described in this dissertation has expanded these techniques of control and characterization, and provided new insight connecting kinesin kinetics, diffusion, and advection in the context of active cytoskeletal fluid.

5.2 REFERENCES

1 Böhm, K. J., Stracke, R., Baum, M., Zieren, M. & Unger, E. Effect of temperature on kinesin-driven microtubule gliding and kinesin ATPase activity. *FEBS Letters* **466**, 59-62 (2000). https://doi.org:https://doi.org/10.1016/S0014-5793(99)01757-3

2 Hong, W., Takshak, A., Osunbayo, O., Kunwar, A. & Vershinin, M. The Effect of Temperature on Microtubule-Based Transport by Cytoplasmic Dynein and Kinesin-1 Motors. *Biophysical Journal* **111**, 1287-1294 (2016). https://doi.org:https://doi.org/10.1016/j.bpj.2016.08.006

3 Kawaguchi, K. & Ishiwata, S. Thermal activation of single kinesin molecules with temperature pulse microscopy. *Cell Motil Cytoskeleton* **49**, 41-47 (2001). https://doi.org:10.1002/cm.1019

4 Kawaguchi, K. & Ishiwata, S. i. Temperature Dependence of Force, Velocity, and Processivity of Single Kinesin Molecules. *Biochemical and Biophysical Research Communications* **272**, 895-899 (2000). https://doi.org:https://doi.org/10.1006/bbrc.2000.2856

5 Kojima, H., Muto, E., Higuchi, H. & Yanagida, T. Mechanics of single kinesin molecules measured by optical trapping nanometry. *Biophysical Journal* **73**, 2012-2022 (1997). https://doi.org:https://doi.org/10.1016/S0006-3495(97)78231-6

6 Young, E. C., Mahtani, H. K. & Gelles, J. One-Headed Kinesin Derivatives Move by a Nonprocessive, Low-Duty Ratio Mechanism Unlike That of Two-Headed Kinesin. *Biochemistry* **37**, 3467-3479 (1998). https://doi.org:10.1021/bi972172n

7 Carter, N. J. & Cross, R. A. Mechanics of the kinesin step. *Nature* **435**, 308-312 (2005). https://doi.org:10.1038/nature03528

8 Einstein, A. Über die von der molekularkinetischen Theorie der Wärme geforderte Bewegung von in ruhenden Flüssigkeiten suspendierten Teilchen. *Annalen der Physik* **322**, 549-560 (1905). https://doi.org:https://doi.org/10.1002/andp.19053220806

9 Bieling, P., Telley, I. A., Piehler, J. & Surrey, T. Processive kinesins require loose mechanical coupling for efficient collective motility. *EMBO reports* **9**, 1121-1127 (2008). https://doi.org:https://doi.org/10.1038/embor.2008.169

10 Thorn, K. S., Ubersax, J. A. & Vale, R. D. Engineering the Processive Run Length of the Kinesin Motor. *Journal of Cell Biology* **151**, 1093-1100 (2000). https://doi.org:10.1083/jcb.151.5.1093

11 Coppin, C. M., Pierce, D. W., Hsu, L. & Vale, R. D. The load dependence of kinesin's mechanical cycle. *Proceedings of the National Academy of Sciences* **94**, 8539-8544 (1997). https://doi.org:10.1073/pnas.94.16.8539

12 Prost, J., Jülicher, F. & Joanny, J. F. Active gel physics. *Nature Physics* **11**, 111-117 (2015). https://doi.org:10.1038/nphys3224

13 Henkin, G., DeCamp, S. J., Chen, D. T., Sanchez, T. & Dogic, Z. Tunable dynamics of microtubule-based active isotropic gels. *Philos Trans A Math Phys Eng Sci* **372** (2014). https://doi.org:10.1098/rsta.2014.0142
14 Sanchez, T., Chen, D. T., DeCamp, S. J., Heymann, M. & Dogic, Z. Spontaneous motion in hierarchically assembled active matter. *Nature* **491**, 431-434 (2012). https://doi.org:10.1038/nature11591
15 Ottino, J. M., Wiggins, S. R., Ottino, J. M. & Wiggins, S. Introduction: mixing in microfluidics. *Philosophical Transactions of the Royal Society of London. Series A: Mathematical, Physical and Engineering Sciences* **362**, 923-935 (2004). https://doi.org:10.1098/rsta.2003.1355
16 Ottino, J. M. Mixing, Chaotic Advection, and Turbulence. *Annual Review of Fluid Mechanics* **22**, 207-254 (1990). https://doi.org:10.1146/annurev.fl.22.010190.001231
17 Sheung, J. Y. *et al.* Motor-driven advection competes with crowding to drive spatiotemporally heterogeneous transport in cytoskeleton composites. *Frontiers in Physics* **10** (2022). https://doi.org:10.3389/fphy.2022.1055441
18 Caspi, A., Granek, R. & Elbaum, M. Diffusion and directed motion in cellular transport. *Physical Review E* **66**, 011916 (2002). https://doi.org:10.1103/PhysRevE.66.011916
19 Joo, S., Durang, X., Lee, O. c. & Jeon, J.-H. Anomalous diffusion of active Brownian particles cross-linked to a networked polymer: Langevin dynamics simulation and theory. *Soft Matter* **16**, 9188-9201 (2020). https://doi.org:10.1039/D0SM01200A
20 Doostmohammadi, A. & Ladoux, B. Physics of liquid crystals in cell biology. *Trends Cell Biol* **32**, 140-150 (2022). https://doi.org:10.1016/j.tcb.2021.09.012
21 Zhang, R., Mozaffari, A. & de Pablo, J. J. Autonomous materials systems from active liquid crystals. *Nature Reviews Materials* **6**, 437-453 (2021). https://doi.org:10.1038/s41578-020-00272-x
22 Gompper, G. *et al.* The 2020 motile active matter roadmap. *Journal of Physics: Condensed Matter* **32**, 193001 (2020). https://doi.org:10.1088/1361-648x/ab6348
23 Ramaswamy, S. Active fluids. *Nature Reviews Physics* **1**, 640-642 (2019). https://doi.org:10.1038/s42254-019-0120-9
24 Foster, P. J., Fürthauer, S., Shelley, M. J. & Needleman, D. J. From cytoskeletal assemblies to living materials. *Current Opinion in Cell Biology* **56**, 109-114 (2019). https://doi.org:https://doi.org/10.1016/j.ceb.2018.10.010
25 Doostmohammadi, A., Ignés-Mullol, J., Yeomans, J. M. & Sagués, F. Active nematics. *Nature Communications* **9**, 3246 (2018). https://doi.org:10.1038/s41467-018-05666-8
26 Ramaswamy, S. Active matter. *Journal of Statistical Mechanics: Theory and Experiment* **2017**, 054002 (2017). https://doi.org:10.1088/1742-5468/aa6bc5
27 Needleman, D. & Dogic, Z. Active matter at the interface between materials science and cell biology. *Nature Reviews Materials* **2** (2017). https://doi.org:10.1038/natrevmats.2017.48